Doctoral theses at NTNU, 2016:78

Mayilvahanan Alagan Chella

Breaking Wave Characteristics and Breaking Wave Forces on Slender Cylinders

NTNU
Norwegian University of
Science and Technology

Doctoral thesis

Mayilvahanan Alagan Chella

ISBN 978-82-471-4196-0 (printed ver.)
ISBN 978-82-326-1494-3 (electronic ver.)
ISSN 1503-8181

NTNU
Norwegian University of
Science and Technology

Doctoral theses at NTNU, 2016:78

NTNU
Norwegian University of
Science and Technology
Thesis for the Degree of
Philosophiae Doctor
Faculty of Engineering Science and Technology
Department of Civil and Transport Engineering

NTNU

Mayilvahanan Alagan Chella

Breaking Wave Characteristics and Breaking Wave Forces on Slender Cylinders

Thesis for the Degree of Philosophiae Doctor

Trondheim, April 2016

Norwegian University of Science and Technology
Faculty of Engineering Science and Technology
Department of Civil and Transport Engineering

NTNU
Norwegian University of
Science and Technology

NTNU
Norwegian University of Science and Technology

Thesis for the Degree of Philosophiae Doctor

Faculty of Engineering Science and Technology
Department of Civil and Transport Engineering

ISBN 978-82-471-4196-0 (printed ver.)
ISBN 978-82-326-1494-3 (electronic ver.)
ISSN 1503-8181

Doctoral theses at NTNU, 2016:78

Printed by NTNU Grafisk senter

To late Prof. Geir Moe and Prof. Alf Tørum

தொட்டனைத் தூறும் மணற்கேணி மாந்தர்க்குக்
கற்றனைத் தூறும் அறிவு.

-திருவள்ளுவர்
திருக்குறள்

As deep you dig the sand, spring flows
As deep you learn, knowledge grows

- Thiruvalluvar
Thirukkural

Abstract

Offshore wind farms have become an increasingly important source of clean and renewable energy. Most recent offshore wind farms are deployed close to the coast in shallow waters. One of the major factors influencing the initial investment of this technology is the design of the substructure and foundation. The physical processes associated with the non-linear shallow water hydrodynamics are rather complex since the wave motion is strongly influenced by the seabed. Breaking waves exert significant hydrodynamic loading on offshore wind turbine substructures and these impulsive loads of short duration can cause permanent structural damage.

Wave impact force characteristics greatly depend on the evolution of free surface profiles and wave height, changes in velocities, and geometric properties associated with the breaking process. Understanding hydrodynamic loads from breaking waves has many design-related implications for structures employed in shallow and intermediate waters. Although extensive experimental, theoretical and numerical research has been carried out on modelling the breaking wave forces, the breaking mechanism and their wave impact characteristics are not yet fully understood due to many parameters involved in the complex physical processes. The main aim of the present research was to investigate wave breaking in shallow waters and breaking wave forces on slender cylinders.

The open source CFD model REEF3D has been used for modelling wave breaking and computing wave breaking forces on slender cylinders in shallow waters. The model is based on the Reynolds-Averaged Navier-Stokes (RANS) equations together with the level set method for the free surface and the $k - \omega$ model for the turbulence. Numerical experiments on wave breaking on sloping sea beds and submerged structures are performed in a three-dimensional wave tank and breaking wave forces on slender cylinders are evaluated. Moreover, the numerical model is thoroughly validated against the experimental measurements for each case individually. First, the characteristics and geometric properties of wave breaking over slopes and submerged structures for different environmental parameters are examined. Comparison of the hydrodynamic characteristics and geometric properties of spilling and plunging breakers are also

presented and discussed. Breaking wave forces on slender cylinders are evaluated for solitary and periodic waves. For both cases, the influence of the relative cylinder location with respect to the breaking point on the breaking wave forces is investigated for different incident wave characteristics.

The numerical results for different cases are consistent with previous studies. A strong dependence of water depth, offshore wave steepness, and seabed slope on the breaking characteristics is observed for different slopes and submerged structures. Further, the evaluation of geometric properties of waves at breaking for different seabed conditions and wave characteristics suggests that the application of the wave steepness and asymmetry factors are appropriate for describing the breaker type and the wave profile at breaking. Analysis of breaking wave forces indicates that the relative cylinder location with respect to the breaking point has a large influence on the breaking wave force. It is seen from the results that the characteristics and geometric properties at breaking can be related to the wave impact forces from breaking waves. Moreover, the prominent flow features associated with breaking waves and their interaction with slender cylinders are reasonably well represented in the numerical simulation.

Acknowledgments

This PhD work has been carried out at the department of Civil and Transport Engineering which is supported by the Norwegian Research Center for Offshore Wind Technology (NOWITECH), Research Council of Norway (Contract no. 193823).
It is a great pleasure to express my deep gratitude to everyone who helped, guided and encouraged me in various phases of my PhD study. First of all, I sincerely would like to thank my former supervisor late Professor Geir Moe for having given this wonderful opportunity to pursue doctoral research in the field of hydrodynamics. His encouragement and help during the initial phase of my PhD were invaluable. I would also like to thank late Professor Alf Tørum for his kindness, support and motivation. Thanks to Michael Muskulus for supervising me after Geir Moe had passed away.
I wish to express my sincere appreciation to my co-supervisor Hans Bihs for his endless support, advice and encouragement throughout my doctoral study. His co-operation during all phases of my research work is gratefully acknowledged. He has inspired me to be positive and confident during my challenging PhD life. I would like to share my immense gratitude to my co-supervisor Professor Dag Myrhaug for being my teacher and mentor. He spent countless hours proofreading my research papers and discussing my research work. His kindness and support have brought me to a new place in my professional life. I am very grateful to my main supervisor Michael Muskulus for being supportive and helpful in numerous ways during the course of my PhD study. He has also provided insightful comments and suggestions on my research work.
I would like to thank Øivind Asgeir Arntsen and Knut Vilhelm Høyland for their support and encouragement. I am grateful to Sonja Marie Ekrann Hammer for her help and support during my initial stay in Norway. I am also thankful to Kjerstina Røhme, Daniel Erland, Marit Skjåk-Bræk, and Elin Mette Tønset for all the administrative help and for being so helpful and friendly.
As a member of the Wind Group, I have really enjoyed the scientific conversations about offshore wind turbines at the group meetings. A special thanks to Daniel Zwick, Sebastian Schafhirt and Chew Kok Hon for being so nice and friendly officemates. I

would also like to thank Marit Reiso, Eric Van Buren, Karl Merz, Ying Tu and Lars Einar Stieng for the nice time and discussions. I would like to thank Arun for many suggestions and the interesting discussions. I also wish to thank my fellow colleagues at the basement; Wenjun Lu, Anna Pustogvar, Wolfgang Kampel Johan Wåhlin, Andrei Tsarau, and Sergey A. Kulyakhtin. Thanks to Mohsen Bardestani and Daniele Borri for their support during the courses. A very special thanks to Navaneethan and Dhandapani for helping me get through the difficult times, and for all the emotional support. I am also thankful to my friends here in Norway Girirajasekhar, Balamurugan, Rajesh, Rengarajan, Kausic, Gireesh and Vinothkumar.

It is my pleasure to acknowledge R. Panneer Selvam from IITM, S. Nagan and T. Bhaskaran from TCE for their constant motivation and moral support. I express my deep gratitude to Appa Alagan, Annan Annamalai, Anni Prema, Anandhavalli and Senthilkumar for their love and support. I am indebted to my wife Kiruthika for being always supportive, patient and understanding. She was the witness of most of the long and not so silent struggles during my PhD. Her love, care and support have been constant source of renewal and strength in all my endeavours.

Contents

List of publications

List of research papers appended in the thesis

Paper 1 Alagan Chella, M., Tørum, A., Myrhaug, D. (2012), An overview of wave impact forces on offshore wind turbine substructures, *Energy Procedia*, Vol. 20, pp. 217-226

Paper 2 Bihs, H. Kamath A., Alagan Chella, M., Aggarwal, A., Arntsen, Ø. A. (2015), A new level set numerical wave tank with improved density interpolation for complex wave hydrodynamics, Submitted to *Computers and Fluids* - under review

Paper 3 Alagan Chella, M., Bihs, H., Myrhaug, D., Muskulus, M. (2015), Breaking characteristics and geometric properties of spilling breakers over slopes, *Coastal Engineering*, Vol. 95, pp. 4-19

Paper 4 Alagan Chella, M., Bihs, H., Myrhaug, D., Muskulus, M. (2015), Hydrodynamic characteristics and geometric properties of plunging and spilling breakers over impermeable slopes, *Ocean Modelling*, DOI: 10.1016/j.ocemod.2015.11.011

Paper 5 Alagan Chella, M., Bihs, H., Myrhaug, D. (2015), Characteristics and profile asymmetry properties of waves breaking over an impermeable submerged reef, *Coastal Engineering*, Vol. 100, pp. 26-36

Paper 6 Kamath, A., Alagan Chella, M., Bihs, H., Arntsen, Ø. A. (2015), Energy transfer due to shoaling and decomposition of breaking and non-breaking waves over a submerged bar, Submitted to *Engineering Applications of Computational Fluid Mechanics* - under review

Paper 7 Alagan Chella, M., Bihs, H., Myrhaug, D., Muskulus, M. (2015), Breaking solitary waves and breaking wave forces on a vertically mounted slender cylinder over an impermeable sloping seabed, Submitted to *Journal of Ocean Engineering and Marine Energy* - Revised version under review

Paper 8 Kamath, A., Alagan Chella, M., Bihs, H., Arntsen, Ø. A. (2015), Breaking wave interaction with a vertical cylinder and the effect of breaker location, Submitted to *Ocean Engineering* - under review

Paper 9 Bihs, H., Kamath, A., Alagan Chella, M., Arntsen, Ø. A. (2015), Breaking wave interaction with tandem cylinders under different impact scenarios, *Journal of Waterway, Port, Coastal, and Ocean Engineering*, DOI:10.1061/(ASCE)WW.1943-5460.0000343

List of research papers not included in the thesis

1 Alagan Chella, M., Bihs, H., and Muskulus, M. (2013), Numerical modeling of breaking waves over a reef with a level-set based numerical wave tank, Proceedings of the ASME 32-nd International Conference on Ocean, Offshore and Arctic Engineering (OMAE 2013), Nantes

2 Alagan Chella, M., Bihs, H., and Muskulus, M. (2014), Numerical simulation of breaking waves on a plane slope with a parallel level set solver, Proceedings of the 11-th International Conference on Hydroscience and Engineering (ICHE 2014), Hamburg, pp. 391-398

3 Alagan Chella, M., Bihs, H., and Myrhaug, D. (2015), An investigation on plunging breaking waves over a slope with a CFD based numerical wave tank, Proceedings of 36-th IAHR World Congress by International Association for Hydro-Environment engineering and Research (IAHR), Delft - The Hague, the Netherlands

4 Kamath, A., Alagan Chella, M., Bihs, H. and Arntsen Ø. A. (2015), Evaluating wave forces on groups of three and nine cylinders using a 3D numerical wave tank, *Engineering Applications of Computational Fluid Mechanics*, Vol. 9, pp. 343-345

5 Kamath, A., Bihs, H. Alagan Chella, M., and Arntsen Ø. A. (2015), CFD simulations to determine wave forces on a row of cylinders, *Procedia Engineering*, Vol. 116, pp. 623-630

6 Kamath, A., Alagan Chella, M., Bihs, H., Arntsen, Ø. A. (2015), CFD investigations of wave interaction with a pair of large tandem cylinders, *Ocean Engineering*, Vol. 108, pp. 738-748

7 Kamath, A., Bihs, H., Alagan Chella, M., Arntsen, Ø. A. (2015), Upstream and downstream cylinder influence on the hydrodynamics of a four cylinder group, *Journal of Waterway, Port, Coastal, and Ocean Engineering*, DOI:10.1061/(ASCE)WW.1943-5460.0000339

8 Kamath, A., Bihs, H. Alagan Chella, M., and Arntsen Ø. A. (2015), CFD simulations of wave propagation and shoaling over a submerged bar, *Aquatic Procedia*, vol. 4, pp. 308-316

1

Introduction

Today's energy systems are required to transform completely to meet the world's future energy demand in a sustainable way. Offshore wind energy is gaining the spotlight as a potentially huge, clean and renewable energy source. Potential shallow and intermediate water sites offer favoured locations for offshore wind turbine development. Currently, most of the offshore wind farms have been developed in shallow waters of depths between 5 to 30m. Some of the recent substructures used for offshore wind turbines are monopiles, truss towers, tripods and gravity based structures. The substructures consisting of cylindrical members are exposed to highly non-linear hydrodynamic loads from intermediate and shallow water waves including breaking waves. Recent developments in offshore wind farm development have enhanced the need for improving the current knowledge concerning the hydrodynamic loads including the wave impact from breaking waves in shallow waters.

In shallow waters, waves undergo different transformation processes such as wave shoaling, refraction, diffraction and breaking due to their non-linear interaction with the seabed. When waves propagate over a varying seabed, wave breaking is always combined with wave shoaling. In addition, the energy transfer between different wave frequency components during the process is highly non-linear. Thus, the associated hydrodynamics are rather complicated to understand when compared to wave breaking in deep water (Lin, 2008). The onset of breaking refers to a transition process between the initial wave evolution and the fully broken condition. Thus, the theoretical description of the breaking process is quite difficult, though the breaking wave characteristics can be obtained using an empirical breaking criterion (Apelt and Piorewicz, 1987; Babanin, 2011). However, the relevant underlying physical processes are not yet fully understood.

Hydrodynamic loading on substructures due to breaking waves is considered as a key criterion for their design of substructures in shallow waters (Alagan Chella et al., 2012). In particular, impulsive loads from wave breaking against substructures are generally much larger than the quasi-static forces. The impact force is characterized by a very impulsive force with a short duration. Its characteristics depend on the wave characteristics, breaker type, seabed slope and structural configuration. These large impulsive forces can cause severe damage to structural elements and affect the design or service life of a structure. Importantly, the extreme wave forces on structures are often identified with breaking waves in shallow waters.

1.1 Motivation and Objectives

This thesis is a numerical investigation of wave breaking in shallow waters and the associated breaking wave forces on slender cylinders. The open source CFD model, REEF3D (Alagan Chella et al., 2015b,a,c; Kamath et al., 2015) has been used to simulate the breaking waves and their interaction with slender cylinders. The motivation for the present research is to improve the current knowledge concerning the hydrodynamic load assessment parameters for breaking waves in shallow waters. Wave breaking in shallow waters is strongly influenced by the seabed slope, wave characteristics and water depth. This causes large impulsive hydrodynamic loads of short duration relative to the wave period. Therefore, the knowledge of breaking wave kinematics and the characteristics is inevitable for an accurate prediction of hydrodynamic loads on structures (Alagan Chella et al., 2012). In addition, one of the important factors influencing breaking wave forces is the wave profile shape, particularly, the geometry of the wave profile above the mean water level at breaking (Kjeldsen and Myrhaug, 1978). The relationship between the characteristics, kinematics and geometric properties are explored further in order to gain new insights into the wave impact force characteristics. Although the previous investigations have been conducted separately to study the characteristics (Grilli et al., 1997; Smith and Kraus, 1990), geometric and hydrodynamic aspects (Hwang, 1984; Iwagaki and Sakai, 1972; Miller and Zeigler, 1964) of wave breaking in shallow water, to the best of the author's knowledge, only few studies describe the relationship between them. Based on the above mentioned issues concerning the breaking process and their interaction with structures, the objectives of the present research are as follows:

- *Modelling of breaking waves in shallow waters:* A comprehensive modelling of breaking waves is inevitable to understand the underlying physical processes. This part deals with the validation of the numerical model for simulating breaking waves in shallow waters against the experimental data.

- *Investigation of the breaking process over slopes and submerged structures:* The

breaking process including the prominent flow features of wave breaking over different seabed conditions is different depending on the hydrodynamics involved in the physical process. This part explores the different aspects of wave breaking over sloping beaches and submerged structures.

- *Assessment of characteristics of breaking waves:* The environmental parameters have a large influence on the wave characteristics at breaking such as breaker location, breaker depth and breaker indices which are important for estimating hydrodynamic loads from breaking waves.

- *Evaluation of geometric properties of breaking waves:* The asymmetric wave profile characteristics at breaking significantly affect the breaking wave forces. This deals with a detailed description of the wave profile asymmetry at breaking for different breaking conditions.

- *Modelling of breaking wave interaction with slender cylinders:* The interaction between breaking waves and structures causes complex flow features in the vicinity of the structure including large impulsive loads, depending on the wave characteristics, the seabed and water depth conditions, the structural configurations and the wave shape at breaking. This part examines the breaking wave forces in connection with the characteristics and the geometric properties at breaking.

1.2 Thesis structure

The thesis consists of a collection of nine journal papers. Chapter 1 presents a general overview of the research context, motivation and objectives and thesis structure. Chapter 2 provides a brief background and the current status of the literature in various scientific contexts. Chapter 3 discusses the important results and presents a brief summary of each paper. Chapter 4 concludes the thesis work with some recommendations for the future work. More detailed information regarding the results of each paper is available in Chapter 6.

1.3 Author′s contribution and declaration of authorship

The thesis consists of nine research papers in which the PhD candidate is the first author of five papers (Paper 1, 3, 4, 5, and 7), the second author of two papers (Paper 6 and 8) and the third author of two papers (Papers 2 and 9). As the first author of Paper 1, 3, 4, 5, and 7, the PhD candidate conducted all the numerical simulations, calculations and analysis of results and wrote the complete manuscript. As the second author of Paper 6 and 8, the PhD candidate was involved in all the scientific discussions and contributed to the scientific part and proofreading of the manuscript. As the third author of Paper 2, the PhD candidate contributed with the simulation and the scientific part related to the

breaking waves and proofreading of the manuscript. As the third author of Paper 9, the PhD candidate contributed with the discussion of research outcomes and proofreading of the manuscript. For all the papers (except Paper 1), the co-author Hans Bihs contributed with the open source CFD (computational fluid dynamics) model REEF3D and with proofreading of the manuscripts. He also advised the PhD candidate concerning the pre-processing and post-processing of the numerical simulations. The PhD research has been done under the supervision of Prof. Michael Muskulus, Prof. Dag Myrhaug and Dr. Hans Bihs. The detailed contribution of co-authors to each of the appended papers are presented below:

Paper 1

An overview of wave impact forces on offshore wind turbine substructures

Alagan Chella, M., Tørum, A. Myrhaug, D. (2012), *Energy Procedia*, Vol. 20, pp. 217-226

This paper provides an overview of the theoretical, experimental and numerical studies on wave impact forces relevant to offshore wind turbine substructures. In addition, the paper discusses the recommendations by the standards to estimate loads from breaking waves and addresses the issues related to the performance of offshore wind turbine structures. Importantly, the study also highlights the inadequacies in the previous load assessment methods for breaking waves.

The PhD candidate contributed the main idea of the study and carried out the complete literature study. He collected all necessary data from previous studies and wrote the paper. Tørum, A. and Myrhaug, D. contributed through scientific discussions and proofreading of the manuscript.

Paper 2

A new level set numerical wave tank with improved density interpolation for complex wave hydrodynamics

Bihs, H., Kamath A., Alagan Chella, M., Aggarwal, A., Arntsen, Ø. A. (2015), Submitted to *Computers and Fluids* - under review

The paper presents the numerical approaches employed in the three-dimensional numerical wave tank REEF3D. The model uses different numerical approaches for the grid architecture, numerical discretization and wave generation and absorption. In order to achieve the realistic representation of the free surface, higher order numerical schemes are employed in the numerical model. The model is fully parallelized and the

parallel efficiency is studied in detail for two- and three-dimensional cases. Numerical simulations of four different test cases are performed to evaluate the performance of the model. The test cases are wave interaction with a rectangular abutment, wave shoaling over a submerged bar and breaking waves over a slope. Good agreement is obtained between the computational results and experimental data.

The PhD candidate contributed to the paper with the simulations and scientific part regarding plunging breaking waves over a slope. He was involved in the testing of numerical parameters for the numerical wave tank and validation of the numerical model for breaking waves during the various phases of the code development. He was also engaged in all scientific discussions and proofreading of the manuscript. The first author Bihs, H. built the numerical model performed the simulations and calculations regarding rectangular abutment. He organized the scientific parts and wrote a major part of the paper. The co-author Kamath, A. contributed to the simulations and scientific part regarding scaling tests and wave forces on cylinder and proofreading of the manuscript. The co-author Aggarwal, A. contributed with the simulations and results regarding the submerged bar case. The co-author Arntsen, Ø. A. contributed through scientific discussion of results and proofreading of the manuscript.

Paper 3

Breaking characteristics and geometric properties of spilling breakers over slopes

Alagan Chella, M., Bihs, H., Myrhaug, D., Muskulus, M. (2015), *Coastal Engineering*, Vol. 95, pp. 4-19 (**Sim 1 in Table 1.1**)

The paper deals with the simulation of breaking waves over slopes. The main concern of the study is to investigate the influence of seabed slope, water depth and wave steepness on the characteristics and geometric properties of breaking waves. The numerical model is validated through the comparison of numerical results with the experimental data reported by Ting and Kirby (1996). The free surface deformations and kinematics during the wave breaking are also studied. Moreover, the experimentally observed flow features are very well captured in the numerical simulations.

The PhD candidate designed and performed all the simulations including the validation of the numerical model. He carried out the post-processing and analysis of the numerical results, interpreted data and wrote the paper. The co-author Bihs, H. was involved in all scientific discussions and contributed with the numerical model. The co-authors Myrhaug, D. and Muskulus, M. contributed through scientific discussions and the proofreading of the manuscript.

Paper 4

Hydrodynamic characteristics and geometric properties of plunging and spilling breakers over impermeable slopes

Alagan Chella, M., Bihs, H., Myrhaug, D., Muskulus, M. (2015), *Ocean Modelling*, DOI:10.1016/j.ocemod.2015.11.011, In press (**Sim 1 in Table 1.1**)

The paper compares the hydrodynamics characteristics and geometric properties of spilling and plunging breakers. The study includes the wave height evolution and attenuation, horizontal and vertical velocity, free surface profile evolution, and the geometric properties during the development of the breaking process. The numerical results are in good agreement with the experimental data by Ting and Kirby (1996) for free surface elevation and horizontal and vertical components of velocity, wave envelope and turbulent intensities for the spilling and plunging breakers. It is found that the free surface deformations of spilling breakers similar to plunging breakers during the breaking process, but this occurs at different scales.

The PhD candidate conceived and designed all the numerical simulations and executed the study. He is responsible for the post-processing and analysis of the simulation results and wrote the paper. The co-author Bihs, H. contributed with the numerical model and manuscript evaluation. The co-authors Myrhaug, D. and Muskulus, M. supervised the work and contributed with the proofreading of the manuscript.

Paper 5

Characteristics and profile asymmetry properties of waves breaking over an impermeable submerged reef

Alagan Chella, M., Bihs, H., Myrhaug, D. (2015), *Coastal Engineering*, Vol. 100, pp. 26-36 (**Sim 2 in Table 1.1**)

The paper presents the numerical study of waves over a submerged reef. The model performance is evaluated by comparing the laboratory measurements by Blenkinsopp and Chaplin (2008) with the computed results for free surface elevations, breaker depth index and breaker height index. The study further examines the role of the offshore wave steepness and the water depth over the reef crest on the breaker characteristics and geometric properties. It is found that the water depth over the reef crest plays a significant role in determining the breaker types and breaker characteristics.

The PhD candidate planned and executed the numerical simulations in the study. He analysed and interpreted the numerical data and wrote the paper. The co-author Bihs, H.

and Myrhaug, D. supervised the work and helped to evaluate and edit the manuscript.

Paper 6

Energy transfer due to shoaling and decomposition of breaking and non-breaking waves over a submerged bar,

Kamath, A., Alagan Chella, M., Bihs, H., Arntsen, Ø. A. (2015), Submitted to *Engineering Applications of Computational Fluid Mechanics* - under review (**Sim 3 in Table 1.1**)

The paper describes the simulation of shoaling and decomposition of breaking and non-breaking waves over a submerged bar. The simulated transformations of breaking and non-breaking results show a good agreement with the experimental data by Beji and Battjes (1993) for free surface elevations measured at eleven different locations along the tank. Further, the spectral analysis of wave transformation over a submerged bar is performed for both breaking and non-breaking cases. The development of free surface for spilling and plunging breaker is presented and discussed.

The PhD candidate was involved in scientific discussions of the numerical results. He contributed to the scientific part related to breaking waves and proofreading of the manuscript. He also helped the first author during the simulation and analysis of breaking waves. The first author Kamath, A. conducted all the simulations and calculations and wrote the paper. The co-author Bihs, H. contributed with the numerical model and valuable scientific discussions regarding the numerical results. The co-author Arntsen, Ø. A. contributed to the proofreading and discussion of results.

Paper 7

Breaking solitary waves and breaking wave forces on a vertically mounted slender cylinder over an impermeable sloping seabed

Alagan Chella, M., Bihs, H., Myrhaug, D, Muskulus, M. (2015), Submitted to *Journal of Ocean Engineering and Marine Energy* - Revised version under review (**Sim 4 in Table 1.1**)

The paper presents the numerical simulation of solitary wave breaking over a steep slope and its interaction with a vertical slender cylinder. Comparison between the numerical results and the experimentally measured free surface elevations, velocities, free surface profiles and the numerically computed breaking wave forces by Mo et al. (2013) shows good agreement. The main concern of the paper is to investigate the influence of the characteristics and geometric properties of breaking solitary waves, the wave impact scenarios and the incident wave characteristics on the breaking wave force

characteristics. The maximum total force occurs when the cylinder is placed just before the breaking point and the local wave height is same as the wave height breaking with relatively less steep wave front.

The PhD candidate conceived and performed the numerical simulations. He carried out the post-processing and analysis of the numerical data and wrote the paper. The co-author Bihs, H. contributed with the numerical model and helped to evaluate and edit the manuscript. The co-author Myrhaug, D. supervised development of work and contributed with the proofreading of the manuscript. The co-author Muskulus, M. contributed with the proofreading of the manuscript.

Paper 8

Breaking wave interaction with a vertical cylinder and the effect of breaker location

Kamath, A., Alagan Chella, M., Bihs, H., Arntsen, Ø. A. (2015), Submitted to *Ocean Engineering* - under review (**Sim 5 in Table 1.1**)

The paper deals with interaction of breaking waves with a slender cylinder and the numerical results are compared with the laboratory measurements by Irschik et al. (2002). The study examines the effect of the breaker location on the total breaking wave force on a cylinder by considering five different breaking wave impact scenarios. It is found that the maximum total force occurred when the wave breaks in front of the cylinder i.e. the overturning wave front impinges on the surface of the cylinder just below the crest level.

The PhD candidate contributed to this work by helping the first author during the simulations and analysing the breaking wave results. The candidate contributed to the scientific part related to breaking waves and proofreading of the manuscript. The first author Kamath, A. performed all the simulations and calculations and wrote the paper. The co-author Bihs, H. contributed with the numerical model, scientific discussions regarding the numerical results and manuscript evaluation. The co-author Arntsen, Ø. A. contributed with scientific discussion of results and the proofreading of the manuscript.

Paper 9

Breaking wave interaction with tandem cylinders under different impact scenarios

Bihs, H., Kamath, A., Alagan Chella, M., Arntsen, Ø. A. (2015), *Journal of Waterway, Port, Coastal, and Ocean Engineering*, DOI: 10.1061/(ASCE)WW.1943- 5460.0000343 (**Sim 6 in Table 1.1**)

This numerical study investigates breaking wave interaction with tandem cylinders under different wave impact scenarios. In the study, four different impact scenarios and six different spacing between the cylinders are studied. The downstream cylinder experience maximum force when wave breaks behind the upstream side cylinder. Most prominent free surface features around the cylinder during the interaction with breaking waves are reasonably represented in the numerical simulations.

The PhD candidate provided the technical inputs, and contributed with scientific discussion of results regarding breaking waves and forces and proofreading of the manuscript. The first author Bihs, H. organized the scientific content and wrote a major part of the paper. The co-author Kamath, A. conducted all the simulations, contributed to a significant scientific part of the paper. The co-author Arntsen, Ø. A. contributed to the proofreading of the manuscript.

Sim. Nos.	Papers	Description	Computational set-up
Sim 1	Paper 3 & 4	Wave breaking over slopes	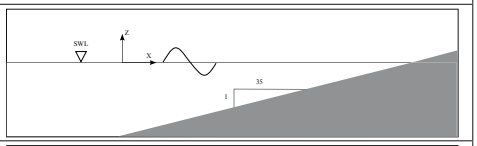
Sim 2	Paper 5	Wave breaking over a submerged reef	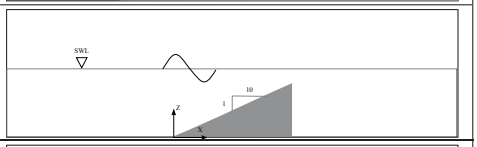
Sim 3	Paper 6	Wave breaking over a submerged bar	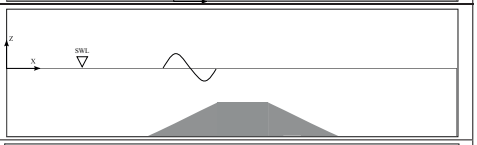
Sim 4	Paper 7	Breaking solitary wave forces on a slender vertical cylinder	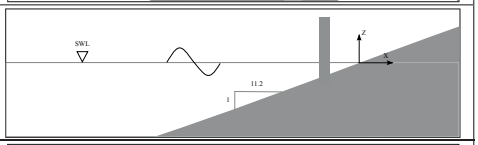
Sim 5	Paper 8	Breaking wave forces on a slender vertical cylinder	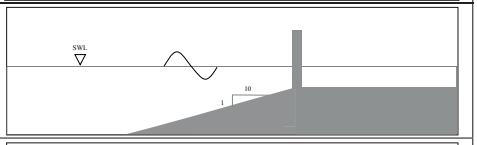
Sim 6	Paper 9	Breaking wave forces on slender vertical cylinders	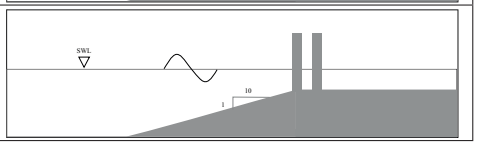

Table 1.1: List of simulation cases

2

Background and state of the art

Wave breaking is a natural process involving transformation of wave energy into turbulent energy leading to a violent transformation of the free surface, that exerts massive hydrodynamic loads on marine structures (Cokelet, 1977). It is a complex two-phase flow process and it is strongly influenced by the air-water interaction. A comprehensive examination of breaking wave properties is inevitable to understand the wave breaking mechanisms and thus, the description of the breaking process. In particular, an accurate description of breaking waves has always been a central issue in estimation of hydrodynamic loads on marine structures. In order to encompass all relevant aspects of breaking waves, this chapter is divided into seven sections. The first and second sections present some background concerning breaking waves and their characteristics and geometric properties. The third and fourth sections explore the theoretical description of breaking waves and breaking wave forces, respectively. Further, the fifth and sixth sections review the relevant literature on the numerical modelling of breaking waves and breaking wave forces, respectively. Finally, the seventh section presents the computational methods and approaches used in the present numerical investigation.

2.1 Breaking waves

As waves approach the shore from deep water, the water depth (d) to wave length (L) ratio decreases. When the water depth is larger than half the wave length (d/L >1/2), the waves corresponding to this water depth are deep water waves since the wave motion is unaffected by the seabed and their celerity depends on the wave length. As the wave length is larger than the water depth i.e. d/L <1/20, the wave motion interferes with the seabed. Then the waves at this water depth are shallow water waves and their celerity is

mainly determined by the water depth. However, in the case of waves in intermediate water depth i.e. 1/20 < d/L <1/2, the wave motion is partially affected by the seabed and their celerity partly depends on both the wave length and water depth (Chakrabarti, 1987). The seabed interaction with waves becomes more significant and the waves decelerate as they enter into shoaling waters. As a result, the wave height and particle velocity at the wave crest increase and the wave length and celerity decrease. This causes the upper part of the wave close to the free surface to propagate much faster than the lower part of the wave near the seabed as the wave motion is retarded by the seabed interaction. Further, the deformation of the wave crest continues until it becomes too steep, unstable and eventually breaks. Numerous studies have reviewed wave breaking including the physical features related to the breaking process in deep and shallow waters (Banner and Peregrine, 1993; Basco, 1985; Cokelet, 1977; Peregrine, 1983; Perlin et al., 2013; Vinje and Brevig, 1981).

2.1.1 Breaking criterion

The theoretical breaking criteria in deep water is always related to the physical properties of the highest steady wave, which limits the wave growth. Whereas, in shallow waters, waves deform as they propagate into decreasing water depth, the effects of sea bottom and shoaling are included as additional terms in defining the breaking criteria. The kinematic criterion was defined by Rankine (1864) and refers to that the horizontal particle velocity at the crest exceeds the phase velocity, applied both to the highest steady waves and the shoaling waves. Miche's criterion for periodic waves breaking in finite water depth is an extension of Stokes theory which limits the wave geometry when the wave steepness reaches H/L=0.142 tanhkd (H, L, k and d are local wave height, wave length, wave number and water depth, respectively) with the enclosed crest angle of 120^0 (Battjes, 1974). Another aspect of the geometric breaking criterion of shallow water waves is that the surface slope becomes infinite, indicating a vertical wave surface. The dynamic criterion is when the downward vertical water particle acceleration exceeds half of the gravitational acceleration. Wave breaking is also related to the local relative growth rates of mean momentum and energy densities (Banner and Tian, 1998). Peregrine et al. (1980) studied the fluid properties in the overturning wave crest when the wave approaches breaking. The authors found high orbital velocities near the wave crest region, high accelerations on the forward face of the wave, and low accelerations on the rear face of the wave.

2.1.2 Wave breaking mechanisms and breaker types

A number of physical processes involving the exchange of mass, momentum and energy between air and water emerge during the wave breaking process. Importantly, there are two completely different physical mechanisms that need to be understood during the

breaking process from the onset of breaking to fully broken waves in the surf zone. One mechanism deals with the evolution of wave height and wave energy before breaking during the initial breaking process up to the breaking point. The other mechanism governs the wave height attenuation and the energy dissipation after breaking in the surf zone. In addition, the wave loses almost more than half of its height after breaking and the energy dissipation occurs rapidly for plunging breakers and slowly for spilling breakers (Miller, 1987).

According to Svendsen et al. (1978), the surf zone can be subdivided into three regions:

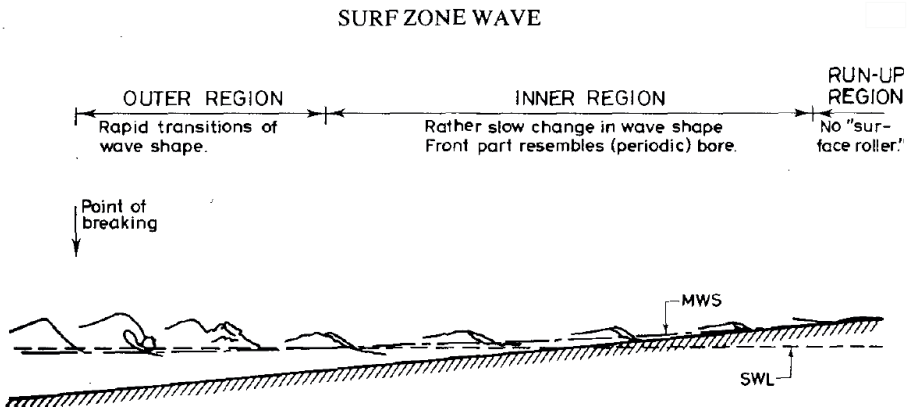

Figure 2.1: A definition sketch of wave characteristics in the surf zone following Svendsen et al. (1978)

outer, inner and run-up region, based on the physical processes involved as shown in Fig. 2.1. As a wave approaches the shore, the front of the wave becomes progressively steeper until the wave front becomes vertical with the flattened wave trough and the wave front overturns and eventually the wave breaks. Consequently, a significant change in the initial wave characteristics occurs rapidly. The outer region refers to the transition from the organized irrotational flow into the rotational flow with considerable changes in the large scale flow characteristics. Further, the overturned wave crest falls down forward into the wave trough and causes a portion of the fluid in trough to flow seaward with the forward motion of the wave front. As a result, a rotating vortex with an air pocket is generated inside the wave and a surface roller at the free surface which propagates with a speed equal to the wave speed as shown in Fig. 2.2. Peregrine (1983) and Basco (1985) pointed out that the main sources of turbulence arises from the translation of the plunger vortex seaward and the surface roller shoreward. Peregrine and Svendsen (1978) indicated that the origin of turbulence starts at the toe of the surface roller and

this spreads downwards from the free surface.

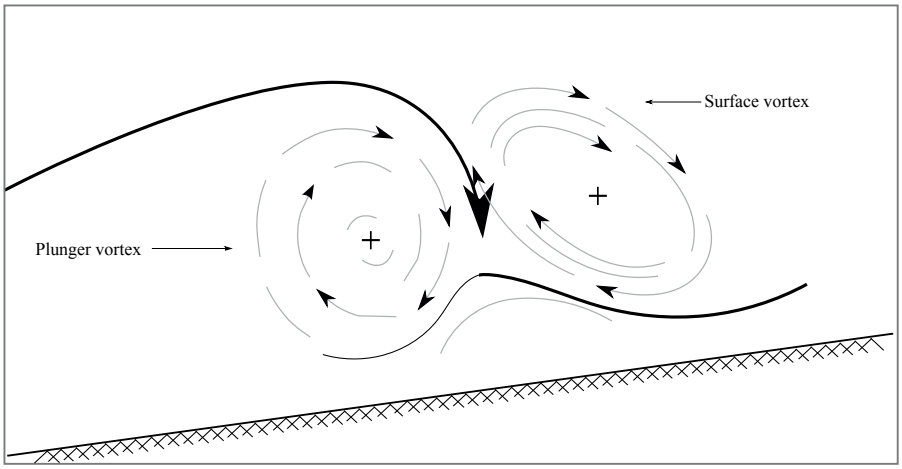

Figure 2.2: A schematic sketch of plunger vortex and surface vortex during breaking (Basco, 1985)

On a plane slope, the breaker type is strongly governed by the seabed slope and incident wave characteristics and it describes the wave profile shape at breaking (Battjes, 1974; Galvin, 1968; Iversen, 1952). The breaker types can be identified based on the surf similarity parameter, $\xi = \frac{m}{\sqrt{H_0/L_0}}$ (where m is the seabed slope and H_0 and L_0 are wave height and wave length in deep water, respectively) suggested by Battjes (1974): spilling ($\xi < 0.5$), plunging ($0.5 < \xi < 3.3$), surging or collapsing ($\xi > 3.3$). Although most of the development features and vortex formations of spilling and plunging breakers are similar, the magnitude of the vortices is significantly different (Basco, 1985; Miller, 1987). In general, the wave crest curls over and generates vortices at the free surface. The dissipation rate due to breaking depends on the size and strength of the vortices (Miller, 1987). The vortices from plunging breakers are larger compared to the water depth, penetrating downward to the bottom with a larger vertical mixing rate. For spilling breakers, the vortices are smaller, detaining close to the free surface region with slow vertical mixing rates (Miller, 1987; Ting and Kirby, 1996). Consequently, spilling breakers have smaller length and velocity scales, since the energy transfer rate due to turbulent motion is smaller than for plunging breakers. Wave height attenuation in the surf zone is gradual for spilling breakers, whereas it is rapid for plunging breakers. In fact, for plunging breakers the main contribution to turbulence production is from both the surface roller and the plunger vortex (Basco, 1985) as shown in Fig. 2.2, while

for spilling breakers the main turbulence contribution is only from the surface roller. Comparison of hydrodynamic characteristics of spilling and plunging breakers over a sloping seabed is presented and discussed in paper 4.

2.1.3 Characteristics of breaking waves

A wave propagating in shallow water begins to shoal and thus, the local wave steepness increases continuously until the breaking point. At the incipient breaking, the wave height reaches its maximum value. Specifically, the breaker height (H_b) and breaker water depth (d_b) (Fig. 2.3) are the important design parameters for evaluating the hydrodynamic loads from breaking waves. Previous studies have reported the relationship between the incident wave characteristics and the breaking wave characteristics in terms of breaker indices (Goda, 2010; Iwagaki and Sakai, 1972; Tsai et al., 2005; Weggel, 1972). The

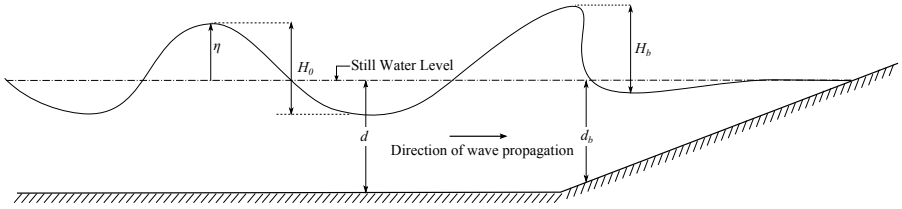

Figure 2.3: A schematic sketch of the wave profile at breaking

breaker depth index and the breaker height index are functions of water depth, wave period and seabed slope. The breaker depth index γ_b is the ratio of the breaker height (H_b) to the breaker depth (d_b):

$$\gamma_b = \frac{H_b}{d_b} \tag{2.1}$$

This describes the non-dimensional wave height at breaking and this is larger for wave breaking farther shoreward at a shallower water depth. The breaker height index, Ω_b is the ratio of the breaker height H_b to offshore wave height H_0:

$$\Omega_b = \frac{H_b}{H_0} \tag{2.2}$$

2.2 Geometric properties of breaking waves

When a wave propagates over a uniform seabed slope, the wave motion is restricted by the seabed interaction resulting in a steepened wave crest and a flattened wave trough. Thus, the wave reaches the breaking point with an asymmetric profile. The geometrical

description of the local wave profile at breaking requires more detailed parameters as the global wave steepness (H/L) is not sufficient to describe the asymmetric profile. This has been studied experimentally in deep waters (e.g. Bonmarin (1989); Kjeldsen and Myrhaug (1978); Lader (2002)) and in shallow waters (e.g. Adeyemo (1968); Hwang (1984); Ippen and Kulin (1954); Iwagaki and Sakai (1972); Miller and Zeigler (1964)). Kjeldsen and Myrhaug (1978) investigated the geometry of the wave profile at breaking in deep water with the steepness and asymmetry factors; crest front steepness (ε=η'/L'), crest rear steepness (δ=η'/L"), vertical asymmetry factor (λ=L"$/L'$) and horizontal asymmetry factor (μ=η'/H) as illustrated in Fig. 2.4. The authors categorized the breaker types based on the steepness and asymmetry factors. Further, the geometric properties were related to the breaking wave forces on ships and floating structures in deep water. They also identified the upper and lower bound values of the steepness and asymmetry parameters for the plunging breakers in deep waters:

$$0.32< \varepsilon <0.78$$
$$0.26< \delta <0.39$$
$$0.90< \lambda <2.18$$
$$0.84< \mu <0.95$$

The first systematic study of geometric properties of breaking waves in shallow waters was performed by Ippen and Kulin (1954). Miller and Zeigler (1964) classified breakers based on an asymmetric shape of wave profile at breaking as: symmetric, asymmetric and intermediate. Further, this has been extensively studied by Adeyemo (1968) including the effect of beach slope on the geometric properties. The authors describe the wave geometry at breaking as: wave vertical asymmetry, wave slope asymmetry and wave horizontal asymmetry. Iwagaki and Sakai (1972) examined the effect of the beach slope in the wave transformation and the geometric properties of waves approaching breaking. Hwang (1984) used the steepness and asymmetric properties proposed by Kjeldsen and Myrhaug (1978) for deep waters to investigate the asymmetric properties of waves on a mild slope. In the same way, the present study uses the steepness and asymmetry factors to examine the geometric properties of breaking waves in shallow waters as proposed by Kjeldsen and Myrhaug (1978).

2.3 Theoretical description of breaking waves

The theoretical knowledge of breaking periodic waves in shallow waters was initially based on solitary wave theory proposed by John Scott Russell (1834) (Miles, 1980). Later, Airy proposed the non-dispersive shallow water equations for waves with finite amplitudes over a gentle slope by neglecting the water particle acceleration with an assumption that the pressure at any point to be equal to the hydrostatic head. The author also showed that the wave transformation in shallow waters leads to the steepened wave

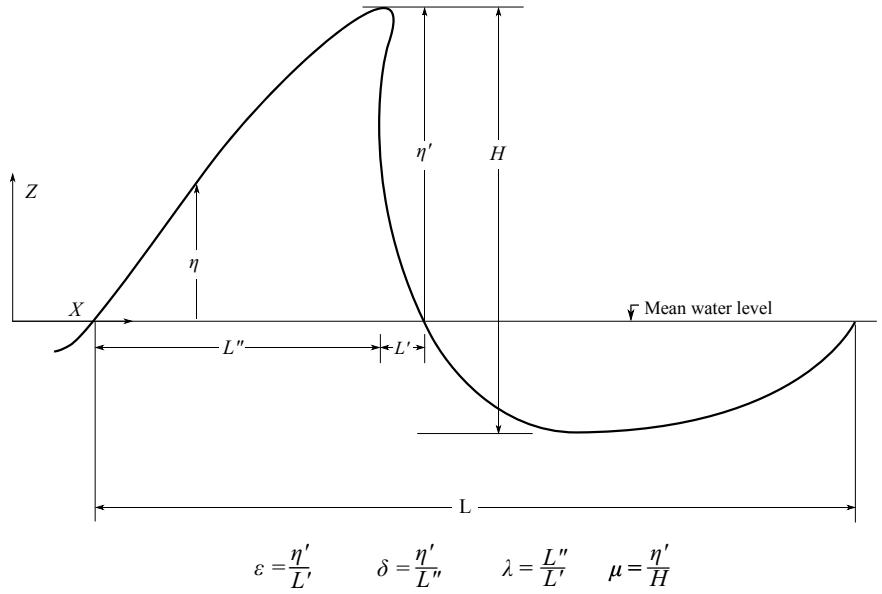

Figure 2.4: A definition sketch of the local steepness and asymmetry factors Kjeldsen and Myrhaug (1978)

front over constant water depth with the maximum particle velocity at the crest top (Peregrine, 1983). The upper part of the wave propagates faster than the lower part of the wave at a velocity that equals the long wave velocity with the horizontal component of water particle velocity as follows:

$$u_{crest} = \sqrt{g(d+\eta)} + u \tag{2.3}$$

where g is the acceleration due to gravity, and u is the horizontal component of water particle velocity. As a result the front face of the wave becomes more steep and this affects the pressure distribution under the wave crest. This has been pointed out by Boussinesq (1871) and Rayleigh (1876) (Miles, 1980). The Boussinesq equations for solitary wave propagation include an additional dispersive term in order to counterbalance the changes in the vertical accelerations due to the wave steepening. The breaking onset was first identified by Stokes (1880) in terms of wave height (H) and wave length (L) as $H/L = 0.141$ with an included crest angle of 120^0. Korteweg and de Vries (1895) developed a shallow water theory based on the Boussinesq equations to describe periodic dispersive long waves. The stability of the KdV equations for a solitary wave

was demonstrated by Benjamin (1972). Sverdrup and Munk (1944) proposed a wave breaking theory based on the steady solitary waves and, later this method was extended to study waves in the surf zone by Munk (1949). A different theoretical approach developed by Stoker (1949) to the periodic wave breaking in shallow waters based on the theory of gas dynamics dealing with the compressible flow of a gas.

As mentioned in Sec. 2.1.2, the important characteristics of waves in the surf zone is the formation of the surface roller at the free surface on the wave front and it propagates shoreward. Svendsen (1984) developed a two-dimensional theoretical model for predicting wave heights and set-up in the surf zone using the surface roller concept. Madsen and Svendsen (1983) modelled turbulent bores and hydraulic jumps using a theoretical approach together with the $k - \epsilon$ model to account for the non-equilibrium in the turbulent kinetic energy. The study was focussed only on a bore of a permanent form with the assumption of steady flow. A theoretical approach was developed by Svendsen and Madsen (1984) to describe the velocity distribution, the energy dissipation and flow features associated with a turbulent bore in the surf zone. They extended the non-linear finite amplitude shallow water equations to include the effect of turbulence in the flow with the $k - \epsilon$ model. A recent study by Yamazaki et al. (2008) attempted to model solitary wave breaking and run-up using the non-linear shallow water equations by describing weakly dispersive waves with a non-hydrostatic pressure term. In addition, the model was able to represent the breaking onset without any empirical or dissipation coefficients for wave breaking. However, the numerical model was not validated for modelling the turbulent characteristics and free surface deformation of waves in the surf zone.

Wave theories are appropriate in describing the transformation of waves of small amplitudes over a uniform beach which do not consider the vertical variation of quantities. They cannot describe the complete wave breaking process due to the underlying approximations, such as the irrotationality, two-dimensional motion, horizontal seabed and hydrostatic pressure assumption (Babanin et al., 2010). Even though the wave evolution aspect of long waves in shallow water is well represented by shallow water theory until incipient breaking, the theory breaks down when the wave surface becomes very steep or vertical. Most of the theoretical models do not account for the backwash or return flow effects in the breaking process, as this would affect the evolution of free surface waves approaching breaking.

2.4 Theoretical evaluation of breaking wave forces

Laboratory experiments have contributed to a large extent to the present knowledge of wave breaking forces on slender cylinders and the associated flow features around

them (e.g. Arntsen et al. (2011); Chaplin et al. (1992); Goda et al. (1966); Sawaragi and Nochino (1984); Wienke and Oumeraci (2005)). However, measurements of velocity and acceleration under breaking waves and their interaction with structures in the controlled experiments are more demanding. In general, wave forces on a slender cylinder from non-breaking waves can be estimated with the Morison equation (Morison et al., 1950). The equation describes the force in terms of the quasi static inertia and drag forces based on the empirical force coefficients as follows:

$$F_{quasi} = F_D + F_M = \frac{1}{2}\int_{-d}^{\eta} \rho_w C_D D u|u| dz + \int_{-d}^{\eta} \rho_w C_M \frac{\pi D^2}{4}\frac{\partial u}{\partial t} dz \qquad (2.4)$$

where F_D is the drag force, F_M is the inertia force, C_D is the drag coefficient, C_M is the inertia coefficient, D is the diameter of the structure, u is the horizontal component of particle velocity, d is the water depth, and η is the instantaneous wave surface elevation. When a wave propagates in shoaling waters, the wave crest height

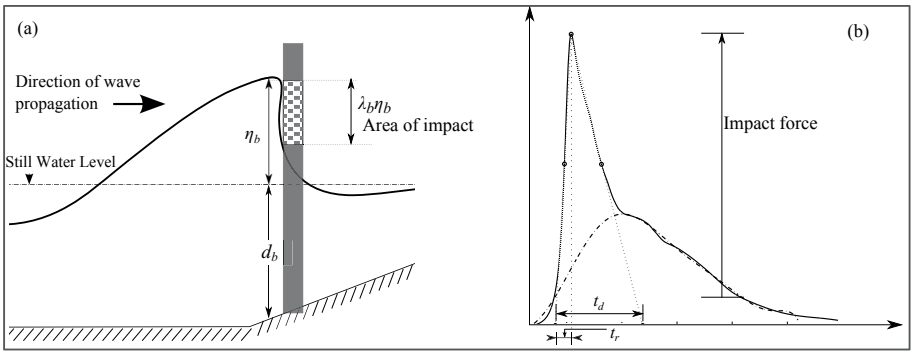

Figure 2.5: A definition sketch of (a) the wave impact scenario and (b) the characteristics of impact force; t_d and t_r are the duration and rise time of the impact.

increases with a steeper wave front and thus the forward momentum of the wave front increases. Specifically, the slope of the wave front increases until the wave breaks, therefore, the wave front becomes nearly vertical at the breaking point especially for the plunging breaker. When the vertical wave front impacts the surface of a structure (Fig. 2.5 (a)) causes a sudden drop in the forward momentum which in turn exerts an impact force of very short duration generally of the order of milliseconds (Goda et al., 1966) (Fig. 2.5 (b)). In addition, the shape of the wave surface at the instant of the wave impact plays a significant role in describing the impact force. In the case of a wave close to breaking in shallow water, the maximum particle velocity occurs at the crest, and thus

the force contribution from the crest is larger than the contribution from the rest of the wave. Therefore, the mechanism of the wave impact mainly depends on the shape of the wave front and the wave celerity at breaking.

The first theoretical model for calculating the wave impact forces was proposed by von Karman (1929). The author derived the impact force equation from the Bernoulli equation for the pressure on the body by neglecting the hydrostatic pressure term and the kinetic energy term. In addition, the free surface deformation along the surface of a structure during the impact, i.e. pile-up effect is not considered which significantly influences the duration and magnitude of the impact force (Tanimoto et al., 1986). The Wagner theoretical model included the pile-up effect and thus, the added mass is also accounted for. The total wave force on a vertical cylindrical pile from breaking waves is described by Goda et al. (1966) based on the von Karman's theory in terms of the quasi-static force (F_D+F_M) and the wave impact force (F_I). In fact, the force components in the Morison equation (Eq. 2.4) are not sufficient to represent the total breaking wave force. Therefore, an impact force term is required in addition to the quasi-static force components to describe the wave impact force of very short duration from breaking waves.

$$F = F_D + F_M + F_I \tag{2.5}$$

$$F_I = \frac{1}{2}\rho_w \pi D \lambda_b \eta_b {C_b}^2 (1 - \frac{2C_b}{D}t) \tag{2.6}$$

where λ_b is the curling factor, η_b is the wave surface elevation at the time of impact above still water level, and C_b is the breaking wave celerity. The curling factor λ_b is a function of the breaker type which signifies the contribution of the wave crest to the impact force. Moreover, the term $\lambda_b \eta_b$ represents the height of the vertical wave front during the wave impact (Fig. 2.5 (a)). The authors defined λ_b in terms of the seabed slope and the relative water depth based on the laboratory experiments for the slopes 1/10 and 1/100. Goda et al. (1966) suggested the maximum λ_b as 0.1 for spilling breakers and 0.4 for plunging breakers (Sawaragi and Nochino, 1984). Wienke and Oumeraci (2005) proposed a theoretical model based on the Wagner theory and they validated the model with the large scale experimental measurements. The experiments were focussed only on plunging breakers in deep waters and the waves were generated using Gaussian wave packets. Irschik et al. (2004) used the model by Wienke and Oumeraci (2005) to estimate the breaking wave loads on a slender cylinders in shallow water. However, the evaluation of the impact solely depends on the wave celerity and the curling at the wave impact which have to be determined from the laboratory experiments.

An overview of the effects of wave impact forces from breaking waves on offshore wind turbine substructures is presented in paper 1. The paper discusses simplified methods to calculate hydrodynamic loads from breaking waves followed by the theoretical description of impact force proposed by Goda et al. (1966). Further, the paper provides an overview of theoretical, experimental and numerical approaches concerning the modelling of wave impact forces. In addition, the design guidelines for calculating the wave impact forces are also discussed. Finally, the paper addresses the effects of the wave impact forces on the design of offshore wind turbine substructures.

2.5 Numerical modelling of breaking waves

2.5.1 Models based on Boussinesq equations

The Boussinesq equations provide a good prediction of non-linear wave transformation of waves including shoaling, refraction, diffraction, and reflection from deep to shallow water especially for solitary wave propagation in a uniform water depth. Later, Peregrine (1967) improved the equations based on depth averaged velocity to take the water depth variations into account. The dispersive properties of the equations were further developed by Madsen et al. (1991) for relatively deep waters and irregular waves.The authors also proposed a numerical approach for solving the equations based on a time-centred implicit finite-difference scheme. Nwogu (1993) extended the Boussinesqe equations and Wei et al. (1995) proposed the fully non-linear Boussinesq equations to model nearly breaking waves in shallow waters. However, these models do not account for the effects of seabed friction and wave breaking. Wei and Kirby (1996) improved the models by adding an energy dissipation term to the extended Boussinesq equations. Some studies used the classical Boussinesq equations together with the surface roller concept Svendsen (1984) to model regular and irregular wave breaking e.g. Schäffer et al. (1993) and Madsen et al. (1997). Other category of models based on adding an artificial viscous term to the depth integrated momentum conservation equations to model the breaking events (see e.g. Heitner and Housner (1970); Kennedy et al. (2000); Zelt (1991)). These methods assume that the energy dissipation depends on horizontal gradients in the depth-averaged velocity. As a result, the model neither predicts the breaking onset nor simulates the breaking process.

Apart from these approaches, Svendsen et al. (1996) developed a two-dimensional theoretical approach based on the Boussinesq equations and the Reynolds transport equations with the effect of vorticity to model the breaking process. This has been utilized to study the surf zone hydrodynamics including the undertow profiles by Veeramony and Svendsen (2000). The breaking process was described by using the development of the vorticity structures by accounting for the rotational motion of the

fluid. The numerical results were in good agreement with experimental data. However, the model underestimates the wave height seaward close to the breaking point and the description of turbulence characteristics was rather limited because of the assumption of uniform eddy viscosity over the water depth. This approach has been further developed by Briganti et al. (2004) to investigate turbulence under breaking waves in detail by defining turbulent stresses with the eddy viscosity which vary over the water depth.

The evolution of strongly nonlinear shallow water waves approaching breaking can be represented with the Boussinesq wave model. It is based on depth-averaged equations with dispersive terms and may be more accurate for describing the wave transformation in shallow waters (see e.g. Brocchini (2013)). In addition, the models can be extended to represent the waves in the surf and swash zones by adding an artificial dissipation term for energy dissipation in breaking waves. However, the application of this type of models is confined to the region before breaking and the model can not be directly used to represent the underlying physics of the breaking process due to the approximations involved in the modelling.

2.5.2 Models based on potential theory

Numerical simulations of breaking waves was first performed by Longuet-Higgins and Cokelet (1976) using a mixed Eulerian-Lagrangian formulation with the boundary integral method based on potential theory. This method uses a conformal mapping of a physical plane applicable to the two-dimensional periodic waves in deep waters. Further, Vinje and Brevig (1981) utilized the same model, but they solved the problem in the physical plane and they extended the model to investigate waves in finite water depth. New et al. (1985) extended the model of Longuet-Higgins and Cokelet (1976) to study breaking waves in finite water depth by including the effect of the horizontal bottom. A boundary integral method was proposed by Dold and Peregrine (1986) based on a Cauchy integral theorem to compute the unsteady motion of a free surface during the wave breaking. Dommermuth et al. (1988) improved the model in terms of a numerical scheme and their computational results show very good agreement with the experimental data measured for a spilling breaker in deep water.

Grilli et al. (1989) developed a two-dimensional fully non-linear wave model with a high order boundary element method by implementing improved methods for wave generation, time stepping and numerical stability. The model was successfully used to simulate solitary waves breaking over submerged break waters (Grilli et al., 1994) and for shoaling and breaking of solitary waves on plane slopes (Grilli et al., 1995, 1997). Xue et al. (2001) proposed a three-dimensional model based on a mixed-Eulerian-Lagrangian approach using a high-order boundary element method and they

studied plunging breaking waves and steep crescent waves in deep water. Guyenne and Grilli (2006) simulated the shoaling and breaking of solitary waves over a sloping ridge in a three-dimensional numerical wave tank. The refined details regarding the kinematics and flow features of the development of the overturning wave crest during the initial breaking process were reasonably well represented in the simulations. It was also pointed out that the simulation of the physical process with the model is limited to the initial evolution of the plunging jet and the model cannot be used to simulate the flow scenario after the impingement of the overturning jet onto the wave surface.

Alternatively, Lachaume et al. (2003) and Grilli et al. (2004) attempted to model two-dimensional breaking and post-breaking stages of solitary waves by combining the fully non-linear potential equations with the volume-of-fluid method (VOF). The authors addressed that the complete breaking process can be described in three dimensions by combining the predictions using the boundary element method until the breaking point and the computations in the wave breaking and the post-breaking region using the VOF model. They demonstrated that the model is capable of simulating the flow features even after the overturning wave crest impinges the free surface. However, the model was not verified against experimental data for simulating the mean and turbulent velocity field in the surf zone. Overall, with the recent developments in the numerical methods, the potential flow models can be used to model the breaking onset including wave kinematics and pressure. But the models can not be used to model the interface reconnection and the associated free surface deformation beyond the breaking point in the surf zone.

2.5.3 Models based on Navier-Stokes equations

An efficient numerical approach based on the full Navier-Stokes (NS) equations was first proposed by Harlow and Welch (1965) for time-dependent, viscous and incompressible free surface fluid flow problem. The model solves the NS equations using the finite difference approximations and describes the free surface with the marker-cell method. However, this approach becomes cumbersome and time-consuming for wave breaking that involves larger free surface deformation and two-phases. The first systematic numerical study of simulating breaking waves in shallow water was performed by Lemos (1992) using RANS equations. The model uses the RANS equations for velocity and pressure with $k - \epsilon$ closure with the assumption of isotropic eddy viscosity and the free surface defined by the VOF method. The flow problem was modelled as a single phase flow, while the interaction of air and water is not included in the study. The author assumed that the internal physical process close to the free surface plays a more significant role than the air-water interaction during the breaking process. It was also reported that this approach is not capable of describing the flow features associated with

the air-water interaction in turbulent free surface flows. Lin and Liu (1998) developed a single phase flow numerical model based on the Reynolds equations which eliminates the isotropic eddy viscosity assumption for investigating the hydrodynamics of waves in the surf zone. Their model uses the two-equation model $k - \epsilon$ for turbulence and the VOF method for the free surface. The numerical results were in good agreement with the experimental data by Ting and Kirby (1996) for the spilling breaker case. Despite the fact that their model represents the mean and turbulence flow field quite well in the surf zone, the model overpredicts the turbulence intensity and underpredicts the wave crest close to the breaking point due to excessive numerical dissipation. Additionally, the small scale turbulence production due to the evolution of the overturning jet at the free surface during the initial breaking process was not captured well in the simulation (Bradford, 2000).

Bradford (2000) simulated spilling and plunging breakers over a slope by using the commercial software based on the RANS equations for the mean flow and the VOF method for the free surface. The study also examined the applicability of k model, linear $k - \epsilon$ model and a Renormalized Group of $k - \epsilon$ model for modelling turbulence under breaking waves in the surf zone. The $k - \epsilon$ model overpredicts the turbulent kinetic energy under the wave crest just before breaking, whereas the RNG modification of the $k - \epsilon$ predicts them quite well. It was also pointed out that the results from the first order computations were underestimating the wave crest as they were too diffusive. Mayer and Madsen (2000) attempted to model spilling breakers with the RANS equations combined with the VOF method and the two-equation $k - \omega$ model. The authors noticed that the large levels of unrealistic turbulence production largely affect the stability of the turbulence model and thus, the wave propagation characteristics. Moreover, this occurs in the highly strained oscillatory motion outside the boundary layer. The flow structures and turbulence under different breaker types were extensively studied using the large eddy simulations by Christensen and Deigaard (2001) and Watanabe et al. (2005). Christensen and Deigaard (2001) computed the three-dimensional flow structures and turbulence from the two-dimensional free surface and vortices during the initial phase of the breaking. A mass-conservation problem occurred near the interface during the evolution of free surface near the breaking point. The free surface was represented by the surface marker method.

Zhao et al. (2004) carried out two-dimensional simulations of spilling and plunging breakers over a slope with the space filtered Navier-Stokes equations with a multi-scale turbulence model. The model overpredicts the wave crest height near the breaking point for both the breakers and after the breaking point for the spilling breaker. But the model represents waves in the surf zone accurately for the plunging breaker. Though

the computed undertow profiles were in good agreement with the experimental data by Ting and Kirby (1994, 1995, 1996), the turbulent characteristics were not directly compared with the experimental data. In addition, the development of the free surface during the breaking process was not well represented in the simulation. Importantly, the numerical models by Bradford (2000); Christensen and Deigaard (2001); Lin and Liu (1998); Watanabe et al. (2005); Zhao et al. (2004) are based on the single flow assumption, i.e. they do not account for the air-water interaction which plays a significant role in describing the evolution of free surface and the small scale turbulence during the wave breaking. These models provide a good prediction of the surf zone characteristics. However, these models are inadequate to describe the underlying physical processes due to the approximations in connection with the free surface boundary conditions such as the velocity and the constant pressure assumption in the air phase.

It was realised that the role of air during the breaking process is an important parameter in describing the complete physical process such as the formation of the forward overturning water jet, air pocket, splash-up and the secondary wave. Thus, the CFD models based on the two-phase flow assumption have received much attention in recent years for the inclusion of the air flow properties in the modelling (Alagan Chella et al., 2013, 2014; Alagan Chella et al., 2015b,a; Chen et al., 1999; Christensen, 2006; Hieu et al., 2004; Jacobsen et al., 2012; Lubin et al., 2006; Ma et al., 2011; Moraga et al., 2008; Shi et al., 2010; Wang et al., 2009b; Xie, 2013). Hieu et al. (2004) proposed a two-phase flow numerical model with the filtered Navier-Stokes equations and the VOF method. The sub-grid scale turbulent Smagorinsky model was used to describe turbulence under breaking waves. The computed two-dimensional results show good agreement with the experimental data for the spilling breaker (Ting and Kirby, 1994). Christensen (2006) carried out three-dimensional large eddy simulations for breaking waves and compared with the experimental data for spilling and plunging breaker by Ting and Kirby (1994, 1995, 1996). The model represents the set-up and undertow profiles in the inner region of the surf zone in the experiments fairly well. However, the wave crest height was overestimated for the spilling breaker and underestimated for the plunging breaker. Consequently, the wave breaking occurs sooner for the spilling breaker and later for the plunging breaker. The model also overestimates the turbulence levels and underestimates the gradient of the undertow profiles. It was pointed out by the author that some uncertainties in the numerical prediction near the breaking point was related to the effect of coarse grid size on the computational solutions and the effect of air. A similar study was performed by Lubin et al. (2006) to model three-dimensional plunging breaking waves with a specific focus on air entrainment during the breaking process.

A two-dimensional numerical approach to model breaking waves was proposed by Wang et al. (2009a) based on the incompressible Navier-Stokes equations and a conservative level set method without an explicit turbulence model. In general, there was good agreement between the numerical and the experimental results by Ting and Kirby (1996) for the spilling breaker. The breaking point was captured reasonably well, though the wave crest height was underestimated largely in the outer region of the surf zone, especially close to the breaking point. Recently, Xie (2012) proposed a numerical model for simulating breaking waves over a slope and over a submerged reef with a CFD model that uses the RANS equations, the $k - \epsilon$ turbulence model and the VOF method. The model shows a good comparison with the experimental data (Ting and Kirby, 1995, 1996) for wave surface elevations, undertow profiles and turbulence intensity. The model predicts the breaking point accurately, but it slightly underestimates the wave height near the breaking point for the spilling breaker and after the breaking point for the plunging breaker. In particular, the velocity and vorticity fields during the breaking process for both the breakers are captured with reasonable accuracy. However, the free surface deformation and the flow features during the wave breaking were not well represented in the numerical simulation. A number of numerical investigations have been performed to model breaking waves based on a two-phase assumption in deep waters e.g. Chen et al. (1999); Hendrickson (2005); Iafrati (2009); Song and Sirviente (2004). A thorough review of the literature on breaking waves in deep waters can be found in Banner and Peregrine (1993); Perlin et al. (2013).

A number of studies aimed at modelling the surf zone hydrodynamics have shown quite good results, but far too little attention has been paid to investigate the evolution of the free surface profile and the prominent flow features during the breaking process. In the hydrodynamic load assessment point of view, the evolution of free surface profiles and wave height, the wave kinematics and the geometric properties associated with the initial breaking process are important for the modelling of breaking wave forces. Meanwhile, there have been limited studies on these hydrodynamic characteristics relevant to the load assessment parameters in shallow waters.

2.6 Numerical modelling of breaking wave forces

Theoretical prediction of breaking wave forces depends on the accuracy of the empirically determined force coefficients and the experimentally measured kinematics at breaking and obtained curling factor (e.g. Goda et al. (1966); Sawaragi and Nochino (1984); Wienke and Oumeraci (2005)). There have been few numerical studies in the open literature on modelling the interaction of breaking waves with structures and the associated forces (see e.g. Bredmose and Jacobsen (2010); Choi et al. (2015); Christensen et al. (2005); Mo et al. (2013); Xiao and Huang (2014)). A preliminary attempt was

made by Christensen et al. (2005) to model total wave forces and wave run-up due to breaking waves in shallow waters with a NS solver and the VOF method. Bredmose and Jacobsen (2010) performed simulations with the open-source software OpenFOAM based on the Navier-Stokes equations and the VOF method for free surface without an explicit turbulence model. One side of the computational domain was modelled based on the assumption of the lateral symmetry in the flow field. In the simulation, breaking waves were generated using the focussed wave group method. A similar approach was employed by Bredmose and Jacobsen (2011) to study the vertical wave impacts on offshore wind turbine inspection platforms with the OpenFOAM.

A recent numerical study of Mo et al. (2013) modelled solitary wave breaking and the interaction with a slender cylinder over a slope both experimentally and numerically. Laboratory measurements of free surface elevations and velocity at different locations along a glass flume of 25 m long were performed using the PIV (Particle Image Velocimetry) technique. In the numerical study, the filtered NS equations were used to model the mean flow and the turbulence was described with a LES model with RNG subgrid model. The simulated free surface elevations, wave profiles and velocities were in good agreement with the measured data. Based on the assumption of the symmetric flow field along the wave tank, only one half of the computational domain was modelled in the numerical simulation. Further, the wave run-up and breaking wave force on the cylinder were studied. Xiao and Huang (2014) investigated solitary wave breaking and force on a vertical cylinder over a sloping beach using a three-dimensional model that uses the RANS equations and the $k - \epsilon$ turbulence model. The free surface was captured with the VOF method. The numerical model was validated with experimental data for breaking solitary wave run-up and forces on a cylinder over a sloping beach. The study also examined the total force on a cylinder at different elevations over a sloping beach in the surf zone. Recently, Choi et al. (2015) computed the free surface elevation and breaking wave forces on vertical and inclined cylinders using a CFD model based on the Navier-Stokes equations. The model employs the VOF method for the free surface and the Smagorinsky SGS (sub-gridscale) model for turbulence. A reasonable agreement was obtained between the computed results and the filtered experimental data.

2.7 Present numerical model

In the present study, the open source CFD model REEF3D is used to simulate breaking waves and the interaction with slender cylinders. The model describes the flow using the incompressible RANS equations together with the continuity equation. The free surface is captured by the level set method (Osher and Sethian, 1988). Turbulence is modelled with the two-equation $k - \omega$, proposed by Wilcox (1994). In contrast to the above mentioned numerical models, the present numerical model uses higher-order

numerical schemes in order to achieve good numerical accuracy and stability. The present numerical model has been successfully used for simulating spilling and plunging breakers over slopes (Alagan Chella et al., 2015a,c), waves breaking over an impermeable slope (Alagan Chella et al., 2015b) and non-breaking wave forces on large cylinders (Kamath et al., 2015).

2.7.1 Governing equations

In the three-dimensional open-source CFD model REEF3D, the two-phase viscous flow is described by solving the incompressible RANS equations together with the continuity equation that represents the conservation of mass and the momentum:

$$\frac{\partial u_i}{\partial x_i} = 0 \tag{2.7}$$

$$\frac{\partial u_i}{\partial t} + u_j \frac{\partial u_i}{\partial x_j} = -\frac{1}{\rho}\frac{\partial p}{\partial x_i} + \frac{\partial}{\partial x_j}\left[(\nu + \nu_t)\left(\frac{\partial u_i}{\partial x_j} + \frac{\partial u_j}{\partial x_i}\right)\right] + g_i \tag{2.8}$$

u is the velocity averaged over time t, ρ is the fluid density, p is the pressure, ν is the kinematic viscosity, ν_t is the eddy viscosity, and g is the gravity term.

2.7.2 Convective and time discretization

The fifth-order weighted essentially non-oscillatory (WENO) scheme is employed for the discretization of the convective terms in the RANS equations (Jiang and Shu, 1996). This higher order scheme assures stable and oscillation-free numerical solutions without artificial damping. Here, three local ENO stencils are weighted according to the smoothness of their solutions, with the smoothest stencil receiving the highest weight. A convex combination of these three stencils results in a higher-order scheme. Due to the consideration of the local smoothness, this scheme can handle large gradients accurately without effecting the numerical stability.

For the temporal discretization, the third-order accurate TVD Runge-Kutta scheme is used which consists of three euler steps (Shu and Osher, 1988).

$$\begin{aligned}
\phi^{(1)} &= \phi^n + \Delta t L\left(\phi^n\right) \\
\phi^{(2)} &= \frac{3}{4}\phi^n + \frac{1}{4}\phi^{(1)} + \frac{1}{4}\Delta L\left(\phi^{(1)}\right) \\
\phi^{n+1} &= \frac{1}{3}\phi^n + \frac{2}{3}\phi^{(2)} + \frac{2}{3}\Delta L\left(\phi^{(2)}\right)
\end{aligned} \tag{2.9}$$

In order to perform more efficient parallel computations without affecting the numerical accuracy and stability, an adaptive time stepping algorithm (Griebel et al., 1998) is employed. The CFL criterion is maintained and the simulation time step is adjusted

for each iteration. Further, this method ensures the convergence of the computational solution to the exact solution for sufficiently small time step sizes based on a local error estimate. Hence, the convergence test of different fixed time steps is not considered in the present investigation. This method is usually much faster than the fixed time step method and provides a higher order accuracy and good numerical stability. Moreover, this method accounts for the effects of velocity and the source term S on the temporal numerical solutions. In this algorithm, the time step size for each iteration is obtained by satisfying the following criterion:

$$\Delta t \leq 2\left(\left(\frac{|u|_{max}}{dx} + D\right) + \sqrt{\left(\frac{|u|_{max}}{dx} + D\right)^2 + \frac{4\,|S_{max}|}{dx}}\right)^{-1} \tag{2.10}$$

which includes the effect of diffusion term D:

$$D = max\,(\nu + \nu_t) \cdot \left(\frac{2}{(dx)^2} + \frac{2}{(dy)^2} + \frac{2}{(dz)^2}\right) \tag{2.11}$$

Moreover, the CFL number of the present simulation cases is 0.1 and the simulations are performed at sufficiently small time steps to capture the nonlinear dynamic effects evolving during the breaking process. The pressure is determined from the Poisson equation which is solved with the BiCGStab algorithm (van der Vorst H., 1992) with Jacobi preconditioning. Then, the velocity field is updated with the corrected pressure (Chorin, 1968). The staggered grid arrangement is employed in the model to avoid the spurious oscillations in the numerical solutions for the pressure and velocity. In addition, this approach provides a strong pressure-velocity coupling.

2.7.3 Free surface representation

The modelling of the free surface dynamics during the breaking process is very demanding due to the complex non-linear interaction at the interface of air and water. The level set method is employed to capture the free surface deformation. The free surface is modelled as the zero level set of the signed distance function $\phi(\vec{x}, t)$ defined on the computational domain. The location and the sign of the zero level set function define the fluid phase as follows:

$$\phi(\vec{x}, t) \begin{cases} > 0\; if\; \vec{x} \in water \\ = 0\; if\; \vec{x} \in \Gamma \\ < 0\; if\; \vec{x} \in air \end{cases} \tag{2.12}$$

The free surface motion is described by the propagation of the zero level set function. The convection equation of the level set function is as follows:

$$\frac{\partial \phi}{\partial t} + u_j \frac{\partial \phi}{\partial x_j} = 0 \tag{2.13}$$

The Eikonal equation $|\nabla \phi| = 1$ is valid in the computational domain. An additional reinitialization technique proposed by Sussman et al. (1994) and Peng et al. (1999) is used to preserve the mass conservation property of the level set method. Another challenge is that the difference in the density and viscosity of the two phases lead to numerical instabilities due to viscosity and density jumps at the interface. With a Heaviside function $H(\phi)$, the fluid properties are smoothed in a transition region near the interface.

$$H(\phi) = \begin{cases} 0 & if\ \phi < -\epsilon \\ \frac{1}{2}\left(1 + \frac{\phi}{\epsilon} + \frac{1}{\pi} sin\left(\frac{\pi\phi}{\epsilon}\right)\right) & if\ |\phi| < \epsilon \\ 1 & if\ \phi > \epsilon \end{cases} \tag{2.14}$$

The thickness of the transition region is 2ϵ, where ϵ=2.1 dx.

2.7.4 Turbulence modelling

Turbulence is generated during the breaking process due to the transformation of the plunger vortex offshore and the surface roller onshore (Peregrine, 1983). A good representation of turbulence is inevitable for a realistic simulation of breaking waves where the turbulent characteristics are important considerations. The two equation $k - \omega$ model accurately represents the main physical features of the turbulent kinetic energy (Wilcox, 1994). The equations for the turbulent kinetic energy k and the specific turbulent dissipation ω are:

$$\frac{\partial k}{\partial t} + u_j \frac{\partial k}{\partial x_j} = \frac{\partial}{\partial x_j}\left[\left(\nu + \frac{\nu_t}{\sigma_k}\right)\frac{\partial k}{\partial x_j}\right] + P_k - \beta_k k\omega \tag{2.15}$$

$$\frac{\partial \omega}{\partial t} + u_j \frac{\partial \omega}{\partial x_j} = \frac{\partial}{\partial x_j}\left[\left(\nu + \frac{\nu_t}{\sigma_\omega}\right)\frac{\partial \omega}{\partial x_j}\right] + \frac{\omega}{k}\alpha P_k - \beta\omega^2 \tag{2.16}$$

P_k is the turbulent production rate, the coefficients have the values α=$\frac{5}{9}$ $\beta_k = \frac{9}{100}$ and β=$\frac{3}{40}$. As it was addressed by Mayer and Madsen (2000), who studied the spilling breakers using the Navier-Stokes equations with the $k - \omega$ turbulence model, the large levels of unrealistic turbulent viscosity affects the wave propagation properties. In the

present study, the unrealistic turbulent viscosity is treated separately by controlling the turbulent eddy viscosity with the limiter as suggested by Durbin (2009).

$$\nu_t \leq min(\frac{k}{\omega}, \sqrt{\frac{2}{3}}\frac{k}{|\mathbf{S}|}) \tag{2.17}$$

On the other hand, the turbulence intensity is overestimated by the RANS turbulence closure at the free surface. Using an additional turbulence damping scheme suggested by Naot and Rodi (1982), the over-production of turbulence is controlled at the interface of air and water.

2.7.5 Wave generation and absorption

The wave generation and absorption in the numerical wave tank is based on a relaxation method proposed by Larsen and Dancy (1983) and Jacobsen et al. (2012). A part of the wave tank is considered for the wave generation at the inlet and the wave absorption at the outlet as relaxation zones. The theoretical values are prescribed at the inlet to modulate the computational solution for free surface elevations and velocity with a relaxation function in the relaxation zone (Jacobsen et al., 2012). Similarly, in the relaxation zone at the outlet, the numerical values for the velocity is smoothly reduced to zero, the pressure is relaxed to the hydrostatic pressure and the free surface to the still water level.

$$\begin{aligned}
u(\tilde{x})_{relaxed} &= \Gamma(\tilde{x})u_{analytical} + (1-\Gamma(\tilde{x}))u_{computational} \\
w(\tilde{x})_{relaxed} &= \Gamma(\tilde{x})w_{analytical} + (1-\Gamma(\tilde{x}))w_{computational} \\
p(\tilde{x})_{relaxed} &= \Gamma(\tilde{x})p_{analytical} + (1-\Gamma(\tilde{x}))p_{computational} \\
\phi(\tilde{x})_{relaxed} &= \Gamma(\tilde{x})\phi_{analytical} + (1-\Gamma(\tilde{x}))\phi_{computational}
\end{aligned} \tag{2.18}$$

The length of the relaxation zones are: one wave length for the wave generation and two wave lengths for the wave absorption zone. The relaxation function is as given below:

$$\Gamma(\tilde{x}) = 1 - \frac{e^{(\tilde{x}^{3.5})} - 1}{e^{(1)} - 1} \; for \; \tilde{x} \in [0;1] \tag{2.19}$$

2.7.6 Wave forces

Wave forces on a structure are calculated directly by integrating the pressure p and the normal component of viscous stress tensor τ over the surface of the structure as given below:

$$F = \int_{\Omega} (-\mathbf{n}p + \mathbf{n}.\tau) d\Omega \tag{2.20}$$

where $\mathbf{n}$ is the unit normal vector to the surface and Ω is the surface of the structure. Solid boundaries are represented using a three-dimensional ghost cell immersed boundary method (GCIBM) (Berthelsen and Faltinsen, 2008). Special attention has been paid to avoid the unphysical damping at the free surface to obtain a more realistic representation of the free surface evolution. The near-wall effects are accounted for through wall functions for the velocities and the variables of the turbulence model. The present numerical model is fully parallelised with the domain decomposition method and MPI (Message passing interface). All the presented simulations are performed on NOTURś supercomputer Vilje on a large number of processors (NOTUR, 2015). Detailed information on the numerical model can be found in Paper 2.

3

Main results

Numerical simulations are performed to investigate the wave breaking process, the breaking wave characteristics, geometric properties, kinematics and forces on vertical circular cylinders in shallow waters. With the assumption of an impermeable rigid seabed condition, as listed in Table 1.1, wave breaking over four different seabed conditions are simulated: a uniform slope (Paper 3, 4 & 7), a submerged reef (Paper 5), a submerged bar (Paper 6), and a slope followed by a flat bed (Paper 8 and 9). Since the three-dimensional effects are not so important before breaking, two-dimensional simulations are carried out to compute the incipient breaking characteristics and geometric properties. On the other hand, three-dimensional simulations are performed to model the prominent flow features and the associated forces arising from the interaction of breaking waves with slender cylinders. The numerical approaches and parameters are the same for all simulations. Moreover, the numerical model is validated by comparing the numerical results with the experimental data for each case. This chapter presents the main results of the present study and the detailed results are found in each of the papers.

3.1 Wave breaking over slopes

3.1.1 Spilling breakers over slopes - Paper 3

As mentioned earlier, the onset of wave breaking in shallow water is mainly determined by the water depth, offshore wave steepness and seabed slope. The breaking wave characteristics such as the breaking location, water depth at breaking and breaker indices are important parameters in describing the breaker type and estimating the hydrodynamic loads. In addition to that, the geometric properties of the wave profile at breaking as defined by Kjeldsen and Myrhaug (1978) are examined for different conditions which can be related to the breaker type. The breaker type plays an important role in describing

the wave shape at breaking. In this part, spilling breakers over slopes are examined. The main objective of the study is to investigate the effects of water depth, offshore wave steepness, and beach slope on the characteristics and geometric properties of spilling breakers over slopes. Firstly, the numerical model is validated against the experimental measurements by Ting and Kirby (1996) for free surface elevations, wave envelope and horizontal velocities. Further, the characteristics and geometric properties of waves with different offshore wave steepnesses over various seabed slopes at different water depths are evaluated with a total of 39 numerical simulations as listed in Table 1 of Paper 3 and the computational set-up is shown in Fig. 2 of Paper 3. The numerical results are in good agreement with the laboratory measured data.

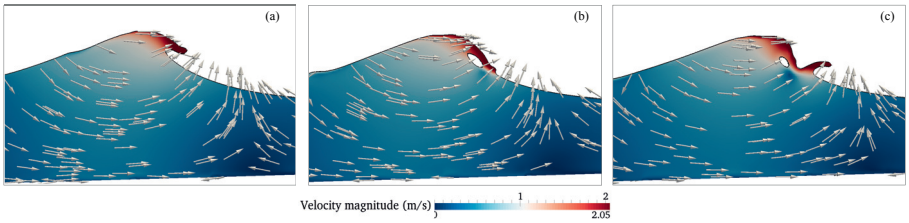

Figure 3.1: Snapshots of free surface evolution with the velocity variation during the breaking process for the spilling breaker at t=10.35s (a), 10.45s (b) and 10.50s (c) (Paper 3)

Fig. 3.1 depicts the free surface transformation and the velocity variation during the breaking process. The upper part of the wave near the free surface travels faster than the lower part of the wave as its motion is retarded by the seabed friction. As a result, the forward face of the wave becomes almost vertical and eventually it breaks. Moreover, the particle velocity is larger than the wave celerity at the tip of the wave crest and it propagates forward with a small scale overturning jet which is similar to the development of a plunging breaker as shown in Fig. 3.1 (a). Then, the overturning jet emerged from the wave crest impinges the preceding wave trough with an air pocket trapped inside the wave as seen in Fig. 3.1 (b) and (c). This leads to the formation of the secondary wave or water jet shoreward with a velocity at the tip of the wave crest that is almost equal to the velocity of the main wave crest. This so-called splash-up phenomenon is shown in Fig. 3.1 (c). Different stages of the breaking process over slopes including formation of a forward moving jet, the motion of air pockets in the water, and the splash-up are well represented in the simulations. The numerically captured flow features are consistent with the laboratory observations by Duncan (2001); Lader (2002); Lubin et al. (2011).

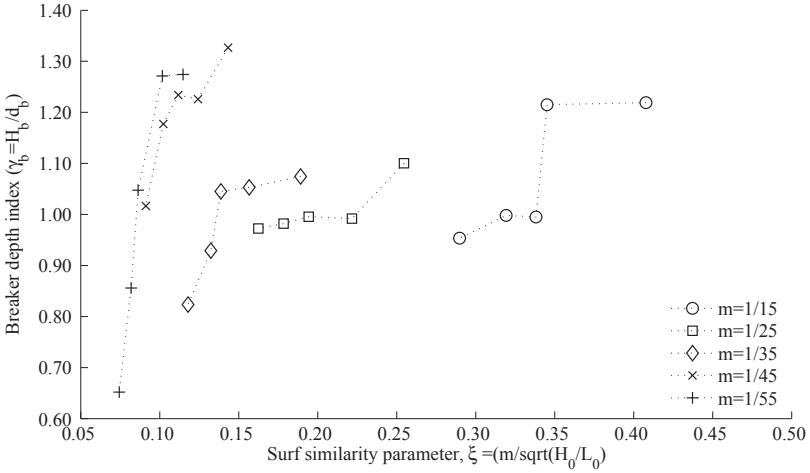

Figure 3.2: Computed breaker depth index (γ_b) versus surf similarity parameter (ξ) for the spilling breaker (Paper 3).

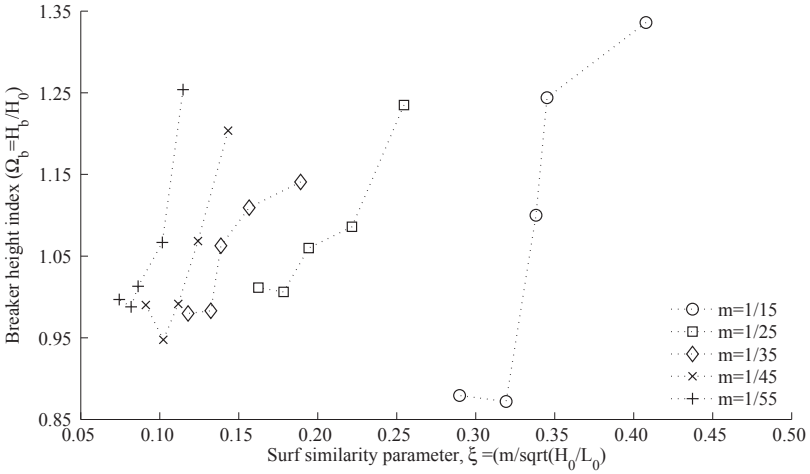

Figure 3.3: Computed breaker height index (Ω_b) versus surf similarity parameter (ξ) for the spilling breaker (Paper 3)

Figs. 3.2 and 3.3 present the variation of the breaker depth index (γ_b) and the breaker index (Ω_b), respectively, versus the surf similarity parameter (ξ). For a given slope, γ_b and Ω_b increase with increasing ξ. It appears that for a given water depth, γ_b decreases and Ω_b increases as the slope becomes steeper for H_0/L_0 = 0.02 to 0.04, and γ_b increases and Ω_b decreases for H_0/L_0 = 0.05 and 0.04. On milder slopes, waves break onshore with larger H_b at shallower d_b and undergo more deformation than for waves on steeper slopes. During the breaking process, the evolution of wave height and shape at breaking are mainly influenced by wave shoaling over milder slopes and by partial reflections over steeper slopes. Moreover, the simulated results clearly show that the environmental parameters largely effect the characteristics and geometric properties of wave breaking over slopes.

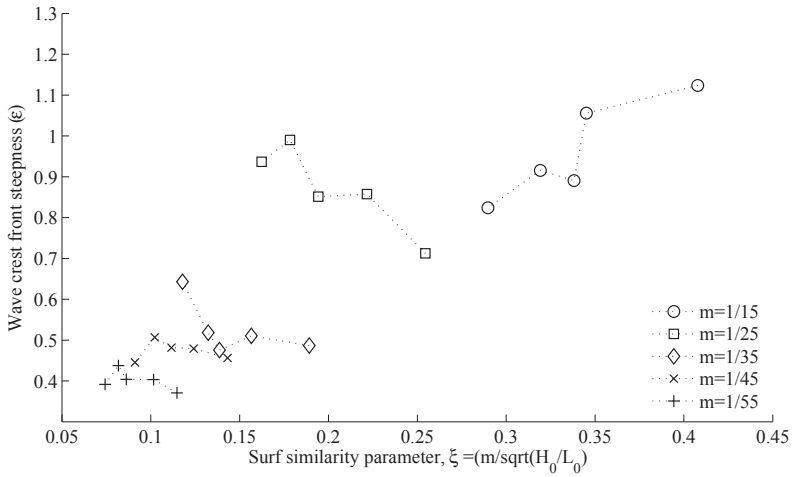

Figure 3.4: Computed crest front steepness (ε) versus surf similarity parameter (ξ) for the spilling breaker (Paper 3).

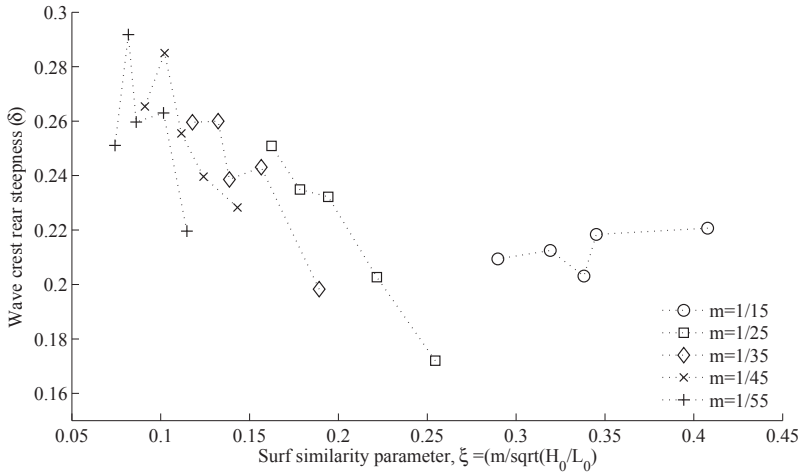

Figure 3.5: Computed crest rear steepness (δ) versus surf similarity parameter (ξ) for the spilling breaker (Paper 3).

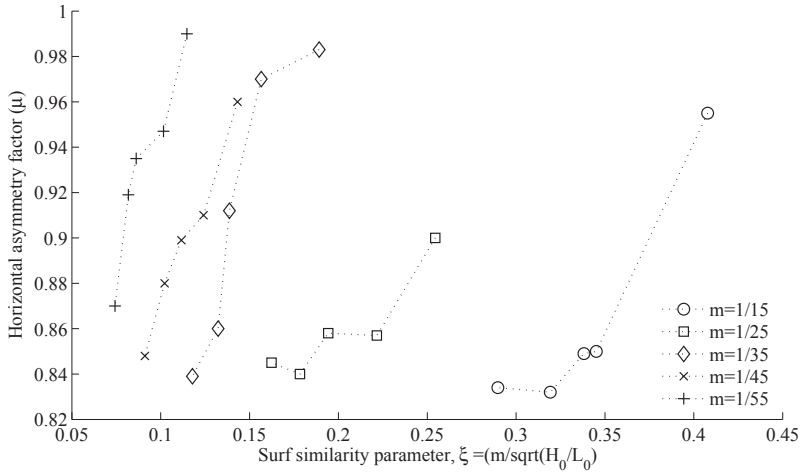

Figure 3.6: Computed horizontal asymmetry factor (μ) versus surf similarity parameter (ξ) for the spilling breaker (Paper 3).

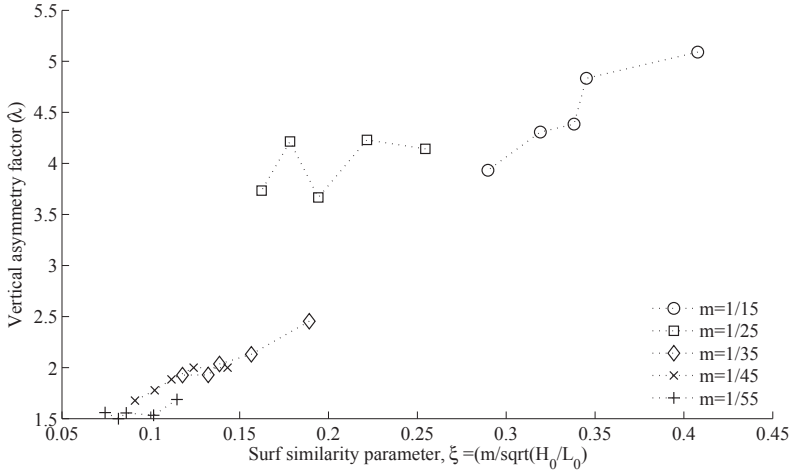

Figure 3.7: Computed vertical asymmetry factor (λ) versus surf similarity parameter (ξ) for the spilling breaker (Paper 3).

Figs. 3.4 and 3.5 present the crest front steepness (ε) and the crest rear steepness (δ), respectively, and Figs. 3.6 and 3.7 show the vertical asymmetry factor (λ) and the horizontal asymmetry factor (μ) , respectively, versus the surf similarity parameter (ξ). On the one hand, for a given slope, ε and δ decrease and μ and λ increase with increasing ξ except for the steepest slope (m=1/15) where ε and δ increase. On the other hand, for a given offshore wave steepness, ε and λ increase δ and μ decrease with increasing ξ. In addition, the wave profile at breaking for m=1/15 and H_0/L_0=0.02 (ξ=0.47) looks like a plunging breaker. Particularly, the dependence of λ on ξ decreases as the seabed becomes flatter. The numerical results show that the wave breaking pattern is mainly determined by the shoaling rate and the partial reflection from the beach slope. It was noticed that the environmental parameters appear to have a larger influence on the geometric properties at breaking. The degree of asymmetry increases as the reference water depth (d) increases and the offshore wave steepness and the seabed slope decrease. Importantly, this also plays a vital role in determining the breaker type.

3.1.2 Plunging breakers over slopes - Paper 4

In this part, the characteristics and the geometric properties of plunging breakers over slopes are assessed and comparison with similar results obtained for spilling breaker (Alagan Chella et al., 2015a) are also discussed. In the present case, the plunging breaker ($T = 5s$) is relatively longer than the spilling breaker ($T = 2.0s$) and thus,

the wave deformation during the interaction with the slope is larger. Fig. 3.8 shows the computed breaker depth index (γ_b) and breaker height index (Ω_b) versus the surf similarity parameter (ξ). The results show that γ_b and Ω_b decrease for larger ξ i.e. for steeper slopes. For both spilling and plunging breakers, a similar trend of results on the breaker indices over a given slope is observed for different offshore wave steepnesses. The breaker depth index becomes larger for steeper slopes for plunging breakers which is consistent with spilling breakers over slopes (Alagan Chella et al., 2015a). Conversely, the breaker height index decreases as the seabed slope becomes steeper for plunging breakers. In general, waves break farther up on the slope at shallower water depths with larger breaker heights for plunging breakers, while waves break farther offshore at larger water depths with small increase in the breaker heights for spilling breakers.

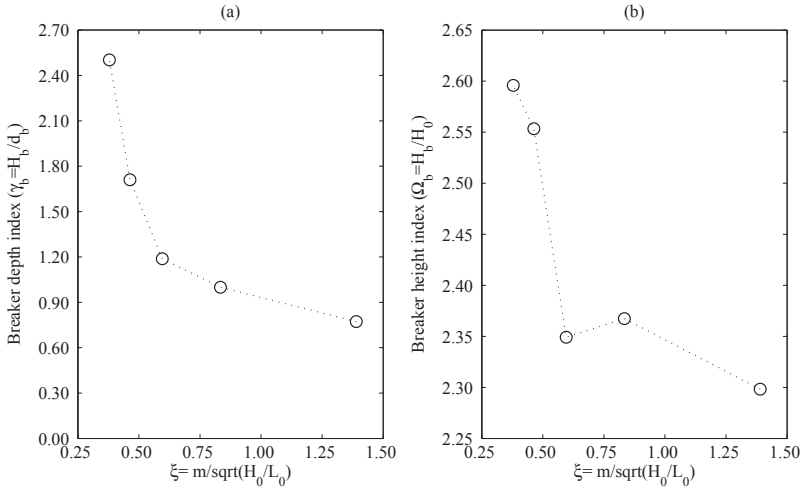

Figure 3.8: Computed (a) breaker depth index (γ_b) and (b) breaker height index (Ω_b) versus surf similarity parameter (ξ) for the plunging breaker (Paper 4).

Fig. 3.9 presents the computed steepness and asymmetric parameters versus the surf similarity parameter (ξ) for different slopes. It appears that ε and λ increase and μ decreases slightly as ξ increases, while δ does not vary much. Despite that the geometric properties of plunging breakers over different slopes exhibit the variability similar to the spilling breakers, the rear part of the wave crests do not change for plunging breakers. However, unlike the spilling breakers, the wave rear part and the vertical asymmetry are almost independent of incident offshore wave steepness for the plunging breakers. The variations of ε and δ are also consistent with the previous findings of spilling breaker

case for m=1/15, H_0/L_0=0.02, and ξ=0.47 (Section 3.1.1). Apparently for both spilling and plunging breakers, the incipient breaking mechanism is strongly influenced by offshore wave steepness and seabed slope with distinctive geometrical features.

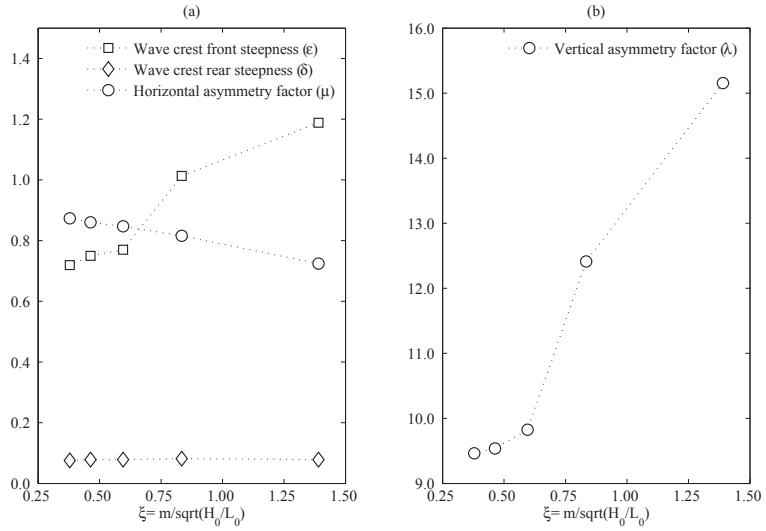

Figure 3.9: Computed wave profile steepnesses and asymmetry factors for the plunging breaker versus surf similarity parameter (Paper 4)

3.1.3 Hydrodynamic aspects of spilling and plunging breakers over a slope - paper 4

A good description of breaking wave force on a structure depends on the prediction of the evolution of free surface profiles, wave height and the changes in the wave kinematics associated with the initial breaking process. The numerical model is validated with the experimental measurements by Ting and Kirby (1995, 1996) for the spilling and plunging breaker. The computational set-up is shown in Fig. 2 of Paper 4. The hydrodynamic characteristics are investigated based on the wave height evolution and attenuation, the variation of horizontal and vertical velocity, free surface profile during the evolution of the breaking process, and the wave envelope for the whole computational domain for both the breakers. The wave parameters used in the simulations and the numerical and experimental results are listed in Table 1 of Paper 4. The computed wave height variation before breaking (H/H_0) and after breaking (H/H_b) is presented in Fig.

3.10. In the present case, the plunging breaker has a deeper wave base, therefore the wave deformation during the interaction with the slope is larger than for the spilling breaker. The wave height at breaking is $2.30H_0$ for the plunging breaker and $1.35H_0$ for the spilling breaker. This implies that the incident wave characteristics change significantly for the plunging breaker due to a deeper wave base and the higher shoaling rate. Comparison of the wave height attenuation after the breaking point shows that the wave height decreases gradually after breaking for the spilling breaker, whereas it is more rapid for the plunging breaker. The horizontal velocity variation over the depth is almost invariable for the plunging breaker, while it gradually varies for the spilling breaker (Figs. 18 and 19 of Paper 4).

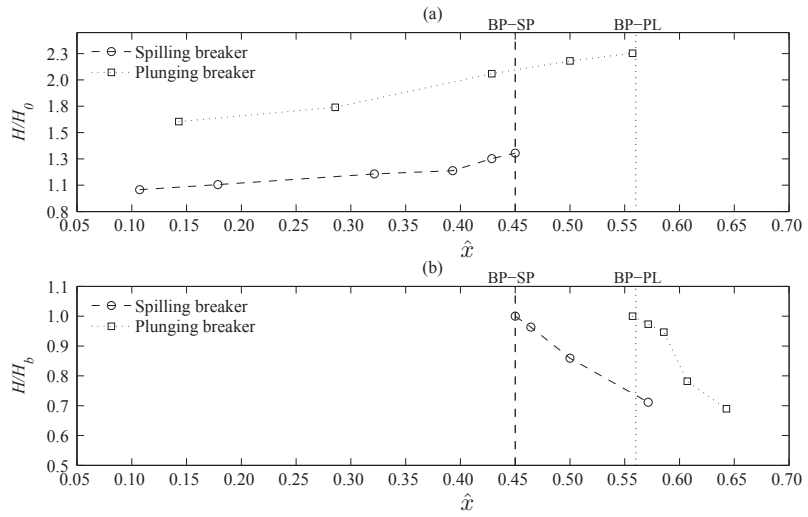

Figure 3.10: Computed wave height variation (a) H/H_0 (before breaking) (b) H/H_b (after breaking) versus the non-dimensional breaking location ($\hat{x}$). BP-SP and BP-PL are the breaking points for the spilling and plunging breaker, respectively (Paper 4)

The geometric properties for spilling and plunging breakers are shown in Figs. 3.11 and 3.12, respectively. When waves approach the breaking point, ε (Fig. 3.11 (a)) and δ (Fig. 3.11 (b)) increase for the spilling breaker, whereas ε (Fig. 3.11 (a)) increases and δ (Fig. 3.11 (b)) almost does not vary for the plunging breaker. For both the breakers, λ (Fig. 3.12 (a)) and μ (Fig. 3.12 (b)) increase during the transition to wave breaking. For the spilling breaker, the front and rear face of the wave crest become steeper and the preceding wave trough depth becomes shallower. Whereas the front face of the

plunging breaker becomes steeper with almost no change in the slope of the rear face. In addition, the wave crest becomes more asymmetric with small changes in the preceding wave trough. The computed results are consistent with the laboratory measurements for deep water waves by Bonmarin (1989) and Lader (2002). Figs. 3.13 and 3.14 depict the

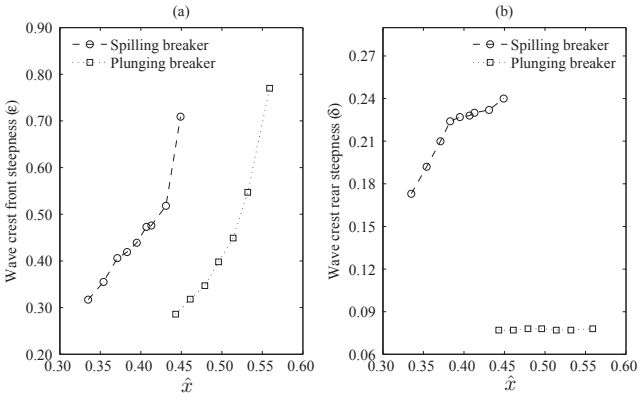

Figure 3.11: Computed development of steepness parameters (a) wave crest front steepness (ε); (b) wave crest rear steepness (δ) versus the non-dimensional breaking location ($\hat{x}$) during the transition to breaking (Paper 4)

free surface changes with the velocity variation during the development of the breaking process for the spilling breaker and the plunging breaker, respectively. As the particle velocity at the wave crest exceeds the wave celerity, the overturning wave crest emerges from the wave crest as shown in Figs. 3.13 (a) and (b) and 3.14 (a) and (b). Then the formation of the splash-up and the displacement of air-pocket are also captured well in the numerical simulations as seen in Figs. 3.13 (c) and (d) and 3.14 (c) and (d). It is noticed the vertical component of particle velocity attains the maximum value at the mean water level near the forward part of the wave crest for both the breakers. Though a small contribution of the vertical velocity to the kinematics of the overturning wave crest, its contribution to the generation of the secondary wave is significant (Figs. 22 and 23 of Paper 4). Finally, the flow features are almost the same for both spilling and plunging breakers, but the breaking mechanism and the characteristics are different.

3.2 Wave breaking over submerged structures

3.2.1 Wave breaking over a submerged reef - Paper 5

Wave breaking over submerged structures is strongly influenced by the water depth and wave height at the reef crest. Unlike the wave breaking over slopes, the surf similarity parameter cannot be used to identify the breaker type (Blenkinsopp and Chaplin, 2008).

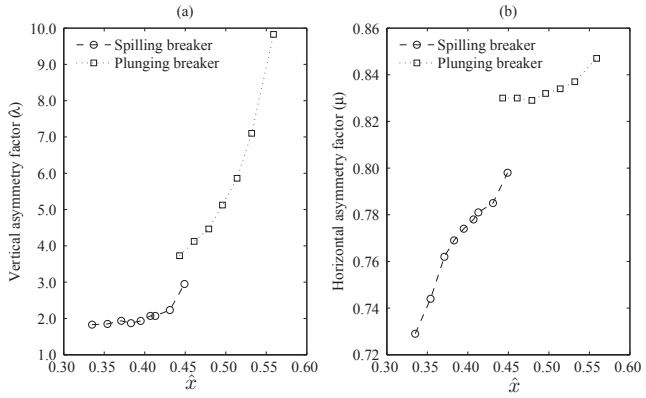

Figure 3.12: Computed development of asymmetry factors (a) vertical asymmetry factor (λ); (b) horizontal asymmetry factor (μ) versus the non-dimensional breaking location ($\hat{x}$) during the transition to breaking (Paper 4)

Importantly, the water depth initially decreases up to the reef crest, and it increases suddenly after the reef crest as shown Fig. 2 of Paper 5. As a result, the wave breaking mechanism is completely different from the wave breaking over slopes. The main focus here is to examine the effect of offshore wave steepness and water depth above the reef crest on the characteristics and the geometric properties of wave breaking over a submerged reef. The numerical model for simulating wave breaking over a submerged reef is validated by comparing the numerical results with the experimental measurements by Blenkinsopp and Chaplin (2008).

The numerically captured free surface changes during the breaking process over the reef are presented in Fig. 3.15. After the breaking point, the wave crest further curls forward with an ejecting water jet as shown in Fig. 3.15 (a) and (b). When the ejected water jet is fully developed, it falls over the forward wave surface (Fig. 3.15 (b) and (c)). In the numerical simulation, a clockwise vortex is formed behind the reef when the wave breaks over the submerged reef. The development of the downstream vortex causes the return flow which opposes the wave motion in the wave propagation direction. It is noticed that its size becomes larger as the water depth over the reef crest increases. The combined effect of the partial reflection from the reef face and the return flow influences the wave breaking process over a submerged reef.

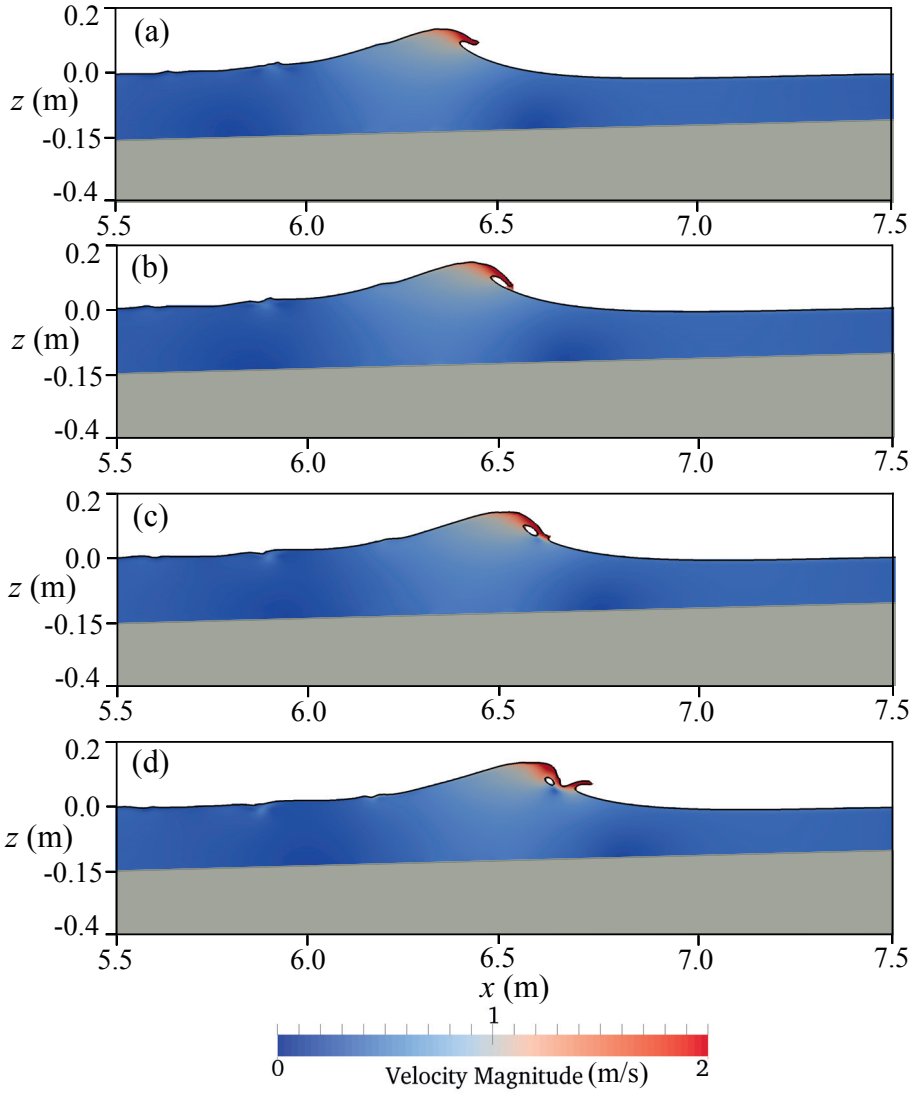

Figure 3.13: Computed velocity variation (m/s) and free surface profile changes during the breaking process at t=10.35s (a), 10.40s (b), 10.45s (c) and 10.50s (d) for the spilling breaker (Paper 4).

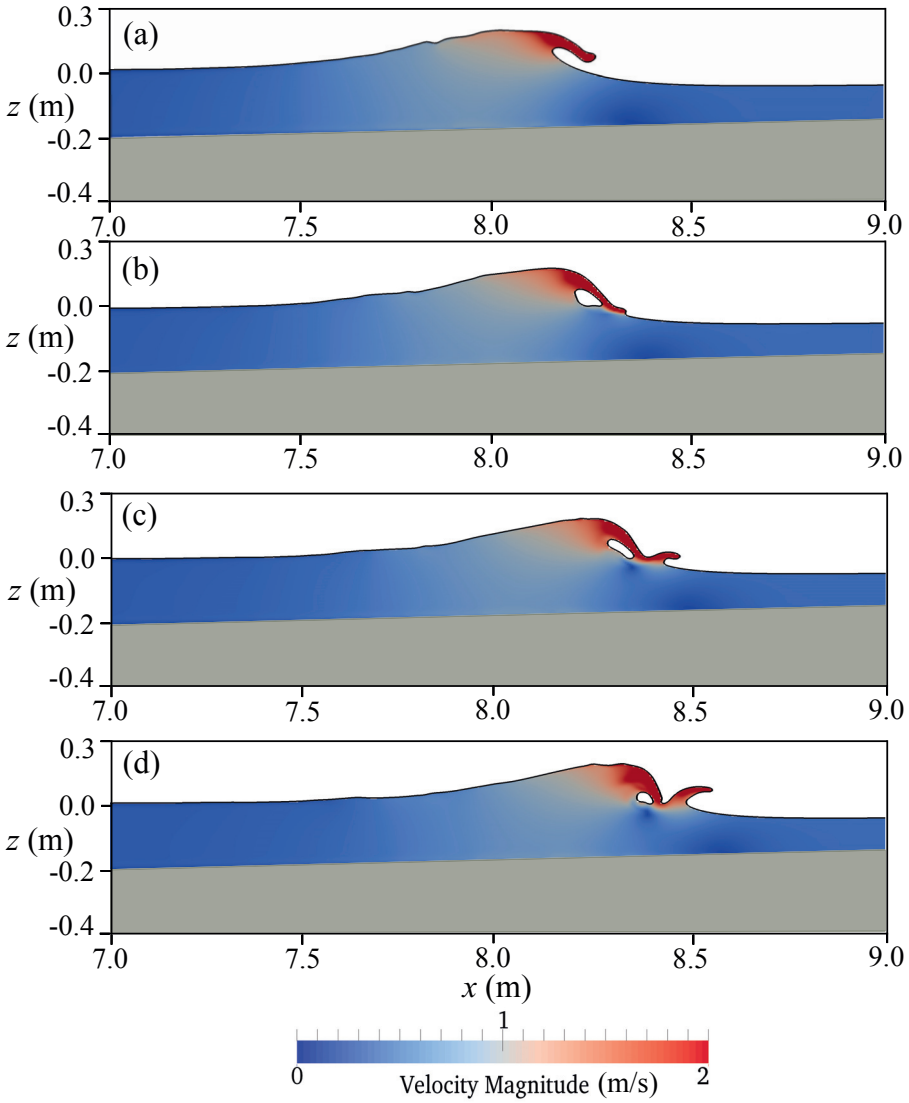

Figure 3.14: Computed velocity variation (m/s) and free surface profile changes during the breaking process at t=10.85s (a), 10.95s (b), 11.00s (c) and 11.05s (d) for the plunging breaker (Paper 4).

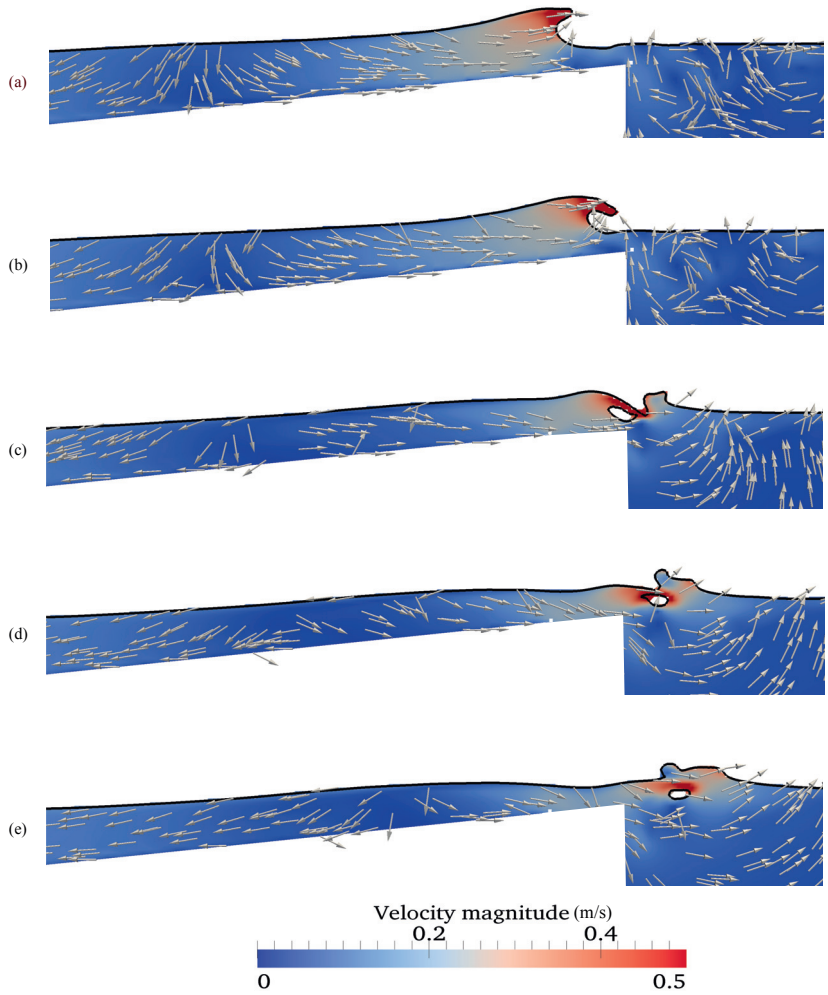

Figure 3.15: Computed free surface profile with velocity (m/s) variation during wave breaking over the reef at t=9.70s (a), 9.75s (b), 9.80 (c), 9.85 (d) and 9.90s (e) for the simulation case H_0/L_0 = 0.033 and d=0.65m. (Paper 5)

The numerically captured flow features are consistent with those of Chang et al. (2005); Iwata et al. (1996); Ting and Kim (1994) who reported the return flow due to the vortex formation behind the submerged structures. Although the flow features during the breaking process over the submerged reef is very similar to the one on slopes, the wave height attenuates rapidly after the breaking point behind the reef where the water depth increases suddenly. Figs. 3.16 and 3.17 present the computed and measured breaker depth index (γ_b) versus the offshore wave steepnesses (H_0/L_0) and versus the relative crest submergence (h_c/H_0), respectively. Figs. 3.18 and 3.19 present the computed and measured breaker height index (Ω_b) versus H_0/L_0 and versus h_c/H_0, respectively. The numerical results agree well with the measured data by Blenkinsopp and Chaplin (2008) and follows the experimental data for wave breaking over a plane slope by Smith and Kraus (1990). It appears that γ_b does not change much with increasing H_0/L_0 and h_c/H_0, although Ω_b becomes smaller for larger H_0/L_0 and increases as h_c/H_0. Therefore, the change in the offshore wave steepness and water depth at the reef crest does not affect the breaker depth index substantially, but it influences the breaker height index.

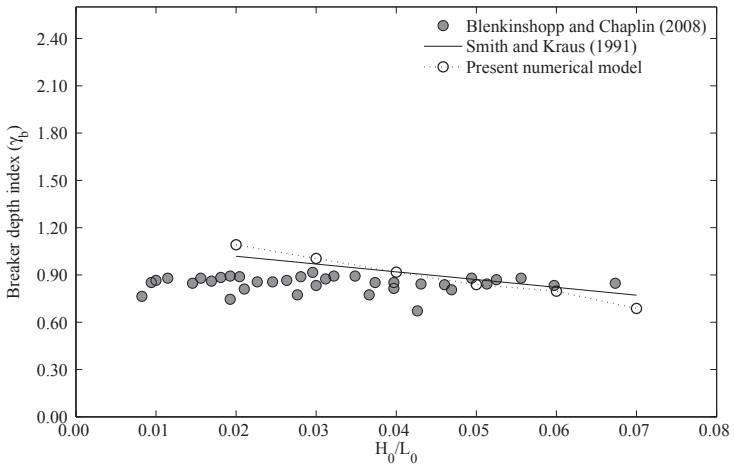

Figure 3.16: Breaker depth index (γ_b) versus offshore wave steepness (H_0/L_0) (Paper 5).

The steepness and asymmetry parameters of wave profiles at breaking over the reef with the relative water depth (h_c/d) are presented in Fig. 3.20. The computed ε and λ decrease and μ and δ increase slightly as the water depth at the reef crest increases. The

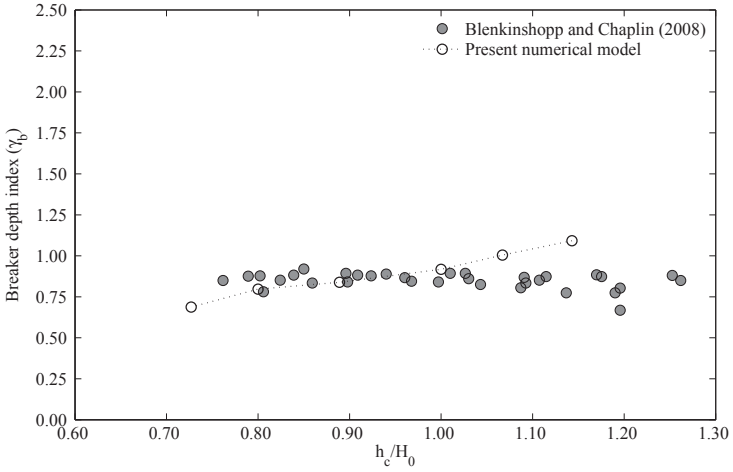

Figure 3.17: Breaker depth index (γ_b) versus relative crest submergence (h_c/H_0) (Paper 5).

wave profile asymmetry increases as the water depth over the reef crest and the offshore wave steepness decrease. Moreover, the water depth at the reef crest appears to play a crucial role in determining the breaker type.

3.2.2 Wave breaking over a submerged bar - Paper 6

The wave transformation process over a submerged bar is investigated for non-breaking and breaking waves and the numerical model is validated against the experimental data reported by Beji and Battjes (1993). In this paper, the wave shoaling on the up-slope and the wave decomposition over the leeside slope for breaking and non-breaking waves are also presented and discussed. The wave surface elevations are calculated at eight different locations along the wave tank from the wave generation to the wave decomposition as shown in Fig. 2 of Paper 6. Moreover, the development of free surface changes during the breaking process over a submerged bar for spilling and plunging breakers are reasonably captured in the numerical simulations.

Fig. 3.21 presents the computed normalized free surface elevations (η/η_c) versus time and the normalized spectra versus normalized frequency (f/f_0) for different wave frequencies at different locations along the submerged bar (WG 2, 4, 6 and 8). It is noticed that the wave transformation properties are different for breaking (H=0.042m and 0.052m) and non-breaking (H=0.022m and 0.035m) waves. At the wave generation,

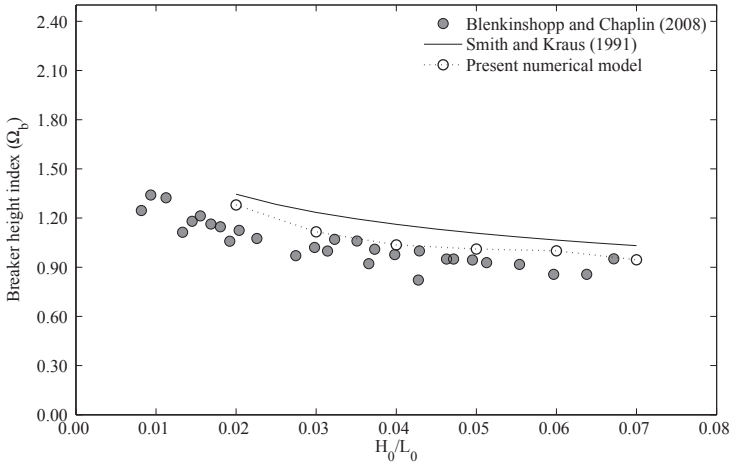

Figure 3.18: Breaker height index (Ω_b) versus offshore wave steepness (H_0/L_0) (Paper 5).

all waves follow the smooth sinusoidal shape and their shape become asymmetric as they propagate over the up-slope due to the shoaling process as shown in Fig. 3.21 (I) (a) and (b). The most of the energy are accumulated at the fundamental frequency (Fig. 3.21 (II) (a)). A secondary and a tertiary wave crest are seen besides the primary wave crest for both breaking and non-breaking waves. Waves with larger offshore wave steepnesses break over the crest of the submerged bar. The spilling breaker (H=0.042m) carries more energy downstream than the plunging breaker (H=0.052m) after breaking (Fig. 3.21 II (c) and (d)). As the waves propagate over the region of increasing water depth, a large part of the energy is distributed upto the fourth harmonics (Fig. 3.21 (II) (c) (d)). However, most of the wave energy is concentrated at the first and third harmonics. This study reveals that the flow characteristics are almost the same for both spilling and plunging breakers, but vary vastly in terms of the breaking mechanism and characteristics. In contrast to the spilling breaker, the plunging breaker dissipates most of its energy during the breaking process. This is also consistent with the results of breaking waves over a slope as presented in Section 3.1.3 (Fig. 3.10).

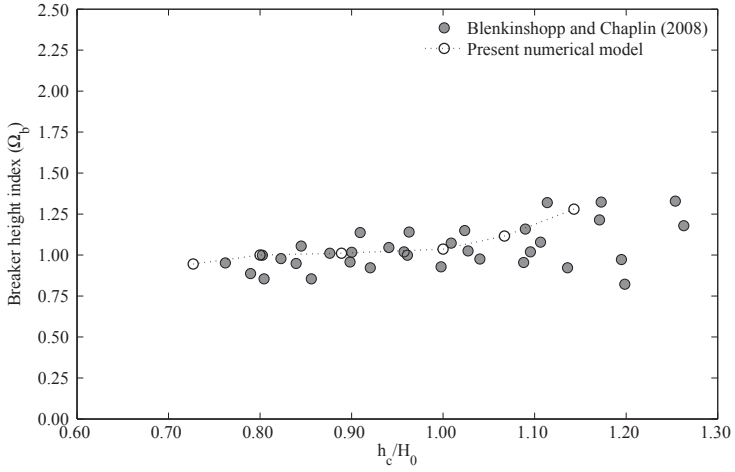

Figure 3.19: Breaker height index (Ω_b) versus relative crest submergence (h_c/H_0) (Paper 5)

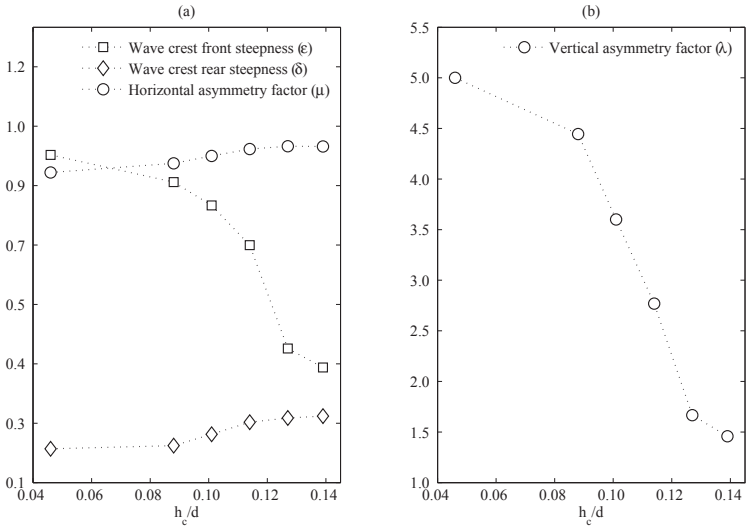

Figure 3.20: Computed wave steepnesses and asymmetry parameters versus relative depth (h_c/d) (Paper 5).

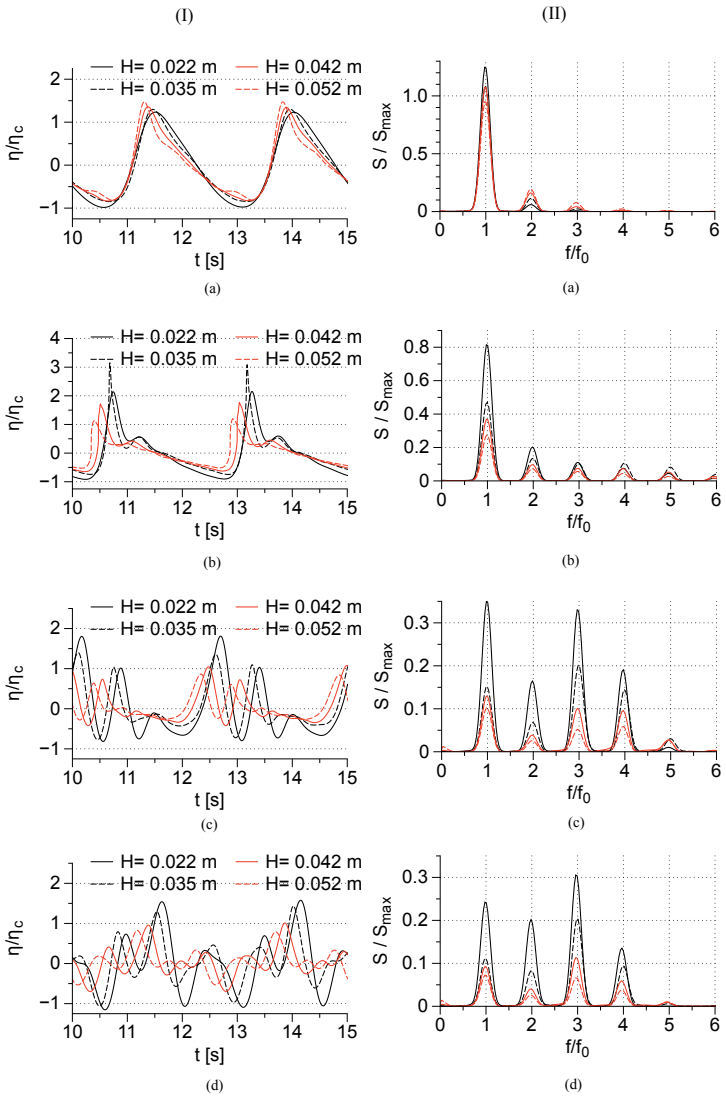

Figure 3.21: Computed normalized free surface elevations (η/η_c) versus time and normalized spectra (S/S_{max}) versus normalized frequency (f/f_0) at x=11m (a), 13m (b), 15m (c) and 17m (d) (Paper 6). η and η_c are the incident and instantaneous water surface elevations and f_0 is the primary frequency (Paper 6)

3.3 Breaking wave interaction with slender cylinders

The characteristics, geometric properties and the prominent flow features of wave breaking over slopes, a submerged reef and a submerged bar have been studied so far. Further, the present investigation is extended to study the hydrodynamics related to the interaction of breaking waves with slender cylinders and the associated breaking wave forces.

3.3.1 Breaking solitary wave forces on a slender cylinder - Paper 7

The knowledge of solitary wave propagation plays an important role in understanding several aspects of the propagation of long-period oscillatory waves in very shallow waters. The numerical model for modelling the interaction of a solitary wave with a slender cylinder is validated against the experimental measurements by Mo et al. (2013). The computational domain is shown in Fig. 3 of Paper 7. The computed results are compared with the experimentally measured free surface elevations, horizontal and vertical velocities, free surface profiles during breaking and the numerically computed breaking wave force. The main purpose of this paper is to assess the characteristics and geometric properties of breaking solitary waves over a sloping seabed and their interaction with a vertical slender cylinder. The connection between the maximum force and the cylinder location relative to the breaking point is examined. Furthermore, the results of the breaking wave forces for different incident waves are discussed in connection with the characteristics and geometric properties at breaking.

Fig. 3.22 shows the breaker depth index (γ_b) and the breaker height index (Ω_b) versus the normalized wave heights (H_0/d_0) for different offshore wave heights (H_0) (since d_0 is fixed). The variation of the breaker indices for different incident wave heights is consistent with the periodic waves in shallow waters (Alagan Chella et al., 2015a). Although the breaker height index does not change much with the increase of incident wave heights, the breaker depth index varies significantly and it is larger than that of periodic waves in shallow water (Alagan Chella et al., 2015a). The results also imply that in the case of solitary waves, the absence of the wave trough interaction with the slope cause the waves to propagate further up the slope, breaking at shallower water depths.

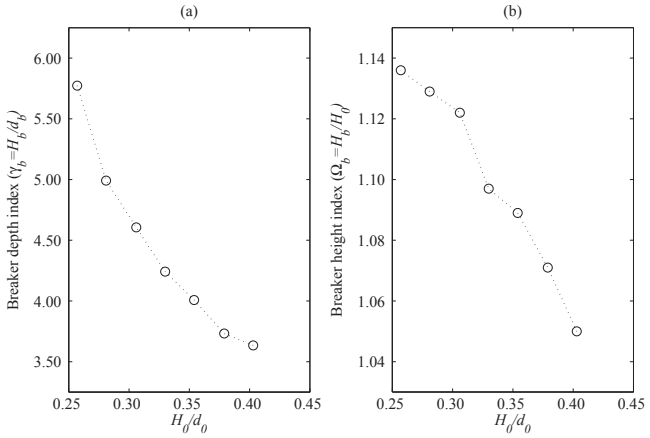

Figure 3.22: Computed (a) breaker depth index (γ_b) and (b) breaker depth index (Ω_b) versus normalized amplitude (H_0/d_0) (Paper 7)

Figs. 3.23 and 3.24 show the computed steepness and asymmetric parameters versus the normalized wave heights (H_0/d_0) for different offshore wave heights (H_0) (since d_0 is fixed). In accordance with previous findings on periodic waves, smaller waves undergo more deformation and thus, the degree of asymmetry increases as the incident wave height decreases. The range of the vertical asymmetry factor is much larger than the typical values of periodic waves in shallow waters (Alagan Chella et al., 2015a). Further, the study investigates the interaction of breaking solitary waves with a slender cylinder and the associated breaking wave forces.

Firstly, the two-dimensional numerical simulations are performed to determine the breaking point for different normalized relative distances ($L_c = H_b x_c/d_b D$) as listed in Table 1 of Paper 7. Fig. 3.25 present the impact scenarios for the selected cases (L_c=4.24, 0.0, -4.24 and -12.72). Figs. 3.26 and 3.27 shows the normalized force (F_{norm}) versus time for different normalized relative cylinder distances ($L_c = H_b x_c/d_b D$) before and after breaking, respectively. The normalized relative distance is based on the relationship between the breaker depth index ($\gamma_b = H_b/d_b$), the diameter (D), the distance between the breaking point and the cylinder (x_c). The maximum total force occurs when the wave hits the cylinder just before breaking for L_c=4.24 (Figs. 3.26 (e) and 3.25 (a)). It seems that the wave front is less steep when compared to the wave front at breaking leading to a larger submergence of the cylinder, causing a larger force than the force

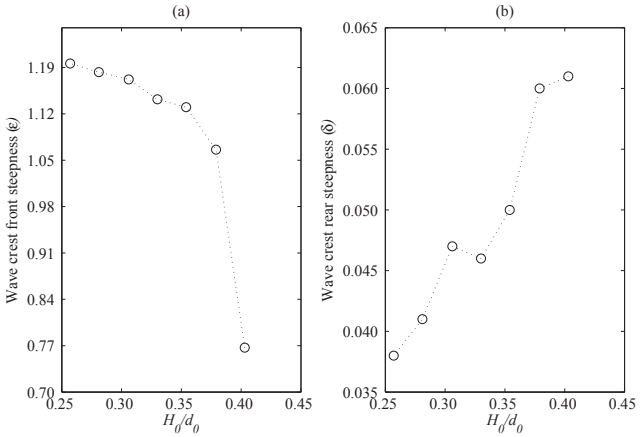

Figure 3.23: Computed (a) wave crest front steepness (ε) and (b) wave crest rear steepness(δ) versus normalized amplitude (H_0/d_0) (Paper 7)

caused by a steeper wave front with a smaller submergence of the cylinder. Therefore, the relative distance between the cylinder and the breaking point is a key parameter in evaluating the breaking wave force. In the case of L_c=-8.48 and L_c=-12.72 (Fig. 3.25 (d)), the wave breaks far before the cylinder and it experiences the maximum force from the impingement of the wave crest with the ejected water jet on the cylinder. Therefore, the total forces acting on the cylinder at L_c=-8.48 (Fig. 3.27 (c)) and -12.72 (Fig. 3.27 (d)) are larger than for the total wave force at breaking for L_c=0.0 (Figs. 3.27 (a) and 3.25 (b)).

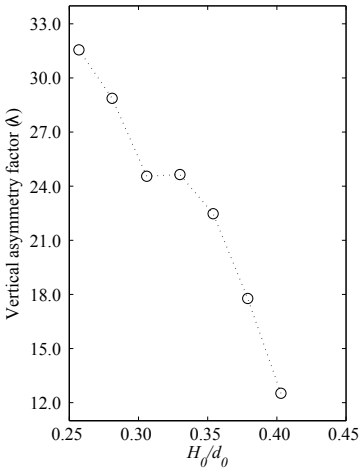

Figure 3.24: Computed wave vertical asymmetry factor (λ) versus normalized amplitude (H_0/d_0)(Paper 7)

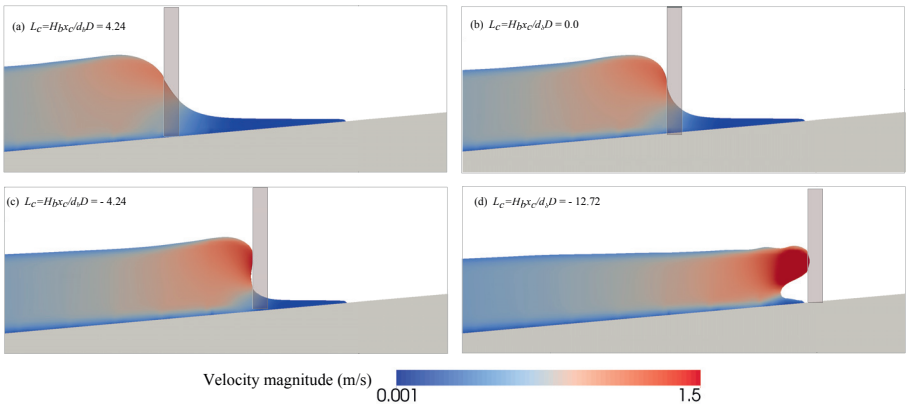

Figure 3.25: Simulated free surface profiles with velocity magnitude variation at different time instants and the corresponding cylinder positions (Paper 7).

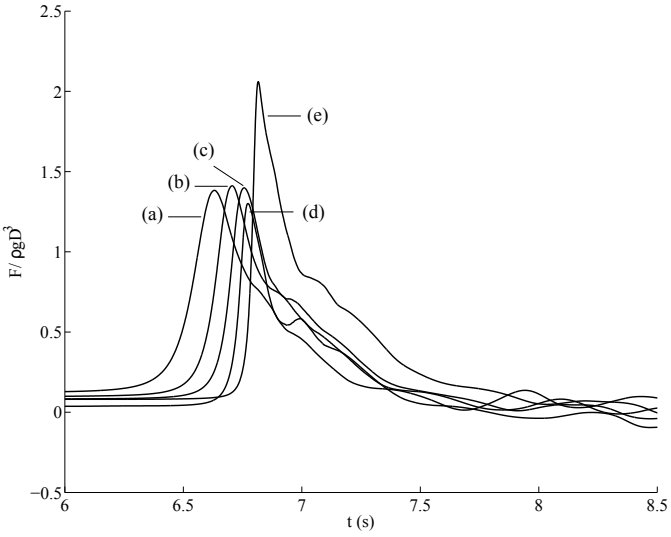

Figure 3.26: Computed normalized force ($F_{norm} = F/\rho g D^3$) versus time for different $L_c = (H_b x_c / d_b D)$ (before breaking): (a) 21.20, (b) 16.96, (c) 12.72, (d) 8.48 and (e) 4.24 (Paper 7).

3.3.2 Periodic breaking wave interaction with slender cylinders - Paper 8 and Paper 9

Furthermore, the study deals with the interaction of periodic breaking waves with a slender cylinder and the resulting breaking wave forces. Additionally, the effect of relative breaker location is also studied for five different impact scenarios as proposed by Irschik et al. (2002). The numerical model for computing the wave forces on a slender cylinder is validated with the experimental measurements by Irschik et al. (2002). Comparison of the numerical results with the experimental data for the wave surface elevation the breaking wave force shows a fairly good agreement. The main focus here is to investigate wave breaking over a sloping seabed followed by a flat bed (Fig. 1 of Paper 8) and to evaluate breaking wave forces on a slender cylinder for five different impact scenarios with three different incident wave heights.

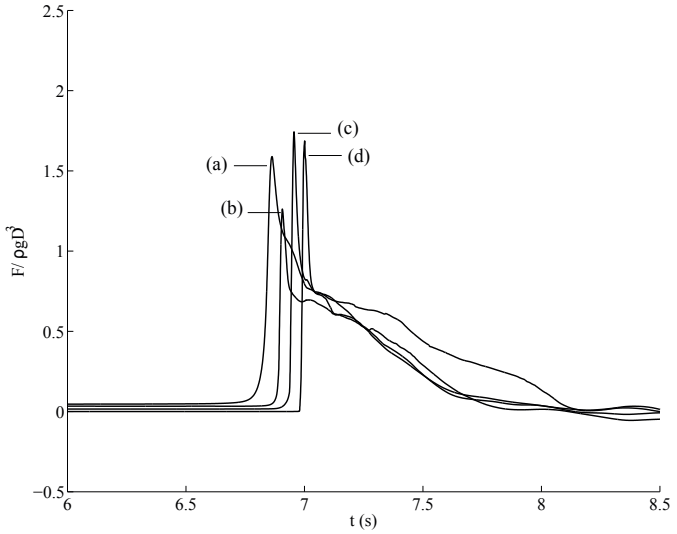

Figure 3.27: Computed normalized force ($F_{norm} = F/\rho g D^3$) versus time for different $L_c = (H_b x_c / d_b D)$ (after breaking): (a) 0.0, (b) -4.24, (c) -8.48, and (d) -12.72 (Paper 7).

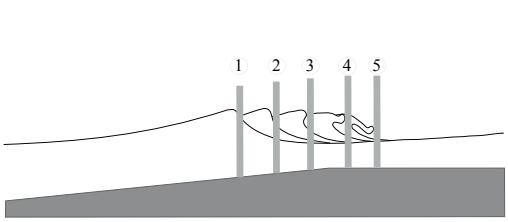

1. Wave breaking behind the cylinder
2. Wave breaking at the cylinder
3. Breaker tongue impact at crest level
4. Breaker tongue impact just below crest level
5. Breaker tongue impact much below crest level

Figure 3.28: A schematic sketch of different wave impact scenario (Paper 8)

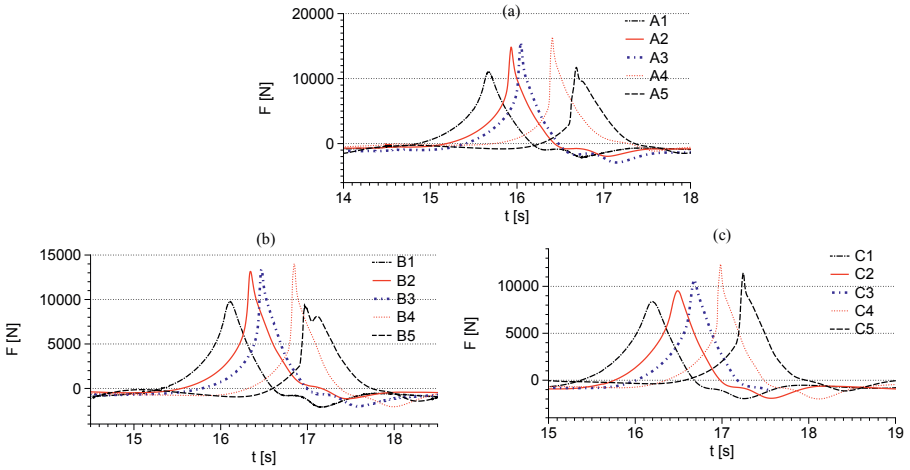

Figure 3.29: Computed total force versus time for (a) H_A=1.44m, (b) H_B=1.30m and (c) H_C=1.23m for different wave impact scenarios (Paper 8)

The five different impact scenarios reported by Irschik et al. (2002) are considered in the present study as illustrated in Fig. 3.28. Fig. 3.29 shows the total force versus time for H=1.44m, 1.30m and 1.23m for different impact scenarios. The cylinder experiences the largest force when the wave breaks in front of the cylinder i.e. the overturning wave front impinges on the cylinder just below the crest level (scenario 4). The lowest total force on the cylinder occurs when the wave breaks behind the cylinder (scenario 1). When the overturning jet hits the cylinder much below crest level (scenario A5 and B5), a secondary force peak is appeared next to the primary peak force for H_A=1.44m (Fig. 3.29 (a)) and H_B=1.30m (Fig. 3.29 (b)). This might be due to the impingement of the breaker tongue followed by the impact of the wave front on the cylinder. Fig. 3.30 presents the free surface changes with horizontal component of velocity (U_x) variation for different time instants. The overturned wave crest hits the cylinder just below the wave crest level (Fig. 3.30 (a) and (b)) and the broken wave front is separated around the cylinder downstream as seen in Fig. 3.30 (c) and (d). As a consequence, a chute-like water jet is formed in the shadow region behind the cylinder (Fig. 3.30 (e) and (f)). Most of the flow features associated with the wave impact process such as the wave deformation around the cylinder and the generation of water jet behind the cylinder are reasonably well captured in the numerical simulations

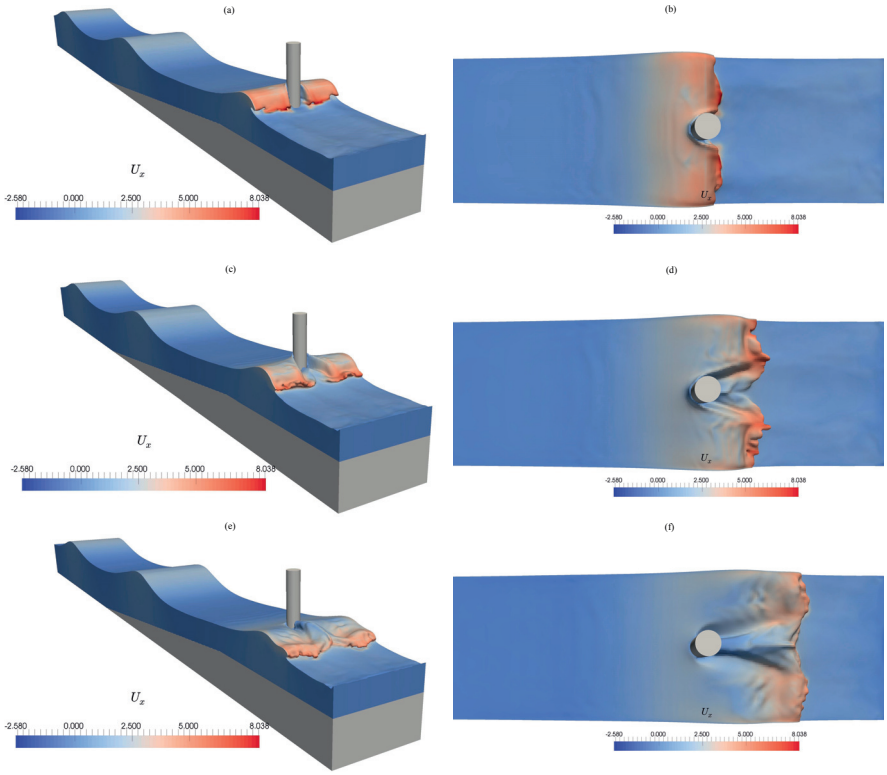

Figure 3.30: Simulated free surface deformations with velocity variations during the breaking wave interact with the cylinder at (a) and (b)=13.20s, (c) and (d)=13.50s and (e) and (f)=13.85s for H_B= 1.30m for the wave impact scenario B5. (Paper 8)

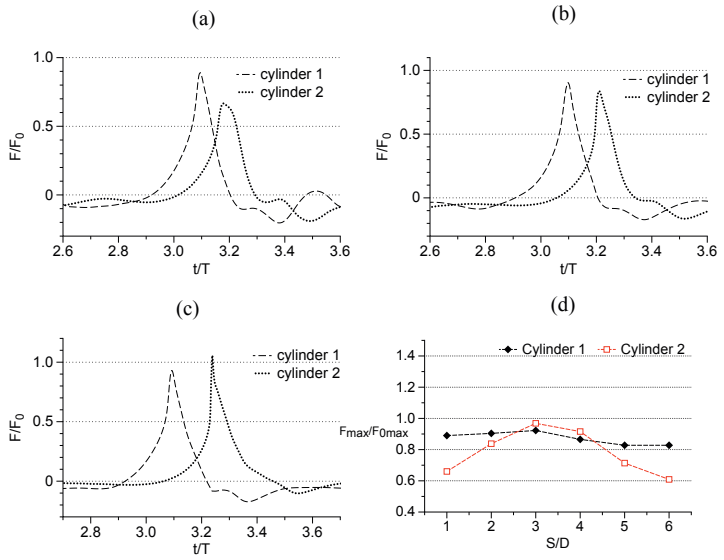

Figure 3.31: Computed normalized wave force (F/F_0) versus normalized time (t/T) for scenario C: wave breaking at cylinder 1 with H=1.3m for S=1D (a), 2D (b), and 3D (c) and (d) computed normalized maximum wave force (F_{max}/F_{0max}) versus non-dimensional distance (S/D). F_0 and F_{0max} are the total wave force and the maximum wave force on a single cylinder, respectively, for H=1.3m and scenario C. (Paper 9)

In the same way, the interaction of breaking waves with a pair of cylinders placed in tandem arrangement is examined for four different wave impact scenarios and six different distances between the cylinders. The impact scenarios considered in the present investigation are: (A) overturning wave crest hits the first cylinder just below the crest level, (B) overturning wave crest hits the first cylinder at the wave crest level, (C) wave breaks exactly at the first cylinder, and (D) wave breaks behind the first cylinder. The free surface deformation around the cylinders and their interaction with the cylinders are also discussed. Fig. 3.31 shows the normalized wave force (F/F_0) versus the normalized time (t/T) for $S = 1D, 2D$ and $3D$ and the normalized maximum wave force (F_{max}/F_{0max}) versus the non-dimensional distances (S/D) for scenario C. The total force on cylinder 1 is larger than on cylinder 2 when the cylinders are separated by S/D=1 (Fig. 3.31 (a)) and 2 (Fig. 3.31 (b)). While the distance between the cylinders is increased to S/D=3 (Fig. 3.31 (c)) and 4, cylinder 2 experiences more force with a sharp peak than cylinder 1. This is due to the impact of fully developed overturning jet on cylinder 2. For S/D=5 and 6 (Fig. 3.31 (d)), cylinder 2 is mainly exposed to the fully broken wave and this exerts a lower force on cylinder 2. Fig. 3.32 shows the normalized wave force (F/F_0)

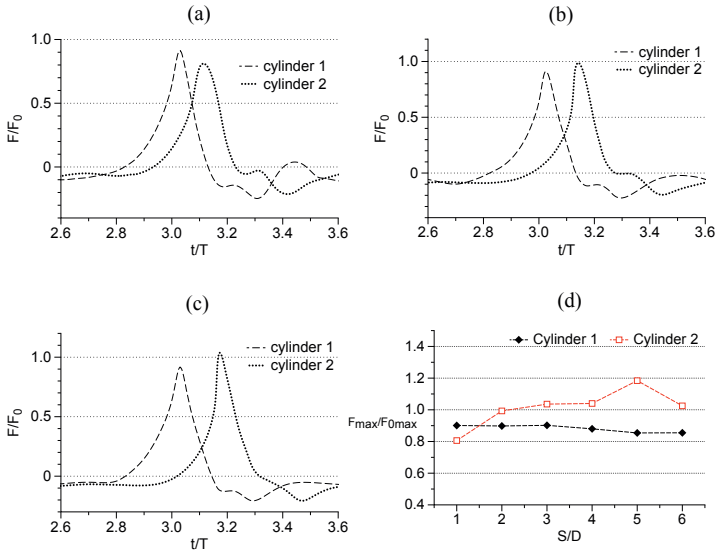

Figure 3.32: Computed normalized wave force (F/F_0) versus normalized time (t/T) for scenario D: wave breaking behind cylinder 1 with H=1.3m for S=1D (a), 2D (b), and 3D (c) and (d) computed normalized maximum wave force (F_{max}/F_{0max}) versus non-dimensional distance (S/D). F_0 and F_{0max} are the total wave force and the maximum wave force on a single cylinder, respectively, for H=1.3m and scenario D. (Paper 9)

versus the normalized time (t/T) for S/D=1, 2 and 3 and the normalized maximum wave force (F_{max}/F_{0max}) versus the non-dimensional distances (S/D) for scenario D. It can be seen from Fig. 3.32 (d) that the normalized force on cylinder 2 is larger than on cylinder 1 for all S/D except for S/D=1 (Fig. 3.32 (a)). For S/D= 2 to 6 (Fig. 3.32 (d)), cylinder 2 experiences larger forces than cylinder 1 as cylinder 1 is exposed to the non-breaking waves while cylinder 2 is impacted by the wave with the overturning wave crest at around the wave crest level, resulting in larger wave forces. When S/D is increased to 6, cylinder 2 is exposed to the fully broken wave, i.e. when the overturning wave crest reconnects the forward wave trough during impact on cylinder 1, leading to a lower force on cylinder 2. The numerically captured free surface flow features for scenario D3 (S/D=3) are presented in Fig. 3.33. In this case, cylinder 1 interacts with the nearly breaking wave and the wave front starts to separate around the cylinder (Fig. 3.33 (a)). As seen from Fig. 3.33 (a), the overturned wave crest impacts cylinder 2 just below the wave crest level and it exerts larger force on cylinder 2 (Fig. 3.32 (c)). This causes the large wave run-up around cylinder 2 (Fig. 3.33 (c)) and the formation of

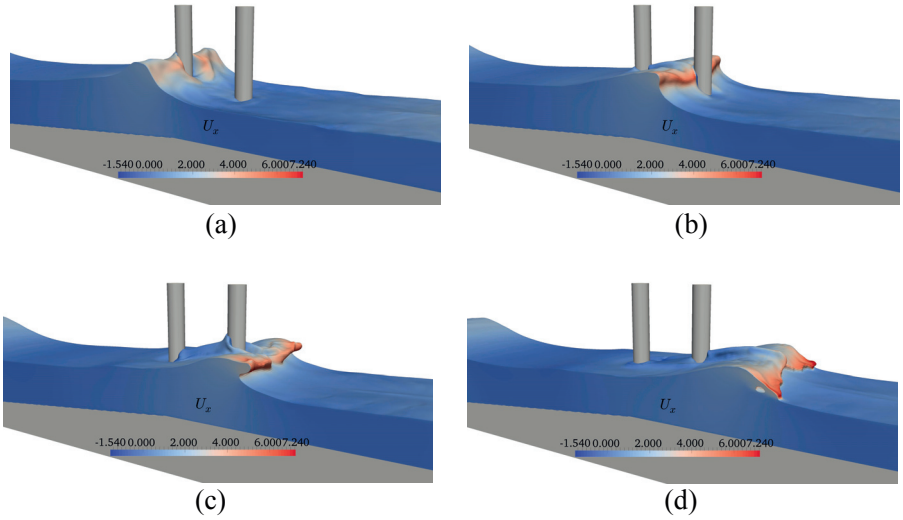

Figure 3.33: Simulated free surface deformations around the cylinders for wave scenario D3 (S/D=3) with horizontal velocity contours at t/T=3.06 (a), 3.11 (b), 3.18 (c), and 3.63 (d) (Paper 9).

water jet behind cylinder 2 (Fig. 3.33 (d)). In general, the breaking wave force on the first cylinder appears to be larger than that of the second cylinder. However, the second cylinder experiences larger force than the first cylinder when the wave crest with the ejected water jet impacts the second cylinder around the wave crest level. Finally, the numerical results suggest that the distance between the tandem cylinders and the breaker location have a significant influence on the breaking wave forces on the cylinders.

4

Conclusions and recommendations for future research

The simulation of wave breaking over slopes and submerged structures and the interaction of breaking waves with slender cylinders have been performed with the three-dimensional open-source CFD model REEF3D. This two-phase flow CFD model is based on the RANS equations coupled with the level set method and the $k - \omega$ turbulence model. The present numerical model uses different approaches for describing the computational grid architecture and discretization schemes. The employment of the Cartesian grid facilitates to implement higher order spatial and temporal discretization schemes that provide very good numerical accuracy and stability. The numerical results are validated carefully against experimental measurements for each case. The comparisons provide good agreement between the computed results and measured data, showing that the model is capable of capturing the prominent physical flow features related to breaking waves in shallow waters and their interaction with structures.

On sloping beaches and submerged structures, the physical flow characteristics during the wave breaking such as the development of the forward overturning wave crest, air pocket, splash-up, and the secondary wave are well represented in the numerical simulations. The numerical model is thoroughly tested and validated for simulating breaking waves by comparing the numerical wave envelope, free surface elevation, horizontal and vertical components of velocity, turbulence intensity with experimental

measurements. The wave kinematics of the primary wave during the breaking process and the secondary wave, that evolves during the splash-up, are captured well in the simulations. The present study also confirms that both spilling and plunging breakers are found to have similar flow features during the initial breaking process. Further, the performance of the numerical model for simulating breaking wave interaction with a slender cylinder in shallow waters is evaluated and verified. The numerical results are compared against experimental data for the free surface elevation around the cylinder, horizontal and vertical components of velocity and breaking wave forces. It has been shown that the numerical model can provide detailed information about the physical flow features such as the free surface deformation, the formation of the downstream water jet, and the run-up during the interaction of breaking waves with slender cylinders. Moreover, the numerical model gives a good representation of the experimentally observed flow features. The present numerical study confirms results of previous studies.

The detailed information concerning the development of the free surface profile, the variation of wave height and velocities and geometric properties during the breaking process are essential in order to evaluate the hydrodynamic loads on structures from breaking waves. Overall, this knowledge allows to learn and to understand more about the physical processes related to wave breaking and the interaction with slender cylinders. The study also examined the characteristics, kinematics and geometrical properties of breaking waves in shallow waters, and evaluated breaking wave forces on slender vertical cylinders. The main results of the PhD study are discussed briefly in Chapter 3 and further details on the results can be found in Papers 1-9. The main conclusions of the present numerical investigations are summarized below:

Characteristics of breaking waves:

- Wave breaking over slopes is largely affected by the change of water depth and offshore wave steepness. The breaker depth index and breaker height index decrease with increasing water depth and offshore wave steepness for a given slope. Waves break earlier at larger breaker depth for smaller waves over steeper slopes due to larger partial reflections from the slope and for larger waves over milder slopes due to the higher shoaling rate.

- The plunging breaker has a larger ratio of the wave height to water depth at breaking than the spilling breaker. Therefore, the plunging breaker undergoes more deformation and thus, a drastic change in the initial wave characteristics occurs. In addition, the wave height decreases immediately after the breaking point in the surf zone for the plunging breaker, but it starts to decrease later for the spilling breaker.

- In addition to the shoaling and the partial reflections from the reef face, the return flow caused by a downstream vortex near the reef crest also affects the breaking process over a submerged reef. The effect of the offshore wave steepness and water depth on the breaker depth index is weak, whereas it is significant for the breaker height index.

Geometric properties of breaking waves:

- The wave profile at breaking for a given slope develops into a more asymmetric shape when the reference water depth increases and the offshore wave steepness decreases. On steeper slopes, the wave front becomes steeper without much change in the rear part of the wave crest and the wave trough. But on the milder slopes, the rear part of the wave crest and the wave trough undergo significant deformation with relatively small changes in the wave front. This indicates that the seabed slope has a larger influence on describing the breaker types.

- In the case of a submerged reef, the wave crest front and rear part and the wave trough deform more with small changes in the vertical asymmetry for waves with larger offshore wave steepness, which is similar to a spilling breaker. On the other hand, for waves with smaller offshore wave steepness, the wave profile at breaking has a smooth rear part and a deeper wave trough with an ejected wave front which is similar to that of a plunging breaker.

- The wave profile evolves into an asymmetric shape for shallower water depth over the reef crest. The water depth at the reef crest has a substantial effect on the breaking process and the breaker type.

Interaction of breaking waves with slender cylinders

- For solitary waves, the maximum breaking wave force occurs when the wave hits the cylinder just before breaking with an inclined wave front and the corresponding wave height is equal to the wave height at breaking. The free surface deformation around the cylinder and the size of the water jet evolved during the reconnection of the free surface behind the cylinder increase as the incident wave height increases.

- For periodic waves, the maximum force occurs when the wave breaks just in front of the cylinder, i.e. the overturning wave front impacts the cylinder surface just below the wave crest level. On the other hand, the cylinder experiences the lowest force when the wave breaks behind the cylinder. When the breaking waves interact with the cylinder, a chute-like water jet is generated behind the cylinder and its size increases as the incident wave becomes larger. Moreover, this flow

feature reconnects to the forward free surface at some distance downstream from the cylinder.

Recommendations for future research

The present research has investigated some aspects concerning the mechanisms, characteristics and geometrical properties of breaking waves in shallow waters and their interaction with slender cylinders. However, more research is needed to understand the complete physical processes involved during the interaction of breaking waves with structures and the related flow characteristics including the wave impact forces. It is recommended to perform further research to address the following issues:

- *Breaking wave forces with respect to global loads and responses:* The breaking wave forces on typical wind turbine substructures can be calculated by applying the breaking wave loads obtained from the CFD model to structural models based on a finite element method. The effects on forces, moments and displacements on the one hand, and on fatigue (damage equivalent loads) on the other hand, should be analysed.

- *Effects of entrained air on the impact loads:* During wave breaking, air is entrained into the water phase, and similar to existing two-dimensional studies, a reduction in the impact pressures is expected. These load reduction effects can be studied in three dimensions using the present model with a compressible flow solver.

- *Irregular wave breaking:* In the present research, regular waves were used in the numerical simulations in order to gain more insights into the fundamental physical processes. However, waves are irregular in real sea conditions; thus the irregular breaking wave kinematics and the corresponding breaking wave forces need to be studied for different environmental parameters characterizing both long-crested and short-crested random waves on seabed slopes. The probability of occurrence of wave breaking under such conditions is also important.

- *Complex structures:* The present study can be extended to investigate the breaking wave forces on other substructures for offshore wind turbines in relatively shallow waters such as tripods, tripiles and truss structures.

5

References

Adeyemo, M. (1968), Effect of beach slope and shoaling on wave asymmetry, *in* 'Proceedings of the 11-th Conference on Coastal Engineering', pp. 145–172.

Alagan Chella, M., Bihs, H., Kamath, A. and Muskulus, M. (2013), Numerical modeling of breaking waves over a reef with a level set based numerical wave tank, *in* 'Proceedings of the 32-nd International Conference on Offshore Mechanics and Arctic Engineering'.

Alagan Chella, M., Bihs, H. and Muskulus, M. (2014), Numerical simulation of breaking waves on a plane slope with a parallel level set solver, *in* 'Proceedings of the 11-th International Conference on Hydroscience and Engineering'.

Alagan Chella, M., Bihs, H. and Myrhaug, D. (2015b), 'Characteristics and profile asymmetry properties of waves breaking over an impermeable submerged reef', *Coast. Eng.* **100**, 26–36.

Alagan Chella, M., Bihs, H., Myrhaug, D. and Muskulus, M. (2015a), 'Breaking characteristics and geometric properties of spilling breakers over slopes', *Coast. Eng.* **95**, 4–19.

Alagan Chella, M., Bihs, H., Myrhaug, D. and Muskulus, M. (2015c), 'Hydrodynamic characteristics and geometric properties of plunging and spilling breakers over impermeable slopes', *Ocean Modelling* . DOI: 10.1016/j.ocemod.2015.11.011.

Alagan Chella, M., Tørum, A. and Myrhaug, D. (2012), 'An overview of wave impact forces on offshore wind turbine substructures', *Energy Procedia* **20**, 217–226.

Apelt, C. J. and Piorewicz, J. (1987), 'Laboratory studies of breaking wave forces acting on vertical cylinders in shallow water', *Coast. Eng.* **11**, 263–282.

Arntsen, Ø. A., Ros, X. and Tørum, A. (2011), Impact forces on a vertical pile from plunging breaking waves, *in* 'Proceedings of the 24-th Conference on Coastal structures'.

Babanin, A. V. (2011), *Breaking and dissipation of ocean surface waves*, Cambridge University Press.

Babanin, A. V., Chalikov, D., Young, I. R. and Savelyev, I. (2010), 'Numerical and laboratory investigation of breaking of steep two-dimensional waves in deep water', *J. Fluid Mech.* **644**, 433.

Banner, M. L. and Tian, X. (1998), 'On the determination of the onset of breaking for modulating surface gravity water waves', *J. Fluid Mech.* **367**, 107–137.

Banner, M. and Peregrine, D. H. (1993), 'Wave breaking in deep water', *Annu. Rev. Fluid Mech.* (25), 373–397.

Basco, D. R. (1985), 'A qualitative description of wave breaking', *J. Waterw. Port Coast. Ocean Eng.* **3**(2), 171–188.

Battjes, J. A. (1974), Surf similarity, *in* 'Proceedings of the 14-th Conference on Coastal Engineering', number 1, pp. 466–480.

Beji, S. and Battjes, J. (1993), 'Experimental investigation of wave propagation over a bar', *Coast. Eng.* **19**, 151–162.

Berthelsen, P. A. and Faltinsen, O. M. (2008), 'A local directional ghost cell approach for incompressible viscous flow problems with irregular boundaries', *J. Comput. Phys.* **227**, 4354–4397.

Blenkinsopp, C. and Chaplin, J. (2008), 'The effect of relative crest submergence on wave breaking over submerged slopes', *Coast. Eng.* **55**(12), 967–974.

Bonmarin, P. (1989), 'Geometric properties of deep-water breaking waves', *J. Fluid Mech.* **209**, 405–433.

Bradford, S. F. (2000), 'Numerical simulation of surf zone dynamics', *J. Waterw. Port Coast. Ocean Eng.* **126**, 1–13.

Bredmose, H. and Jacobsen, N. G. (2010), Breaking wave impacts on offshore wind turbine foundations: Focused wave groups and CFD, *in* 'Proceedings of the 29-th International Conference on Ocean, Offshore and Arctic Engineering', pp. 397–404.

Bredmose, H. and Jacobsen, N. G. (2011), Vertical wave impacts on offshore wind turbine inspection platforms, *in* 'Proceddings of the 30-th International Conference on Ocean, Offshore and Arctic Engineering', pp. 645–654.

Briganti, R., Musumeci, R. E., Bellotti, M., Brocchini, M. and Foti, E. (2004), 'Boussinesq modeling of breaking waves: Description of turbulence', *J. Geophys. Res.* **109**, 1–17.

Brocchini, M. (2013), 'A reasoned overview on Boussinesq-type models: the interplay between physics, mathematics and numerics', *Proceedings of the Royal Society of London A: Mathematical, Physical and Engineering Sciences* **469**.

Chakrabarti, S. K. (1987), *Hydrodynamics of offshore structures*, WIT press.

Chang, K. A., Hsu, T. J. and Liu, P. L. F. (2005), 'Vortex generation and evolution in water waves propagating over a submerged rectangular obstacle Part II: Cnoidal waves', *Coast. Eng.* **52**(3), 257–283.

Chaplin, J., Flintham, T., Greated, C. and Skyner, D. (1992), Breaking wave forces on a vertical cylinder, Technical report, Health and Safety Executive, London, UK.

Chen, G., Kharif, C., Zaleski, S. and Li, J. (1999), 'Two-dimensional Navier-Stokes simulation of breaking waves', *Phys. Fluids* **11**, 121–133.

Choi, S., Lee, K. and Gudmestad, O. (2015), 'The effect of dynamic amplification due to a structures vibration on breaking wave impact', *Ocean Eng.* **96**, 8–20.

Chorin, A. (1968), 'Numerical solution of the Navier-Stokes equations', *Math. Comput.* **22**, 745–762.

Christensen, E. D. (2006), 'Large eddy simulation of spilling and plunging breakers', *Coast. Eng.* **53**(5-6), 463–485.

Christensen, E. D., Bredmose, H. and Hansen, E. A. (2005), Extreme wave forces and wave run-up on offshore windturbine foundations, *in* 'Proceedings of Copenhagen Offshore Wind', pp. 1–10.

Christensen, E. D. and Deigaard, R. (2001), 'Large eddy simulation of breaking waves', *Coast. Eng.* **42**, 53–86.

Cokelet, E. (1977), 'Breaking waves', *Nature* **267**, 769–774.

Dold, J. W. and Peregrine, D. H. (1986), 'An efficient boundary-integral method for steep unsteady water waves', *Numerical methods for fluid dynamics II* **671**, 679.

Dommermuth, D. G., Yue, D. K., Lin, W. M., Rapp, R. J., Chan, E. S. and Melville, W. K. (1988), 'Deep-water plunging breakers : a comparison between potential theory and experiments', *J. Fluid Mech.* **189**, 423–442.

Duncan, J. H. (2001), 'Spilling breakers', *Annu. Rev. Fluid Mech.* **33**, 519–547.

Durbin, P. A. (2009), 'Limiters and wall treatments in applied turbulence modeling', *Fluid Dynamics Research* **41**, 1–18.

Galvin, C. J. (1968), 'Breaker type classification on three laboratory beaches', *J. Geophys. Res.* **73**(12), 3651–3659.

Goda, Y. (2010), 'Reanalysis of regular and random breaking wave statistics', *Coast. Eng. Journal* **52**(01), 71–106.

Goda, Y., Haranaka, S. and Kitahata, M. (1966), Study of impulsive breaking wave forces on piles, Technical report, Port and Harbor Research Institute, Ministry of Transport.

Griebel, M., Dornseifer, T. and Neunhoeffer, T. (1998), *Numerical Simulation in Fluid Dynamics, a Practical Introduction*, SIAM.

Grilli, S. T., Gilbert, R. W., Lubin, P., Vincent, S., Astruc, D., Legendre, D., Duval, M., Kimmoun, O., Branger, H., Devrard, D. et al. (2004), Numerical modeling and experiments for solitary wave shoaling and breaking over a sloping beach, *in* 'Proceedings of the 14-th International Ocean and Polar Engineering Conference'.

Grilli, S. T., Losada, M. A. and Martin, F. (1994), 'Characteristics of solitary wave breaking induced by breakwaters', *J. Waterw. Port Coast. Ocean Eng.* **120**, 74–92.

Grilli, S. T., Skourup, J. and Svendsen, I. A. (1989), 'An efficient boundary element method for nonlinear water waves', *Engineering Analysis with Boundary Elements* **6**, 97–107.

Grilli, S. T., Subramanya, R., Svendsen, I. A. and Veeramony, J. (1995), 'Shoaling of solitary waves on plane beaches', *J. Waterw. Port Coast. Ocean Eng.* **120**(6), 609–628.

Grilli, S. T., Svendsen, I. A. and Subramanya, R. (1997), 'Breaking criterion and characteristics for solitary waves on slopes', *J. Waterw. Port Coast. Ocean Eng.* **123**(3), 102–112.

Guyenne, P. and Grilli, S. T. (2006), 'Numerical study of three-dimensional overturning waves in shallow water', *J. Fluid Mech.* **547**(-1), 361.

Harlow, F. H. and Welch, J. E. (1965), 'Numerical calculation of time-dependent viscous incompressible flow of fluid with free surface', *Phys. Fluids* **8**(12), 2182–2189.

Heitner, K. L. and Housner, G. W. (1970), 'Numerical model for tsunami runup', *J. Waterw. Port Coast. Ocean Eng.* **96**, 701–719.

Hendrickson, K. L. (2005), Navier-Stokes simulations of steep breaking water waves with a coupled air-water interface, PhD thesis, Massachusetts Institute of Technology.

Hieu, P. D., Katsutoshi, T. and Ca, V. T. (2004), 'Numerical simulation of breaking waves using a two-phase flow model', *Appl. Math. Model.* **28**(11), 983–1005.

Hwang, P. A. (1984), Profile asymmetry of shoaling waves on a mild slope, *in* 'Proceedings of the 19-th Conference on Coastal Engineering', pp. 1016–1027.

Iafrati, A. (2009), 'Numerical study of the effects of the breaking intensity on wave breaking flows', *Journal of Fluid Mechanics* **622**, 371–411.

Ippen, A. T. and Kulin, G. (1954), The shoaling and breaking of the solitary wave, *in* 'Proceedings of the 5-th Conference on Coastal Engineering', pp. 27–47.

Irschik, K., Sparboom, U. and Oumeraci, H. (2002), Breaking wave characteristics for the loading of a slender pile, *in* 'Proceedings of the 28-th Conference on Coastal Engineering', pp. 1341–1352.

Irschik, K., Sparboom, U. and Oumeraci, H. (2004), Breaking wave loads on a slender pile in shallow water, *in* 'Proceedings of the 29-th Conference on coastal engineering'.

Iversen, H. W. (1952), Laboratory study of breakers, *in* 'Proceedings of the NBS Semicentennial Symposium on Gravity Waves, National Bureau of Standards Circular 521', pp. 9–32.

Iwagaki, Y. and Sakai, T. (1972), Shoaling of finite amplitude long waves on a beach of constant slope, *in* 'Proceedings of the 13-th Conference on Coastal Engineering', pp. 347–364.

Iwata, K., Kawasaki, K. and Kim, D. S. (1996), Breaking limit, breaking and post-breaking wave deformation due to submerged structures, *in* 'Proceedings of the 24-th Conference on Coastal Engineering', pp. 2338–2351.

Jacobsen, N. G., Fuhrman, D. R. and Fredsøe, J. (2012), 'A wave generation toolbox for the open-source CFD library : OpenFoam', *Int. J. Numer. Methods Fluids* **70**(November), 1073–1088.

Jiang, G. S. and Shu, C. W. (1996), 'Efficient implementation of weighted ENO schemes', *J. Comput. Phys.* **126**, 202–228.

Kamath, A., Alagan Chella, M., Bihs, H. and Arntsen, Ø. A. (2015), 'CFD investigations of wave interaction with a pair of large tandem cylinders', *Ocean Eng.* **108**, 734–748.

Kennedy, A. B., Chen, Q., Kirby, J. T. and Dalrymple, R. A. (2000), 'Bousssinesq modelling of wave transformation, breaking, and runup. I:1D', *J. Waterw. Port Coast. Ocean Eng.* **126**(1), 701–719.

Kjeldsen, S. P. and Myrhaug, D. (1978), Kinematics and dynamics of breaking waves, Technical report, River and Harbour Laboratory (NHL), The Norwegian Institute of Technology.

Lachaume, C., Biausser, B., Fraunié, P., Grilli, S. T. and Guignard, S. (2003), Modeling of breaking and post-breakingwaves on slopes by coupling of BEM and VOF methods, *in* 'Proceedings of the 13-th International Ocean and Polar Engineering Conference'.

Lader, P. F. (2002), Geometry and Kinematics of Breaking Waves, PhD thesis, Norwegian University of Science and Technology.

Larsen, J. and Dancy, H. (1983), 'Open boundaries in short wave simulations - a new approach', *Coast. Eng.* **7**, 285–297.

Lemos, C. M. (1992), 'A simple numerical technique for turbulent flows with free surfaces', *Int. J. Numer. Methods Fluids* **15**, 127–146.

Lin, P. (2008), *Numerical modeling of water waves*, CRC Press.

Lin, P. and Liu, P. L.-F. (1998), 'A numerical study of breaking waves in the surf zone', *J. Fluid Mech.* **359**, 239–264.

Longuet-Higgins, M. S. and Cokelet, E. D. (1976), 'The deformation of steep surface waves on water I- A numerical method of computation', *Proceedings of the Royal Society of London. Series A, Mathematical and Physical Sciences* **350**(1660), 1–26.

Lubin, P., Glockner, S., Kimmoun, O. and Branger, H. (2011), 'Numerical study of the hydrodynamics of regular waves breaking over a sloping beach', *European Journal of Mechanics - B/Fluids* **30**(6), 552–564.

Lubin, P., Vincent, S., Abadie, S. and Caltagirone, J. P. (2006), 'Three-dimensional large eddy simulation of air entrainment under plunging breaking waves', *Coast. Eng.* **53**, 631–655.

Ma, G., Shi, F. and Kirby, J. T. (2011), 'A polydisperse two-fluid model for surf zone bubble simulation', *J. Geophys. Res.* **116**.

Madsen, P. A., Murray, R. and Sørensen, O. R. (1991), 'A new form of the boussinesq equations with improved linear dispersion characteristics', *Coast. Eng.* **15**, 371–388.

Madsen, P. A., Sørensen, O. R. and Schäffer, H. A. (1997), 'Surf zone dynamics simulated by a Boussinesq type model. Part I. Model description and cross-shore motion of regular waves', *Coast. Eng.* **32**, 51–80.

Madsen, P. A. and Svendsen, I. A. (1983), 'Turbulent bores and hydraulic jumps', *J. Fluid Mech.* **129**, 1–25.

Mayer, S. and Madsen, P. A. (2000), Simulation of breaking waves in the surf zone using a navier-stokes solver, *in* 'Proceedings of the 27-th Conference on Coastal Engineering', pp. 928–941.

Miles, J. W. (1980), 'Solitary waves', *Annu. Rev. Fluid Mech.* (12), 11–43.

Miller, R. L. (1987), 'Role of vortices in surf zone prediction: sedimentation and wave forces', *The Society of Economic Paleontologists and Mineralogists, Special Publications* (24), 92–114.

Miller, R. L. and Zeigler, J. M. (1964), The internal velocity field in breaking waves, *in* 'Proceedings of the 9-th Conference on Coastal Engineering', pp. 103–122.

Mo, W., Jensen, A. and Liu, P. L.-F. (2013), 'Plunging solitary wave and its interaction with a slender cylinder on a sloping beach', *Ocean Eng.* **74**, 48–60.

Moraga, F., Carrica, P., Drew, D. and Lahey Jr., R. (2008), 'A sub-grid air entrainment model for breaking bow waves and naval surface ships', *Computers and Fluids* **37**(10), 281–298.

Morison, J. R., Johnson, J. W. and Schaaf, S. A. (1950), 'The force exerted by surface waves on piles', *J. Petrol. Technol.* **2**, 149–154.

Munk, W. H. (1949), 'The solitary wave theory and its application to surf problems', *Annals of the New York Academy of Sciences* **3**, 376–424.

Naot, D. and Rodi, W. (1982), 'Calculation of secondary currents in channel flow', *J. Hydr. Div., ASCE* **108**(8), 948–968.

New, A. L., McIver, P. and Peregrine, D. H. (1985), 'Computations of overturning waves', *J. Fluid Mech.* **150**, 233–251.

NOTUR (2015), 'The Norwegian Metacenter for Computational Science', *http://www.notur.no/hardware/vilje* .

Nwogu, O. (1993), 'Alternative form of boussinesq equations for nearshore wave propagation', *J. Waterw. Port Coast. Ocean Eng.* **119**(6), 618–638.

Osher, S. and Sethian, J. A. (1988), 'Fronts propagating with curvature-dependent Speed: Algorithms based on Hamilton-Jacobi formulations', *J. Comput. Phys.* **79**, 12–49.

Peng, D., Merriman, B., Osher, S., Zhao, H. and Kang, M. (1999), 'A PDE-based fast local level set method', *J. Comput. Phys.* **155**, 410–438.

Peregrine, D. H. (1967), 'Long waves on a beach', *J. Fluid Mech.* **27**(04), 815–827.

Peregrine, D. H. (1983), 'Breaking waves on beaches', *Annu. Rev. Fluid Mech.* (15), 149–178.

Peregrine, D. H., Cokelet, E. D. and Mclver, P. (1980), The fluid mechnics of waves approaching breaking, *in* 'Proceedings of the 17-th Conference on Coastal Engineering', pp. 512–528.

Peregrine, D. and Svendsen, I. (1978), Spilling breakers, bores and hydraulic jumps, *in* 'Proceedings of the 16-th Conference on Coastal Engineering', pp. 540–550.

Perlin, M., Choi, W. and Tian, Z. (2013), 'Breaking waves in deep and intermediate waters', *Annu. Rev. Fluid Mech.* (45), 115–145.

Sawaragi, T. and Nochino, M. (1984), 'Impact forces of nearly breaking waves on a vertical circular cylinder', *Coastal Engineering Journal* **27**, 249–263.

Schäffer, H. A., Madsen, P. A. and Deigaard, R. (1993), 'A Boussinesq model for waves breaking in shallow water', *Coast. Eng.* **20**, 185–202.

Shi, F., Kirby, J. T. and Ma, G. (2010), 'Modeling quiescent phase transport of air bubbles induced by breaking waves', *Ocean Modelling* **35**, 105–117.

Shu, C. W. and Osher, S. (1988), 'Efficient implementation of essentially non-oscillatory shock capturing schemes', *J. Comput. Phys.* **77**, 439–471.

Smith, E. R. and Kraus, N. C. (1990), Laboratory study on macro-features of wave breaking over bars and artificial reefs, Technical report, Coastal Engineering Research Center.

Song, C. and Sirviente, A. I. (2004), 'A numerical study of breaking waves', *Physics of Fluids* **16**(7), 2649–2667.

Stoker, J. J. (1949), *Water waves: The mathematical theory with applications*, John Wiley and Sons.

Sussman, M., Smereka, P. and Osher, S. (1994), 'A level set approach for computing solutions to incompressible two-phase flow', *J. Comput. Phys.* **114**, 146–159.

Svendsen, I. A. (1984), 'Wave heights and set-up in a sruf zone', *Coast. Eng.* **8**, 303–329.

Svendsen, I. A. and Madsen, P. A. (1984), 'A turbulent bore on a beach', *J. Fluid Mech.* **148**, 73–96.

Svendsen, I. A., Madsen, P. A. and Hansen, J. B. (1978), Wave characteristics in the surf zone, *in* 'Proceedings of the 16th Conference on Coastal Engineering', pp. 520–539.

Svendsen, I. A., Yu, K. and Veeramony, J. (1996), A boussinesq breaking wave model with vorticity, *in* 'Proceedings of the 25th conference on Coastal Engineering', pp. 1192–1204.

Tanimoto, K., Takahashi, S., Kaneko, T. and Shiota, K. (1986), Impulsive breaking wave forces on an inclined pile exerted bi random waves, *in* 'Proceedings of the 20th Conference on Coastal Engineering'.

Ting, F. C. K. and Kim, Y. K. (1994), 'Vortex generation in water waves propaga over a submerged obstacle', *Coast. Eng.* **24**(1), 23–49.

Ting, F. C. K. and Kirby, J. T. (1994), 'Observation of undertow and turbulence in a laboratory surf zone', *Coast. Eng.* **24**(1-2), 51–80.

Ting, F. C. K. and Kirby, J. T. (1995), 'Dynamics of surf-zone turbulence in a strong plunging breaker', *Coast. Eng.* **24**(3-4), 177–204.

Ting, F. C. K. and Kirby, J. T. (1996), 'Dynamics of surf-zone turbulence in a spilling breaker', *Coast. Eng.* **27**, 131–160.

Tsai, C. P., Chen, H. B., Hwung, H. H. and Huang, M. J. (2005), 'Examination of empirical formulas for wave shoaling and breaking on steep slopes', *Ocean Eng.* **32**(3-4), 469–483.

van der Vorst H. (1992), 'Bi-CGSTAB: A fast and smoothly converging variant of Bi-CG for the solution of nonsymmetric linear systems', *SIAM Journal on scientific and Statistical Computing* **13**, 631–644.

Veeramony, J. and Svendsen, I. A. (2000), 'The flow in surf-zone waves', *Coast. Eng.* **39**, 93–122.

Vinje, T. and Brevig, P. (1981), 'Numerical simulation of breaking waves', *Adv. Water Resour.* **4**(2), 77–82.

Wang, Z., Yang, J., Koo, B. and Stern, F. (2009a), 'A coupled level set and volume-of-fluid method for sharp interface simulation of plunging breaking waves', *Int. J. Multiphas. Flow* **35**(3), 227–246.

Wang, Z., Zou, Q. and Reeve, D. (2009b), 'Simulation of spilling breaking waves using a two phase flow CFD model', *Computers and Fluids* **38**(10), 1995–2005.

Watanabe, Y., Saeki, H. and Hosking, R. J. (2005), 'Three-dimensional vortex structures under breaking waves', *J. Fluid Mech.* **545**, 291–328.

Weggel, J. R. (1972), Maximum breaker height for design, *in* 'Proceedings of the 13-th Conference on Coastal Engineering', pp. 419–432.

Wei, G. and Kirby, J. T. (1996), A coastal processes model based on time-domain Boussinesq equations, Technical report, Center for applied coastal research.

Wei, G., Kirby, J. T., Grilli, S. and Subramanya, R. (1995), 'A fully nonlinear Boussinesq model for surface waves. Part 1. Highly nonlinear unsteady waves', *J. Fluid Mech.* **294**, 71–92.

Wienke, J. and Oumeraci, H. (2005), 'Breaking wave impact force on a vertical and inclined slender pile-theoretical and large-scale model investigations', *Coast. Eng.* **52**, 435–416.

Wilcox, D. C. (1994), *Turbulence Modeling for CFD*, DCW Industries Inc., La Canada, California.

Xiao, H. and Huang, W. (2014), 'Three-dimensional numerical modeling of solitary wave breaking and force on a cylinder pile in a coastal surf zone', *J. Eng. Mech. - ASCE* **141(8)**.

Xie, Z. (2012), 'Numerical study of breaking waves by a two-phase flow model', *Int. J. Numer. Methods Fluids* **70**, 246–268.

Xie, Z. (2013), 'Two-phase flow modelling of spilling and plunging breaking waves', *Appl. Math. Model.* **37**, 3698–3713.

Xue, M., Xü, H., Liu, Y. and Yue, D. K. (2001), 'Computations of fully nonlinear three-dimensional wave-wave and wave-body interactions. Part 1. Dynamics of steep three-dimensional waves', *J. Fluid Mech.* **438**, 11–39.

Yamazaki, Y., Kowalik, Z. and Cheung, K. F. (2008), 'Depth-integrated, non-hydrostatic model for wave breaking and run-up', *Int. J. Numer. Methods Fluids* **61**(5), 473–497.

Zelt, J. A. (1991), 'The run-up of nonbreaking and breaking solitary waves', *Coast. Eng.* **15**, 205–246.

Zhao, Q., Armfield, S. and Tanimoto, K. (2004), 'Numerical simulation of breaking waves by a multi-scale turbulence model', *Coast. Eng.* **51**(1), 53–80.

6

Papers

Paper 1 Alagan Chella, M., Tørum, A. Myrhaug, D. (2012), An overview of wave impact forces on offshore wind turbine substructures, *Energy Procedia*, Vol. 20, pp. 217-226

Paper 2 Bihs, H. Kamath A., Alagan Chella, M., Aggarwal, A., Arntsen, Ø. A. (2015), A new level set numerical wave tank with improved density interpolation for complex wave hydrodynamics, Submitted to *Computers and Fluids* - under review

Paper 3 Alagan Chella, M., Bihs, H., Myrhaug, D., Muskulus, M. (2015), Breaking characteristics and geometric properties of spilling breakers over slopes, *Coastal Engineering*, Vol. 95, pp. 4-19

Paper 4 Alagan Chella, M., Bihs, H., Myrhaug, D., Muskulus, M. (2015), Hydrodynamic characteristics and geometric properties of plunging and spilling breakers over impermeable slopes, *Ocean Modelling*, DOI: 10.1016/j.ocemod.2015.11.011

Paper 5 Alagan Chella, M., Bihs, H., Myrhaug, D. (2015), Characteristics and profile asymmetry properties of waves breaking over an impermeable submerged reef, *Coastal Engineering*, Vol. 100, pp. 26-36

Paper 6 Kamath, A., Alagan Chella, M., Bihs, H., Arntsen, Ø. A. (2015), Energy transfer due to shoaling and decomposition of breaking and non-breaking waves over a submerged bar, Submitted to *Engineering Applications of Computational Fluid Mechanics* - under review

Paper 7 Alagan Chella, M., Bihs, H.,Myrhaug, D., Muskulus, M. (2015), Breaking solitary waves and breaking wave forces on a vertically mounted slender cylinder over an

impermeable sloping seabed, Submitted to *Journal of Ocean Engineering and Marine Energy* - Revised version under review

Paper 8 Kamath, A., Alagan Chella, M., Bihs, H., Arntsen, Ø. A. (2015), Breaking wave interaction with a vertical cylinder and the effect of breaker location, Submitted to *Ocean Engineering* - under review

Paper 9 Bihs, H., Kamath, A., Alagan Chella, M., Arntsen, Ø. A. (2015), Breaking wave interaction with tandem cylinders under different impact scenarios, *Journal of Waterway, Port, Coastal, and Ocean Engineering*, DOI: 10.1061/(ASCE)WW.1943-5460.0000343.

Paper 1

6.1 Paper 1

An overview of wave impact forces on offshore wind turbine substructures

Alagan Chella, M., Tørum, A., Myrhaug, D.
Energy Procedia, 2012, Vol.20, pp. 217-226
DOI: 10.1016/j.egypro.2012.03.022

Available online at www.sciencedirect.com

SciVerse ScienceDirect

Energy Procedia 20 (2012) 217 – 226

Energy Procedia

Technoport RERC Research 2012

An Overview of Wave Impact Forces on Offshore Wind Turbine Substructures

Mayilvahanan Alagan Chella[a]*, Alf Tørum[a] and Dag Myrhaug[a]

Norwegian University of Science and Technology, NO-7491 Trondheim, Norway

Abstract

Offshore wind turbines are always subjected to highly varying aerodynamic and hydrodynamic loads which dictate the design phase of the wind turbine substructures. The breaking wave forces yield the highest hydrodynamic loads on substructures in shallow water, particularly plunging breaking waves. Due to the complex and transient nature of the impact forces, the description requires more details concerning the physical properties of breaking waves and the response of the structure. The objective of this paper is to give an overview of the previous and recent research on wave impact forces and the key issues pertaining to these forces on offshore wind turbine substructures.

Keywords: Breaking waves; slamming force; offshore wind turbine substructures; wave forces.

1. Introduction

The offshore wind turbine structures are slender and wave and wind loads act on the lower and the upper part of the tower. Near to the free surface zone, the wave forces may obtain their maximum values. Most of the recent substructures for wind turbines are monopiles, truss structures, tripods, gravity based structures etc. The substructures exposed to the harsh sea environment, experience the extreme impact force, run-up, scour etc. Breaking waves exert very high impact forces in very short duration on the substructures and the analysis is extremely intricate. Due to the impact force on the substructures, the

*Corresponding author. Tel.: +47-73594667, Mobile: +47-48348518
E-mail addresses: acm@ntnu.no.(Mayilvhanan, Alagan Chella), alf.torum@ntnu.no (Alf Tørum), dag.myrhaug@ntnu.no (Dag Myrhaug)

1876-6102 © 2011 Published by Elsevier Ltd. Selection and/or peer-review under responsibility of the Centre for Renewable Energy.
doi:10.1016/j.egypro.2012.03.022

performance and fatigue life of the offshore wind turbine is affected [1]. Wave run-up affects the design of boat landing and platform facilities of the offshore wind turbine structures.

Many laboratory and numerical studies have investigated the impact forces caused by breaking waves for oil and gas structures. The offshore wind structure is a long slender member, extending high above the mean water level and it carries the mass at the tip (rotor and nacelle). Hence, it is obvious that the dynamic characteristics of the wind turbine substructures are completely different from fixed oil and gas structures. Hence the effect of breaking wave forces on an offshore wind turbine needs to be investigated in more detail to improve the current design methods. The aim of this paper is to discuss the previous and recent research on the experimental results, numerical modeling, theoretical description of wave impact forces, design guidelines and the key issues concerning the wave impact forces on offshore wind turbine substructures.

2. Breaking wave force characteristics

2.1 Breaking waves

Breaking is initiated when the wave gains more energy, becomes unstable and dissipating the energy in the form of turbulence. During the wave breaking process, the energy of the wave system is focused close to the crest of the wave and a spatial spread of wave energy occurs [2].According to the Stokes criterion for wave breaking the particle velocity at the crest of the wave reaches the celerity. The common ratio of the wave height to the water depth at breaking is between 0.8 and 1.2. Breaking waves may occur at the site depending on the water depth, wave height, sea bed slope, wave period and steepness. Breaking waves are classified as spilling, plunging, surging and collapsing where the latter is the combination of plunging and surging [3]. The spilling and surging wave forces can be approximated as a quasi-static force. The breaking waves most relevant to offshore wind turbine structures are spilling and plunging breakers [4]. The energy from the plunging breakers is dissipated over a relatively small area, and high impulsive loads and high local pressures are exerted. Breaking wave properties are also depending on the wind-wave interaction, wave-wave interaction and wave-current interaction. There are two major uncertainties in breaking wave forces: the kinematics of the flow and the relationship between the flow and the breaking wave forces [5].

2.2 Breaking wave forces

The non-breaking wave force is normally calculated using Morison equation as the sum of the quasi static inertia and drag force, and the values of the inertia and drag coefficients are dependent on Keulegan-Carpenter number, Reynolds number, roughness parameters and interaction parameters [6]

$$F = F_D + F_M = \frac{1}{2}\int_{-d}^{\eta} \rho_w C_D D u|u|\,dz + \int_{-d}^{\eta} \rho_w C_M \frac{\pi D^2}{4}\frac{\partial u}{\partial t}\,dz \tag{1}$$

where F_D is the drag force, F_M is the inertia force, C_D is the drag coefficient, C_M is the inertia coefficient, ρ_w is the mass density of water, D is the pile diameter, u is the water particle velocity and t is time. The Morison equation is generally valid for small diameter members that do not considerably modify the incident waves, and it depends on the ratio of the wave length to the member diameter. The Morison equation is applicable when this ratio is larger than 5.0.

For design purposes, the impact force is previously approximated by considering only the drag force component and multiplying by a factor of 2.5 [7]. The total wave force on a sub-structure due to breaking waves can be divided into a quasi-static force and an impact force called slamming force. The quasi-static

force can be well described by the Morison equation and the impact force component must be added with

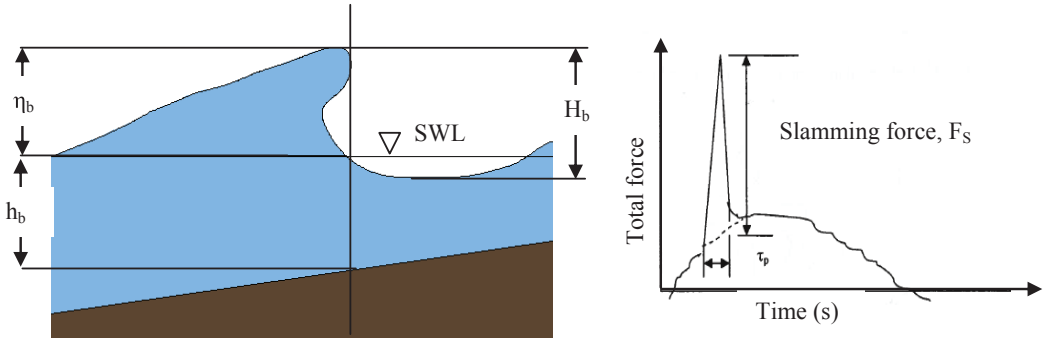

the Morison equation to determine the total wave force due to the breaking waves.

Figure 1 (a) Breaking wave parameters (SWL= Sea water level) and (b) The nature of the slamming force.

Three different approaches are used to account for the impact forces due to breaking waves in the structural design. First, a simple approach to estimate the impact force by applying the non-linear wave kinematics (non-linear wave theory) in the breaking zone to the structural members using Morison equation with conventional force coefficients [8].

Second, the impact force can be represented by the drag term of Morison's equation based on the relative velocity of the member to the water particle and with a suitable drag coefficient, because of the uncertainty involved in the prediction of accelerations caused by breaking waves [5, 9, 10]. In the splash zone, submerged structural members are vulnerable to wave impact due to the action of breaking waves. Moreover, the influence of the change in the momentum (inertia forces) is very important to account for the impact forces.

Third, if the wave breaks against the structure the Morison equation ought to be modified or expanded to include the wave breaking effect, especially due to plunging breakers on the slender structure. The nature of the slamming force is indicated in Fig. 1(a). However, the force coefficients in the Morison equation cannot describe the impact force of very short duration typically of the order of milliseconds. Hence it is imperative to add an extra term in Eqn. (1) to include the impact force effect (slamming force) in the total wave force [5, 11],

$$F = F_D + F_M + F_S \tag{2}$$

$$F_S = 0.5\rho_w C_s D C_b^2 \lambda \eta_b \tag{3}$$

Here F_s is the slamming force, C_s is the slamming force factor, C_b is the breaking wave celerity (the water particle velocity is set equal to the wave celerity at breaking), and λ is the curling factor which indicates how much of the wave crest is active in the slamming force as shown in Fig. 1(a).

2.3 Impact force characteristics

Basically, the impact force is caused by the collision of the upright wave front with a structure leading to a change in the forward momentum which yields a force of large magnitude in a short duration [11]. A

particular characteristic of plunging wave impacts is the considerable variation of the peak between different impacts. Fig. 2 shows a circular cylinder exposed to a breaking wave and the various parameters of the breaking process. The wave breaking is always associated with extreme velocities and accelerations with high surface elevations.

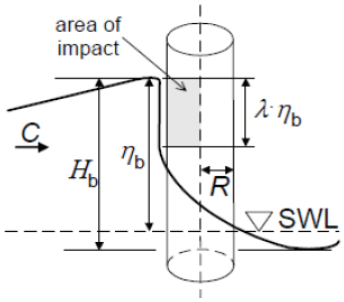

C is the wave celerity

H_b is the wave height at the breaking location

η_b is the maximum free surface elevation

R is the radius of the cylinder

λ is the curling factor

Figure 2 Breaking wave impact force on a circular cylinder [13]

Hence the structural members in the splash zone experience the severe loading due to breaking waves [5].The rising time is the time at which the impact force reaches its maximum value and it plays a vital role in the dynamic response of the structure. In fact, the rising time distribution affects the slamming force amplification since it is nondeterministic. Further, the maximum impact force response may be driven by the dynamic response of the structure [10]. According to Goda's theory [11], the rising time is zero as in the case of vertical wall. Later, the importance of the wave front inclination is addressed by Sawaragi et al. [12]. The angle of inclined wave front is an important parameter to find the rising time and the initial sudden rise in the impact force [12]. In addition to that the surface roughness of the structure also tends to increase the rise time and reduces the magnitude of the amplification. The factors affecting the impact forces are the compressibility of the air between the cylinder and the water surface, water depth, curling factor, entrapped gases in the water, cylinder surface irregularities, rise time etc. [10].

3. Wave impact models

The wave impact acts for a very short time relative to the wave period and with high amplification. In general various factors affect the wave impact force such as irregular sea, the compressibility of air between the structural member, the compressibility at the beginning of impact, three-dimensional shape of the sea surface, size and shape of the air bubbles near the free surface and sea bed slope [13]. Hence the description of the wave impact model becomes complex. One of the first attempts to investigate the impact force on a body during landing on the water was performed by von Karman [14]. The impact force on the cylinder is approximated as a flat plate with a width equal to the immersed width of the cylinder and integrating the force over the height of the impact area results the impact force. In his theoretical model, the raise of the free surface elevation during the impact, the so called pile-up effect, is neglected, which affects the duration and magnitude of the impact force [2]. Later, the model developed by Wagner [2] includes the pile-up effect. Thus, the wetted surface estimated by Wagner's model is higher than the von Karman's model and hence the slamming coefficient is also higher in the former case. The maximum inline force at the beginning of the impact can be obtained by applying the approach of von Karman and Wagner. The von Karman model is implemented by Goda et al. [11] and Tanimoto et al. [15] to calculate the wave impact forces on vertical cylinders. The theoretical model presented by Wienke and Oumerachi, [7] is based on the Wagner's theory. The non-linear velocity terms in the Bernoulli equation are

considered in order to account for the temporal development of the impact. The description of the shape of the body is very important to predict the immersed width of the cylinder and is approximated as an ellipse by Fabula [7] and a parabolic shape by Cointe and Armand [7].

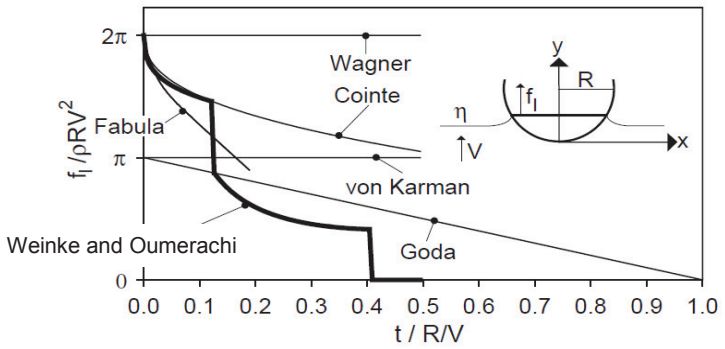

Figure 3 Comparison of time histories of the inline force, (t=time, R=cylinder radius, V=cylinder velocity) [7]

For the direct impact force on the upright cylinder, the quadratic parabola representation is applicable at the beginning of the impact; it is not valid for the total duration of the impact [7]. To improve the approximation, Wienke and Oumerachi [7] described it as a circular shape and introduced a polynomial stepwise function to describe the wetted surface of the circular cylinder. In the case of impact with an angle (oblique), then the shape of the body has to be described as an elliptical shape instead of a circular shape. The comparison of time histories of inline force for the different theoretical models is shown in Fig. 3.

There are two theoretical models based on the study of the penetration of a horizontal circular cylinder entering into calm water at various constant down ward velocities: Sarpkaya [10] and Campbell-Weynberg [16]. The theoretical model by Sarpkaya [10] predicts the design forces on a horizontal cylinder subjected to impact, but this model does not describe the impact area and the curling factor [13]. Though, the wave slamming coefficient depends on the rising time and the natural period of the structure. The impact model by Campbell and Weynberg [16] recommends that the slamming coefficient of the fully submerged cylinder is 0.8, but the model does not define the curling factor [16].

4. Experimental investigations of impact forces due to breaking waves

4.1 Investigations on cylindrical structures

Goda et al. [11] investigated the impact forces on the circular and triangular vertical cylinders and the study includes the information of force-time relationship. They assumed that the impact force is the result of the change in momentum of the water mass of a vertical wave front and they have not considered the rising time of the impact force [12]. The experiments by Sawaragi and Nochino [12] revealed that the wave front is not always vertical and that the front shape of breaking wave determines the rising time of the impact force. Moreover, its magnitude depends on the wave breaking pattern and the wave breaking point. The vertical distribution of the peak values was found to be a triangular shape whose peak appears at the height about 70% of the wave crest above the still water level. They defined the total force as the

sum of three forces; the impact force, the force by Morison's equation and the static pressure caused by the difference of water levels between the leeward and the seaward sides of the cylinder, and the largest value of the total force is seven times as large as the Morison's force. Watanabe and Horikawa [11] observed that the phase difference between the accelerations of the water particles and the inertia forces must be considered for the estimation of both the drag and the inertia coefficient.
All the previous tests, except those by Wienke and Oumeraci [7], have been carried out at a fairly small scale with cylinder diameters typically 5–10 cm. They carried out tests in a large wave flume with a cylinder with diameter 0.70 m, water depths approximately 4 m and with wave heights up to 2.8 m. They found that the pile-up effect considerably affects both the duration and the magnitude of the impact force. Further, they observed that the distance between wave breaking and cylinder greatly influences the magnitude of the impact force, and the impact force is proportional to the curling factor, which depends on inclination angle of the cylinder and on the angle of the wave front inclination. Ros [17] and Arntsen et al. [18] carried out tests on the wave slamming forces on a single pile where local force responses were measured at different elevations.

4.2 Investigations on truss structures

The wave forces on a truss structure on this scale are subjected to scale effects, especially the Morison type forces. However the results obtained are nevertheless of interest and suggest that tests on a larger scale are needed before any final conclusion on wave slamming forces on truss structures can be made. There has not been carried out any major investigation on the wave impact forces on truss structures. Results from an introductory experimental study carried out to find impact forces on truss structures in scale1:50 by Aune [19] are shown in Fig. 4(a). Aune [19] made a brief analysis of the wave forces and used these forces to calculate the response of a full scale structure. Tørum [20] has made some additional analysis of the responses measured by Aune [19]. As seen in the Fig.4 (b), there is a low frequency part and a high frequency part of the response. The low frequency part is the Morison force part, while the high frequency part is from the wave impact. The recorded response force is corrupted from dynamic effects on the model from the impacts. The challenge is to extract the wave impact force from the force response signal, taking the dynamic effects of the model-measuring system into account. This is normally done by using a convolution technique, e.g. similar to what Ros [17] did for a monopile. However, this has not been pursued so far on the truss structure model. As aforesaid, the wave slamming force on a monopile occurs when the crest region of the wave hits the pile.

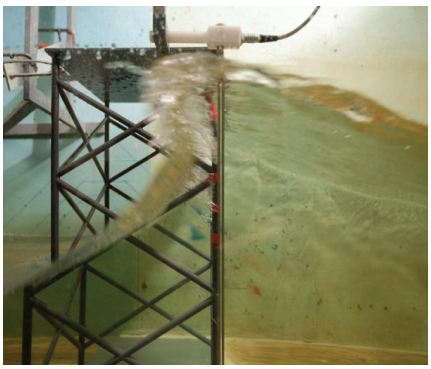

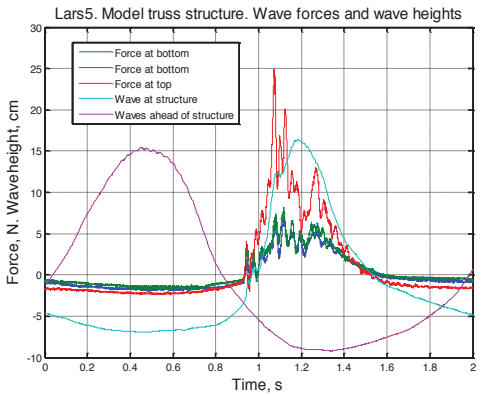

Figure 4 (a) Wave impact test at NTNU (b) General appearanse of the wave and response force recordings.

Table 1 Comparison of different wave impact models

Authors	Theory	C_S	Vertical force distribution
Goda et al. [11]	von Karman	π	Uniform
Sarpkaya [10]	A method by Kaplan [16]	For dynamic analysis: π or otherwise 5.5	Depends on the rise time and natural period
Sawaragi and Nochino [12]	Experimental study	π	Triangular
Tanimoto et al. [15]	Von Karman and Wagner	π	Triangular
Weinke and Oumerachi [7]	Wagner	2π	Uniform
Ros [17]	Experimental study	4.3	Triangular

In the case of truss structures, there are apparently some impacts caused by low wave surface elevations from the mean water level (approximately) as shown in Fig. 4(b). A truss structure has been designed for the Thornton bank outside the Belgian coast, where plunging breakers have been specified, and that the wave slamming forces from plunging breakers are governing the stresses in this structure [22]. Table 1 provides a comparison of different experimental and theoretical wave impact models for single circular cylindrical structures.

5. Numerical simulations of impact loads due to breaking waves

The estimation of the total wave force using Morison equation with the von Karman or the Wagner impact models requires the input of wave kinematics. Nevertheless, there are many uncertainties in the application of the wave theories to describe steep and breaking waves in shallow water [21]. Hence the numerical simulation may be an alternative to the exact description of the shallow water impact forces. The numerical description requires the modeling of wave-structure-air interaction during the impact [22]. The most destructive impact occurs when a breaking wave approaches the structure with almost vertical front and entrapping a small air pocket at the wall [23]. Numerical simulations of offshore wind turbines should include a fully non-linear model to account for breaking wave impact loads on offshore wind turbines.

Wu et al. [24] simulated the impact wave force due to breaking waves without entrapped air on a vertical wall by describing the complex free surface and splashing, and breaking by the Volume of Fluid (VOF) technique. Zhang et al. [25] studied the impact of a two-dimensional plunging wave on a rigid vertical wall using a Boundary Element Method (BEM) and scaled the maximum impact pressure by the breaker parameters. BEM has some limitations in modeling the post-breaking and the extreme turbulent impacts. Hence the model must include the complete flow physics based on the solution of Navier-Stokes equation [26]. Christensen et al. [22] demonstrated the coupling of a Boussinesq wave model with a Computational Fluid Dynamics (CFD) solver for the wave-structure interaction problems. This model is applied to calculate the wave loads on the wind turbine substructures and the new model reduced the computational time. Mokrani et al. [26] investigated the impact force and the overtopping flow generated by plunging breaking waves on a vertical wall by combining Navier-Stokes equations and VOF technique (NS-VOF).

Bredmose and Jacobsen [23] studied the extreme spilling breaking wave loads on a monopile foundation of an offshore wind turbine using Open Field Operation and Manipulation (OpenFOAM).
Christensen et al. [22] studied the extreme wave run-up and wave forces on monopile for offshore wind turbines using the NS-VOF. It was observed that the run-up caused by nearly breaking waves is higher than the run-up due to periodic waves. Corte and Grilli [27] modeled the extreme wave slamming on monopile offshore structures using a NS-VOF for two-phase flow. Nielsen et al. [28] studied experimentally and numerically the effect of three-dimensional waves on the wave run-up and predicted the maximum run-up using a fully non-linear NS-VOF technique. Bredmose and Jacobsen [29] investigated the vertical wave impact force and subsequent run-up on a monopile sub-structure using a VOF method.

6. Recommendations from standards for the wave impact forces

There are several design guidelines for the prediction of design wave impact forces from wave breaking on vertical cylinders. Though, there are limited guidelines for design impact forces on truss structures. The IEC 61400-3 [4] standard recommends that extreme events for the design load phase should account for the stochastic nature of both wind and wave loading, the flexibility of the structure and the non-linear nature of waves simultaneously. The load due to the wave run-up should be considered to the design of the low level platforms. If an offshore turbine is located near a coastal breaking wave zone, the coupled wave and current model should take into account the surf currents generated by the breaking waves. API RP 2A-WSD [30] suggests the slamming coefficient value between 0.5π and 1.7π depending on the rise time and the natural period according to Sarpkaya [10]. Slamming forces affect the local structural member design. According to DNV- OS-J101 [15] and DNV-RP-C205 [16], slamming on horizontal cylinders can be predicted using a method described by Kaplan [16] and slamming on vertical cylinders can be represented by the Campbell and Weynberg [16] impact model.

The air entrainment increases the rise time and reduces the maximum impact forces. In sea water, the bubbles are smaller and disappear slowly where as in fresh water, the bubbles are larger and disappear quickly. Hence it is recommended that the water properties should be considered for the slamming experiments [16]. Table 2 shows the comparison of design guidelines for the impact loads.

7. The key issues in the performance of an offshore wind turbine under the influence of wave impact forces

First, in the case of impact forces, the reaction forces are highly important and do distinctly depend on the structural response and the shape of the structure [32]. Breaking waves may potentially cause significant dynamic amplifications of the structural response on substructures.

Table. 2 Comparison of design guidelines for the impact loads [14]

Design standards	IEC 61400-3 [4] GL [31] ABS [21]	DNV-OS-J101[15] DNV-RP-C205[16]	API RP 2A-WSD [30]
Theoretical model	Wienke and Oumerachi model [7]	For Horizontal cylinders-Kaplan [16] For Vertical cylinders-Campbell & Weynberg [16]	Sarpkaya [10]
Slamming Coefficient (C_S)	2π at t=0 for force per unit length	5.15 at t=0 for force per unit length	0.5π to 1.7 force per unit length

	Time invariant	Time invariant	For dynamic analysis- π Otherwise 5.5

The consequence of large breaking wave forces would increase the probability of fatigue failure and affect the design of the offshore wind turbine structures, which will result in large stiff structures that are more expensive [1]. Moreover, breaking waves affect the global dynamic load and responses [13].

Second, wave run up indicates a complex process that is dependent on a number of wave characteristics, structure conditions and local effects. The strong wave run-up induces an additional inline force and overturning moment on the lower level platforms. Moreover, the short duration vertical impact forces may excite structural ringing at very high frequencies [23]. The report [28] has shown that wave run-up has removed the grating at the access platforms located 9m above mean sea level and affected the access ladders at the Horns Rev offshore wind farm [28]. Experiments have shown that the long waves with higher crest velocities have large influence on the wave run-up [33]. The important design parameters of these platforms are maximum wave run-up height and the associated forces.

Third, the scour process around the base of the sub-structure is due to erosion of the bed soil due to the combined wave and current induced flow velocities and it is the complex interaction between the incoming flow, the base of the sub-structure and the sea bed. The depth of this scour is in the order of 1.5 times the pile diameter. However, combination of a current with waves in the same direction is relative long waves, results in an increase of scour around the base of truss structure, so called “dish pan scour” [34]. It is clear that the scour affects the stability and the dynamic behavior of the offshore substructures. Hence the substructure design should consider the wave and current induced scour.

8. Summary

A detailed literature review is carried out to study the influences of the breaking waves and the associated effects on offshore wind turbine structures. The considerable uncertainties in the estimation of hydrodynamic loads, fatigue life and the extreme loads are caused by the breaking waves. The design loads of offshore wind turbine are more sensitive to the dynamic characteristics than the offshore oil and gas structures [21]. Hence the design methods and guidelines need to be investigated in detail for offshore wind turbine substructures.

References

[1] Det Norske Veritas (DNV), 2010a. OS-J101 Design of Offshore Wind Turbine Structures.

[2] Faltinsen, O. M., 1990. Sea Loads on Ships and Offshore Structures. Cambridge Ocean Technology Series. Cambridge University Press.

[3] Galvin, C.J., Jr., Breaker Type Classification on Three Laboratory Beaches, Jour. Geophys. Res., 73(12), 3651, 1968.[19]

[4] International Electrotechnical Commission (IEC), 2009. IEC 61400-3: Wind Turbines – Part 3: Design Requirements for Offshore Wind Turbines, 1st Edition.

[5] Chaplin, J., Flintham, T., Greated, C., and Skyner, D., 1992. Breaking Wave Forces on a Vertical Cylinder. Report 90 324, Health and Safety Executive, London, UK.

[6] Morison, J. R, O'Brien, M. P., Johnson, J. W., and Schaaf, S. A, 1950. "The forces exerted by surface waves on monopiles". 1. Petrol. Teehn., 189, pp. 149-154.

[7] Wienke, J. and Oumeraci, H., 2005. Breaking Wave Impact Force on a Vertical and Inclined Slender Pile - Theoretical and Large-Scale Model Investigations. Coastal Engineering, 52:435–462.

[8] Birkinshaw M., Easson W.J., Greated C.A. & Webb R.A. 1988 Breaking wave design - a case history. Proc. ICE, Part 2,85, 415-433.

[9] NORSOK Standard N-003, 2007. Actions and Action Effects, Edition 2. Standards Norway, Lysaker, Norway.

[10] Sarpkaya, T., 1978. Wave Impact Loads on Cylinders. In Proc., Offshore Technology Conference, Houston, TX, Paper No. OTC 3065.

[11] Goda, Y., Haranaka, S., and Kitahata, M., 1966. Study of Impulsive Breaking Wave Forces on Piles. Report of Port and Harbor Research Institute, 5(6): 1–30. Concept also in English language in Watanabe, A. and Horikawa, K., 1974. Breaking Wave Forces on Large Diameter Cell. Proc. 14th Intern. Conf. on Coastal Eng. pp 1741-1760.

[12] Sawaragi, T., Nochino, M., 1984. Impact forces of nearly breaking waves on a vertical circular cylinder. Coastal Engineering in Japan 27, 249– 263.

[13] Design Standards for Offshore Wind Farms- Project report no. 670, 2011.American Bureau of Shipping, USA

[14] von Karman, T., 1929. The Impact of Seaplane Floats during Landing. Technical Note 321, NACA, Washington.

[15] Tanimoto, K., Takahashi, S., Kaneko, T., Shiota, K., 1986. Impulsive breaking wave forces on an inclined pile exerted by random waves. Proceedings of the 20th International Conference on Coastal Engineering, vol. 3, pp. 2288–2302.

[16] Det Norske Veritas (DNV), 2010. RP-C205 Environmental Conditions and Environmental Loads.

[17] Ros, X., 2011 Impact forces on a vertical pile from plunging breaking waves. Master thesis, Norwegian University of Science and Technology, Department of Civil and Transport Engineering, Trondheim, Norway.

[18] Arntsen, Ø., Ros, X., and Tørum, A., 2011. Impact Forces on a Vertical Pile from Plunging Breaking Waves. In Coastal Structures 2011, Yokohama, Japan.

[19] Aune, L, 2011 Forces from plunging breaking waves on a truss structure. Master thesis submitted June 2011, Norwegian University of Science and Technology, Department of Civil and Transport Engineering, Trondheim, Norway.

[20] Tørum, A, 2012 Wave slamming force on truss structures. Preliminary note, NTNU, IBAT, Marine Group.

[21] American Bureau of Shipping (ABS), 2010. Guide for Building and Classing Offshore Wind Turbine Installations.

[22] Christensen, E. D., Bredmose, H., and Hansen, E. A, 2005. Extreme wave forces and run-up on offshore wind turbine foundations. In Proc. Copenhagen Offshore Wind.

[23] Bredmose, H. and Jacobsen, N. G., 2010. Breaking Wave Impacts on Offshore Wind Turbine Foundations: Focused Wave Groups and CFD. In Proc. 29th Int. Conf. Ocean Offshore Arctic Engng., ASME. Shanghai, China.

[24] Wu .N.T, Oumeraci.H and Partenscky. H.W. 1994: Numerical modelling of breaking wave impacts on a wall. Proc. Int. Conf. On Coastal Engineering 1994.pp.1672-1686.

[25] Zhang.S, Yue.K.P.D and Tanizawa 1996: Simulation of plunging waveimpact on a vertical wall. Journal of fluid mechanics, Vol. 327. pp. 221-254

[26] Mokrani, C., Abadie, S., Grilli, S., and Zibouche, K., 2010. Numerical Simulation of The Impact of a Plunging Breaker on a Vertical Structure and Subsequent over Topping Event Using a Navier-Stokes VOF Model. In Proceedings of the Twentieth (2010) International Offshore and Polar Engineering Conference, pages 729–736, Beijing, China.

[27] Corte, C. and Grilli, S. T., 2006. Numerical Modeling of Extreme Wave Slamming on Cylindrical Offshore Support Structures. In Proceedings of the Sixteenth 2006 International Offshore and Polar Engineering Conference, pages 394–401, San Francisco, California, USA.

[28] Nielsen, A W, Mortensen, S. B., and Jacobsen, v., 2008. "Numerical modelling of wave run-up on a wind turbine foundation". In Proc. 27th Int. Conf. Offshore Mech. Arctic Engng., Estoril, Portugal, ASME.

[29] Bredrnose, H., and Jacobsen, N. G., 2011. Vertical wave impacts on offshore wind turbine inspection platforms. In Proc. 29th Int. Conf. Ocean Offshore Arctic Engng., ASME.

[30] American Petroleum Institute (API), 2007. API RP 2A-WSD: Recommended Practice for Planning Designing and Constructing Fixed Offshore structures–Working Stress Design, 21st Edition.

[31] Germanischer Lloyd (GL), 2005. Guideline for the Certification of Offshore Wind Turbines.

[32] Irschik, K., Sparboom, U. and Oumeraci, H., 2004. Breaking Wave Loads on a Slender Pile in Shallow Water. Proceedings of the 29th International Conference on Coastal Engineering (ICCE), Lisbon, Portugal.

[33] Lykke Andersen.T, Frigaard.P, Damsgaard.M.L. and DeVos.L, 2011. Wave run-up on slender piles in design condotions-modal tests and design rules for offshore wind. Coastal Engineering, Vol.58, pp 281-289.

[34] Sumer.M.B and Fredsøe J, 2005. The Mechnics of Scour in the Sea Environment. World scientific Press.

Paper 2

6.2 Paper 2

A new level set numerical wave tank with improved density interpolation for complex wave hydrodynamics

Bihs, H., Kamath, A., Alagan Chella, M., Aggarwal, A., and Arntsen, Ø. A.
Submitted to *Computers and Fluids*, 2015 - under review

A New Level Set Numerical Wave Tank with Improved Density Interpolation for Complex Wave Hydrodynamics

Hans Bihs[a,*], Arun Kamath[a], Mayilvahanan Alagan Chella[a], Ankit Aggarwal[a], Øivind Asgeir Arntsen[a]

[a]*Department of Civil and Transport Engineering, Norwegian University of Science and Technology (NTNU), NO-7491 Trondheim, Norway*

Abstract

The three-dimensional numerical wave tank REEF3D is developed for the calculation of wave propagation and wave hydrodynamics by solving the incompressible Navier-Stokes equations. The free surface is modeled with the level set method based on a two-phase flow approximation, allowing for the simulation of complex phenomena such as wave breaking. The convection terms of the momentum and the level set equations are discretized with the finite difference version of the fifth-order WENO scheme. Time stepping is handled with the third-order TVD Runge-Kutta scheme. The equations are solved on a staggered Cartesian grid, with a ghost cell immersed boundary method for the treatment of irregular cells. Waves are generated at the inlet and dissipated at the numerical beach with the relaxation method. The choice of the numerical grid and discretization methods leads to excellent accuracy and stability for the challenging calculation of free surface waves. The performance of the numerical model is validated and verified through several benchmark cases: solitary wave interaction with a rectangular abutment, wave forces on a vertical cylinder, wave propagation over a submerged bar and plunging breaking waves on a sloping bed.

Keywords: numerical wave tank, wave propagation, wave hydrodynamics, breaking waves, wave forces

1. Introduction

The choice of model for the wave propagation and transformation calculation depends on the required detail and resolution. For large scale wave modeling, such as the wave transformation from deep to shallow waters, spectral wave models such as SWAN [5] are used. This type of model solves the wave action or energy balance equation, which describes the wave

*Corresponding author
Email address: hans.bihs@ntnu.no (Hans Bihs)

spectrum evolution in space and time. The modeled waves are consequently phase averaged. Spectral wave models have been successfully applied to a variety of coastal problems [37][49]. For a range of water wave engineering problems, more detail is required concerning the wave transformation process, including phase information. Phase resolving models based on the Boussinesq equations [27][33] or the parabolic mild-slope equation [24] have the capability to accurately model wave reflection and diffraction. The mild-slope approach is based on the assumption of a mildly sloping sea bottom and linear monochromatic waves. Standard Boussinesq-type models are based on the shallow water equations for non-dispersive linear wave propagation. Extended versions of the Boussinesq equations make it possible to predict wave propagation and transformation from deep to shallow water with the help of improved dispersive terms [26]. When it comes to engineering applications, such as wave propagation in nearshore and harbor areas, Boussinesq-type models are often the preferred engineering solution.

Yet another approach to wave modeling is the class of Fully Nonlinear Potential Flow Models (FNPF), which neglect the effects of viscosity and rotational flow. Here, the Laplace equation for the flow potential is solved with the Boundary Element Method. The method works well for a range of problems, such as wave propagation in deep water [9] or wave shoaling in shallow water [14]. All mentioned wave models have in common, that they give up a certain level of detail for the benefit of reduced computational cost. For a lot of water wave engineering problems, this is a perfectly reasonable choice.

On the other hand there are complex cases, such as breaking wave kinematics or flow around slender structures, where a more detailed solution is required in order to capture the relevant flow physics. The solution of the three-dimensional Navier-Stokes equations resolves even more detail of the flow processes. Here, the approach is to solve for the basic underlying flow variables, such as the velocities, the pressure and turbulence. Together with the appropriate algorithms for the interface capturing, the free surface and resulting water wave dynamics can be calculated based on the three-dimensional flow field. In order to avoid the unphysical damping of propagating waves due to numerical diffusion, the usage of the Navier-Stokes equations imposes strict criteria for the mesh resolution, the time step size as well as the general accuracy of the numerical algorithm. There have been several papers where a Navier Stokes solver in conjunction with interface capturing schemes has been used to calculate complex free surface flows such as [45], [52], [8] and [6]. In contrast, the current model focuses on the very demanding problem of wave propagation and wave hydrodynamics. Some successful

efforts have been made to use a CFD program as a numerical wave tank, e.g. [21] or [17]. In these methods, the CFD model calculates the free surface with a Volume-of-Fluid (VOF) algorithm, based on convection of the fraction function and interface-compression [46]. The governing equations are solved on a collocated unstructured grid with second-order accuracy for the spatial and temporal discretization. In both cases, algorithms for the wave generation and absorption were implemented, resulting in a three-dimensional numerical wave tank. The models were applied to typical laboratory experiments for wave propagation, showing that with today's efficient numerical models and computational resources, very complex wave propagation simulations can be performed [35][19][38].

In this work, the open-source model REEF3D [1] is presented with alternative approaches for the underlying grid architecture, discretization of the governing equations and treatment of the complex free surface. As mentioned above, numerical accuracy and stability are essential for the good performance of a Navier-Stokes equations based numerical wave tank. Under that premise, the appropriate numerical algorithms were chosen in REEF3D. The level set method is used for the capturing of the free water surface [34]. It has been used for describing two-phase flow with water-air interfaces in several studies [52][51][8]. Geometric Volume-of-Fluid (VOF) algorithms have shown to give better mass conservation properties than the level set method [45]. On the other hand, high-order temporal and spatial discretization can be used for the level set function, which avoid unphysical damping of the propagating water waves. Further, the equations of fluid motion are solved on a staggered grid, ensuring tight velocity-pressure coupling. The Cartesian grid makes it possible to employ the fifth-order Weighted Essentially Non-Oscillatory (WENO) scheme [23] for convection discretization, which delivers accurate and stable solutions. Also for the discretization in time, a high-order method is selected with the third-order total variation diminishing (TVD) Runge-Kutta scheme [39]. As a result, wave propagation and transformation can be calculated throughout the wave steepness range up to the point of wave breaking and beyond, with no artificially high air velocities impacting the quality of the free surface. In Section 2, the numerical methods for the solution of the Navier-Stokes equations are discussed. In Section 3, the free surface treatment and the details of the numerical wave tank implementation are presented. The numerical results of several benchmark wave applications are given in Section 4, before the conclusion in Section 5.

2. Numerical Model

2.1. Governing Equations

The incompressible fluid flow is described by the three-dimensional Reynolds-Averaged Navier-Stokes equations (RANS), which are solved together with the continuity equation for prescribing momentum and mass conservation:

$$\frac{\partial u_i}{\partial x_i} = 0 \tag{1}$$

$$\frac{\partial u_i}{\partial t} + u_j \frac{\partial u_i}{\partial x_j} = -\frac{1}{\rho}\frac{\partial p}{\partial x_i} + \frac{\partial}{\partial x_j}\left[(\nu + \nu_t)\left(\frac{\partial u_i}{\partial x_j} + \frac{\partial u_j}{\partial x_i}\right)\right] + g_i \tag{2}$$

where u is the velocity averaged over time t, ρ is the fluid density, p is the pressure, ν is the kinematic viscosity, ν_t is the eddy viscosity and g the acceleration due to gravity.

The eddy viscosity ν_t in the RANS equations is determined through the two-equation k-ω model [48], with the equations for the turbulent kinetic energy k and the specific turbulent dissipation ω as follows:

$$\frac{\partial k}{\partial t} + u_j \frac{\partial k}{\partial x_j} = \frac{\partial}{\partial x_j}\left[\left(\nu + \frac{\nu_t}{\sigma_k}\right)\frac{\partial k}{\partial x_j}\right] + P_k - \beta_k k\omega \tag{3}$$

$$\frac{\partial \omega}{\partial t} + u_j \frac{\partial \omega}{\partial x_j} = \frac{\partial}{\partial x_j}\left[\left(\nu + \frac{\nu_t}{\sigma_\omega}\right)\frac{\partial \omega}{\partial x_j}\right] + \frac{\omega}{k}\alpha P_k - \beta\omega^2 \tag{4}$$

where P_k is the turbulent production rate, the coefficients have the values $\alpha = \frac{5}{9}$, $\beta_k = \frac{9}{100}$, $\beta = \frac{3}{40}$, $\sigma_k = 2$ and $\sigma_\omega = 2$. In the oscillatory flow motion that characterizes the wave flow field, the mean rate of strain $\mathbf{S}$ can be large. In order to avoid overproduction of turbulence in highly strained flow outside the boundary layer, the turbulent eddy viscosity ν_t is bounded through the following limited formulation [10]:

$$\nu_t = \min\left(\frac{k}{\omega}, \sqrt{\frac{2}{3}}\frac{k}{|\mathbf{S}|}\right) \tag{5}$$

The turbulent length scales in the water are reduced in the proximity of the free surface, leading to increased turbulent dissipation in this region. Also, the turbulent fluctuations normal to the free surface are damped, as their intensity is redistributed to the ones parallel to the interface. When modeling two-phase flow, this behavior is not directly captured by a RANS turbulence model. As $\mathbf{S}$ can be large especially in the vicinity of the interface between

water and air, standard RANS turbulence closure will incorrectly predict maximum turbulence intensity at the free surface. Through the implementation of an additional turbulence damping scheme, a more realistic representation of the free surface effect on the turbulence can be achieved [31]. The specific turbulent dissipation at the free surface is defined as:

$$\omega_s = \frac{c_\mu^{-\frac{1}{4}}}{\kappa} k^{\frac{1}{2}} \cdot \left(\frac{1}{y'} + \frac{1}{y^*} \right) \tag{6}$$

where $c_\mu = 0.07$ and $\kappa = 0.4$. The variable y' is the virtual origin of the turbulent length scale, and was empirically found to be 0.07 times the mean water depth [20]. Including the distance y^* from the nearest wall gives a smooth transition from the free surface value to the wall boundary value of ω. The term for the specific turbulent dissipation ω_s is activated around the interface of thickness ϵ by multiplying it with the Dirac delta function $\delta(\phi)$:

$$\delta(\phi) = \begin{cases} \frac{1}{2\epsilon} \left(1 + \cos\left(\frac{\pi\phi}{\epsilon} \right) \right) & if \ \ |\phi| < \epsilon \\ 0 & else \end{cases} \tag{7}$$

The pressure gradient term in the RANS equations is modeled with Chorin's projection method [7] for incompressible flow on a staggered grid. The staggered grid configuration ensures a tight velocity-pressure coupling. The pressure gradient is removed from the momentum equations. The updated velocity after each Euler step of the Runge-Kutta time discretization is the intermediate velocity u_i^*. Then the Poisson equation for the pressure is formed by calculating the divergence of the intermediate velocity field:

$$\frac{\partial}{\partial x_i} \left(\frac{1}{\rho(\phi^n)} \frac{\partial p}{\partial x_i} \right) = -\frac{1}{\Delta t} \frac{\partial u_i^*}{\partial x_i} \tag{8}$$

The Poisson equation is solved using the fully parallelized Jacobi-preconditioned BiCGStab algorithm [43]. The pressure is then used to correct the intermediate velocity field, resulting in the divergence free velocity at the new time step:

$$u_i^{n+1} = u_i^* - \frac{\Delta t}{\rho(\phi^n)} \frac{\partial p}{\partial x_i} \tag{9}$$

2.2. Discretization of the Convective Terms

The convective terms of the RANS equations are discretized with the fifth-order WENO scheme [23] in the conservative finite-difference framework. The convection term of the velocity component in x-direction is approximated as follows:

$$u_i \frac{\partial u_i}{\partial x_i} \approx \frac{1}{\Delta x} \left(\widetilde{u}_{i+1/2} \; u_{i+1/2} - \widetilde{u}_{i-1/2} \; u_{i-1/2} \right) \tag{10}$$

Here $\widetilde{u}$ is the convection velocity, which is obtained at the cell faces through simple interpolation. For the cell face $i + 1/2$, $u_{i+1/2}$ is reconstructed with the WENO procedure:

$$U^{\pm}_{i+1/2} = \omega^{\pm}_1 U^{1\pm}_{i+1/2} + \omega^{\pm}_2 U^{2\pm}_{i+1/2} + \omega^{\pm}_3 U^{3\pm}_{i+1/2} \tag{11}$$

The $\pm$ sign indicates the upwind direction. U^1, U^2 and U^3 represent the three possible ENO stencils. For upwind direction in the positive i-direction, they are:

$$\begin{aligned} U^{1-}_{i+1/2} &= \frac{1}{3} u_{i-2} - \frac{7}{6} u_{i-1} + \frac{11}{6} u_i, \\ U^{2-}_{i+1/2} &= -\frac{1}{6} u_{i-1} + \frac{5}{6} u_i + \frac{1}{3} u_{i+1}, \\ U^{3-}_{i+1/2} &= \frac{1}{3} u_i + \frac{5}{6} u_{i+1} - \frac{1}{6} u_{i+2} \end{aligned} \tag{12}$$

The nonlinear weights $\omega^{\pm}_n$ are determined for each ENO stencil and calculated based on the smoothness indicators IS [23]. Large smoothness indicators indicate a non-smooth solution in the particular ENO stencil. Accordingly, the non linear weights ω_n for this stencil will be small. The WENO scheme favors stencils with a smooth solution and assigns them the largest weights ω_n. As a result the scheme can handle large gradients right up to the shock very accurately. In the worst-case situation, the WENO scheme will achieve a third-order of accuracy. In the areas where the solution is smooth, it will deliver fifth-order accurate results. In comparison to high resolution schemes such as MUSCL [44] or TVD [16] schemes, the WENO scheme does not smear out the solution. Instead, it maintains the sharpness of the extrema. The conservative WENO scheme is used to treat the convective terms for the velocities u_i, while the Hamilton-Jacobi version is used for the variables of the free surface and turbulence algorithms.

2.3. Time Advancement Scheme

For the time treatment of the momentum and the level set equations, a third-order accurate TVD Runge-Kutta scheme is employed, consisting of three Euler steps [39].

$$\begin{aligned}\phi^{(1)} &= \phi^n + \Delta t L\left(\phi^n\right) \\ \phi^{(2)} &= \frac{3}{4}\phi^n + \frac{1}{4}\phi^{(1)} + \frac{1}{4}\Delta L\left(\phi^{(1)}\right) \\ \phi^{n+1} &= \frac{1}{3}\phi^n + \frac{2}{3}\phi^{(2)} + \frac{2}{3}\Delta L\left(\phi^{(2)}\right)\end{aligned} \tag{13}$$

This scheme provides a high-order of temporal accuracy, and for CFL numbers below 1 it shows very good numerical stability through its TVD properties. Adaptive time stepping is used in order to control the CFL number and takes the influence from velocity, diffusion and the source term S, such as for example gravity, into account [13]. The time step size Δt is determined as follows:

$$\Delta t \leq 2\left(\left(\frac{|u|_{max}}{dx} + D\right) + \sqrt{\left(\frac{|u|_{max}}{dx} + D\right)^2 + \frac{4\,|S_{max}|}{dx}}\right)^{-1} \tag{14}$$

with the contribution from the diffusion term D:

$$D = max\left(\nu + \nu_t\right) \cdot \left(\frac{2}{(dx)^2} + \frac{2}{(dy)^2} + \frac{2}{(dz)^2}\right) \tag{15}$$

For a RANS model, where the turbulence magnitude is expressed through the eddy viscosity, the diffusion criterion of the order $\nu_{\max}/dx^2$ can become prohibitively restrictive. As a solution, the diffusion part of the RANS equation is treated implicitly in the current numerical model, thus removing it from the CFL criterion. The third-order accurate TVD Runge-Kutta scheme is used for all transport equations in the numerical wave tank with the exception of the turbulence model. A special characteristic of two-equation turbulence models is that they are mostly source term driven, namely by the turbulent production and dissipation terms. In comparison to the momentum equation, the convective and diffusive terms play only a minor role. For explicit time discretization of the k and ω equations, the large source terms result in a significantly smaller time step than for the momentum equations due to the CFL criterion. Instead of letting the turbulence model determine the time step, its equations are discretized with a first-order implicit Euler scheme.

2.4. Immersed Boundary

The numerical model uses a Cartesian grid in order to employ high-order discretization schemes. An additional benefit comes from the straightforward implementation of numerical

algorithms, as the geometry of the numerical cells is trivial in this case. The challenge of irregular, non-orthogonal solid boundaries is overcome with the implementation of the immersed boundary method. In REEF3D, a ghost cell immersed boundary method (GCIBM) is used [4]. In this method, the solution is analytically continued through the solid boundary by updating fictitious ghost cells in the solid region by extrapolation. This way, the numerical discretization does not need to account for the boundary conditions explicitly, instead they are enforced implicitly. The algorithm is based on the local directional approach [4], which was implemented in two dimensions. For the current model it has been extended to three dimensions. In the original GCIBM, the fluid values are extrapolated orthogonal to the boundary into the solid [42][29], which can become difficult for sharp corners. In the local directional GCIBM the values from the fluid are extrapolated into the solid along the coordinate directions [4].

In REEF3D, grids can be generated based on geometric primitives, such as boxes, cylinders and wedges. More complex geometries can be read in .STL format and immersed into the Cartesian grid, following the strategy presented in [50]. For natural bathymetries with measured x, y and z coordinates, the solid boundary can be represented by a level set function. Then, the location of the level set function is calculated from the coordinates with either inverse-distance or kriging interpolation.

2.5. Parallelization

The efficient computation of CFD results depends to a large extent on the strategy for the parallelization of the numerical model. In REEF3D, parallelization is achieved through domain decomposition. Here the simulation domain is split into smaller parts, each of them communicating with their neighbors through ghost cells. Because REEF3D already uses the ghost cell method for the solid boundaries, this approach is straightforward to code and consistent with the treatment of the other domain boundaries. The message passing interface (MPI) is used for the implementation of the ghost cell value exchange. Since a fifth-order WENO scheme is used for the convection discretization of the velocities, the level set function and the variables of the turbulence model, three ghost cell levels are required. For the pressure, only one level of ghost cells is needed. The code is employed on NOTUR's supercomputer Vilje [32], which is an "SGI Altix 8600" cluster. Vilje consists of 1404 nodes with two 8-core processors on each node, resulting in a total of 22464 cores. In order to investigate the parallel efficiency of REEF3D, 2D and 3D tests were performed. For the 2D test, a

rectangular wave tank with the domain size ($L_x \times L_z = 62$ m $\times$ 4 m) and a mesh size of $dx = 0.005$ m has a total of 9.92 million cells. For the 3D test, a wave tank with the domain size of ($L_x \times L_y \times L_z = 250$ m $\times$ 5 m $\times$ 8 m), a mesh size of $dx = 0.1$ m and a total of 10 million cells is used. As seen from Fig. (1a), the parallel speedup for the 2D case follows the ideal scaling closely up to 256 processors. After that, a speedup is still achieved, but visibly reduced as the parallel communication overhead increases more than the parallelization gains. For the 3D test case, the parallel speedup of the model is close to the ideal situation up to 144 processors. The speedup is reduced for 256 processors and flattens out towards 512 processors. As expected, the parallel scaling for 2D cases is more efficient than for 3D, as messages have to be passed in one dimension lesser.

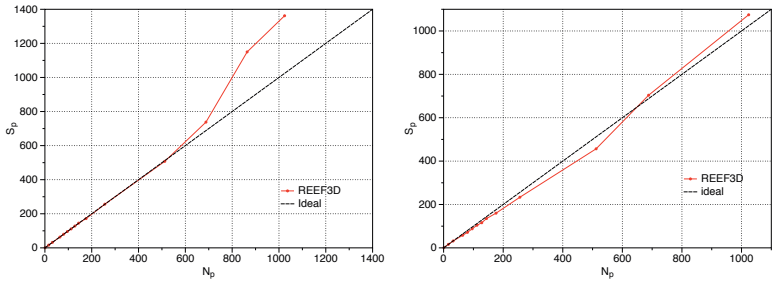

(a) 2D (b) 3D

Figure 1: Parallel scaling test for 2D and 3D wave tanks

3. Numerical Wave Tank

3.1. Free Surface Capturing

The location of the free water surface is represented implicitly by the zero level set of the smooth signed distance function $\phi(\vec{x}, t)$ [34]. The level set function gives the closest distance to the interface Γ and the two phases are distinguished by the change of the sign. This results in the following properties:

$$\phi(\vec{x}, t) \begin{cases} > 0 \; if \; \vec{x} \in phase \; 1 \\ = 0 \; if \; \vec{x} \in \Gamma \\ < 0 \; if \; \vec{x} \in phase \; 2 \end{cases} \tag{16}$$

In addition, the Eikonal equation $|\nabla \phi| = 1$ is valid. When the interface Γ is moved under an externally generated velocity field $\vec{u}$, a convection equation for the level set function is

obtained:

$$\frac{\partial \phi}{\partial t} + u_j \frac{\partial \phi}{\partial x_j} = 0 \tag{17}$$

The convection term in Eq. (17) is solved with the Hamilton-Jacobi version of the WENO scheme [22]. For time stepping, the third-order TVD Runge-Kutta scheme is used [39]. When the interface evolves, the level set function loses its signed distance property. In order to maintain this property and to ensure mass conservation, the level set function is reinitialized after each time step. In the present paper, a PDE based reinitialization equation is solved [40]:

$$\frac{\partial \phi}{\partial t} + S(\phi) \left(\left| \frac{\partial \phi}{\partial x_j} \right| - 1 \right) = 0 \tag{18}$$

where $S(\phi)$ is the smoothed sign function [36].

3.2. Density Location

With the level set function in place, the material properties of the two phases can be defined for the whole simulation domain. On a staggered grid, the cell face density is required for the calculation of the Poisson equation for the pressure in Eq. (8) and the correction of the velocity with the pressure gradient in Eq. (9). In previous level set based numerical models with staggered grids [45], [6], the density is usually determined at the cell centers with the smoothed Heaviside function in a first step:

$$\rho_i = \rho_1 H(\phi_i) + \rho_2 (1 - H(\phi_i)), \tag{19}$$

with ρ_1 and ρ_2 representing the densities of the two fluids and the Heaviside function defined as:

$$H(\phi_i) = \begin{cases} 0 & if\ \phi_i < -\epsilon \\ \frac{1}{2}\left(1 + \frac{\phi_i}{\epsilon} + \frac{1}{\pi} sin\left(\frac{\pi \phi_i}{\epsilon}\right)\right) & if\ |\phi_i| < \epsilon \\ 1 & if\ \phi_i > \epsilon \end{cases} \tag{20}$$

Typically the thickness of the smoothed out interface is chosen to be $\epsilon = 1.6dx$ on both sides of the interface. In a second step, the density at the cell faces is evaluated through

simple averaging of the density at the two neighboring cell centers [8]:

$$\rho_{i+\frac{1}{2}} = \frac{1}{2}\left(\rho_i + \rho_{i+1}\right) \tag{21}$$

In another example [51], the cell face density is calculated through a linear interpolation based on the location of the interface in the second step. In the current numerical model for the calculation of propagating waves, it was observed that this two-step strategy for the cell face density evaluation leads to small scale oscillations of the free surface. For other types of free-surface flows, such as open-channel flow, this phenomenon could not be reproduced. For the simulation of waves, the oscillations are more pronounced for lower steepness waves. In general, the problem occurs when the free surface is mildly sloped with respect to the orientation of the gridlines in the presence of a vertical velocity component, as is the case for waves.

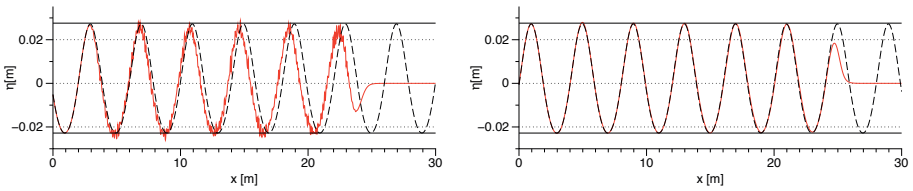

(a) Density calculation at cell centers

(b) Density calculation at cell faces

Figure 2: Influence of cell face density calculation on the free surface for periodic waves with wave length $L = 4$ m, wave height $H = 0.05$ m and still water level $d = 0.5$ m in a 30 m long wave flume with $dx = 0.01$ m after 90 s. The black dashed line shows the wave theory, the black solid line the theoretical wave envelope and the red line the numerical model.

In order to illustrate the effect, 2nd-order Stokes waves with a wavelength $L = 4$ m and a wave height $H = 0.05$ m are generated in a 30 m long and 1 m high 2D wave flume with a water depth $d = 0.5$ m on a mesh with $dx = 0.01$ m. Fig. (2a) shows the computed wave surface elevation after 90 s. Comparing it with the theoretical wave profile along the wave flume, the free surface oscillations and a phase shift become visible. The relatively long simulation time of 90 s is chosen, so that the oscillations are fully developed. Even though the quality of the numerical results is clearly degraded, the numerical solution remains stable throughout the simulation with neither excess velocities nor pressure values occurring. As a remedy for the free surface oscillations, the density at the cell faces is calculated in a modified manner. Using a single step, the density at the cell face is calculated with the smoothed Heaviside function right away:

$$\rho_{i+\frac{1}{2}} = \rho_1 H\left(\phi_{i+\frac{1}{2}}\right) + \rho_2\left(1 - H\left(\phi_{i+\frac{1}{2}}\right)\right), \tag{22}$$

The level set function at the cell face is calculated through averaging:

$$\phi_{i+\frac{1}{2}} = \frac{1}{2}\left(\phi_i + \phi_{i+1}\right) \tag{23}$$

As can be seen in Fig. (2b), the resulting free surface is oscillation-free and the numerical solution matches the theoretical wave profile in both amplitude and phase. Similar to the current findings, [47] identified the importance of the density averaging for the quality of the free surface in the context of the VOF method on a staggered grid. Fig. (3) shows the density profile for the cell faces i across the interface, in a case where the interface is normal to the x-direction. Three different situations are considered: the interface located directly on the cell face, between the cell face and the cell center and directly at the cell center. The density calculation at the cell centers is denoted ρ_{center}, and the density calculation at the cell faces ρ_{face}. Compared to the curve for the cell-centered density evaluation ρ_{center} with $\epsilon = 1.6dx$, the density profile is actually less smoothed out across the interface for ρ_{face} with $\epsilon = 1.6dx$,

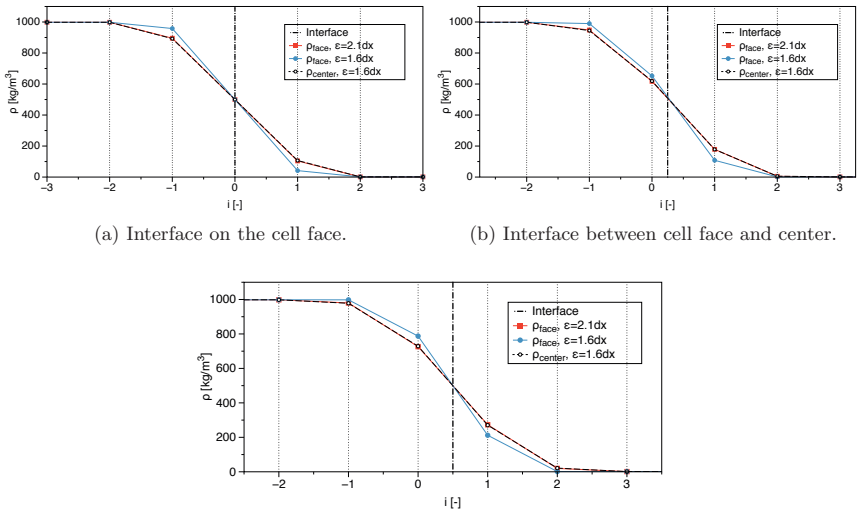

(a) Interface on the cell face.

(b) Interface between cell face and center.

(c) Interface on the cell center.

Figure 3: Density profile along the interface at the cell faces for different interface locations and density evaluation schemes. The x-axis i represents the cell centers.

because the second step with the averaging of the densities is missing. In order to account for this, the current method of the cell face density evaluation uses the interface thickness $\epsilon = 2.1dx$. As can be seen from Fig. (3), for ρ_{face} with $\epsilon = 2.1dx$, the width of the density transition area and the magnitude of the density gradient across the interface at the cell faces is the same as for ρ_{center} with $\epsilon = 1.6dx$.

3.3. Wave Generation and Absorption

Typical inlet boundary conditions for free surface flow applications are of Dirichlet type. When generating waves at the inlet, the free surface is in constant motion and the flow direction is changing periodically. As a result, simple Dirichlet type wave generation does not necessarily deliver waves of the highest quality. In REEF3D, waves are generated with the relaxation method, which is presented in [28] and extended for CFD models in [21]. Here, the wave generation takes place in a relaxation zone with a typical size of one wavelength (see Fig. (4)).

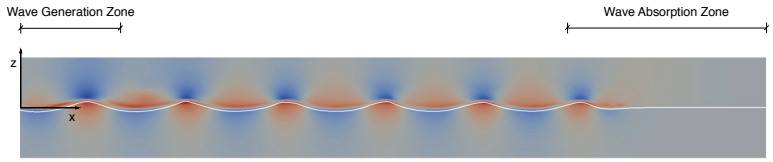

Figure 4: Sketch of the numerical wave tank with wave generation and absorption zones. The contour shows the horizontal velocity component.

The values for the velocities and the free surface are ramped up from the computational values to the values obtained from wave theory (Eq. (24)). The waves are generated without any disturbances occurring at the interface. In addition, reflected waves that travel back towards the inlet are absorbed with this method. At the outlet of a wave flume, the waves need to be dissipated in order to avoid reflections that can negatively impact the numerical results. This can be achieved with the relaxation method. In the numerical beach relaxation zone, the computational values for the horizontal and vertical velocities are smoothly reduced to zero, the free surface to the still water level and the pressure is relaxed to the hydrostatic distribution for the still water level. Thus, the wave energy is effectively absorbed and reflections are prevented.

$$
\begin{aligned}
u(\widetilde{x})_{relaxed} &= \Gamma(\widetilde{x})u_{analytical} + (1-\Gamma(\widetilde{x}))u_{computational} \\
w(\widetilde{x})_{relaxed} &= \Gamma(\widetilde{x})w_{analytical} + (1-\Gamma(\widetilde{x}))w_{computational} \\
p(\widetilde{x})_{relaxed} &= \Gamma(\widetilde{x})p_{analytical} + (1-\Gamma(\widetilde{x}))p_{computational} \\
\phi(\widetilde{x})_{relaxed} &= \Gamma(\widetilde{x})\phi_{analytical} + (1-\Gamma(\widetilde{x}))\phi_{computational}
\end{aligned}
\tag{24}
$$

The relaxation function presented in [21] is used. The wave generation zone has the length of one wavelength, the numerical beach extends over two wavelengths.

$$
\Gamma(\widetilde{x}) = 1 - \frac{e^{(\widetilde{x}^{3.5})} - 1}{e - 1} \; for \; \widetilde{x} \in [0;1] \tag{25}
$$

The coordinate $\widetilde{x}$ is scaled to the length of the relaxation zone. Several wave theories are implemented in REEF3D: linear waves, second-order and fifth-order Stokes waves, first-order and fifth-order cnoidal waves, first-order and fifth-order solitary waves and first-order irregular and focused waves. In case of linear waves for general water depths, the horizontal and vertical velocities u and w and the level set function ϕ for the free surface location are given as:

$$
\begin{aligned}
u(x,z,t)_{analytical} &= \frac{\pi H}{T}\frac{cosh\left[k\left(z+d\right)\right]}{sinh\left(kd\right)}cos\theta \\
w(x,z,t)_{analytical} &= \frac{\pi H}{T}\frac{sinh\left[k\left(z+d\right)\right]}{sinh\left(kd\right)}sin\theta \\
\phi(x,z,t)_{analytical} &= \frac{H}{2}cos\theta - z + d
\end{aligned}
\tag{26}
$$

The wave number k and the wave phase θ are defined as follows:

$$
\begin{aligned}
k &= \frac{2\pi}{L} \\
\theta &= kx - \omega t
\end{aligned}
\tag{27}
$$

where H is the wave height, L the wavelength, T the wave period, ω the angular wave frequency and z the vertical coordinate with the origin at the still water level d. In the wave generation zone, the pressure is not prescribed in the current numerical model, in order not to over define the boundary conditions. The omission of the pressure prescription in the wave

generation zone has not shown a loss in wave quality. At the numerical beach, the pressure is always set to its hydrostatic values based on the still water level d, independent of the wave input.

3.4. Numerical Calculation of Wave Forces

Wave forces can be determined by the numerical model in a straightforward manner. The pressure and the normal component of viscous stress tensor τ are integrated over the surface Ω of the structure. The integration is performed in a discrete manner, by using p and τ for each cell surface of the structure:

$$F = \int_{\Omega} (-\mathbf{n}p + \mathbf{n} \cdot \tau) d\Omega \tag{28}$$

here $\mathbf{n}$ is the unit normal vector to the surface, pointing into the fluid. The Navier-Stokes equations in Eq. (2) are solved including the gravity term. Then the pressure obtained from the projection method includes the hydrostatic part in addition to the dynamic part. Consequently, it is the total force acting on a structure that is determined by Eq. (28).

4. Results

In this section, several numerical results for wave propagation benchmark cases are presented. The numerical model is tested in order show the numerical accuracy and convergence in addition to the overall capabilities of REEF3D.

4.1. Grid and Time Step Convergence Tests

At first the general performance of the numerical model regarding wave propagation is tested in a rectangular wave flume with a two-dimensional setup. Regular waves are generated based on wave theory. Since there is no obstacle or other change in geometry along the wave flume, no wave transformation should take place and the wave should maintain the exact same shape and propagation speed as in the generation zone. As a consequence, the grid and time step convergence tests can be evaluated by comparing the numerical wave profile along the wave flume with the theoretical profile.

For these tests, a wave height of $H = 0.1$ m and a wave length of $L = 2$ m are selected for a still water depth of $d = 0.5$ m in a 20 m long wave flume. The resulting wave is of relatively high steepness ($\xi = 0.05$), requiring wave generation with fifth-order Stokes theory [11]. This makes it also more challenging for the numerical model to maintain the wave height along the

flume without numerical damping. The grid convergence test is performed on four different meshes with $dx = (0.05\text{ m}, 0.025\text{ m}, 0.01\text{ m}, 0.005\text{ m})$. For the comparisons in Figs. (5) and (6), the result after 90 s is used. For the grid convergence, the CFL number is kept at 0.1. Fig. (5a) shows the result for $dx = 0.05$ m. Here, the simulated wave troughs and crests are damped out. Also, the wave goes slightly out of phase. For $dx = 0.025$ m (Fig. (5b)) the numerical result improves. Wave crest damping occurs only towards the second half of the wave flume and the wave is in phase. From $dx = 0.01$ m on, the numerical model converges to the theoretical solution (Fig. (5c)). For both $dx = 0.01$ m and $dx = 0.005$ m, no wave crest damping occurs. Only a very slight under prediction of the wave troughs can be observed.

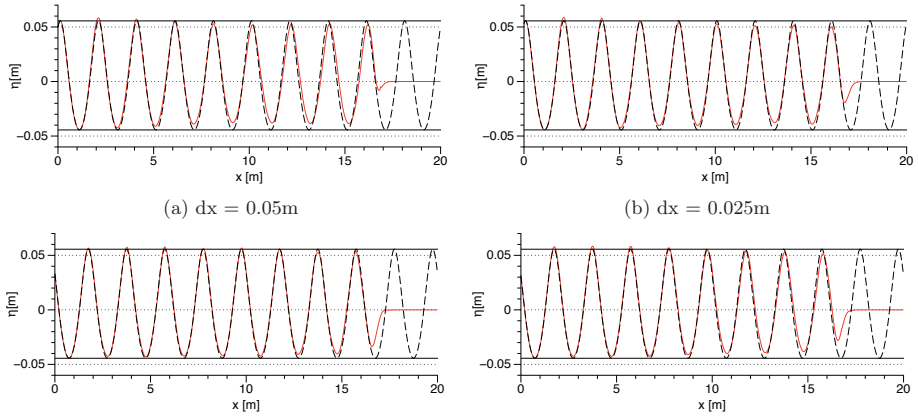

(a) dx = 0.05m

(b) dx = 0.025m

(c) dx = 0.01m

(d) dx = 0.005m

Figure 5: Grid convergence test in a 20 m long 2D wave flume with wave height $H = 0.1$ m, wave length $L = 2$ m and a CFL number of 0.1.The black dashed line shows the wave theory, the black solid line the theoretical wave envelope and the red line the numerical model.

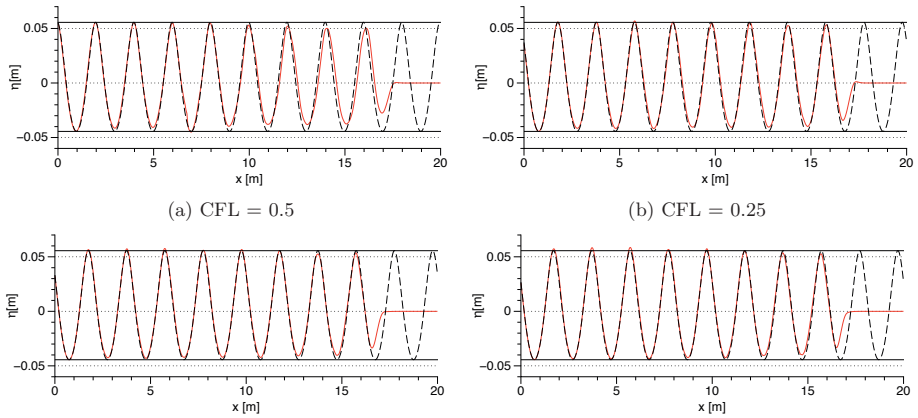

(a) CFL = 0.5

(b) CFL = 0.25

(c) CFL = 0.1

(d) CFL = 0.05

Figure 6: Time step convergence test in a 20 m long 2D wave flume with wave height $H = 0.1$ m, wave length $L = 2$ m and $dx = 0.01$ m. The black dashed line shows the wave theory, the black solid line the theoretical wave envelope and the red line the numerical model.

For the time step convergence test, the same wave conditions as for the grid convergence are used. Since the grid convergence tests showed a converged solution for $dx = 0.01$ m for these wave conditions, this grid size is used here. As presented above, the numerical model employs adaptive time stepping, so instead of testing fixed time step sizes, the CFL numbers 0.5, 0.25, 0.1 and 0.05 are tested. Fig. (6a) with CFL = 0.5 shows wave damping and a phase shift towards the end of the flume. For CFL = 0.25, the wave is in phase, but minor wave crest damping occurs at the end of the flume. For CFL = 0.1 and CFL = 0.05, the numerical results look similar (Fig. (6c-d)). No wave crest damping is observed, just a slight under prediction of the the wave trough. The CFL number incorporates information about the mesh width dx, so CFL = 0.1 is used for all of the following numerical applications. The mesh width on the other hand is tested for all cases individually.

4.2. Solitary Wave Interaction with a Rectangular Abutment

In this benchmark case, solitary wave propagation and the interaction with a rectangular abutment is investigated. The simulated results are compared with experimental data [25][18]. In the experiments, a rectangular abutment is placed in a 0.58 m wide wave flume, obstructing the flow over a width of 0.28 m. The side wall and the bottom of the wave flume are made of glass. The still water level is $d = 0.45$ m, a solitary wave with height $H = 0.1$ m is generated with a piston-type wavemaker. A fully reflective wall is placed at the end of the wave flume. In Fig. (7a) the plan view of the setup, including the wave gage locations, can

be seen. In the numerical model, the solitary wave is generated from third-order theory [15] in a relaxation zone with the length $l = 8$ m. The numerical domain has the size of ($L_x \times L_y \times L_z = 23.8$ m $\times 0.58$ m $\times 0.9$ m). The front face of the abutment is located 14.84 m away from the inlet boundary. This distance is 4 m longer than in the experimental setup, in order to accommodate the wave generation zone. For the grid convergence tests, four different meshes are used with $dx = (0.1\text{ m}, 0.05\text{ m}, 0.02\text{ m}, 0.01\text{ m})$, resulting in meshes with totals of 0.012 million, 0.1 million, 1.54 million and 12.36 million cells. As can be seen in Fig. (7a), there are nine wave gages placed around the abutment, both in the experimental and the numerical setup and the free surface data comparison is shown in Fig. (8).

All wave gages show two peaks. The first one is for the incoming solitary wave originating from the wavemaker. Then the wave passes the vertical structure and is reflected from the downstream wall. The reflected wave is recorded by the wave gages as the second peak. In order to perform the grid convergence tests, wave gage 7 is selected for comparison, as it is located downstream of the abutment and the influence of the structure can be seen for the first wave. Remarkably, the first peak is reproduced equally well on all four grids. Only for the reflected wave, the coarsest grid with $dx = 0.1$ m shows a reduced wave peak. The solitary wave is a single crest wave. The higher order WENO discretization of the convection terms ensures that there is no damping of the soliton, making the accurate solution less dependent

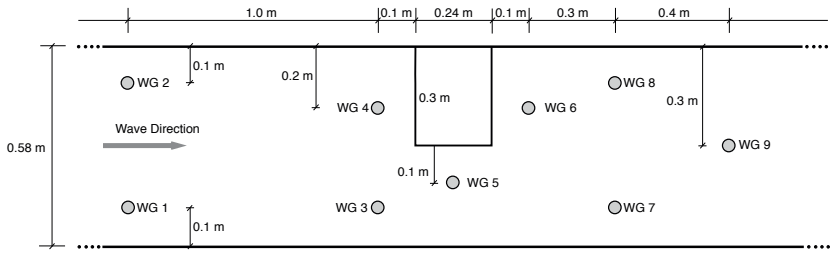

(a) Top view of the setup with wave gage locations.

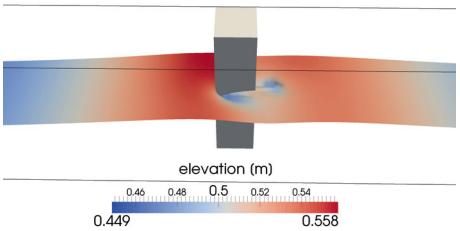

(b) Incident solitary wave just before passing the abutment.

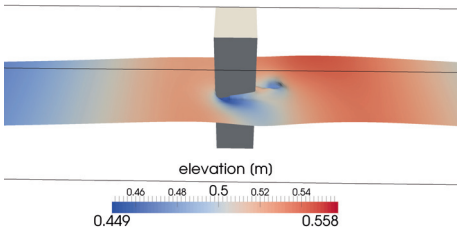

(c) Incident solitary wave just after it passing the abutment.

Figure 7: Solitary wave interaction with a rectangular abutment with setup and numerical free surface results.

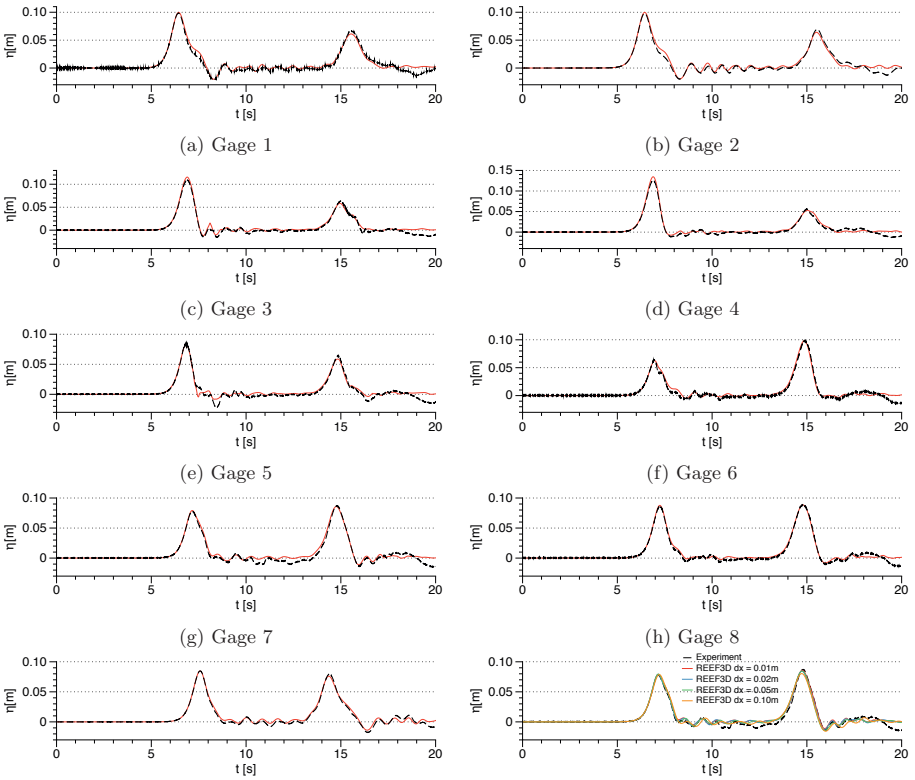

(a) Gage 1 (b) Gage 2

(c) Gage 3 (d) Gage 4

(e) Gage 5 (f) Gage 6

(g) Gage 7 (h) Gage 8

(i) Gage 9 (j) Gage 7, Grid Convergence

Figure 8: Solitary wave interaction with a vertical structure, black lines are laboratory experiments, red lines are REEF3D.

on the grid size. In Figs. (8a-8i), the results from the fine grid $dx = 0.01$ m are presented.

Gage 1 and 2 in Fig. (8a-b) show the generated solitary wave. The crest of the incident solitary wave is still unaffected by the abutment, maintaining the input wave height of $H = 0.1$ m. Directly after the peak, a slight bump in the wave shape occurs, which is attributed to the partial reflection from the abutment structure. The second peak resulting from the wave reflected by the downstream wall is clearly reduced. Gages 3 and 4 in Fig. (8c-d) show the effect of the channel narrowing. The numerical model calculates increased waves heights of $H = 0.11$ m and $H = 0.13$ m respectively for the incoming wave, slightly higher than the experimental data. For gage 4, the reflected wave is reduced with $H = 0.05$ m as it is the shadowed by the vertical structure. Wave gage 5 (Fig. (8e)) is located in the part of the flume that is constricted by the abutment. Here the incoming wave height is reduced. As the flow accelerates and the pressure decreases, a considerable drop in the free surface elevation in the

vicinity of the abutment can be observed (Fig. (7b-c)) for the incoming wave. Wave gage 6 (Fig. (8f)) is situated on the downstream side of the abutment. Here the incoming wave height is lower than the reflected wave, mirroring the behavior for gage 4. For gages 7 to 9 (Fig. (7g-i)), the incoming and reflected waves are nearly of the same magnitude. The reason is that between the incoming wave and the reflection, the wave is not further transformed. In general, the numerical model maintains all the wave peaks and also predicts the wave celerity correctly.

4.3. Wave Interaction with a Vertical Circular Cylinder

The data from the experiments carried out at the Large Wave Flume (GWK), Hannover, Germany presented by [30] is used for the comparison of the numerical results for wave interaction with a single vertical cylinder. The wave tank in the experiments is 309 m long, 5 m wide and 7 m deep. A cylinder of diameter $D = 0.7$ m is placed at a distance of 110 m from the wavemaker. Regular waves of period $T = 4$ s and wave height $H = 1.20$ m are generated in a water depth of $d = 4.76$ m. The wave force on the cylinder is measured using two strain gages placed at the top and the bottom of the cylinder. The free surface elevation near the wall of the wave flume along the frontline of the cylinder, in front of the cylinder, behind the cylinder and beside the cylinder are measured.

The water particle velocities at depths of $z = -0.93$ m, -1.53 m and -2.73 m from the still water level are measured near the wall along the frontline of the cylinders using ADVs. Fifth-order Stokes waves of height $H = 1.20$ m, period $T = 4.0$ s are generated in a water depth $d = 4.76$ m. The numerical wave tank is 132 m long, 5 m wide and 8 m high and a cylinder of diameter $D = 0.7$ m is placed at a distance of 44 m from the wave generation zone.

The computed wave force on the cylinder is compared to the experimental result in Fig.(9i) and a good agreement is seen. A grid resolution study is carried out with $dx = (0.2\text{ m}, 0.15\text{ m}, 0.1\text{ m})$ and the computed wave force converges to the experimental result at $dx = 0.1$ m resulting in 5.28 million cells in the numerical domain. The selected grid resolution is found to be sufficient for the computation of the wave force on the cylinder. The computed free surface elevations near the wall of the flume (WG 1) and around the cylinder (WG2, WG3 and WG4) are compared to the experimental observations in Fig. (9b-9e). The results are scaled with $\eta_{max,wall}$, the maximum elevation at $t/T = 5$ in Fig. (9b). A good agreement is seen between the computed and experimental results. The presence of the cylinder does not affect the free surface elevation close to the wall, which is equal to the

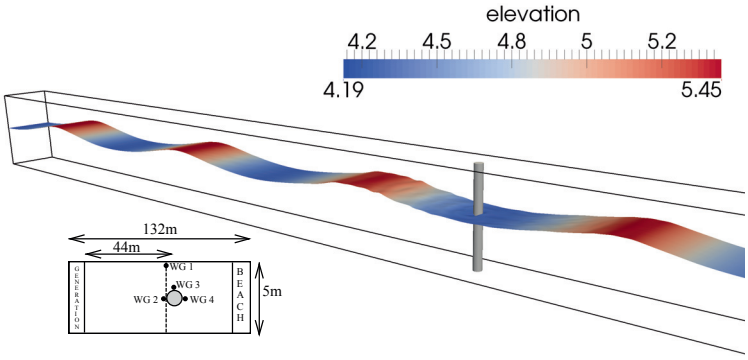

(a) Vertical circular cylinder setup.

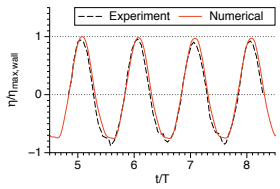

(b) Free surface, front line of the cylinder near the wall, WG 1.

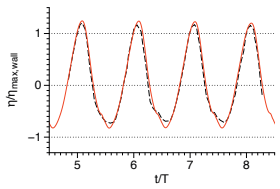

(c) Free surface, in front of the cylinder, WG 2.

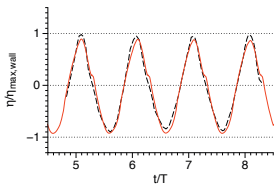

(d) Free surface, at the side of the cylinder, WG 3.

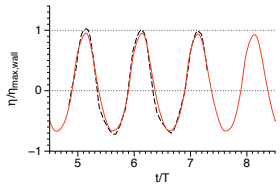

(e) Free Surface, behind the cylinder, WG 4.

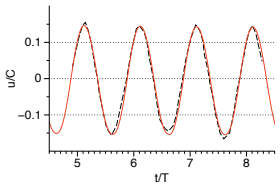

(f) Inline horizontal velocity $z = -0.93$m.

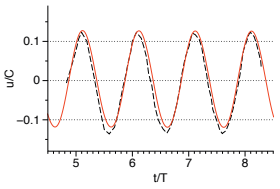

(g) Inline horizontal velocity $z = -1.53$m.

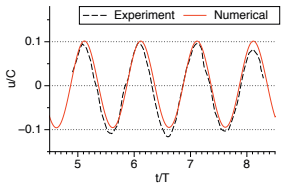

(h) Inline horizontal velocity $z = -2.73$m.

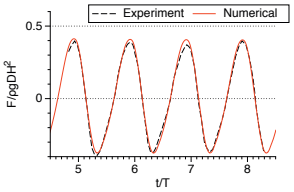

(i) Inline Wave Force, numerical vs. experimental.

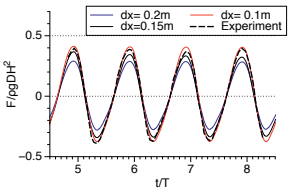

(j) Grid convergence study for forces.

Figure 9: Wave forces on a vertical cylinder

incident wave profile. A higher free surface elevation is seen in front of the cylinder compared to the back of the cylinder. This leads to a pressure difference around the cylinder, resulting in a net inline force on the cylinder. The computed horizontal water particle velocities at depths of $z = -0.93$ m, -1.53 m and -2.73 m from the still water level are compared to the experimental data scaled with the wave celerity C in Fig. (9f-9h) and a good agreement is seen. The horizontal water particle velocity is seen to reduce with increasing depth from the free surface as the influence of the wave on the water particle decreases.

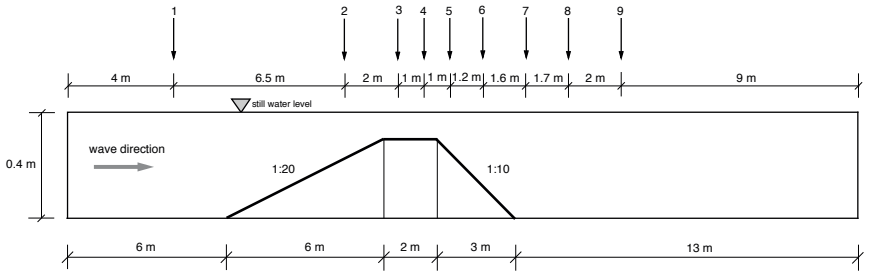

Figure 10: Submerged Bar setup with wave gage locations

4.4. Wave Propagation over a Submerged Bar

A well known benchmark is the submerged bar case by [2]. Here, monochromatic regular waves are generated in a rectangular wave flume of size ($L_x \times L_y \times L_z = 37.7$ m$\times 0.8$ m$\times 0.75$ m). A trapezoidal submerged bar is placed 6 m downstream of the wave maker, see Fig. (10). Nine wave gages are placed along the wave flume. The incident wave height is $H = 0.02$ m with a wave period of $T = 2$ s, resulting in a wavelength $L = 3.73$ m. In the numerical model, linear waves are generated in a relaxation zone of one wavelength. On the upslope of the bar, the waves shoal, yet breaking does not occur. After the crest of the bar, wave decomposition takes place and higher wave harmonics are formed. As a result, the free surface is typically very difficult to predict in the downslope and downstream region of the bar [3]. High-order numerical discretization schemes are needed in order to predict the correct dispersion characteristics and avoid wave crest damping and wave phase shifting. Thus, this case is well suited to test the accuracy of the proposed numerical wave tank. For the grid convergence study, two wave gages are selected: wave gage 4 on the crest of the submerged bar and wave gage 9 on the downstream side. Grids with $dx = (0.05$ m$, 0.02$ m$, 0.01$ m$, 0.005$ m$)$ are tested. Fig. (11j) reveals that the two finer meshes closely match the experimentally observed effect from shoaling. For the two coarser meshes, the shoaling is under predicted

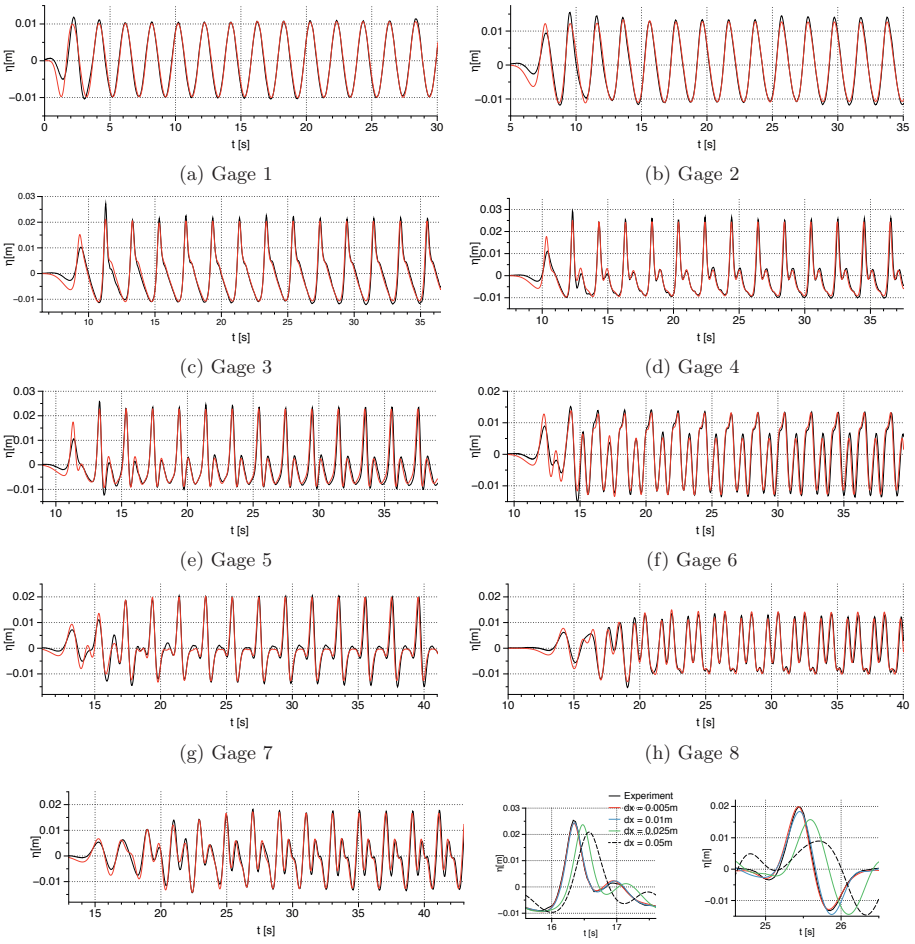

(a) Gage 1 (b) Gage 2

(c) Gage 3 (d) Gage 4

(e) Gage 5 (f) Gage 6

(g) Gage 7 (h) Gage 8

(i) Gage 9 (j) Gage 4, Grid Convergence (k) Gage 9, Grid Convergence

Figure 11: Wave transformation on a submerged bar, black lines are laboratory experiments, red lines are REEF3D.

with lower free surface elevations in addition to slower moving waves. In Fig. (11k), it can be seen that the mesh with $dx = 0.005$ m can capture the transformed wave very well, both in amplitude and phase. The phase is also maintained for $dx = 0.01$ m, while the wave crest is slightly reduced. For $dx = 0.025$ m, the phase shift and the amplitude reduction is clearly visible, for $dx = 0.05$ m even more. As a result, the mesh with $dx = 0.005$ m is selected for the comparison with the experimental data. Wave gage 1 shows the input wave, with the wave crests and trough symmetric around the still water level, the typical characteristics for

linear waves. Wave gage 2 shows the beginning of the shoaling on the sloping bed, but the waves maintain their sinusoidal shape. Gages 3 and 4 show the waves on the crest of the submerged bar. The loss of the sinusoidal shape indicates appearance of the secondary crests. This becomes more prominent on the downslope (gages 5 and 6) and on the downstream side of the submerged bar (gages 7-8). For all gages, the free surface predicted by the numerical model closely follows the one recorded in the laboratory experiment. This demonstrates the capabilities of REEF3D due to the high-order spatial WENO and temporal TVD Runge-Kutta discretization in addition to the staggered grid arrangement. Also, the immersed boundary handles the irregular grid cells well on the slopes of the submerged bar.

4.5. Plunging Breaking Waves over a Sloping Bed

In the previous section, shoaling non-breaking waves were modeled. A more difficult situation arises, when the shoaling effect is so strong, that the steepened wave crest becomes unstable and breaks. A sloping seabed with a slope of 1/35 is chosen for the case study of wave breaking over a plane slope. The computational setup and wave parameters in the present case study are similar to the experimental conditions reported by [41]. The wave tank has a horizontal bed with the water depth of $d = 0.4$ m. A 4 m long stretch with a flat bottom is followed by the slope. The laboratory arrangements and the computational domain for the plunging breaker case are shown in Fig. (12). The origin of the horizontal and vertical coordinates is at the toe of the slope at the still water level. A fifth-order cnoidal wave theory developed by [12] is used to represent the incident wave with the height of $H = 0.128$ m and period of $T = 5.0$ s. A simulation length of 30 s is used to obtain a quasi-steady state for the mean wave quantities. Then the simulated values from the last five waves are used for the evaluation of the breaking point and breaking height.

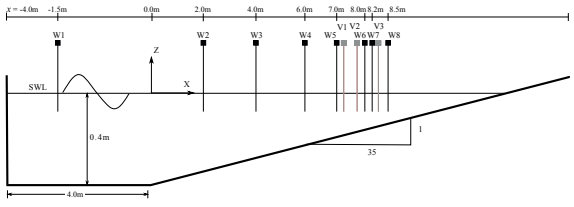

Figure 12: Computational set-up: W1-W8 are wave gauge locations and V1-V3 are velocity probe locations

The sensitivity of the computational results to the grid resolution is investigated with four different mesh sizes $dx = (0.025\text{ m}, 0.01\text{ m}, 0.005\text{ m}, 0.0025\text{ m})$. The simulated breaking location (x_b) and the breaker height (H_b) are compared with the measured data in Fig. (13).

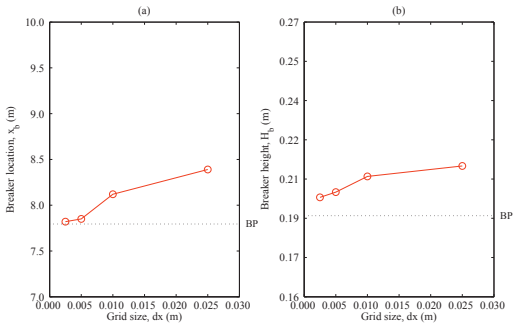

Figure 13: Grid sensitivity study on simulated results (a) breaker location (x_b) and (b) breaker height (H_b). The dotted line shows the breaking point observed in the experiments.

The simulated waves break later shoreward with slightly larger breaker height on coarser grids ($dx = 0.025$ m and $dx = 0.01$ m) than in the experiments. Whereas on finer grids ($dx = 0.005$ m and $dx = 0.0025$ m) waves break at almost the same location $x_b = 7.84$ m with the breaker height $H_b = 0.205$ m as in the experiments, where waves break at $x_b = 7.795$ m with $H_b = 0.196$ m. The comparison of the experimental and numerical values indicates that the best comparison with experimental data occurs with the finer grids ($dx = 0.005$ m and $dx = 0.0025$ m). The grid size $dx = 0.005$ m is selected for the computation since the simulated waves on this grid size yield good results with reasonable computational time and the difference between the $dx = 0.005$ m and $dx = 0.0025$ m is also insignificant. Compared to the previous section, a finer mesh is required. Here, the additional challenge arises not from the wave shoaling, but from the breaking process. The breaking occurs at a much smaller scale, than the wave propagation itself. Also, wave breaking is a true two-phase flow problem, where complex interface deformations occur.

The simulated free surface elevations are compared with experimental data at different locations along the wave tank in order to assess the ability of the numerical model to simulate hydrodynamic processes from wave generation to the surf zone. The free surface elevations are computed at eight different locations (W1-W8): $x = -1.5$ m, 2.0 m, 4.0 m, 6.0 m, 7.0 m, 8.0 m, 8.2 m and 8.5 m from the toe of the slope (see Fig. (12)). Fig. (14) shows the comparison of the simulated free surface elevations with the experimental measurements [41] for the plunging breaker case. The free surface profile evolves continuously from a wide crest to a narrow and steep crest. The wave height increases due to shoaling, as the wave propagates over the slope. The wave crest becomes unstable and breaks at $x_b = 7.84$ m with a breaker

height of $H_b = 0.205$ m. The numerical breaking condition is almost the same as measured in the experiments. It can be seen from Figs. 14 (f), (g) and (h), that the wave height diminishes after breaking as the wave approaches the shore. The simulated free surface profiles precisely represent the characteristics of the cnoidal waves in shallow water and display a good match with the experimental data.

The computed horizontal component of the fluid velocity at $x = 7.295$ m (incipient breaking), $x = 7.795$ m (during breaking) and $x = 8.345$ m (after breaking) are compared with the experimental data in Fig. (15) - Fig. (17). As can be seen from Fig. (15), in the region just prior to breaking, the variation of the horizontal velocity is almost constant with the water depth, which is consistent with the experimental observation by [41]. As the wave propagates further over the slope, the wave height increases due to shoaling. This leads to a rise in the potential energy in the region close to the wave crest. When the fluid particle velocity exceeds the wave speed, wave breaking occurs at $x = 7.84$ m, with the maximum velocity at the tip of

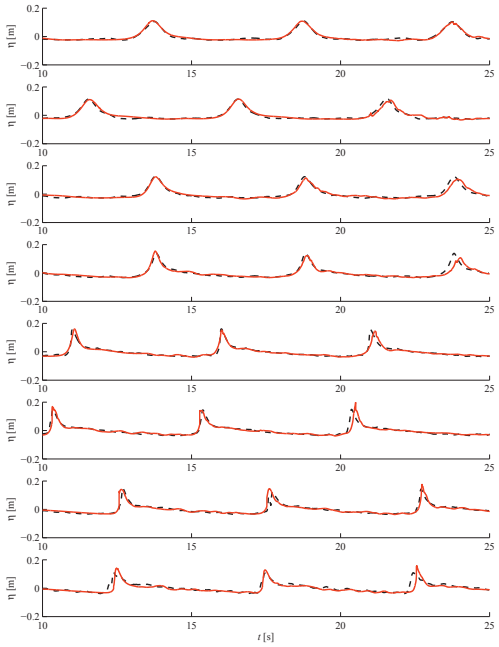

Figure 14: Comparison of simulated and measured water surface elevations for plunging breaker case at x= -1.5 m (a), 2.0 m (b), 4.0 m (c), 6.0 m (d), 7.0 m (e), 8.0 m (f), 8.2 m (g) and 8.5 m (h). Red lines: present numerical model; Black lines: experimental data by [41]

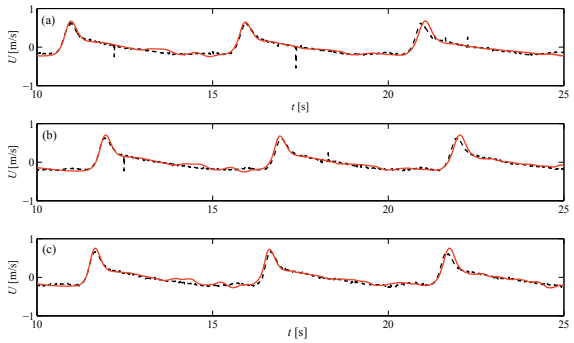

Figure 15: Comparison of simulated and measured horizontal velocities for plunging breaker case at x=7.275 m and z=-0.05 m (a), -0.10 m (b), and -0.15 m (c). Red lines: present numerical model; Black lines: experimental data by [41]

the horizontal overturning jet followed by a small velocity gradient over the depth (Fig. (16)). At the point of jet impingement, the horizontal velocity increases as the distance from the free surface increases, as shown in Fig. (17). This is due to the penetration of the large scale water jet into the preceding wave surface. The present model predicts the horizontal velocity variation along the water depth accurately and the simulated results are in good agreement with the experimental measurements.

The evolution of the wave breaking process with the velocity magnitude and velocity vector distribution is shown in Fig. (18). At the incipient breaking stage, the wave profile gets steeper and sharper and a portion of the wave crest attains the maximum fluid velocity. The total wave energy is focused near the wave crest and eventually wave breaking occurs. The portion of the wave crest with high velocity moves forward and evolves into an overturning plunging jet (Fig. (18a)). When the plunging jet impinges on the surface of the preceding wave (Fig. (18b)), a splash-up occurs as shown in Fig. (18c) and Fig. (18d). This creates a secondary wave followed by a pocket of air with different characteristics than the original wave. The rapid transition from a strong plunger vortex into small scale turbulence at the free surface takes place over a short distance. The simulated physical flow features of the plunging breaker during the wave breaking process such as wave profile evolution, the generation of the overturning water jet, the enclosed air pocket and the secondary wave, the splash-up phenomenon and the mixing of air and water in the surf zone are consistent with the experimental observation [41].

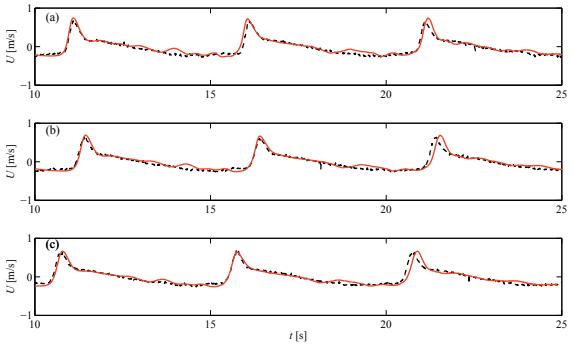

Figure 16: Comparison of simulated and measured horizontal velocities for plunging breaker case at x=5.945 m and z=-0.05 m (a), -0.10 m (b), and -0.145 m (c). Red lines: present numerical model; Black lines: experimental data by [41]

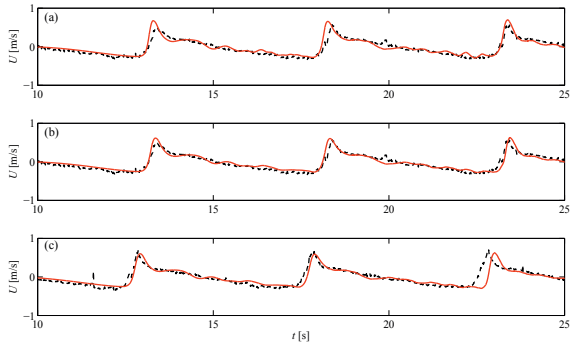

Figure 17: Comparison of simulated and measured horizontal velocities for plunging breaker case at x=6.665 m and z=-0.05 m (a), -0.10 m (b), and -0.13 m (c). Red lines: present numerical model; Red lines: experimental data by [41]

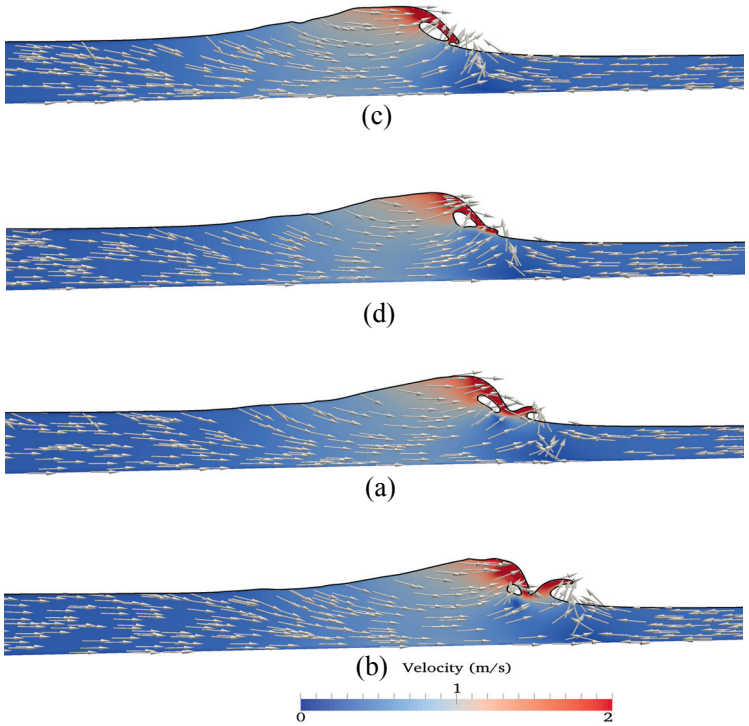

Figure 18: Snapshots of simulated wave profile during breaking process over a slope at $t = 10.90$ s (a), 10.95 s (b), 11.00 s (c) and 11.05 s (d)

5. Conclusions

The new numerical wave tank REEF3D has been presented. The incompressible Navier-Stokes equations are solved with RANS turbulence closure. In order to achieve stable and accurate wave propagation results, high-order numerical discretization schemes on a Cartesian mesh are selected. For the convection terms of the momentum equations, the fifth-order WENO scheme is chosen. Time-stepping is performed with the third-order TVD Runge-Kutta scheme. The pressure is solved on a staggered grid with the projection method, ensuring tight pressure-velocity coupling. Irregular boundaries are taken into account with an extension of an existing ghost cell immersed boundary method to three dimensions. The numerical model is fully parallelized based on the domain decomposition strategy and MPI (message passing interface). The free surface is modeled with the level set method. Special attention has been given to the evaluation of the density. It was found that density evaluation at the cell center leads to small-scale free surface oscillations, when periodic regular waves are simulated. The proposed density calculation scheme at the cell face showed a much improved free surface, comparing well against the theoretical wave profile. The waves are generated and absorbed with the relaxation method.

The performance of the proposed numerical wave tank has been tested with several benchmark applications. At first, grid and time step convergence tests have been performed for periodic regular waves. Next, the interaction of a solitary wave with a vertical structure was calculated. The comparison with experimental free surface measurements showed good agreement. Also, the coarse grids performed well for the solitary wave propagation problem. Further, the model was used to calculate non-breaking wave forces on a vertical cylinder. The model matched the experimental free surface, velocity and wave force data well, showing that the model also predicts the wave kinematics and wave dynamics very realistically. The challenging submerged bar case revealed that the numerical wave tank has the capability to accurately predict wave shoaling and the following wave transformation. In the last test, plunging breaking waves were modeled. The model compared favorably against the experimentally recorded free surface and velocity data. The plunging breaking waves were simulated in a realistic manner and all the stages of the breaking process were captured. The benchmark tests show that the new numerical wave tank REEF3D achieves the goal of accurately representing the physics of wave propagation and hydrodynamics, including the complex problem of wave breaking.

Acknowledgment

The authors would like to thank Prof. Iñigo J. Losada for providing the experimental data for the solitary wave interaction with a vertical structure. The authors would also like to thank Dr. James Kirby and Dr. Francis Ting for sharing the experimental data of the plunging breaking waves case. This study has been carried out under the OWCBW project (No. 217622/E20) and the authors are grateful to the grants provided by the Research Council of Norway. This study was supported in part with computational resources at the Norwegian University of Science and Technology (NTNU) provided by NOTUR, http://www.notur.no.

References

[1] M. Alagan Chella, H. Bihs, D. Myrhaug, and M. Muskulus. Breaking characteristics and geometric properties of spilling breakers over slopes. *Coastal Engineering*, 95:4–19, 2015.

[2] S. Beji and J. A. Battjes. Experimental investigation of wave propagation over a bar. *Coastal Engineering*, 19:151–162, 1993.

[3] S. Beji and J. A. Battjes. Numerical simulation of nonlinear wave propagation over a bar. *Coastal Engineering*, 23:1–16, 1994.

[4] P. A. Berthelsen and O. M. Faltinsen. A local directional ghost cell approach for incompressible viscous flow problems with irregular boundaries. *Journal of Computational Physics*, 227:4354–4397, 2008.

[5] N. Booij, R. C. Ris, and L. H. Holthuijsen. A third-generation wave model for coastal regions, 1. model description and validation. *Journal of Geophysical Research*, 104:7649–7666, 1999.

[6] A. Calderer, S. Kang, and F. Sotiropoulos. Level set immersed boundary method for coupled simulation of air/water interaction with complex floating structures. *Journal of Computational Physics*, 277:201–227, 2014.

[7] A. Chorin. Numerical solution of the Navier-Stokes equations. *Mathematics of Computation*, 22:745–762, 1968.

[8] R. Croce, M. Griebel, and M. A. Schweitzer. Numerical simulation of bubble and droplet deformation by a level set approach with surface tension in three dimensions. *International Journal for Numerical Methods in Fluids*, 62:963–993, 2010.

[9] D. G. Dommermuth, D. K. P. Yue, W. M. Lin, R. J. Rapp, E. S. Chan, and W. K. Melville. Deep-water plunging breakers : a comparison between potential theory and experiments. *Journal of Fluid Mechanics*, 189:434–442, 1988.

[10] P. A. Durbin. Limiters and wall treatments in applied turbulence modeling. *Fluid Dynamics Research*, 41:1–18, 2009.

[11] J. D. Fenton. A fifth-order Stokes theory for steady waves. *Journal of Waterway, Port, Coastal and Ocean Engineering*, 111(2):216–234, 1985.

[12] J. D. Fenton. *The cnoidal theory of water waves*, chapter 2, pages 55–100. Developments in Offshore Engineering, Gulf, Houston. J. B. Herbich edition, 1999.

[13] M. Griebel, T. Dornseifer, and T. Neunhoeffer. *Numerical Simulation in Fluid Dynamics, a Practical Introduction*. SIAM, 1998.

[14] S. T. Grilli, R. Subramanya, I. A. Svendsen, and J. Veeramony. Shoaling of solitary waves on plane beaches. *Journal Waterway Port Coastal and Ocean Enigneering*, 120(6):609–628, 1994.

[15] R. Grimshaw. The solitary wave in water of variable depth. part 2. *Journal of Fluid Mechanics*, 46:611–622, 1971.

[16] A. Harten. High resolution schemes for hyperbolic conservation laws. *Journal of Computational Physics*, 49:357–393, 1983.

[17] P. Higuera, L. J. Lara, and I. J. Losada. Realistic wave generation and active wave absorption for Navier-Stokes models application to OpenFOAM. *Coastal Engineering*, 71:102–118, 2013.

[18] P. Higuera, L. J. Lara, and I. J. Losada. Simulating coastal engineering processes with OpenFOAM. *Coastal Engineering*, 71:119–134, 2013.

[19] P. Higuera, L. J. Lara, and I. J. Losada. Three-dimensional interaction of waves and porous coastal structures using OpenFOAM. Part II: Application. *Coastal Engineering*, 83:259–270, 2014.

[20] M. S. Hossain and W. Rodi. Mathematical modeling of vertical mixing in stratified channel flow. *2nd Symposium on Stratified Flows, Trondheim, Norway*, 1980.

[21] N. G. Jacobsen, D. R. Fuhrman, and J. Fredsøe. A wave generation toolbox for the open-source CFD library: OpenFOAM. *International Journal for Numerical Methods in Fluids*, 70(9):1073–1088, 2012.

[22] G. S. Jiang and D. Peng. Weighted ENO schemes for Hamilton Jacobi equations. *SIAM Journal of Scientific Computing*, 21:2126–2143, 2000.

[23] G. S. Jiang and C. W. Shu. Efficient implementation of weighted ENO schemes. *Journal of Computational Physics*, 126:202–228, 1996.

[24] J. T. Kirby and R. A. Dalrymple. A parabolic equation for the combined refraction-diffraction of Stokes waves by mildly varying topography. *Journal of Fluid Mechanics*, 136:453–466, 1983.

[25] L. J. Lara, M. del Jesus, and I. J. Losada. Three-dimensional interaction of waves and porous coastal structures part II: Experimental validation. *Coastal Engineering*, 64:26–46, 2012.

[26] P. A. Madsen, H. B. Bingham, and H. Liu. A new Boussinesq method for fully nonlinear waves from shallow to deep water. *Journal of Fluid Mechanics*, 462:1–30, 2002.

[27] P. A. Madsen, R. Murray, and O. R. Sørensen. A new form of the Boussinesq equations with improved linear dispersion characteristics. *Coastal Engineering*, 15:371–388, 1991.

[28] S. Mayer, A. Garapon, and L. S. Sørensen. A fractional step method for unsteady free surface flow with applications to non-linear wave dynamics. *International Journal for Numerical Methods in Fluids*, 28:293–315, 1998.

[29] R. Mittal, H. Dong, M. Bozkurttas, F. M. Najjar, A. Vargas, and A. von Loebbecke. A versatile sharp interface immersed boundary method for incompressible flows with complex boundaries. *Journal of Computational Physics*, 227:4825–4852, 2008.

[30] W. Mo, K. Irschik, H. Oumeraci, and P. L.-F. Liu. A 3D numerical model for computing non-breaking wave forces on slender piles. *Journal of Engineering Mathematics*, 58:19–30, 2007.

[31] D. Naot and W. Rodi. Calculation of secondary currents in channel flow. *Journal of the Hydraulics Division, ASCE*, 108(8):948–968, 1982.

[32] NOTUR. Notur - the Norwegian Metacenter for Computational Science. http://www.notur.no, 2015.

[33] O. Nwogu. Alternative form of Boussinesq equations for nearshore wave propagation. *Journal of Waterways, Port, Coastal, and Ocean Engineering*, 119(6):618–638, 1993.

[34] S. Osher and J. A. Sethian. Fronts propagating with curvature-dependent speed: Algorithms based on Hamilton-Jacobi formulations. *Journal of Computational Physics*, 79:12–49, 1988.

[35] B. T. Paulsen, H. Bredmose, and H. Bingham. An efficient domain decomposition strategy for wave loads on surface piercing circular cylinders. *Coastal Engineering*, 86:57–76, 2014.

[36] D. Peng, B. Merriman, S. Osher, H. Zhao, and M. Kang. A PDE-based fast local level set method. *Journal of Computational Physics*, 155:410–438, 1999.

[37] W. E. Rogers, J. M. Kaihatu, L. Hsu, R. E. Jensen, J. D. Dykes, and K. T. Holland. Forecasting and hindcasting waves with the SWAN model in the Southern California Bight. *Coastal Engineering*, 54:1–15, 2007.

[38] B. Seiffert, M. Hayatdavoodi, and R. C. Ertekin. Experiments and computations of solitary-wave forces on a coastal-bridge deck. Part I: Flat plate. *Coastal Engineering*, 88:194–209, 2014.

[39] C. W. Shu and S. Osher. Efficient implementation of essentially non-oscillatory shock capturing schemes. *Journal of Computational Physics*, 77:439–471, 1988.

[40] M. Sussman, P. Smereka, and S. Osher. A level set approach for computing solutions to incompressible two-phase flow. *Journal of Computational Physics*, 114:146–159, 1994.

[41] F. C. K. Ting and J. T. Kirby. Dynamics of surf-zone turbulence in a strong plunging breaker. *Coastal Engineering*, 24:177–204, 1995.

[42] Y. H. Tseng and J. H. Ferziger. A ghost-cell immersed boundary method for flow in complex geometry. *Journal of Computational Physics*, 192:593–623, 2003.

[43] H. van der Vorst. BiCGStab: A fast and smoothly converging variant of Bi-CG for the solution of nonsymmetric linear systems. *SIAM Journal of Scientific Computing*, 13:631–644, 1992.

[44] B. van Leer. Towards the ultimate conservative difference scheme V. A second order sequel to Godunovs method. *Journal of Computational Physics*, 32:101–136, 1979.

[45] Z. Wang, J. Yang, and F. Stern. A coupled level set and volume-of-fluid method for sharp interface simulation of plunging breaking waves. *International Journal of Multiphase Flow*, 35:227–246, 2009.

[46] H. G. Weller. A new approach to VOF-based interface capturing methods for incompressible and compressible flow. *Technical Report. OpenFOAM*, 2008.

[47] R. Wemmenhove. *Numerical Simulation of Two-Phase Flow in Offshore Environments*. PhD thesis, Faculty of Mathematics and Natural Sciences, University of Groningen, 2008.

[48] D. C. Wilcox. *Turbulence Modeling for CFD*. DCW Industries Inc., La Canada, California., 1994.

[49] F. Xu, W. Perrie, B. Toulany, and P. C. Smith. Wind-generated waves in Hurricane Juan. *Ocean Modeling*, 16:188–205, 2007.

[50] J. Yang and F. Stern. Robust and efficient setup procedure for complex triangulations in immersed boundary simulations. *Journal of Fluids Engineering*, 135(10):101107.1–101107.11, 2014.

[51] J. Yang, Z. Wang, and F. Stern. Sharp interface immersed-boundary/level-set method for wave–body interactions. *Journal of Computational Physics*, 228:6590–6616, 2009.

[52] W. Yue, C.-L. Lin, and V. C. Patel. Numerical simulation of unsteady multidimensional free surface motions by level set method. *International Journal for Numerical Methods in Fluids*, 42:853–884, 2003.

6.3 Paper 3

Breaking characteristics and geometric properties of spilling breakers over slopes

Alagan Chella, M., Bihs, H., Myrhaug, D., Muskulus, M.
Coastal Engineering, 2015, Vol. 95, pp. 4-19
DOI: 10.1016/j.coastaleng.2014.09.003

Paper 3

Coastal Engineering 95 (2015) 4–19

Contents lists available at ScienceDirect

Coastal Engineering

journal homepage: www.elsevier.com/locate/coastaleng

Breaking characteristics and geometric properties of spilling breakers over slopes

Mayilvahanan Alagan Chella [a,*], Hans Bihs [a], Dag Myrhaug [b], Michael Muskulus [a]

[a] Department of Civil and Transport Engineering, Norwegian University of Science and Technology (NTNU), NO-7491 Trondheim, Norway
[b] Department of Marine Technology, Norwegian University of Science and Technology (NTNU), NO-7491 Trondheim, Norway

ARTICLE INFO

Article history:
Received 16 July 2014
Received in revised form 12 September 2014
Accepted 15 September 2014
Available online 12 October 2014

Keywords:
Breaking waves
Wave profile asymmetry
Spilling breakers
Numerical modeling
Breaker indices

ABSTRACT

A two-phase flow CFD model based on the Reynolds-Averaged Navier–Stokes (RANS) equations coupled with the level set method (LSM) and $k-\omega$ turbulence model is used to simulate spilling breakers over a sloping bed. In order to validate the present numerical model, the simulated results are compared with the experimental data measured by Ting and Kirby (1996). The simulated horizontal velocities and free surface elevations are in good agreement with the experimental measurements. Moreover, the present model is able to model the prominent features associated with the breaking process such as the motion of air pockets in the water, formation of a forward moving jet, the splash-up phenomenon and the mixing of air and water in the breaking region. The numerical model has been utilized to study the influences of three important environmental parameters; water depth, offshore wave steepness and beach slope on the characteristics and geometric properties of spilling breakers over slopes. A total of 39 numerical experiment cases are performed to investigate the characteristics of breaking waves such as breaking location, incipient breaker height and water depth at breaking, incipient breaker indices and geometric properties with different offshore wave steepnesses at different water depths over a wide range of beach slopes. The geometric properties associated with breaking waves in shallow water are described using the wave steepness and asymmetry factors introduced by Kjeldsen and Myrhaug (1978). The computed results appear to give reasonable predictions and consistency with previous studies.

1. Introduction

Wave breaking is a natural process involving transformation of wave energy into turbulent energy leading to a violent transformation of the free surface, that exerts massive hydrodynamic loads on marine structures (Cokelet, 1977). During wave breaking for shoaling waves, the dissipation of energy takes place in order to approximately balance the increase in the local wave energy due to shoaling. However, the wave breaking process is primarily responsible for the creation of the surface turbulence and is increasing the turbulent kinetic energy, that plays an important role in the vertical mixing of momentum through the water column (Craig, 1996; Ting and Kirby, 1996). Massel (2007) gives a wide perspective of the breaking of both regular and random waves and how this is linked with the aerosol production and air-sea gas interaction. Based on the steepness of the wave and the seabed slope, breaker types can be categorized into four different types, namely spilling, plunging, surging and collapsing (Galvin, 1968). The breaking process depends on many physical parameters; water depth, wave height, wave length and seabed slope. Breaking waves are three-dimensional (3D) due to the interaction with waves, current or wind in a real sea environment. Moreover, e.g. in a wave tank waves always begin to propagate down the tank as undisturbed two-dimensional (2D) waves and reach the critical point at which the unstable water front evolves into a 3D flow. Therefore, 2D models can capture most of the wave breaking characteristics up to the breaking point, where 3D effects are minimal.

A symmetrical wave can be expressed by the wave steepness. As it propagates over a plane slope, the wave starts to deform and the wave front moves forward, thus the shape of the wave profile is not symmetric anymore. Several studies have been carried out to investigate the geometric properties of breaking waves in deep water (Babanin et al., 2010; Bonmarin, 1989; Kjeldsen and Myrhaug, 1978; Lader, 2002). Although a considerable amount of literature has been reported on wave steepness and asymmetry factors of shallow water waves (Adeyemo, 1968; Ippen and Kulin, 1954; Iwagaki and Sakai, 1972; Miller and Zeigler, 1964), there have been limited studies on the geometrical asymmetry associated with breaking waves on slopes in shallow water. A definition sketch of the wave asymmetry profile at breaking in shallow water is shown in Fig. 1. The breaking asymmetry profile parameters can be related to breaking wave forces on coastal structures, which influence the global design of a structure (Adeyemo, 1968). Much uncertainty still exists about the relationship between the wave asymmetry profile parameters and the breaking wave forces,

* Corresponding author.
E-mail address: acm@ntnu.no (M. Alagan Chella).

http://dx.doi.org/10.1016/j.coastaleng.2014.09.003
0378-3839/

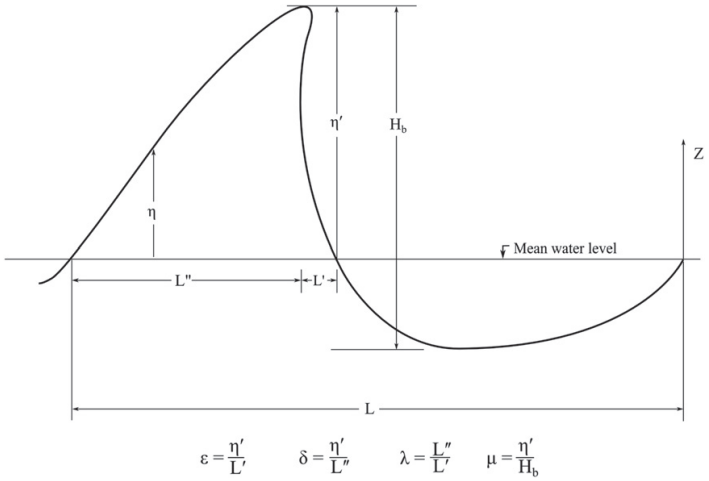

Fig. 1. Definition sketch of local wave geometry parameters following (Kjeldsen and Myrhaug (1978).

suggesting a need to understand the geometric properties of breaking waves on slopes in shallow water and the effect of breaking wave forces on coastal structures. The maximum wave height governs the critical design condition for coastal structures, which is greatly influenced by the wave breaking process.

The wave transformation over a sloping bed, such as shoaling, overturning and onset of wave breaking can be described theoretically or numerically by classical potential flow theory. However, this disregards the influence of viscosity and turbulence production, which plays a vital role in wave breaking, especially for waves over sloping beds. The first numerical computation of breaking waves in deep water was performed by Longuet-Higgins and Cokelet (1976) by applying a mixed Eulerian–Lagrangian formulation (MEL) with the boundary integral method based on potential theory and a conformal mapping of physical plane limited to a periodic domain in deep water. Vinje and Brevig (1981) applied the same method in the physical plane, and they extended the application to finite water depth. Most recent MEL based models are capable of modeling both arbitrary waves and water depths. The MEL method is able to model the breaking waves until breaking but cannot model the interface reconnection phenomenon that occurs during the breaking process (Chen et al., 1999). Other models based on the Boussinesq approximation have been used to simulate only the wave deformation. This method cannot be used directly to model the wave breaking (Christensen, 1998), but the model can be used to calculate the wave transformation in the surf zone together with a model for the dissipation of energy. The description of the breaking process is highly demanding due to unsteady non-linear viscous flow, the complex air-water interface, small scale free surface turbulence transport and dissipation process. Moreover, the theoretical description of the entire process is only possible with gross simplifications and assumptions (Cokelet, 1977). Thus, most of the studies on breaking waves are limited to field and laboratory experiments. Many theories and formulas to predict the breaking wave characteristics have been proposed based on the physical experiments (Goda, 2010; Iwagaki and Sakai, 1972; Tsai et al., 2005). Due to the complexity in describing the wave breaking process, most of the existing formulas are empirical and semi-empirical, and thus subjected to the experimental conditions and scale effects. However, none of the relationships have been established globally for obtaining the breaking wave properties for practical engineering applications (Southgate, 1993).

An efficient model based on Computational Fluid Dynamics (CFD) can describe the wave breaking process without specifying breaking criteria. The prominent features of the physical process can be obtained in detail without much simplifications, assumptions and approximations in the fluid flow properties (Christensen, 1998). CFD solves the fundamental fluid dynamic equations including the air-water interface. The small scale free surface turbulence transport and dissipation process can be represented by a suitable turbulence model. Hence, the method is capable of determining the detailed information concerning fluid flow properties such as velocities, turbulence, interface deformation etc. A number of numerical studies based on viscous computations attempted to simulate the breaking process with a single phase model such as Lin and Liu (1998), Bradford (2000) and Zhao et al. (2004). Since a single phase model ignores the motion of the air over the free surface and the density variation across the interface, which are primarily responsible for the surface deformation phenomenon, the complete description of the breaking process is still not fully represented. Hence, all the previously mentioned models have some significant discrepancies compared with the experimental data. Other studies such as Chen et al. (1999), Hieu et al. (2004), Christensen (2006), Jacobsen et al. (2012) used a two-phase flow model to describe the wave breaking process. Detailed literature reviews on the methods and results can be found in Lin and Liu (1998), Chen et al. (1999), Zhao et al. (2004), Hieu et al. (2004) and Bradford (2000). Christensen (2006) studied the undertow profiles and turbulence levels in breaking waves with a Navier–Stokes solver and the volume of fluid method (VOF). The Large Eddy Simulation (LES) technique was used to model the turbulence in the breaking waves. The predicted turbulence levels and the wave heights at breaking were higher than in the experiments. Jacobsen et al. (2012) presented the application of OpenFOAM to model spilling breaking waves using the Reynolds-Averaged Navier–Stokes (RANS) equations, coupled with the VOF method. They compared the numerical results with the experimental data by Ting and Kirby (1996) using a geometric cut-off (i.e. a significant modification at the end of the tank). Moreover, their model slightly over-predicted the wave crest height before the breaking point and under-predicted the wave crest height in the surf zone. These studies proposed to model the undertow profiles, turbulence levels and turbulent characteristics for different types of breakers. However, uncertainty still exists about the relationship between the environmental parameters, characteristics and geometrical properties of wave breaking on slopes.

The purpose of the present work is to investigate the effects of water depth, offshore wave steepness, and beach slope on the characteristics and geometric properties of spilling breakers over slopes. A 3D two-phase flow CFD model solving the RANS equations is applied in a 2D

setting to simulate the breaking waves with the level set method to capture the air-water interface deformation. Although wave breaking is a 3D process, most of the physical characteristics inducing wave breaking can be obtained in detail by a 2D study. To validate the present numerical model, the results from the simulation of breaking waves over a sloping bed are compared with the experimental data by Ting and Kirby (1996). The simulated results are in good agreement with experimental measurements. The characteristics of breaking waves such as breaking location, the incipient breaker height and water depth at breaking, incipient breaker indices and geometric properties for different offshore wave steepnesses at different water depths over a wide range of beach slopes are also examined and discussed.

1.1. Wave breaking

When waves propagate from deep to shallow water, the wave motion is restricted by the change in water depth; e.g. the wave celerity is reduced. Since the wave period remains the same, the wave length becomes shorter, resulting in increased wave heights. The behavior of long waves over a sloping bed is strongly affected by the wave base, which is the depth at which the wave motion becomes negligible, i.e. the circular orbital motion decreases quickly with increasing depth (Thurman and Trujillo, 2001). The wave length influences the wave base and it is equal to one half of a wave length and thus, small steepness waves are normally long waves that have a deeper wave base. The longer the wave, the faster and longer the interaction with a sloping seabed. Many experimental, numerical, theoretical and field studies have examined the limits of the onset of wave breaking. Breaking criteria can be categorized on the basis of geometric, kinematic and dynamic breaking aspects. The geometric breaking criterion describes the limiting wave steepness in terms of wave height (H) and wave length (L), and according to Stokes (1880) wave breaking occurs when H/L reaches 0.141 and the crest angle attains 120°. Although, when a wave gains more energy and advances breaking, then the wave crest overturns and results in an asymmetric profile both horizontally and vertically (Kjeldsen and Myrhaug, 1978). Hence, the global steepness limitation is not appropriate to characterize the onset of breaking as it does not account for the local wave profile asymmetry. Kjeldsen and Myrhaug (1978) introduced steepness and asymmetry factors to describe the geometry of breaking waves: crest front steepness (ε), crest rear steepness (δ), the vertical asymmetry factor (λ) and the horizontal asymmetry factor (μ) as defined in Fig. 1. The kinematic criterion of wave breaking is that the crest particle velocity exceeds the wave celerity. The ratio of the crest particle velocity and the wave celerity is approximately 1.5 for plunging breakers and 1.0 for spilling breakers (Wu and Nepf, 2002). From a dynamic point of view, a wave breaks when the downward acceleration at the crest exceeds half of the gravitational acceleration, and when the energy variation of high frequency waves is rapid.

Predictions of wave height and water depth at breaking and breaker types are the prominent characteristics of breaking waves used to describe the maximum hydrodynamic forces on coastal structures. The breaker depth index, γ_b describes the wave height at breaking, and is defined as the ratio of the wave height H_b and the water depth at breaking d_b:

$$\gamma_b = \frac{H_b}{d_b} \tag{1}$$

The breaker height index, Ω_b is defined as the ratio of the breaker height H_b and offshore wave height H_0:

$$\Omega_b = \frac{H_b}{H_0} \tag{2}$$

1.2. Wave profile asymmetry of shallow water waves

The degree of wave asymmetry increases as the wave propagates into shallow water and it is maximum at the breaking point. Considering the nonlinear behavior of shallow water waves, i.e. the shortening of wave length and the resulting larger wave heights, the typical values for the asymmetry profile parameters in shallow water become higher than those in deep water. A symmetrical wave propagates over a slope where it undergoes deformation (shallow water steepening) due to shoaling. The crest elevation reaches the maximum value with a decrease of trough depth, thus the wave becomes steeper but symmetric in shape. Closer to breaking, the wave starts to deform. The shape of the wave is not symmetric anymore, and the face of the wave in the crest region becomes vertical, a portion of the wave surface then overturns shoreward. Peregrine et al. (1980) investigated the changes in fluid properties during overturning in three prominent regions of a forward moving water jet: high orbital velocities near the wave crest region, high accelerations on the forward face of the wave, and the low accelerations on the rear face of the wave.

Experimental and numerical studies have mainly focused on the characteristics of breaking waves in shallow waters based on the kinematic and dynamic evaluation of wave breaking. The analysis of the geometric properties of breaking waves in shallow water was initiated by Ippen and Kulin (1954). Ippen and Kulin (1954), and later by Miller and Zeigler (1964), classified the breakers as symmetric, asymmetric and intermediate based on their deformation stage during shoaling. Adeyemo (1968) examined the effect of the beach slope and the shoaling process on wave asymmetry, categorizing the wave asymmetry with three parameters: wave vertical asymmetry, wave slope asymmetry and wave horizontal asymmetry. He tested asymmetry profile parameters of breaking wave profile over six different slopes from 1/10 to 1/18 and established the correlations between these asymmetry profile parameters. Iwagaki and Sakai (1972) studied experimentally and theoretically the influence of the beach slope on the change in wave height and wave asymmetry profile during breaking. They investigated the wave transformation including wave asymmetry over slopes of 1/10, 1/20 and 1/30. Hwang (1984) investigated the application of the wave steepness and asymmetry factors introduced by Kjeldsen and Myrhaug (1978), for shoaling waves on a mild slope in order to study the evaluation of wave asymmetry in shallow waters. In fact, there are different steepness and asymmetry factors proposed by previous studies to specify the wave profile during shoaling and breaking. However, the wave steepness and asymmetric factors proposed by Kjeldsen and Myrhaug (1978) to account for the prominent features of wave asymmetry at breaking are considered in the present study.

1.3. Environmental conditions and simulation cases

Numerous experimental studies have been conducted to predict the initiation of wave breaking and the breaking process. The main intention of the present simulation cases is to examine the prominent characteristics of breaking waves including the geometry of breaking waves in order to enhance the assessment of the wave breaking mechanism for different environmental conditions. The shallow water breaking wave properties including geometric properties are largely influenced by three prominent environmental parameters; the water depth, offshore steepness and beach slope. The simulation cases consist of three main cases, A, B and C as listed in Table 1. The influence of water depth (d) during breaking over a fixed slope of 1/35 with a fixed offshore steepness of 0.02 is investigated and the wave parameters are listed in case A (A1 to A6). The intention of case B (B7 to B14) is to study the changes in wave properties with a wide range of offshore wave steepnesses (H_0/L_0) from 0.01 to 0.06 over a slope 1/35 at $d = 0.5$ m. Finally, in order to consider the effects of seabed slopes (m) on wave breaking, five seabed slopes, 1/15, 1/25, 1/35, 1/45 and 1/55 are examined. For each slope, steepnesses ranging from 0.02 to 0.06 at $d = 0.5$ m are

Table 1
List of simulation cases.

Simulation cases	Simulation no.	Surf similarity parameter, ξ	Reference water depth, d (m)	Steepness, H_0/L_0	Slope, m
Based on reference water depth (d): Case (A)	1	0.202	0.35	0.020	1/35
	2		0.40		
	3		0.45		
	4		0.50		
	5		0.55		
	6		0.60		
Based on offshore wave steepness (H_0/L_0): Case (B)	7	0.286	0.50	0.010	1/35
	8	0.233		0.015	
	9	0.202		0.020	
	10	0.181		0.025	
	11	0.165		0.030	
	12	0.143		0.040	
	13	0.128		0.050	
	14	0.117		0.060	
Based on seabed slope (m): Case (C)	15	0.471	0.50	0.020	1/15
	16	0.283			1/25
	17	0.202			1/35
	18	0.157			1/45
	19	0.128			1/55
	20	0.385		0.030	1/15
	21	0.231			1/25
	22	0.165			1/35
	23	0.128			1/45
	24	0.105			1/55
	25	0.333		0.040	1/15
	26	0.200			1/25
	27	0.143			1/35
	28	0.111			1/45
	29	0.091			1/55
	30	0.298		0.050	1/15
	31	0.179			1/25
	32	0.128			1/35
	33	0.099			1/45
	34	0.081			1/55
	35	0.272		0.060	1/15
	36	0.163			1/25
	37	0.116			1/35
	38	0.091			1/45
	39	0.074			1/55

simulated, as tabulated in case C (C15 to C39). In brief, a total of 39 cases covering a wide range of the three important parameters are investigated in the study.

2. Numerical model

2.1. Governing equations

In the present study, a 3D numerical model is employed and the RANS equations are solved together with the continuity equation for incompressible flow, prescribing mass and momentum conservation:

$$\frac{\partial U_i}{\partial x_i} = 0 \tag{3}$$

$$\frac{\partial U_i}{\partial t} + U_j \frac{\partial U_i}{\partial x_j} = -\frac{1}{\rho}\frac{\partial P}{\partial x_i} + \frac{\partial}{\partial x_j}\left[(\nu + \nu_t)\left(\frac{\partial U_i}{\partial x_j} + \frac{\partial U_j}{\partial x_i}\right)\right] + g_i \tag{4}$$

U is the velocity averaged over time t, ρ is the fluid density, P is the pressure, ν is the kinematic viscosity, ν_t is the eddy viscosity and g the acceleration of gravity term. The numerical model is used as a numerical wave tank. High-order schemes are selected for the current study to avoid unphysical damping of propagating waves. The convection term of the RANS equations is discretized with the Weighted Essentially Non-Oscillatory (WENO) scheme in the conservative finite difference version (Jiang and Shu, 1996). Here, a discretization stencil consists of three substencils, which are weighted according to the local smoothness of the discretised function. The scheme achieves a minimum of 3rd-order accuracy for discontinuous solutions, and up to 5th-order accuracy for a smooth solution. At the same time, very robust numerical stability is achieved, without the negative side effects of numerical limiters. For the time treatment, a third-order accurate total variation diminishing (TVD) Runge-Kutta scheme is employed, consisting of three Euler substeps (Shu and Osher, 1988). The pressure term is solved with the projection method (Chorin, 1968) after each of the Euler substeps for the velocities. The BiCGStab algorithm (van der Vorst, 1992) with Jacobi scaling preconditioning solves the Poisson equation for the pressure. The RANS equations are closed with the two-equation k- ω turbulence model (Wilcox, 1994), with transport equations for the turbulent kinetic energy k and the specific dissipation ω.

2.2. Numerical grid and parallelization

At the solid boundaries of the fluid domain a ghost cell immersed boundary method is employed. In this method, the solution is analytically continued through the solid boundary by updating fictitious ghost cells in the solid region through extrapolation. This way, the numerical discretization does not need to account for the boundary conditions explicitly. The algorithm is based upon the local directional approach by Berthelsen and Faltinsen (2008). With this method, complex geometries and cut cells can be accounted for. The ghost cell approach has several advantages: Grid generation becomes trivial, the numerical stability and the order of the overall scheme is not affected. In addition, the method integrates well into the domain decomposition strategy for the parallelization of the numerical model. Here ghost cells are used to update the values from the neighboring processors via MPI (Message Passing Interface).

2.3. Level set method

The main feature of breaking waves is the complex motion of the free surface. In order to account for this, the interface-capturing level set method is employed, describing the interface between the two phases water and air. With the level set method (Osher and Sethian, 1988), the location of the interface is represented implicitly by the zero level set of the smooth signed distance function $\phi\left(\vec{x}, t\right)$. In every point of the computational domain, the level set function gives the closest distance to the interface and the phases are distinguished by the change of the sign. This results in the following properties:

$$\phi\left(\vec{x}, t\right)\begin{cases} > 0 \text{ if } \vec{x} \in water \\ = 0 \text{ if } \vec{x} \in \Gamma \\ < 0 \text{ if } \vec{x} \in air \end{cases} \tag{5}$$

Also the Eikonal equation $|\nabla\phi| = 1$ is valid. When the interface is moved under an externally generated velocity field $\vec{v}$, a convection equation for the level set function is obtained:

$$\frac{\partial \phi}{\partial t} + U_j \frac{\partial \phi}{\partial x_j} = 0 \tag{6}$$

With the level set function in place, the material properties of the two phases can be defined for the whole domain. Without special treatment, there is a jump in the density ρ and the viscosity ν across the interface, which can lead to numerical instabilities. This is avoided by smoothing the material properties in the region around the interface with a regularized Heaviside function $H(\phi)$. This region is 2ϵ thick, with ϵ being proportional to the grid spacing Δx. In the present paper

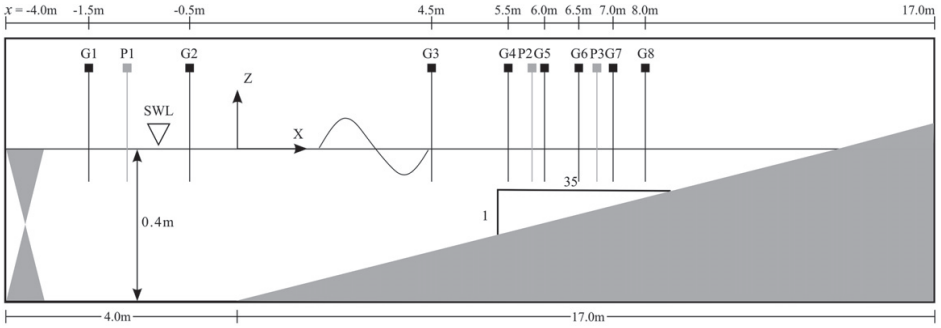

Fig. 2. Computational set-up: G1–G8 are wave gauge positions and P1–P3 are velocity probe positions.

it was chosen to be $\epsilon = 1.6\Delta x$. The density and the viscosity can then be written as:

$$\rho(\phi) = \rho_{water}H(\phi) + \rho_{air}(1-H(\phi)),$$
$$\nu(\phi) = \nu_{water}H(\phi) + \nu_{air}(1-H(\phi)) \tag{7}$$

and the regularized Heaviside function:

$$H(\phi) = \begin{cases} 0 & \text{if } \phi < -\epsilon \\ \frac{1}{2}\left(1 + \frac{\phi}{\epsilon} + \frac{1}{\pi}\sin\left(\frac{\pi\phi}{\epsilon}\right)\right) & \text{if } |\phi| < \epsilon \\ 1 & \text{if } |\phi| > \epsilon \end{cases} \tag{8}$$

2.4. Numerical wave tank

A numerical wave tank needs to generate waves at the inlet boundary and absorb waves at the outlet boundary in order to simulate the flow and free surface dynamics of a wave flume. In the present numerical model, the relaxation method is selected for the generation and absorption of waves. The relaxation method was first presented by Larsen and Dancy (1983), where the analytical solution is used to moderate the computationally generated waves. This method has been presented by Mayer et al. (1998) and Engsig-Karup (2006). The relaxation function presented by Jacobsen et al. (2012) is used in the present study. In the wave generation relaxation zone, the values for the velocities and the free surface are ramped up from the computational values to the the values obtained by wave theory. This generates high quality waves and reflections traveling towards the generation zone are effectively absorbed. In the numerical beach relaxation zone, the computational values for the velocities are smoothly reduced to zero, the free surface modulated to the still water level and the pressure to the according hydrostatic distribution. In the current case of the sloping beach, the relaxation zone for the numerical beach is not employed.

3. Results and discussion

3.1. Comparison of experimental measurements and numerical model results

3.1.1. Computational set-up

The numerical experiment of breaking waves on a sloping bed is carried out in the numerical wave tank in a 2D setting, allowing for more computationally efficient simulations. To verify the performance of the numerical model, the simulated results are compared with the experimental data for the spilling breaker case from the physical model test reported by Ting and Kirby (1996). The present numerical set up and the wave parameters resemble the experimental conditions given by Ting and Kirby (1996). The numerical wave tank consists of a 4 m long horizontal bed with the constant water depth of 0.4 m, followed by a slope 1/35 as shown in the Fig. 2. The coordinate system is the same as in the experimental study. The water surface elevation and the kinematics in the wave generation zone are specified using the 5th-order cnoidal wave theory presented by Fenton (1999). The

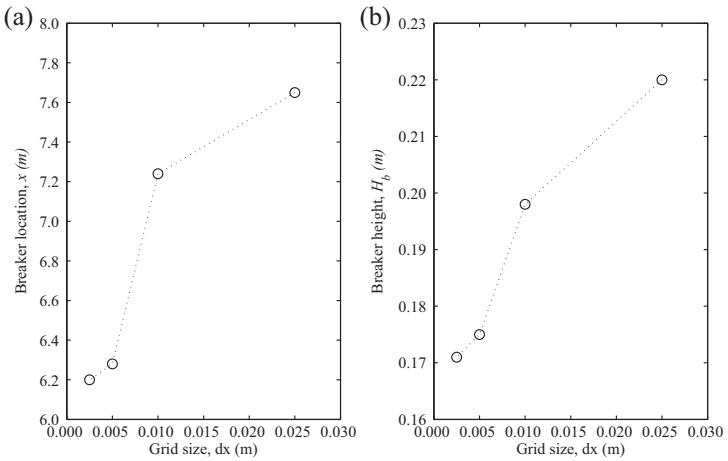

Fig. 3. Grid refinement study on simulated results (a) breaker location (x) and (b) breaker height (H_b).

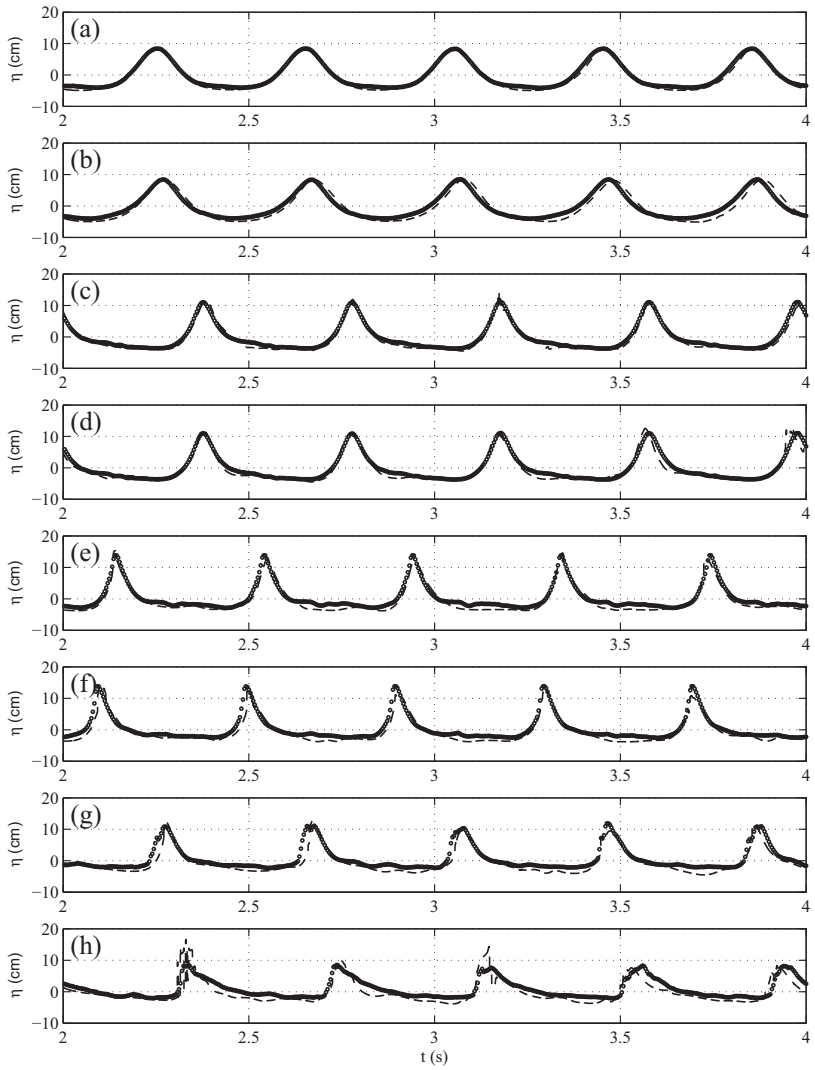

Fig. 4. Comparison of computed and measured water surface elevations for spilling breaker case at $x = -1.5$ m (a), -0.5 m (b), 4.5 m (c), 5.5 m (d), 6.0 m (e), 6.5 m (f), 7.0 m (g) and 8.0 m (h). Dashed lines: present numerical model; circles/full line: experimental data from Ting and Kirby (1996).

incident wave height and period of the Cnoidal waves are $H = 0.125m$ and $T = 2.0s$ in the horizontal bed region. The instantaneous free surface elevations and horizontal velocities are calculated using wave gauges and velocity probes at several locations identical with the experimental positions along the wave tank. The computational domain is discretized with a uniform grid size in both directions x and y. The length of the simulation in the present study is 25 s in order to achieve a quasi-steady state for the mean quantities, and the mean wave quantities are calculated from the last five waves.

3.1.2. Grid refinement study

The effect of the grid size on the numerical simulation of breaking waves are investigated with four different grid sizes $dx = 0.025$ m, $dx = 0.01$ m, $dx = 0.005$ m and $dx = 0.0025$ m. The breaking location and the breaker height are considered to examine the grid convergence through comparison with the experimental breaking location, $x_b = 6.4$ m and breaker height, $H_b = 0.163$ m as shown in Fig. 3(a) and (b), respectively. On coarser grid sizes $dx = 0.025$ m and $dx = 0.01$ m, the wave breaks later shoreward with higher breaker height than in the experiments. Although the results of the finer grids are in good agreement with the experimental data at the breaking point, the grid size $dx = 0.005$ m with 808614-number of grid cells is chosen for the present study since the difference between 0.0025 m and 0.005 m is negligible as shown in Fig. 3 and the computational time is extremely high for the $dx = 0.0025$ m with 3234513-number of grid cells.

3.1.3. Wave breaking over a sloping bed

The simulated results are compared with the experimental measurements for spilling breakers. The comparison of simulated and measured instantaneous free surface elevations for eight wave gauges along the wave tank is shown in Fig. 4. The eight wave gauges (G1–G8) are positioned at $x = -1.5$ m, -0.5 m, 4.5 m, 5.5 m, 6.0 m, 6.5 m, 7.0 m and 8.0 m from the toe of the slope (see Fig. 1) to evaluate the performance

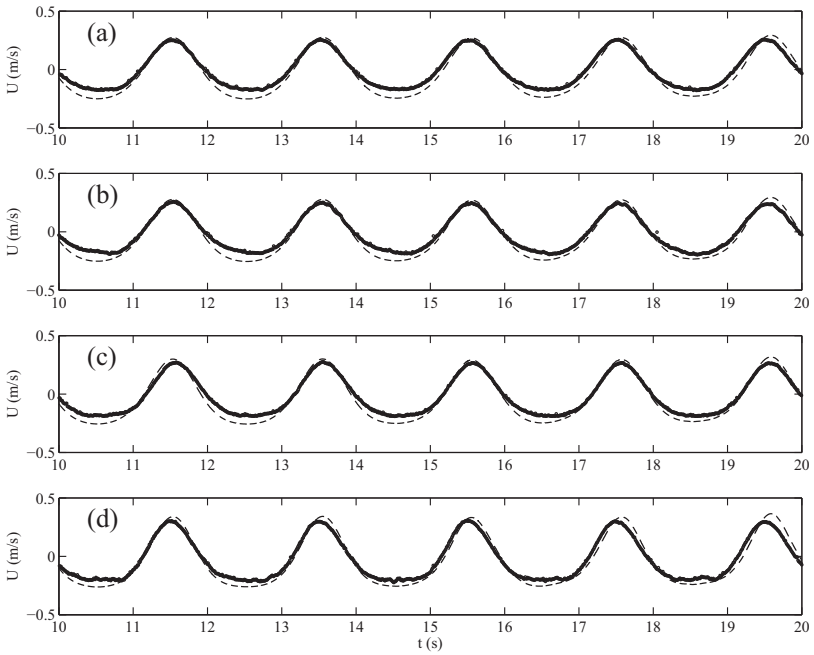

Fig. 5. Comparison of computed and measured horizontal velocities for spilling breaker case at $x = -1.265$ m and $z = -0.36$ m (a), -0.30 m (b), -0.20 m (c) and -0.10 m (d). Dashed lines: present numerical model; circles/full line: experimental data from Ting and Kirby (1996).

of the numerical model on predicting the complete wave transformation process from wave generation, shoaling and onset of wave breaking to post-breaking.

It is observed that the wave height increases and the trough flattens as the wave advances over the sloping bed. In fact, the crest becomes shorter and steeper and the trough becomes longer and flatter as the

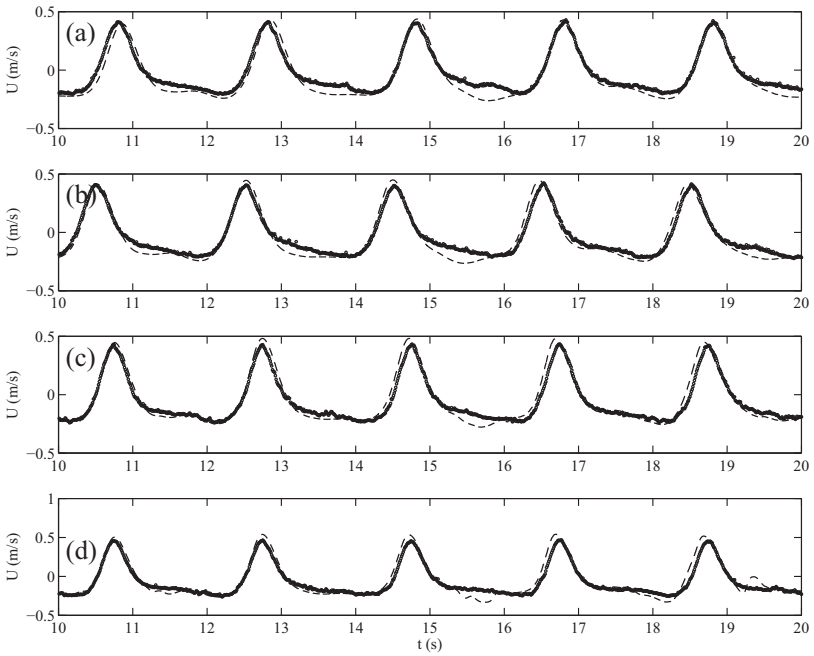

Fig. 6. Comparison of computed and measured horizontal velocities for spilling breaker case at $x = 5.945$ m and $z = -0.18$ m (a), -0.15 m (b), -0.10 m (c) and -0.05 m (d). Dashed lines: present numerical model; circles/full line: experimental data from Ting and Kirby (1996).

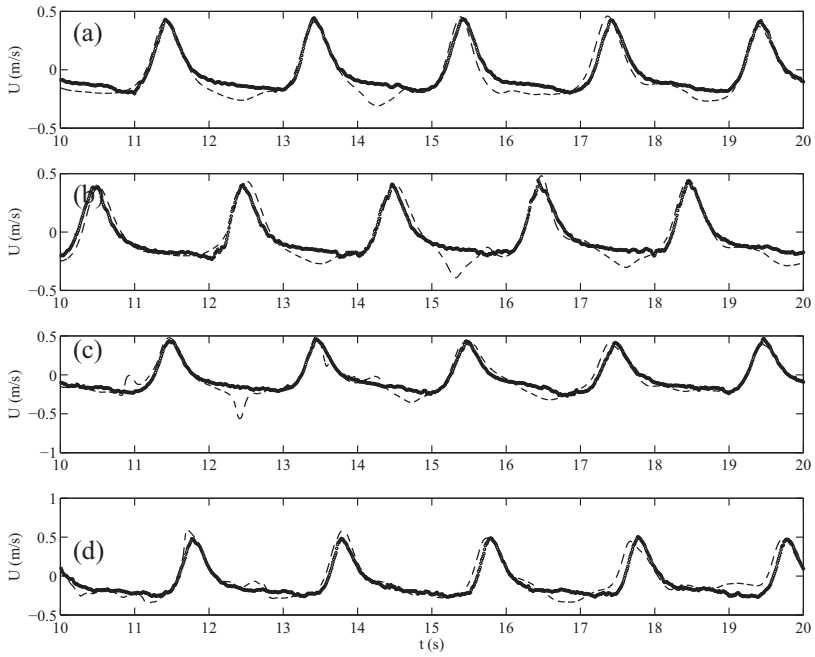

Fig. 7. Comparison of computed and measured horizontal velocities for spilling breaker case at $x = 6.665$ m and $z = -0.17$ m (a), -0.15 m (b), -0.10 m (c) and -0.05 m (d). Dashed lines: present numerical model; circles/full line: experimental data from Ting and Kirby (1996).

water depth decreases in order to maintain the constant energy flux during the shoaling process. Further, the momentum and energy in the vicinity of the wave crest increase as the shoaling proceeds until the wave crest reaches a maximum height and the wave front becomes almost vertical and eventually breaks at $x_b = 6.28$ m. Thus, the numerical waves break at almost the same location as the experimental waves at $x_b = 6.4$ m. Finally, the wave height decreases after breaking as the waves propagate further over the slope. The simulated free surface elevations exhibit the typical behavior of the cnoidal waves on sloping beds (non-linear shallow water waves). Moreover, the numerical prediction of free surface elevations is also in good agreement with the experimental measurements in all the regions from the wave generation region to the post-breaking region.

The horizontal velocity variations over depth are measured using velocity probes at three different locations (P1–P3): in the wave generation region ($x = -1.265$ m), before ($x = 5.945$ m) and after ($x = 6.665$ m) breaking are shown in Figs. 5, 6 and 7 respectively. It is observed that the horizontal velocities are higher in the vicinity of the wave crest near the free surface (Fig. 5(d)) and decrease away from the free surface (Fig. 5(a)). Fig. 7 shows that the computed horizontal velocities at x = 6.665 m are in the post breaking region. The crest velocities agree well with the experimental data, but some short downspikes are observed in the trough region. The reason for the short downspikes in the trough portion is unclear but this might be related to the interaction of active turbulence with air entrainment which affects the dissipation of energy in the surf zone. As the main intention of the study is to investigate the effect of environmental parameters on breaking characteristics, the air entrainment and associated processes are not investigated in details further. Moreover, during breaking the large fluid flow structures degenerate into smaller flow structures with air entrainment and extreme turbulent behavior. It is therefore intricate to measure and calculate the horizontal velocity in this region. The velocities increase as the wave approaches the slope until breaking as shown in Figs. 6(a) and 7(a). Overall, the wave height and the velocity increase and the wave length decreases as the waves shoal over the slope, thus a further increase in the wave height causes the fluid particles to move faster than the wave celerity and eventually breaking occurs. From the simulated results it is evident that the present

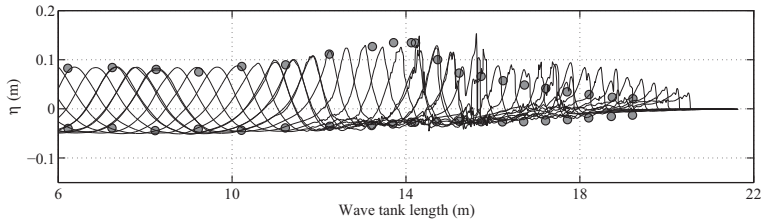

Fig. 8. Comparison of computed and measured envelope of water surface elevation for spilling breaker case. Solid lines: the present numerical model; circles: experimental data from Ting and Kirby (1996).

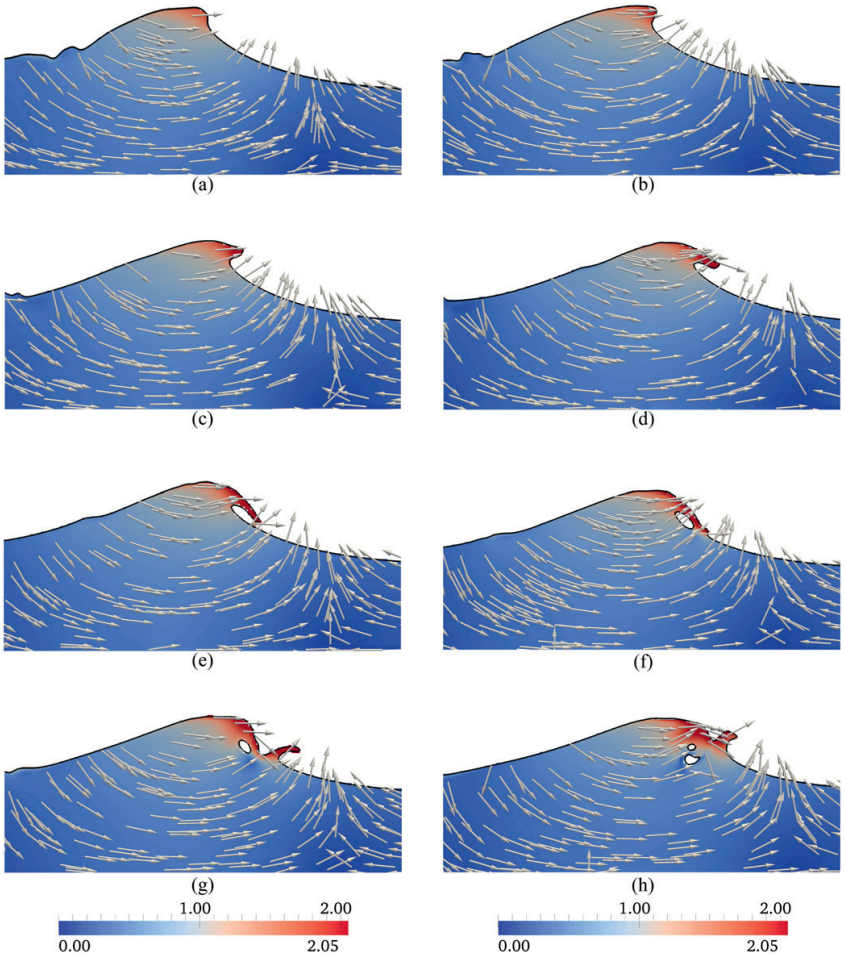

Fig. 9. Computed wave profile with the velocity (m/s) variation during the wave breaking process of the spilling breaker (from (a) to (h)).

numerical model is able to predict the trend of the horizontal velocity variation versus the depth and the tank length quite well. The simulation results are also consistent with the experimental results.

Fig. 8 shows comparison of the measured and simulated distribution of wave amplitudes. The wave height increases as the waves traverse over the slope until breaking occurs, and the wave height diminishes shoreward after breaking. The wave height reaches the maximum before breaking and the waves break at $x_b = 6.28$ m; thus the numerical waves break close to the measured breaking point at $x_b = 6.4$ m. Moreover, the present model yields a good prediction of shoaling wave heights, wave crest and trough heights in the breaker zone (before breaking and at breaking). In the surf zone, the present model slightly overestimates the wave crest but yields a good prediction of the wave troughs. The reason for the over-prediction of the wave crest in the surf zone is not clear, though it might be related to the slower numerical dissipation of energy than in the experiments.

3.1.4. Breaking process

Fig. 9 presents the change in the wave surface profile and the velocity distribution near the breaking region at different stages of the breaking process. The velocity of the displacement of fluid particles in the wave depends on the wave amplitude. The sequence of the breaking process evolution depicts the mixing of air and water and the return velocity from the slope during breaking. It is noticed that the onset of wave breaking is associated with a small water jet at the wave crest for spilling breakers. As presented in the Section 3.1.3, the particle velocity increases near the wave crest as the wave propagates over the slope and the wave celerity is reduced. When the wave advances over the slope, it becomes higher due to shoaling; the potential energy increases and accordingly, the wave crest particle velocity. When the crest particle velocity exceeds the wave celerity, it leads to an overturning motion of the wave crest with the forward ejection of a small scale water jet similar to that developed for a plunging breaker. The simulated topological features of spilling breakers are consistent with those of other studies (Duncan, 2001; Lader, 2002; Lubin et al., 2011). In fact, the particles close to crest with higher amplitudes propagate faster, thus the steepness of the wave is enhanced and the wave profile is continuously deformed. At a certain point the wave crest falls down and hits the water surface with the forward wave front enclosing a pocket of air as shown in Fig. 9 (f), the so-called splash-up phenomenon. Consequently, the impact of the jet with a pocket of air on the surface generates another forward upstream jet with a cavity of air as seen in Fig. 9 (g), thus drastic flow circulation is created immediately.

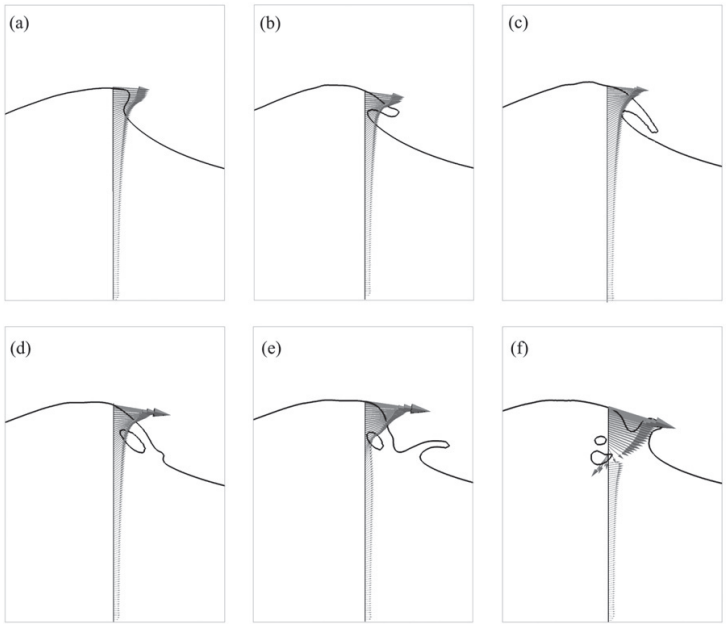

Fig. 10. Computed velocity profile during the wave breaking process of the spilling breaker (from (a) to (f)).

Fig. 10 presents the vertical variation of the velocity over the depth with maximum velocity at the wave crest front and changes in the velocity at the wave crest during breaking. The velocity profile close to wave crest becomes wider as the water jet grows faster. It can be seen from Figs. 9 and 10, that initially the particle velocities at the interface are almost equal and directed horizontally. As the wave grows further, the particles with higher velocities move forward with the ejected wave front. It is also observed, that the particle velocities are higher in the breaking region. The velocity vectors are focused close to the wave crest and thus, a portion of the wave crest that has higher velocities overturns and impinges the water surface. A topology induced vorticity is created and the jet impingement modifies the flow pattern, which is responsible for the production of turbulence and vorticity at the free surface. The numerical model can simulate the flow pattern during wave breaking including the displacement of the air pocket as shown in Fig. 10.

3.2. Prediction of breaking wave characteristics

As presented in Section 1.3, simulations are performed for the runs given in Table 1. Incipient breaking can be defined based on kinematic, geometric and dynamic breaking criteria. However, there are two

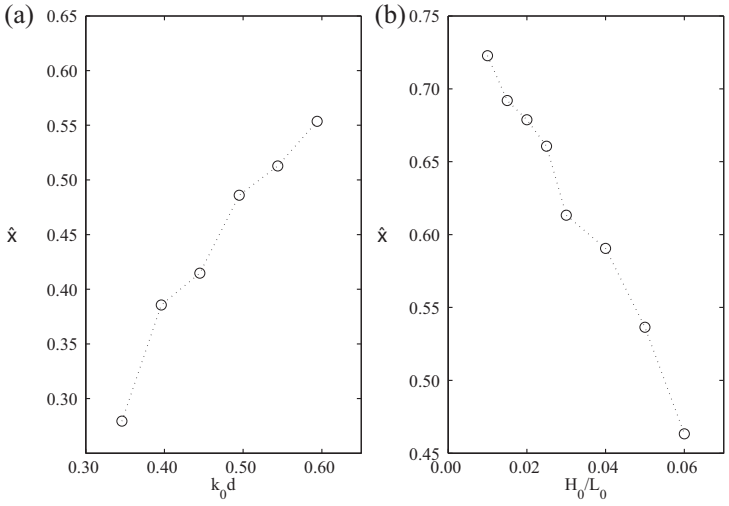

Fig. 11. Computed non-dimensional breaker location ($\hat{x}$) as a function of (a) non-dimensional water depth ($k_0 d$) and (b) offshore wave steepness (H_0/L_0).

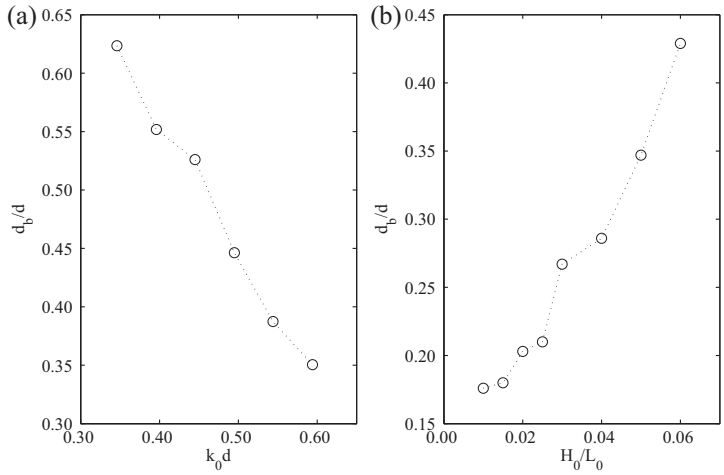

Fig. 12. Computed relative water depth at breaking (d_b/d) as a function of (a) non-dimensional water depth ($k_0 d$) and (b) offshore wave steepness (H_0/L_0).

breaking conditions that are considered for spilling breakers in the study. Firstly, the breaking point is defined as the point where most of the wave front becomes vertical, and secondly, the point where the water starts falling down at the wave front. The assessment of the breaker height, water depth at breaking, location of breaking point and wave steepness and asymmetry factors are indicated in Fig. 1. The breaker location (x) is measured from the toe of the slope and the breaker water depth d_b is measured from the still water level at which wave breaking occurs.

3.2.1. Onset of wave breaking

The breaker location is presented in the non-dimensional form, $\hat{x} = x/L$ from the toe of the slope ($x = 0$) to the end of the slope ($x = L$). Figs. 11(a) and 12(a) present the non-dimensional breaker location ($\hat{x}$) and the non-dimensional breaker depth (d_b/d), respectively, versus the non-dimensional water depth ($k_0 d$). It appears that $\hat{x}$ increases and d_b/d decreases almost linearly as $k_0 d$ increases for cases A1 to A6 (see Table 1), i.e. the shallower the reference water depth (d), the larger the breaker water depth (d_b). This implies that the wave profile has sufficient time to alter the equilibrium profile to the proximity water depth. Moreover, it deforms later as d increases. A wave with a given offshore steepness (H_0/L_0) breaks further shoreward as d increases (case A6), corresponding to $d_b/d = 0.350$, $k_0 d = 0.595$ in Fig. 12(a). Figs. 11(b) and 12(b) show the non-dimensional breaker location ($\hat{x}$) and the breaker depth (d_b/d), respectively, versus the offshore steepness (H_0/L_0). It appears that $\hat{x}$ decreases and d_b/d increases as H_0/L_0 increases for cases B7 to B14. When a wave advances over a given slope and reference water depth, the height of the wave increases and the length of the wave decreases as the wave shoals and consequently, a small increase in wave height causes waves with larger H_0/L_0 to reach the breaking point sooner than waves with small H_0/L_0. Hence, x moves shoreward and d_b becomes shallower as H_0/L_0 decreases. Fig. 13 shows $\hat{x}$ versus the surf similarity parameter ($\xi = \frac{m}{\sqrt{H_0/L_0}}$) for different slopes (cases C15–C39). It appears that $\hat{x}$ increases as ξ increases for a given slope, and that the $\hat{x}$ versus ξ dependence decreases as the slope increases.

The wave shoaling distance over steep slopes is shorter than on milder slopes due to the wave base effect, implying that significant partial reflection from the steep slope during shoaling causes wave breaking earlier on steeper slopes (Grilli et al., 1995; Tsai et al., 2005). Moreover, the reflection coefficient of waves on sloping sea beds can be calculated using an empirical formula proposed by Battjes (1974):

$$K_r = 0.1\xi \tag{9}$$

where K_r is the reflection coefficient. It is noticed from the above equation that long waves would experience more reflection than short waves. Although waves are reflected from the beach, this does not

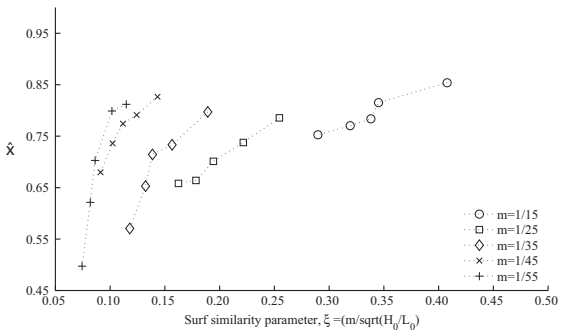

Fig. 13. Computed non-dimensional breaker location ($\hat{x}$) as a function of surf similarity parameter (ξ) for different slopes.

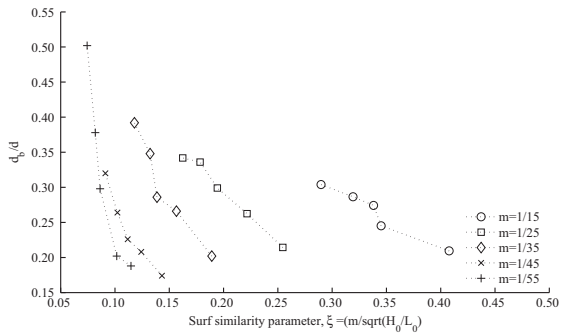

Fig. 14. Computed relative water depth at breaking (d_b/d) as a function of surf similarity parameter (ξ) for different slopes.

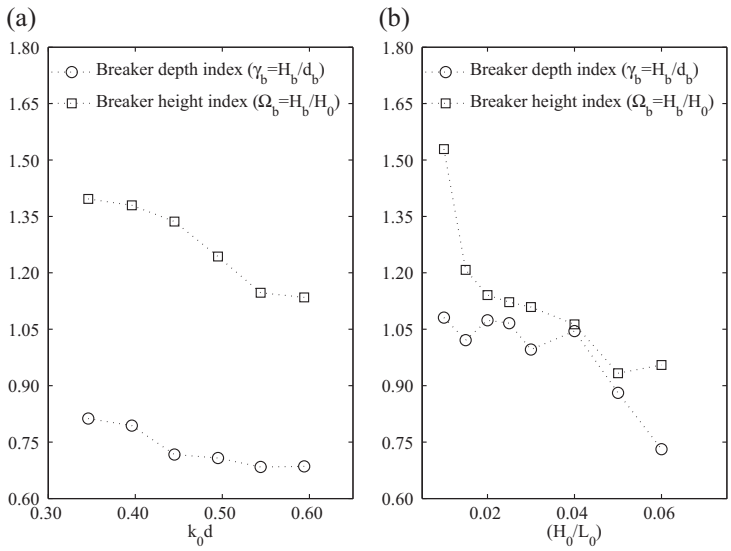

Fig. 15. Breaker depth index (γ_b) and breaker height index (Ω_b) as a function of (a) non-dimensional water depth (k_0d) and (b) offshore wave steepness (H_0/L_0).

mean that all of the wave energy is reflected back, hence partially reflected waves may contribute to amplify the incident wave height, depending on the period and phase of the reflected wave. Hence, wave reflection and the effect of reflection increase with steeper seabed slopes, as studied experimentally and theoretically by Tsai et al. (2005).

Fig. 14 presents d_b/d versus ξ for different slopes. It appears that d_b/d decreases as ξ increases, and that the d_b/d versus ξ dependence decreases as the slope increases. This also means that d_b/d increases with slopes for $H_0/L_0 = 0.02$ to 0.04 (cases C15 to C29) and that d_b/d decreases with slopes for $H_0/L_0 = 0.05$ and 0.06 (cases C30 to C39). A possible explanation for this might be that the partial wave reflection and shoaling effect increase with the slope for $H_0/L_0 = 0.02$ to 0.04 and these effects enhance the steepening of the local wave slope, therefore waves break offshore at higher d_b over steeper slopes. In the case of $H_0/L_0 = 0.05$ and 0.06, the wave shoaling rate is higher for milder slopes and thus the wave breaks sooner. Therefore it is possible that waves with larger H_0/L_0 break earlier at higher d_b on milder slopes. This is in agreement with the theoretical study by Iwagaki and Sakai (1972) and the numerical study by Grilli and Horrillo (1997). They reported that the shoaling rate is lower for steeper slopes than for milder slopes. On steeper slopes, the wave height does not change much under shoaling, until the wave experiences the partial wave reflection from the slope, resulting in a delay of wave breaking.

3.2.2. Breaker depth index (γ_b) and breaker height index (Ω_b)

The breaker height (H_b) and the water depth at breaking (d_b) are calculated from the numerical evaluation of the wave surface elevation. Fig. 15(a) shows the breaker depth index ($\gamma_b = H_b/d_b$) and the breaker height index ($\Omega_b = H_b/H_0$) versus the non-dimensional water depth (k_0d) (cases A1 to A6). It appears that γ_b and Ω_b reduce as d increases. For a given offshore steepness and slope, H_b decreases as the wave shoals for larger reference water depth (d). Thus, these results suggest that waves advancing over shallower d experience more shoaling and break sooner at larger d_b, corresponding to $\dot{x} = 0.280$, $k_0d = 0.34$ in Fig. 11(a) and $d_b/d = 0.62$, $k_0d = 0.34$ in Fig. 12(a). The prediction of this non-linear behavior of waves is also reported in the study by Iwagaki and Sakai (1972). Moreover, the wave celerity is directly proportional to the square root of the water depth in shallow water. Another possible explanation for this is that a wave propagating from larger d, needs to propagate further shoreward until the breaking point at which the orbital velocity overcomes the celerity of the wave.

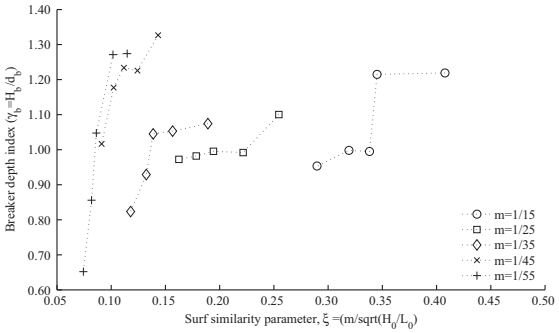

Fig. 16. Breaker depth index (γ_b) as a function of surf similarity parameter (ξ) for different slopes.

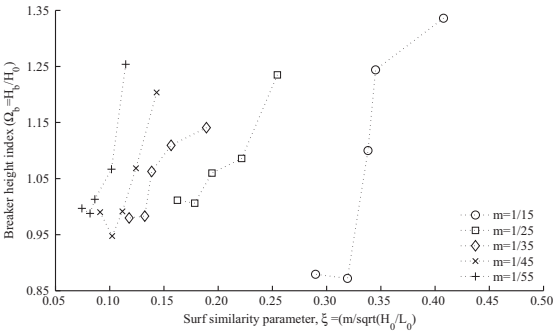

Fig. 17. Breaker height index (Ω_b) as a function of surf similarity parameter (ξ) for different slopes.

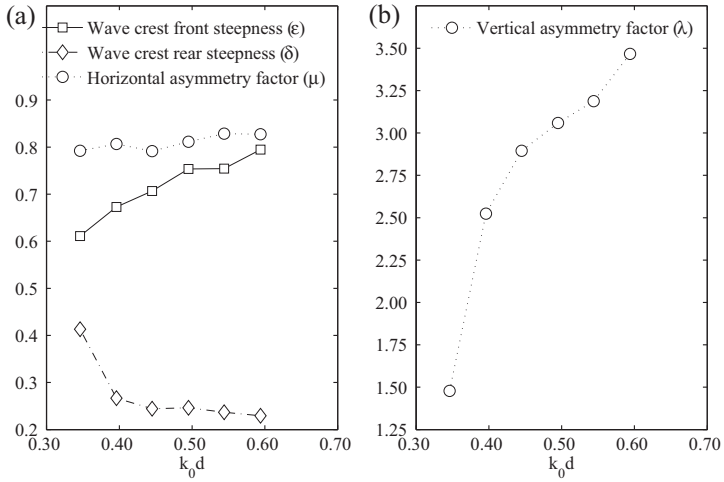

Fig. 18. Computed wave steepness and asymmetry factors for different non-dimensional water depth (k_0d).

Fig. 15(b) shows the breaker depth index (γ_b) and the breaker height index (Ω_b) versus H_0/L_0 (cases B7 to B14). It appears that γ_b and Ω_b decrease with increasing H_0/L_0. The reduction in H_b with increasing H_0/L_0 shows that the wave with larger H_0/L_0 advancing over a slope breaks earlier (i.e. further offshore) during shoaling at larger d_b, corresponding to case B14, $\dot{x} = 0.46$, $H_0/L_0 = 0.06$ in Fig. 11(b) and $d_b/d = 0.43$, $H_0/L_0 = 0.06$ in Fig. 12(b). In the same way, waves with low H_0/L_0 propagate further up on the slope and break at shallower d_b corresponding to case B7, $\dot{x} = 0.72$, $H_0/L_0 = 0.01$ in Fig. 11(b) and $d_b/d = 0.17$, $H_0/L_0 = 0.01$ in Fig. 12(b). This is consistent with the study by Grilli et al. (1995).

Figs. 16 and 17 present the breaker depth index (γ_b) and the breaker height index (Ω_b), respectively, versus the surf similarity parameter (ξ) for different slopes. Overall it appears that γ_b and Ω_b increase as ξ increases for a given slope. This also means that at a given water depth, γ_b decreases and Ω_b increases with slopes for $H_0/L_0 = 0.02$ to 0.04 (cases C15 to C29) and γ_b increases and Ω_b decreases with slopes for $H_0/L_0 = 0.05$ and 0.06 (cases C30 to C39). Thus these results suggest that the waves break further shoreward at shallower d_b with an increase in H_b under shoaling, resulting in higher γ_b on milder slopes, i.e. corresponding to case C19, $\xi = 0.128$ and $\dot{x} = 0.81$ (Fig. 13), $d_b/d = 0.19$ (Fig. 14), $\gamma_b = 1.29$ (Fig. 16), $\Omega_b = 1.25$ (Fig. 17). This variation over milder slopes suggests that the smaller the offshore wave steepness, the larger the deformation. This is consistent with the numerical study on breaking characteristics for solitary waves on slopes by Grilli and Horrillo (1997). It seems that the increase of Ω_b with steeper slopes is due to the effect of partial reflection being more pronounced on steeper slopes during shoaling. The waves with larger H_0/L_0 on milder slopes undergo more shoaling and experience almost no reflection, thus higher γ_b and d_b/d are obtained than for waves on steeper slopes, corresponding to case C39 ($\xi = 0.074$, $\Omega_b = 1.0$, $d_b/d = 0.5$; Fig. 17 and Fig. 14) and C35 ($\xi = 0.272$, $\Omega_b = 0.879$, $d_b/d = 0.32$; Fig. 17 and Fig. 14). Moreover, the results suggest that the breaker depth index (γ_b) is more influenced by the water depth at breaking (d_b) than by the breaker height (H_b). Interestingly, the variation of H_b on slopes is mainly influenced by wave

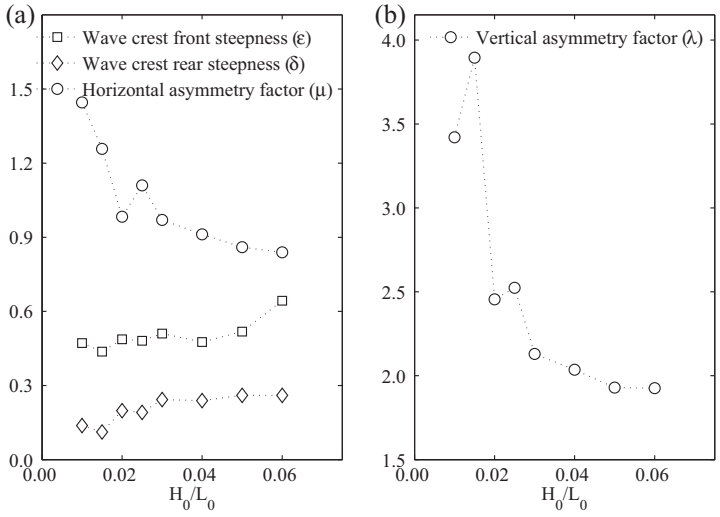

Fig. 19. Computed wave steepness and asymmetry factors for different offshore wave steepness (H_0/L_0).

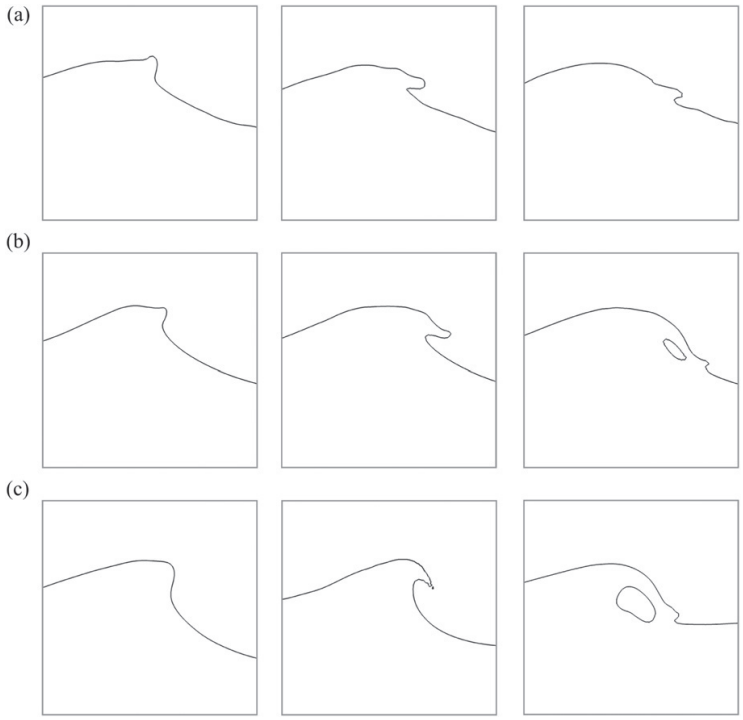

Fig. 20. Wave profile during breaking process for different slopes and offshore wave steepness: (a) $m = 1/55$ and $H_0/L_0 = 0.06$, (b) $m = 1/15$ and $H_0/L_0 = 0.06$ and (c) $m = 1/15$ and $H_0/L_0 = 0.02$.

shoaling on milder slopes and by partial reflections on steeper slopes. It is therefore reasonable to consider the combined effect of shoaling and partial reflections on breaking over steep slopes. To the present authors knowledge no data exist in the open literature on the behavior of waves on different slopes. Although previous studies have reported partial reflection on steeper slopes (Grilli et al., 1995; Schultz et al., 2006; Tsai et al., 2005; Walker and Headland, 1982), this effect has not been described based on the relationship between H_0/L_0 and H_b over moderate slopes.

3.2.3. Geometric properties of breaking waves

The steepness and asymmetry factors introduced by Kjeldsen and Myrhaug (1978) defined in Fig. 1 are used to describe wave asymmetry at the onset of wave breaking. Fig. 18 shows the crest front steepness (ε), the crest rear steepness (δ), the horizontal asymmetry factor (μ) and the vertical asymmetry factor (λ) versus the non-dimensional water depth ($k_0 d$) for cases A1 to A6. It appears that ε, λ and μ increase whereas δ decreases with increasing $k_0 d$. It is observed that the dependence of μ on $k_0 d$ seems to be very weak. Thus, waves from larger d propagates further up the slope and reach the breaking point at smaller d_b with steeper crest, corresponding to $k_0 d = 0.59$ (case A6), and $\dot{x} = 0.56$ (Fig. 11(a)), $d_b/d = 0.35$ (Fig. 12(a)), $\varepsilon = 0.79$ (Fig. 18(a)) and $\lambda = 3.5$ (Fig. 18(b)). This implies that the wave front becomes vertical, overturns and ejects forward at the breaking point as the reference water depth increases. Accordingly, the degree of asymmetry increases with increasing water depth.

Fig. 19 shows the crest front steepness (ε), the crest rear steepness (δ), the horizontal asymmetry factor (μ) and the vertical asymmetry

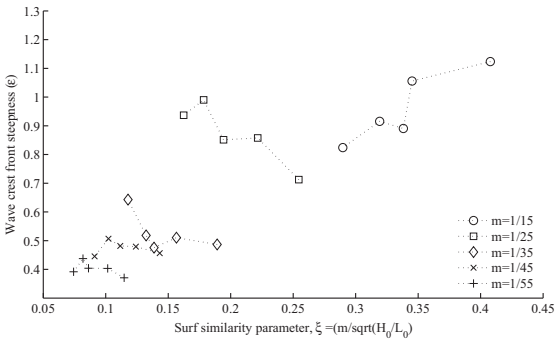

Fig. 21. Computed crest front steepness (ε) as a function of surf similarity parameter (ξ) for different slopes.

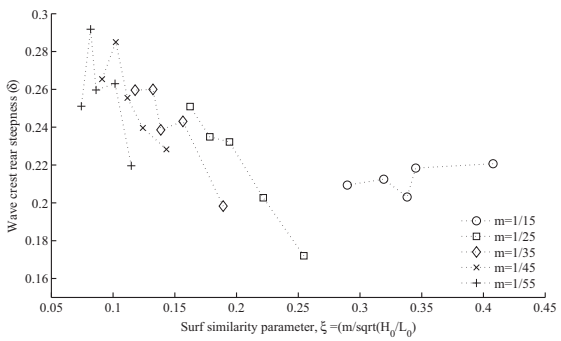

Fig. 22. Computed crest rear steepness (δ) as a function of surf similarity parameter (ξ) for different slopes.

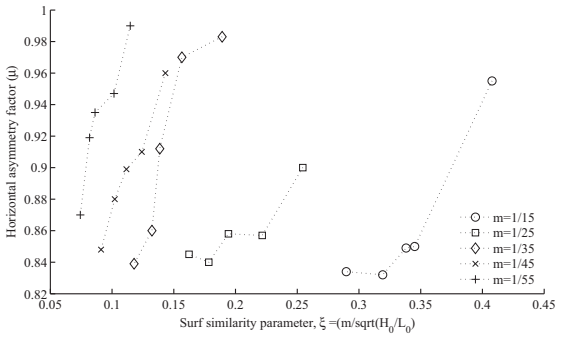

Fig. 23. Computed horizontal asymmetry factor (μ) as a function of surf similarity parameter (ξ) for different slopes.

factor (λ) versus H_0/L_0 for cases B7 to B14. It appears that ε and δ increase whereas λ and μ decrease with increasing H_0/L_0. The results imply that waves with high H_0/L_0 propagating over a slope, do not change much from their initial geometry since they break further offshore at higher d_b with lower Ω_b, corresponding to $H_0/L_0 = 0.06$ (case B14) and $\hat{x} = 0.46$ (Fig. 11(b)), $d_b/d = 0.43$ (Fig. 12(b)), $\Omega_b = 0.95$ (Fig. 15(b)). This suggests that the geometry of waves with large H_0/L_0 has a high and steep wave front and wide rear part with a lower wave trough, corresponding to $\varepsilon = 0.64$, $\delta = 0.27$, $\mu = 0.86$ and $\lambda = 1.93$ in Fig. 19. The degree of horizontal and vertical asymmetry decreases with increasing deep water steepness.

Fig. 20 shows the wave profile changes during the breaking process for different slopes. Figs. 21 and 22 show the crest front steepness (ε) and the crest rear steepness (δ), respectively, versus the surf similarity parameter (ξ) for different slopes for cases C15 to C39. It appears that ε and δ decrease as ξ increases for a given slope (except for $m = 1/15$), while for $m = 1/15$ (cases C15, C20, C25, C30, C35), ε and δ increase as ξ increases. This is consistent with the previous results for different H_0/L_0 as shown in Fig. 19. The changes in ε and δ for $m = 1/15$ are most probably due to partial reflections from the slope as discussed in Sections 3.2.1 and 3.2.2. Moreover, the wave with $H_0/L_0 = 0.02$ on the slope $m = 1/15$ (case C15) has the highest value of Ω_b, corresponding to $\xi = 0.47$, $\Omega_b = 1.33$ in Fig. 17. The surf similarity parameter of case C15 is 0.47, which is very close to the plunging breaker value of 0.5. Additionally, the wave profile geometry of case C15 also looks more like a plunging breaker, as presented in Fig. 20 (c). This is consistent with the experimental investigation of breaking waves by Lader et al. (2000). Overall, for a given H_0/L_0, ε increases and δ decreases as ξ increases. It is also noticed that the ε versus ξ dependence reduces as the seabed slope reduces.

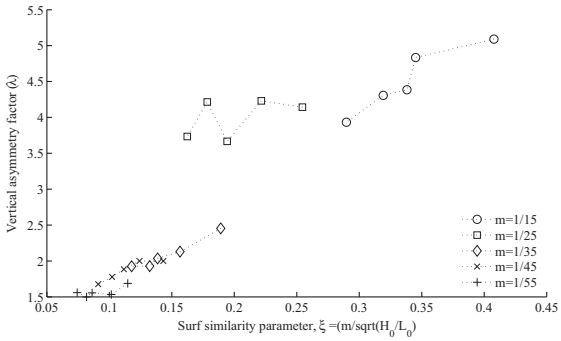

Fig. 24. Computed vertical asymmetry (λ) as a function of surf similarity parameter (ξ) for different slopes.

Figs. 23 and 24 show the horizontal asymmetry factor (μ) and the vertical asymmetry factor (λ), respectively, versus the surf similarity parameter (ξ) for different slopes. It appears that μ and λ increase as ξ increases for a given slope, which is consistent with the previous results for different H_0/L_0 as shown in Fig. 19. It is also noticed that the λ versus ξ dependence decreases as the seabed slope decreases. At breaking, a wave with large H_0/L_0 propagating over a steep slope has a high and steep wave crest (i.e. large ε and μ; low δ and λ). This is clearly demonstrated in Fig. 20 (b), corresponding to $\xi = 0.272$ (case C35) and $\varepsilon = 0.82$ (Fig. 21), $\delta = 0.21$ (Fig. 22), $\mu = 0.83$ (Fig. 23), $\lambda = 3.93$ (Fig. 24). Moreover, at breaking, a wave with large H_0/L_0 propagating over a milder slope has a small portion of ejecting wave front at the crest with low crest rear steepness and a shallower wave trough as shown in Fig. 20 (a), corresponding to $\xi = 0.074$ (case C39) and $\varepsilon = 0.39$ (Fig. 21), $\delta = 0.25$ (Fig. 22), $\mu = 0.87$ (Fig. 23) and $\lambda = 1.56$ (Fig. 24). Overall, the present results of the geometrical features of spilling breakers at breaking appear to be consistent with those obtained in previous studies (Duncan, 2001; Iwagaki and Sakai, 1972; Lader, 2002).

4. Conclusions

The simulation of wave shoaling and wave breaking over a sloping seabed has been performed with a two-phase flow CFD model based on the RANS equations coupled with the level set method and the $k-\omega$ turbulence model. The computed horizontal velocities and free surface elevations were compared with experimental measurements by Ting and Kirby (1996). The comparisons give good agreement between the computed results and the measured data, showing that the model can describe the wave breaking process over a slope with reasonable accuracy.

A series of numerical experiments are conducted to examine the effects of water depth, offshore wave steepness and beach slope on the characteristics and geometric properties of spilling breakers over slopes. The following conclusions can be drawn from the computational results for the different cases:

4.1. Characteristics of breaking waves

- For a given offshore wave steepness and reference water depth, the wave shoaling distance on steeper slopes is shorter, enhancing the breaking process; the waves break further offshore as the beach slope increases.
- Waves propagating over shallower reference water depth are subject to higher shoaling, break earlier at larger water depth with larger breaker height than for waves over larger reference water depth. Consequently, the breaker depth index and the breaker height index decrease with increasing reference water depth.
- For a given slope and reference water depth, waves with low offshore steepness break further shoreward at shallower water depths with larger breaker height index. Therefore the breaker depth index and the breaker height index decrease with increasing offshore steepness.
- The water depth at breaking over different slopes is very sensitive to the offshore wave steepness. The shoaling rate and the partial reflections from the beach slope influence the wave breaking process. Waves with low offshore steepness over steeper slopes experience more reflections from the slope, thus the wave breaking occurs further offshore at higher water depths. On the other hand, waves with larger offshore steepness experience higher shoaling rate on milder slopes, thus the wave breaking occurs earlier than on steeper slopes.
- For wave breaking over steeper slopes, waves with low offshore steepness are greatly influenced by the partial reflection from the slope, and break faster with a higher breaker height. At the same time, waves with larger offshore steepness break shoreward at shallower water depths with lower breaker heights. The present results show that the breaker height is determined by the partial reflection on steeper slopes and by the shoaling rate on milder slopes. In

fact, the breaker depth index over slopes is affected more by the water depth at breaking than by the breaker height.

4.2. Geometric properties of breaking waves

- The forward face of the wave front tends to be steeper and the rear steepness of the wave crest reduces as the reference water depth increases. Hence, the degree of asymmetry is larger and waves deform more for a larger reference water depth.
- The horizontal asymmetry and vertical asymmetry factors decrease, whereas the crest front and crest rear steepnesses increase as the offshore steepness increases. This suggests that the low offshore steepness waves are subject to more crest and trough deformation, with an overturning crest that resembles the development of plunging breakers, while waves with larger offshore steepness experience a smaller wave crest and trough deformation.
- The wave crest front steepness and the vertical asymmetry factor increase and the wave crest rear steepness and horizontal asymmetry factor decrease as the seabed slope increases. The changes in the wave asymmetry indicate that the wave front becomes vertical, the wave trough becomes deeper and the crest rear steepness of wave crest decreases as the seabed slope increases. The waves on milder slopes experience more crest deformation with an ejected wave front and a shallower trough.

Acknowledgment

The first author wishes to express his gratitude to the late Prof. Geir Moe and the late Prof. Alf Tørum for their support. The authors would like to thank Dr. James Kirby and Dr. Francis Ting for sharing the experimental data. The authors wish to acknowledge support from the Norwegian Research Center for Offshore Wind Technology (NOWITECH), Research Council of Norway (Contract no. 193823). The authors gratefully acknowledge the computing time granted by NOTUR (NN9240K) and provided on the Vilje system at the super computing facilities at NTNU.

References

Adeyemo, M., 1968. Effect of beach slope and shoaling on wave asymmetry. Coastal Engineering Proceedings, pp. 145–172.
Babanin, A.V., Chalikov, D., Young, I.R., Savelyev, I., 2010. Numerical and laboratory investigation of breaking of steep two-dimensional waves in deep water. J. Fluid Mech. 644, 433–463.
Battjes, J.A., 1974. Surf similarity. Coastal Engineering Proceedings, pp. 466–480.
Berthelsen, P.A., Faltinsen, O.M., 2008. A local directional ghost cell approach for incompressible viscous flow problems with irregular boundaries. J. Comput. Phys. 227, 4354–4397.
Bonmarin, P., 1989. Geometric properties of deep-water breaking waves. J. Fluid Mech. 209, 405–433.
Bradford, S.F., 2000. Numerical simulation of surf zone dynamics. J. Waterw. Port Coast. Ocean Eng. 126, 1–13.
Chen, G., Kharif, C., Zaleski, S., Li, J., 1999. Two-dimensional Navier–Stokes simulation of breaking waves. Phys. Fluids 11, 121–133.
Chorin, A., 1968. Numerical solution of the Navier Stokes equations. Math. Comput. 22, 745–762.
Christensen, E.D., 1998. Turbulence in Breaking Waves — A Numerical Investigation(Ph.D. thesis) Technical University of Denmark.
Christensen, E.D., 2006. Large eddy simulation of spilling and plunging breakers. Coast. Eng. 53, 463–485.
Cokelet, E., 1977. Breaking waves. Nature 267, 769–774.
Craig, P., 1996. Velocity profiles and surface roughness under breaking waves. J. Geophys. Res. 101, 1265–1277.
Duncan, J.H., 2001. Spilling breakers. Annu. Rev. Fluid Mech. 33, 519–547.
Engsig-Karup, A.P., 2006. Unstructured Nodal DG-FEM Solution of High-order Boussinesq-type Equations(Ph.D. thesis) Technical University of Denmark.
Fenton, J.D., 1999. The cnoidal theory of water waves. In: Herbich, J.B. (Ed.), Developments in Offshore Engineering. Gulf, Houston, pp. 55–100 (chapter 2).
Galvin, C.J., 1968. Breaker type classification on three laboratory beaches. J. Geophys. Res. 73, 3651–3659.
Goda, Y., 2010. Reanalysis of regular and random breaking wave statistics. Coast. Eng. J. 52, 71–106.
Grilli, S.T., Horrillo, J., 1997. Numerical generation and absorption of fully nonlinear periodic waves. J. Eng. Mech. 123, 1060–1069.
Grilli, S.T., Subramanya, R., Svendsen, I.A., Veeramony, J., 1995. Shoaling of solitary waves on plane beaches. J. Waterw. Port Coast. Ocean Eng. 120, 609–628.
Hieu, P.D., Katsutoshi, T., Ca, V.T., 2004. Numerical simulation of breaking waves using a two-phase flow model. Appl. Math. Model. 28, 983–1005.
Hwang, P.A., 1984. Profile asymmetry of shoaling waves on a mild slope. Coastal Engineering Proceedings, pp. 1016–1027.
Ippen, A.T., Kulin, G., 1954. The shoaling and breaking of the solitary wave. Coastal Engineering Proceedings, pp. 27–47.
Iwagaki, Y., Sakai, T., 1972. Shoaling of finite amplitude long waves on a beach of constant slope. Coastal Engineering Proceedings, pp. 347–364.
Jacobsen, N.G., Fuhrman, D.R., Fredsøe, J., 2012. A wave generation toolbox for the open-source CFD library: OpenFoam. Int. J. Numer. Methods Fluids 70, 1073–1088.
Jiang, G.S., Shu, C.W., 1996. Efficient implementation of weighted ENO schemes. J. Comput. Phys. 126, 202–228.
Kjeldsen, S.P., Myrhaug, D., 1978. Kinematics and dynamics of breaking waves. Technical Report. River and Harbour Laboratory (NHL) — The Norwegian Institute of Technology.
Lader, P.F., 2002. Geometry and Kinematics of Breaking Waves(Ph.D. thesis) Norwegian University of Science and Technology.
Lader, P.F., Myrhaug, D., Pettersen, B., 2000. Wave crest kinematics of deep water breaking waves. Coastal Engineering Proceedings, pp. 355–368.
Larsen, J., Dancy, H., 1983. Open boundaries in short wave simulations — a new approach. Coast. Eng. 7, 285–297.
Lin, P., Liu, P.L.F., 1998. A numerical study of breaking waves in the surf zone. J. Fluid Mech. 359, 239–264.
Longuet-Higgins, M.S., Cokelet, E.D., 1976. The deformation of steep surface waves on water I — A numerical method of computation. Proceedings of the Royal Society of London. Series A, Mathematical and Physical Sciences, pp. 1–26.
Lubin, P., Glockner, S., Kimmoun, O., Branger, H., 2011. Numerical study of the hydrodynamics of regular waves breaking over a sloping beach. Eur. J. Mech. B. Fluids 30, 552–564.
Massel, S.R., 2007. Ocean Waves Breaking and Marine Aerosol Fluxes. Springer.
Mayer, S., Garapon, A., Sørensen, L.S., 1998. A fractional step method for unsteady free surface flow with applications to non linear wave dynamics. Int. J. Numer. Methods Fluids 28, 293–315.
Miller, R., Zeigler, J., 1964. The internal velocity field in breaking waves. Coastal Engineering Proceedings, pp. 103–122.
Osher, S., Sethian, J.A., 1988. Fronts propagating with curvature-dependent speed: algorithms based on Hamilton–Jacobi formulations. J. Comput. Phys. 79, 12–49.
Peregrine, D.H., Cokelet, E.D., McIver, P., 1980. The fluid mechanics of waves approaching breaking. Coastal Engineering Proceedings, pp. 512–528.
Schultz, W.W., Huh, J., Griffin, O.M., 2006. Potential energy in steep and breaking waves. J. Fluid Mech. 278, 201–208.
Shu, C.W., Osher, S., 1988. Efficient implementation of essentially non-oscillatory shock capturing schemes. J. Comput. Phys. 77, 439–471.
Southgate, H.N., 1993. Review of wave breaking in shallow water. Proceedings of Advances in Underwater Technology, Ocean Science and Offshore Engineering Conference, pp. 251–273.
Stokes, G.G., 1880. Appendices and supplement to a paper on the theory of oscillatory waves. Math. Phys. Pap. 1, 219–229.
Thurman, H.V., Trujillo, A.P., 2001. Essentials of Oceanography. Prentice Hall.
Ting, F.C.K., Kirby, J.T., 1996. Dynamics of surf-zone turbulence in a spilling breaker. Coast. Eng. 27, 131–160.
Tsai, C.P., Chen, H.B., Hwung, H.H., Huang, M.J., 2005. Examination of empirical formulas for wave shoaling and breaking on steep slopes. Ocean Eng. 32, 469–483.
van der Vorst, H., 1992. BiCGStab: a fast and smoothly converging variant of Bi-CG for the solution of nonsymmetric linear systems. SIAM J. Sci. Stat. Comput. 13, 631–644.
Vinje, T., Brevig, P., 1981. Numerical simulation of breaking waves. Adv. Water Resour. 4, 77–82.
Walker, J., Headland, J., 1982. Engineering approach to nonlinear wave shoaling. Coastal Engineering Proceedings, pp. 523–542.
Wilcox, D.C., 1994. Turbulence Modeling for CFD. DCW Industries Inc., La Canada, California.
Wu, C.H., Nepf, H.M., 2002. Breaking criteria and energy losses for three-dimensional wave breaking. J. Geophys. Res. 107, 3177.
Zhao, Q., Armfield, S., Tanimoto, K., 2004. Numerical simulation of breaking waves by a multi-scale turbulence model. Coast. Eng. 51, 53–80.

6.4 Paper 4

Hydrodynamic characteristics and geometric properties of plunging and spilling breakers over impermeable slopes

Alagan Chella, M., Bihs, H., Myrhaug, D., Muskulus, M.
Ocean Modelling, 2015
DOI: 10.1016/j.ocemod.2015.11.011

Paper 4

Ocean Modelling 000 (2015) 1–20

Contents lists available at ScienceDirect

Ocean Modelling

journal homepage: www.elsevier.com/locate/ocemod

Virtual Special Issue
Ocean Surface Waves

Hydrodynamic characteristics and geometric properties of plunging and spilling breakers over impermeable slopes

Mayilvahanan Alagan Chella [a,*], Hans Bihs [a], Dag Myrhaug [b], Michael Muskulus [a]

[a] Department of Civil and Transport Engineering, Norwegian University of Science and Technology (NTNU), NO-7491 Trondheim, Norway
[b] Department of Marine Technology, Norwegian University of Science and Technology (NTNU), NO-7491 Trondheim, Norway

ARTICLE INFO

Article history:
Received 16 January 2015
Revised 9 November 2015
Accepted 19 November 2015
Available online xxx

Keywords:
Breaking waves
Spilling breaker
Plunging breaker
Hydrodynamic characteristics
REEF3D
Sloping seabed

ABSTRACT

The two-phase flow CFD model REEF3D has been used for modeling waves breaking over a sloping seabed for a spilling and a plunging breaker. This model is based on Reynolds-averaged Navier–Stokes (RANS) equations with the level set method (LSM) for the free surface and k–ω model for turbulence. First, the characteristics and geometric properties of plunging breaking waves with different offshore wave steepnesses over slopes are examined and discussed. The study further explores the hydrodynamic characteristics of spilling and plunging breakers in terms of the wave height evolution and attenuation, horizontal and vertical velocity, free surface profile evolution, and the geometric properties during the development of the breaking process. The numerical results show a good agreement with experimental data in terms of free surface elevation, horizontal and vertical velocity, wave envelope and turbulent intensity for the spilling and plunging breakers. Results of numerical simulations describing the physical flow characteristics such as the formation of the forward overturning water jet, air pocket, splash-up, and the secondary wave during the breaking process are presented for both cases. For both cases, the physical flow process is found to have similar flow features, but the breaking process occurs at significantly different scales.

1. Introduction

Wave breaking is a two-phase flow process composed of air and water, which transforms the large scale deterministic irrotational flow into rotational flow resulting in turbulence and vortices of different types and scales. The wave breaking process in shallow waters naturally influences many physical processes such as wave energy dissipation, air–sea interaction, wave–structure interaction, rip current, cross-shore and along-shore currents and sediment transport. Breaking waves are strongly influenced by the local wave parameters and seabed slope, and are described by four different types: spilling, plunging, collapsing and surging (Galvin, 1968). Breaking waves exert significant hydrodynamic loading on offshore platforms and foundations of offshore wind turbines in intermediate and shallow water. A recent feasibility study on the deployment of offshore wind turbines on Thornton bank outside the Belgian coast shows that hydrodynamic forces from plunging breaking waves govern the design criteria of a truss substructure (Alagan Chella et al., 2012). Understanding the breaking process remains a challenge since both measurements and simulations are extremely intricate.

Svendsen et al. (1978) divided the surf zone from inception to broken waves into three regions: outer, inner and run-up region. In the outer region, waves undergo drastic changes in the shape and the flow features, i.e. the flow pattern changes from irrotational flow to rotational flow. As the wave propagates farther shoreward, the wave motion becomes turbulent with low frequency components leading to the formation of wave rollers in the inner region. The region closest to the shore is the run-up region. The two-dimensional effects and longitudinal variations are more pronounced when waves approach the breaking point. On the other hand, the three-dimensional effects become more significant just after breaking and the flow becomes highly turbulent where waves undergo drastic changes in the deterministic flow characteristics. Therefore, three-dimensional effects and the surface tension effects need to be considered for a better description of air entrainment during the breaking process and the turbulent flow characteristics in the surf zone. The present study focuses on the physical process up to the inner breaking region where the three-dimensional effects are minimal, i.e. the

* Corresponding author. Tel.: +4748348518.
E-mail address: acm@ntnu.no, m.vahanan@gmail.com (M. Alagan Chella).

http://dx.doi.org/10.1016/j.ocemod.2015.11.011
1463-5003/

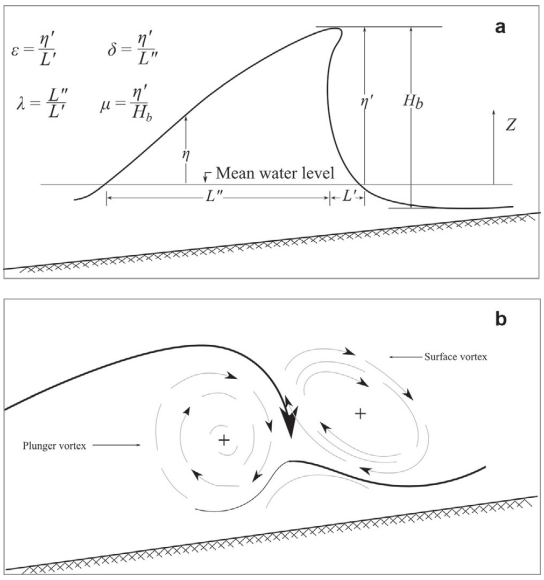

Fig. 1. (a) Definition sketch of local steepness and asymmetry parameters following Kjeldsen and Myrhaug (1978). (b) Schematic of formation of plunger vortex and surface vortex during breaking following Basco (1985).

large-scale changes in the incident deterministic flow pattern. The wave breaking process primarily depends on the following parameters: local water depth (d), offshore wave steepness (H_0/L_0, where H_0 and L_0 are wave height and wave length, respectively in deep water) and sea bed slope (m). The wave characteristics and the seabed slope are key factors in determining the breaker type (Iversen, 1952; Galvin, 1968; Battjes, 1974). Battjes (1974) described the breaker types based on the surf similarity parameter ($\xi_0 = \frac{m}{\sqrt{H_0/L_0}}$), which is a function of the wave steepness in deep water (H_0/L_0) and the seabed slope (m). For $\xi_0 < 0.5$, spilling breakers develop for waves of high steepness over mild slopes with the formation of white water foam or a small overturning water jet at the wave crest. For $0.5 < \xi_0 < 3.3$ corresponding to waves of low steepness propagating over moderate seabed slopes, waves break as plunging breakers with the larger forward overturning jet at the wave crest. Surging or collapsing breakers occur for $\xi_0 > 3.3$. Many laboratory experiments have been performed to obtain more insights into the breaking wave geometric, kinematic, dynamic and turbulent characteristics in deep and shallow waters, such as Kjeldsen and Myrhaug (1978), Adeyemo (1968), Stive and Wind (1982), Miller (1987), Nadaoka et al. (1989), Smith and Kraus (1990), and Ting and Kirby (1994). Kjeldsen and Myrhaug (1978) proposed steepness and asymmetry parameters from zero-downcross analysis to describe the prominent asymmetry features of a wave that approaches breaking: crest front steepness (ε), crest rear steepness (δ), vertical asymmetry factor (λ) and horizontal asymmetry factor (μ) as defined in Fig. 1(a). A detailed experimental study by Ting and Kirby (1994, 1995, 1996) investigated the dynamics of surf zone turbulence under waves breaking over a sloping seabed using fibre-optic laser-Doppler anemometer (LDA) technique. They addressed the basic differences in the turbulent characteristics and turbulence production mechanisms between spilling and plunging breakers. A number of studies have reviewed the wave evolution, flow properties and physical characteristics of waves breaking in deep and shallow water (Cokelet (1977), Peregrine (1983), Basco (1985), Banner and Peregrine (1993), Perlin et al. (2013)). Importantly, most numerical studies have addressed the deformation of solitary waves during the breaking process in shallow waters including Emarat et al. (2012) and Mo et al. (2013). Though a very few numerical studies have investigated the periodic waves breaking in shallow waters.

The wave transformation process in the surf zone is well represented by the Navier–Stokes equations and a direct solution of these equations is extremely complicated (Lemos, 1992). With the advancements in the development of computational fluid dynamics (CFD), a numerical model that solves the Navier–Stokes equations coupled with a free surface capturing scheme is capable of solving the complex free surface flow problem and details of the fluid flow properties can be obtained. The first numerical investigation of free surface flows by directly solving the Navier–Stokes equations was demonstrated by Harlow and Welch (1965). A class of computational methods based on the Reynolds-averaged Navier–Stokes (RANS) equations was first proposed by Lemos (1992) together with the volume-of-fluid method (VOF) and the k–ϵ turbulence model to simulate breaking waves in shallow water. Several studies attempted to model the breaking process using a single-phase flow model (Lin and Liu, 1998; Bradford, 2000; Zhao et al., 2004; Christensen and Deigaard, 2001). The major inadequacies of the single-phase flow models to represent the complete wave breaking process are that they do not account for the air phase, the constant pressure assumption in air and the associated boundary conditions at the free surface. Therefore, these models cannot represent the complex air–water interaction, which has a prominent role in the breaking process. Hence, two-phase flow models are crucial to model the wave breaking process, such as Hieu et al. (2004), Christensen (2006), Lubin et al. (2006), Moraga et al. (2008), Wang et al. (2009), Shi et al. (2010), Ma et al. (2011), Jacobsen et al. (2012), Xie (2013), Alagan Chella et al. (2015a) and Alagan Chella et al. (2015b). Alagan Chella et al. (2015a) used the present numerical model to simulate spilling breakers over slopes. The authors compared the numerical results to the experimental data for the spilling breaker case in order to validate the numerical model. Moreover, the main aim of the study was to investigate the effects of water depth, offshore wave steepness, and beach slope on the characteristics and geometric properties of spilling breakers over slopes.

The present numerical study uses the incompressible Reynolds-averaged Navier–Stokes equations based numerical wave tank. Unlike most of the previous numerical studies on breaking waves, in the current numerical model, different approaches have been proposed for describing the computational grid architecture and discretization schemes. The employment of the Cartesian grid facilitates to implement higher order spatial and temporal discretization schemes that provide very good numerical accuracy and stability. Particular attention has been given to achieve a more accurate representation of free surface waves in order to avoid the unrealistic damping at the free surface. Several numerical studies that are aimed at modeling the surf zone hydrodynamics have shown quite good results, but far too little attention has been paid to investigate the evolution of the free surface profile and the prominent flow features during the breaking process. In the hydrodynamic load assessment point of view, the evolution of free surface profiles, wave height and changes in velocities and geometric properties associated with the initial breaking process are important for the modeling of breaking wave forces. Meanwhile, there have been limited studies on these hydrodynamic characteristics relevant to the load assessment parameters in shallow waters.

The main purpose of the present paper is to investigate the hydrodynamic and geometric properties of plunging breakers over slopes with the two-phase flow CFD model REEF3D (Alagan Chella et al., 2015a). Comparison with similar results obtained for spilling breakers in Alagan Chella et al. (2015a) are also discussed. First, the study assesses the characteristics and geometric properties of plunging breaking waves of different offshore wave steepnesses over different slopes. This has been accomplished by examining the breaking characteristics such as breaker water depth (d_b), breaker depth

Please cite this article as: M. Alagan Chella et al., Hydrodynamic characteristics and geometric properties of plunging and spilling breakers over impermeable slopes, Ocean Modelling (2015), http://dx.doi.org/10.1016/j.ocemod.2015.11.011

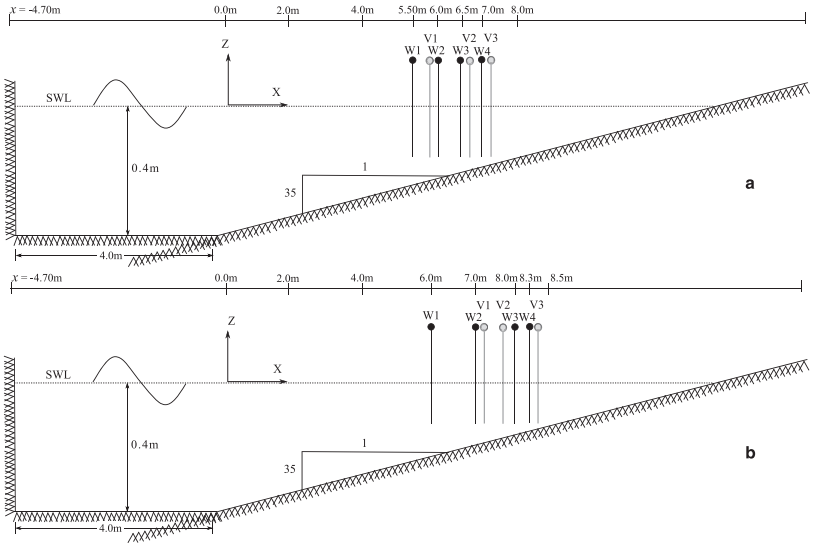

Fig. 2. Computational and experimental arrangements: W1–W4 are wave gauge locations and V1–V3 are velocity probe locations for (a) the spilling case and (b) the plunging case.

Table 1
Wave conditions and the experimental data in the laboratory observations by Ting and Kirby (1994); present numerical results (grid size, $dx = 0.005$ m).

Breaker type	Deep water wave height, H_0 (m)	Wave period, T (s)	Experimental data			Numerical results		
			x_b(m)	H_b(m)	H/d	x_b(m)	H_b(m)	H/d
Spilling	0.127	2.0	6.40	0.165	0.78	6.28	0.172	0.775
Plunging	0.089	5.0	7.795	0.191	1.24	7.84	0.205	1.164

index ($\gamma_b = H_b/d_b$, where H_b is the wave height at breaking), breaker height index ($\Omega_b = H_b/H_0$), and the profile asymmetry parameters as proposed by Kjeldsen and Myrhaug (1978) at the breaking point. Further, the hydrodynamic characteristics during the initial breaking process over a sloping seabed are compared for both cases. This assessment has been carried out based on the wave height evolution and attenuation, horizontal and vertical velocities, free surface profile evolution, and geometric properties during the development of the breaking process.

2. Computational model

2.1. Governing equations

The governing equations for the two-phase viscous flow in the open-source CFD model REEF3D are the incompressible Reynolds-averaged Navier–Stokes equations:

$$\frac{\partial U_i}{\partial x_i} = 0 \tag{1}$$

$$\frac{\partial U_i}{\partial t} + U_j \frac{\partial U_i}{\partial x_j} = -\frac{1}{\rho}\frac{\partial P}{\partial x_i} + \frac{\partial}{\partial x_j}\left[(\nu + \nu_t)\left(\frac{\partial U_i}{\partial x_j} + \frac{\partial U_j}{\partial x_i}\right)\right] + g_i \tag{2}$$

where U is the velocity averaged over time t, ρ is the fluid density, P is the pressure, ν is the kinematic viscosity, ν_t is the eddy viscosity and g is the gravity term.

To prevent the unrealistic damping of free surface waves, higher order schemes are used in the numerical model. The fifth-order weighted essentially non-oscillatory (WENO) scheme is employed to discretize the convection term of the RANS equations (Jiang and Shu, 1996). This produces numerical solutions with higher order accuracy and provides good numerical stability with non-oscillatory performance near the interface, i.e. discontinuities. In order to achieve higher order accuracy in the temporal discretization, the third-order total variation diminishing (TVD) Runge–Kutta scheme (Shu and Osher, 1988) is employed in the present study and this method includes three Euler substeps. The pressure term is treated with the projection method (Chorin, 1968) after each of the Euler substeps. The Poisson equation for the pressure is solved with the BiCGStab algorithm with Jacobi preconditioning (van der, 1992). With an adaptive time stepping method proposed by Griebel et al. (1998), the CFL stability criterion is maintained and the simulation time step is adjusted for each iteration. This method includes the effects of velocity and the source term S on the temporal numerical solutions. In this algorithm, the time step size for each iteration is obtained by satisfying the

Table 2
List of simulation cases.

Simulation cases	Offshore wave steepness (H_0/L_0)	Seabed slope (m)	Surf similarity parameter (ξ)
Case A	0.0023	1/15	0.84
		1/25	0.72
		1/35	0.60
		1/45	0.50
		1/55	0.42
Case B	0.0011	1/35	0.84
	0.0016		0.72
	0.0023		0.60
	0.0035		0.49
	0.0046		0.42

Please cite this article as: M. Alagan Chella et al., Hydrodynamic characteristics and geometric properties of plunging and spilling breakers over impermeable slopes, Ocean Modelling (2015), http://dx.doi.org/10.1016/j.ocemod.2015.11.011

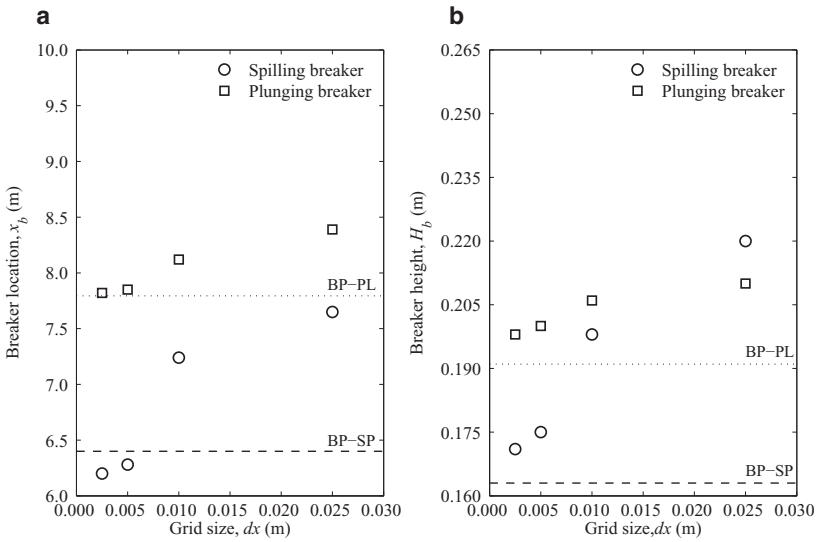

Fig. 3. Comparison of (a) x_b and (b) H_b for different grid sizes. BP-SP and BP-PL are the measured data by Ting and Kirby (1996, 1995) for the spilling and plunging breaker, respectively.

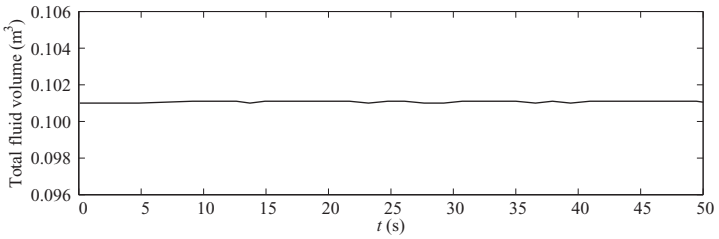

Fig. 4. Total fluid volume during the simulation of the spilling breaker case (Ting and Kirby, 1996).

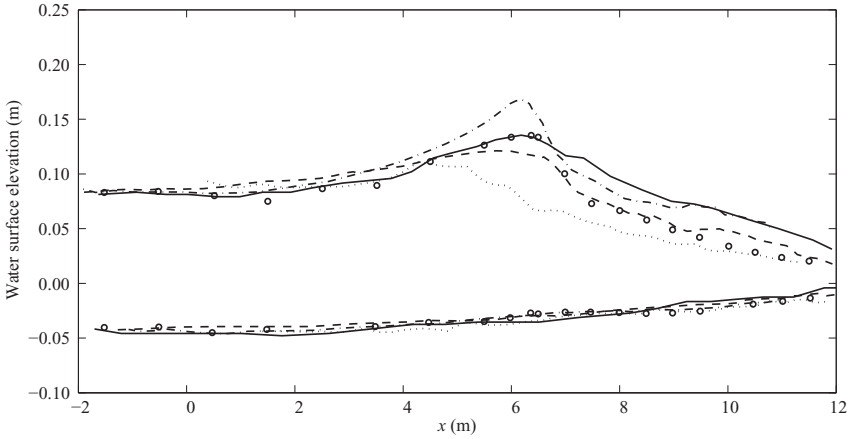

Fig. 5. Comparison of the computed and measured maximum (upper curves) and minimum (lower curves) wave surface elevation for the spilling breaker. Solid lines: the present numerical model; circles: experimental data from Ting and Kirby (1996); dotted lines, numerical: Bradford (2000); dashed lines, numerical: Xie (2013); dashed-dotted lines, numerical: Zhao et al. (2004).

Please cite this article as: M. Alagan Chella et al., Hydrodynamic characteristics and geometric properties of plunging and spilling breakers over impermeable slopes, Ocean Modelling (2015), http://dx.doi.org/10.1016/j.ocemod.2015.11.011

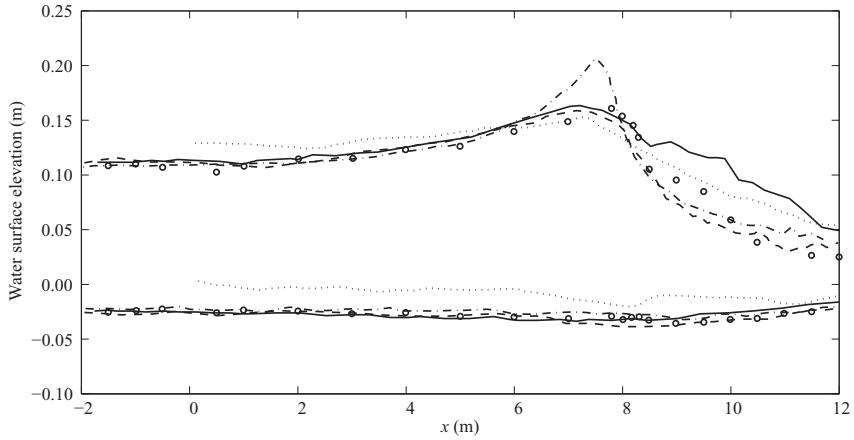

Fig. 6. Comparison of the computed and maximum (upper curves) and minimum (lower curves) wave surface elevation for the plunging breaker. Solid lines: the present numerical model; circles: experimental data from Ting and Kirby (1996); dotted lines, numerical: Bradford (2000); dashed lines, numerical: Xie (2013); dashed-dotted lines, numerical: Zhao et al. (2004).

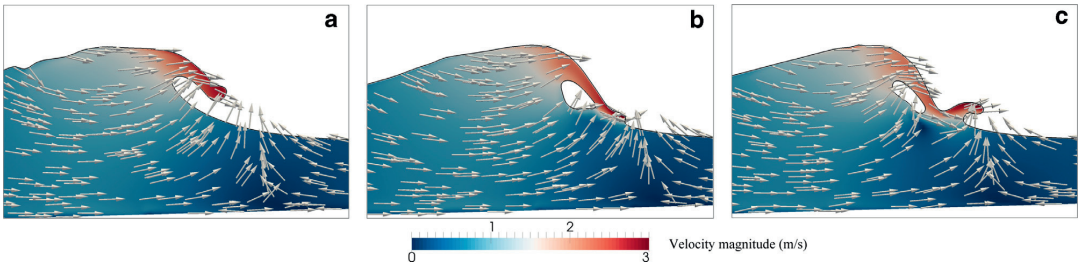

Fig. 7. Wave surface profile with velocity vectors and velocity magnitude for the plunging breaker.

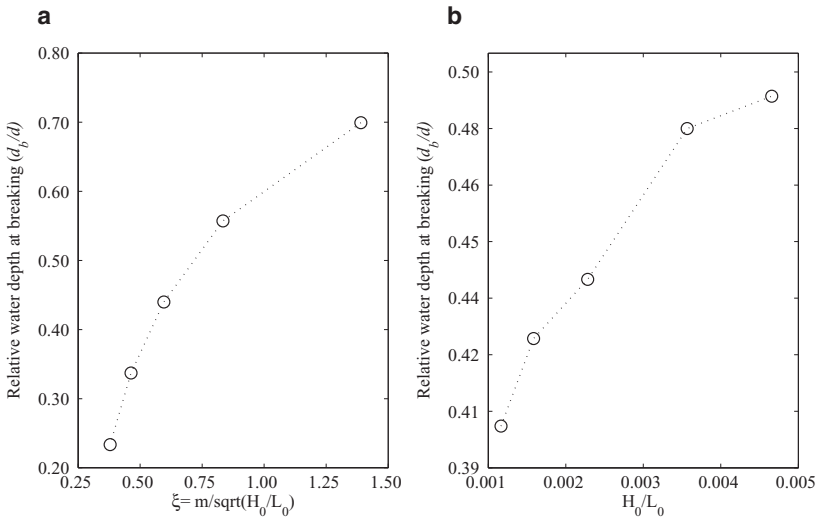

Fig. 8. Numerical relative water depth (d_b/d) for different (a) surf similarity parameter ($\xi = \frac{m}{\sqrt{H_0/L_0}}$) and (b) offshore wave steepness (H_0/L_0).

Please cite this article as: M. Alagan Chella et al., Hydrodynamic characteristics and geometric properties of plunging and spilling breakers over impermeable slopes, Ocean Modelling (2015), http://dx.doi.org/10.1016/j.ocemod.2015.11.011

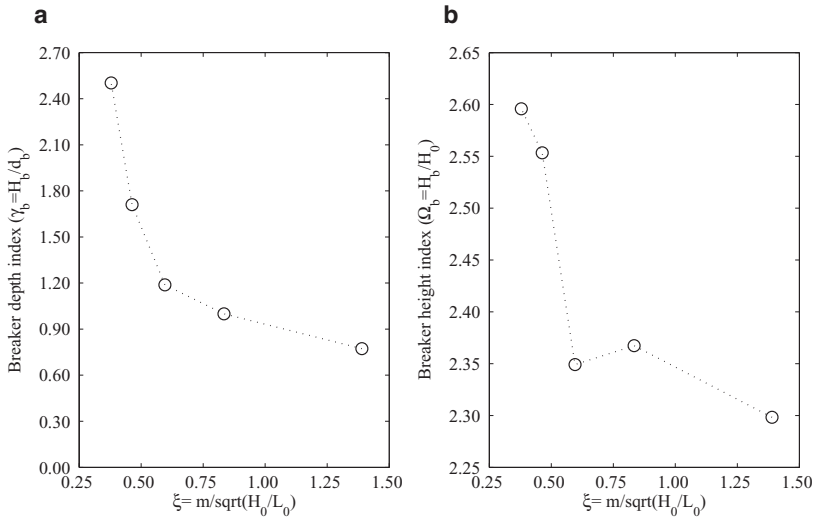

Fig. 9. Numerical (a) breaker depth index ($\gamma_b = H_b/d_b$) and (b) breaker height index ($\Omega_b = H_b/H_0$) for different surf similarity parameter ($\xi = \frac{m}{\sqrt{H_0/L_0}}$).

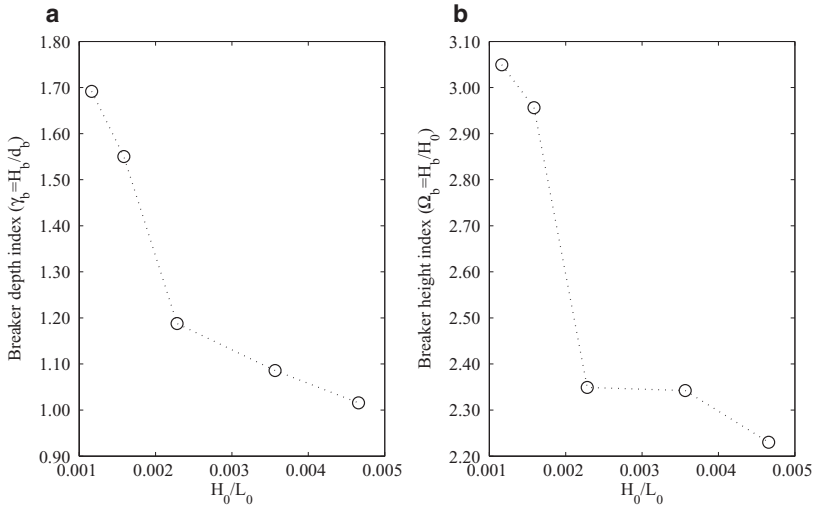

Fig. 10. Numerical (a) breaker depth index ($\gamma_b = H_b/d_b$) and (b) breaker height index ($\Omega_b = H_b/H_0$) for different offshore wave steepness (H_0/L_0).

following criterion:

$$\Delta t \le 2\left(\left(\frac{|u|_{\max}}{dx}+D\right)+\sqrt{\left(\frac{|u|_{\max}}{dx}+D\right)^2+\frac{4|S_{\max}|}{dx}}\right)^{-1} \quad (3)$$

Which includes the effect of diffusion term D:

$$D = \max(\nu+\nu_t)\cdot\left(\frac{2}{(dx)^2}+\frac{2}{(dy)^2}+\frac{2}{(dz)^2}\right) \quad (4)$$

Moreover, the CFL number of the present simulation cases is 0.1 and the simulations are performed at sufficiently small time steps to capture the nonlinear dynamic effects evolve during the breaking process.

The prominent features associated with the breaking process are the production, dissipation and diffusion of vorticity and turbulence. The two-equation k–ω model (Wilcox, 1994) is employed in the numerical model in order to obtain the turbulence closure for the RANS equations and the equations for k and ω as follows:

$$\frac{\partial k}{\partial t}+U_j\frac{\partial k}{\partial x_j}=\frac{\partial}{\partial x_j}\left[\left(\nu+\frac{\nu_t}{\sigma_k}\right)\frac{\partial k}{\partial x_j}\right]+P_k-\beta_k k\omega \quad (5)$$

$$\frac{\partial \omega}{\partial t}+U_j\frac{\partial \omega}{\partial x_j}=\frac{\partial}{\partial x_j}\left[\left(\nu+\frac{\nu_t}{\sigma_\omega}\right)\frac{\partial \omega}{\partial x_j}\right]+\frac{\omega}{k}\alpha P_k-\beta\omega^2 \quad (6)$$

P_k is the turbulent production rate, the coefficients have the values $\alpha = \frac{5}{9}$ $\beta_k = \frac{9}{100}$ and $\beta = \frac{3}{40}$.

Wilcox (1994) extensively investigated the performance of the k–ω turbulence model for a wide range of applications including the problems relevant to free surface flows. This model has also been applied to study the breaking waves by Mayer and Madsen (2000)

Please cite this article as: M. Alagan Chella et al., Hydrodynamic characteristics and geometric properties of plunging and spilling breakers over impermeable slopes, Ocean Modelling (2015), http://dx.doi.org/10.1016/j.ocemod.2015.11.011

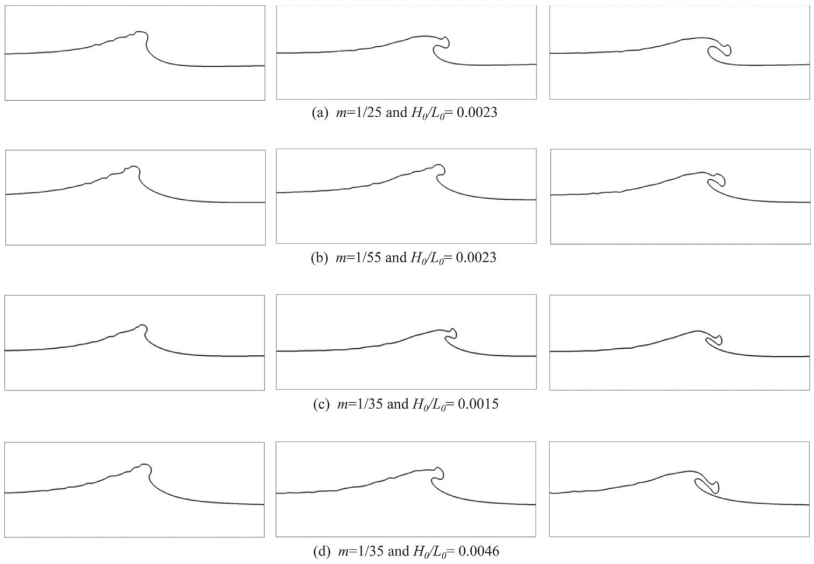

Fig. 11. Computed wave profiles (a) $m = 1/25$ and $H_0/L_0 = 0.0023$, (b) $m = 1/55$ and $H_0/L_0 = 0.0023$, (c) $m = 1/35$ and $H_0/L_0 = 0.0015$ and (d) $m = 1/35$ and $H_0/L_0 = 0.0046$.

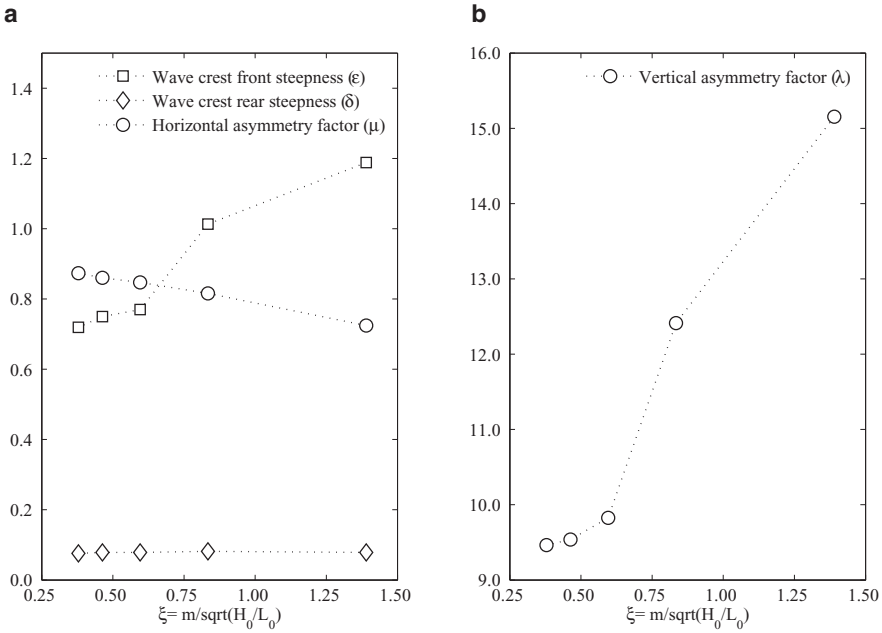

Fig. 12. Numerical wave profile steepnesses and asymmetry factors for different surf similarity parameter ($\xi = \frac{m}{\sqrt{H_0/L_0}}$).

and Bradford (2000). The k–ω model together with the RANS equations are used to model the turbulence under the breaking waves. Mayer and Madsen (2000) studied the spilling breakers using the Navier–Stokes equations with a k–ω turbulence model. The authors addressed that the large levels of unphysical turbulence production affect the wave propagation characteristics and this occurs in the highly strained oscillatory motion outside the boundary layer. In the present study, the unphysical turbulence production is avoided by limiting the turbulent eddy viscosity using the limiter as suggested by Durbin (2009). In the case of a two-phase flow scenario, the RANS turbulence closure over predicts the turbulence intensity at the free surface, which leads to over production of turbulence at the free surface as well. This has been controlled by implementing an additional turbulence damping scheme at the interface as

Please cite this article as: M. Alagan Chella et al., Hydrodynamic characteristics and geometric properties of plunging and spilling breakers over impermeable slopes, Ocean Modelling (2015), http://dx.doi.org/10.1016/j.ocemod.2015.11.011

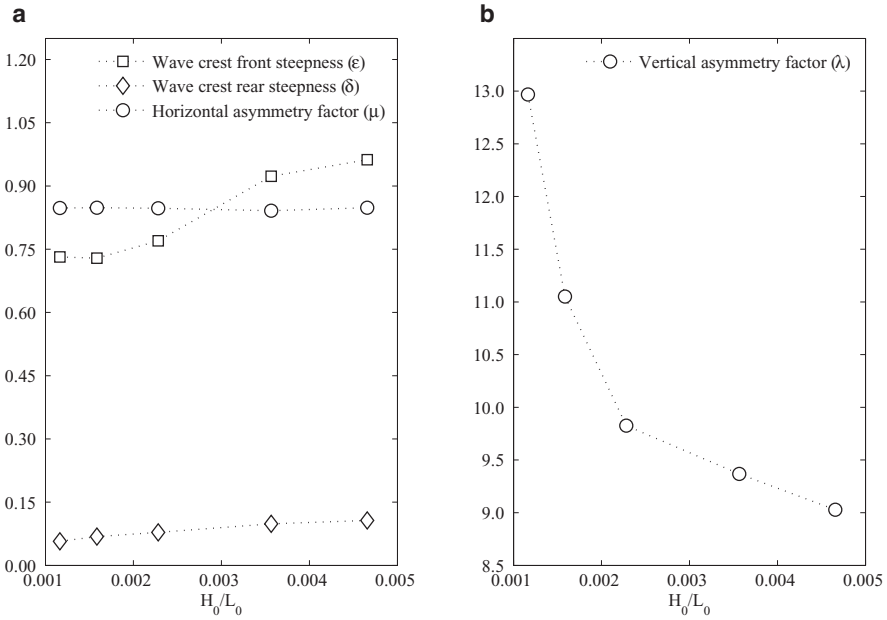

Fig. 13. Numerical wave profile steepnesses asymmetry factors for different offshore wave steepness (H_0/L_0).

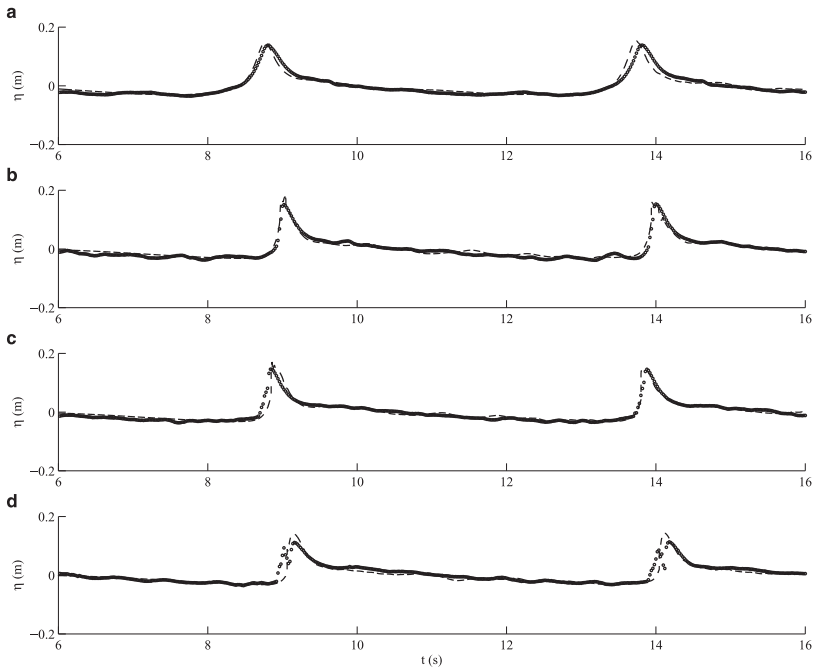

Fig. 14. Comparison of numerical and experimental instantaneous wave surface elevation for the plunging breaker at $x = 6.0$ m (a), 7.0 m (b), 8.0 m (c) and 8.3 m (d). Dashed lines: present numerical results; circles/full line: experimental results by Ting and Kirby (1995).

Please cite this article as: M. Alagan Chella et al., Hydrodynamic characteristics and geometric properties of plunging and spilling breakers over impermeable slopes, Ocean Modelling (2015), http://dx.doi.org/10.1016/j.ocemod.2015.11.011

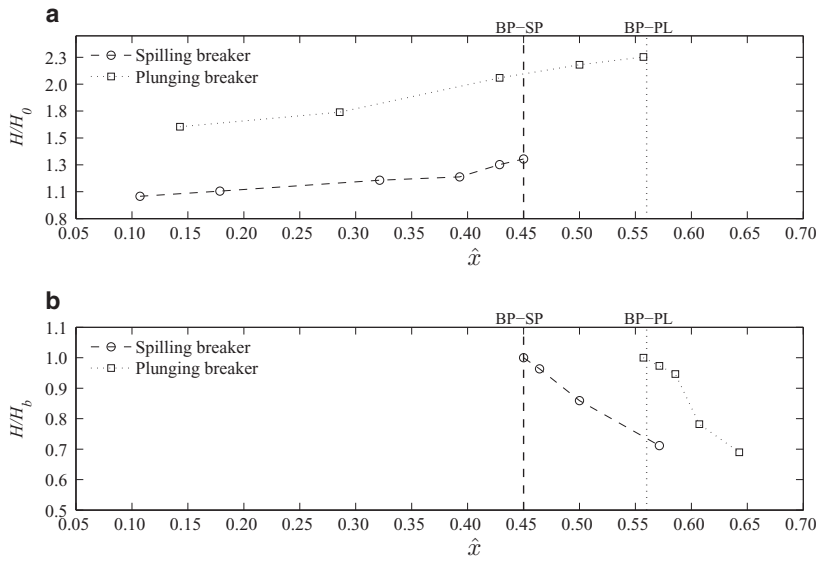

Fig. 15. Computed wave height variation (a) H/H_0 (before breaking); (b) H/H_b (after breaking) versus the non-dimensional breaking location ($\hat{x}$). BP–SP and BP–PL are the measured data by Ting and Kirby (1996, 1995) for the spilling and plunging breaker, respectively.

proposed by Naot and Rodi (1982). The specific turbulent dissipation at the interface and the corresponding term is imposed around the interface. The solid boundaries of the fluid domain are represented with a ghost-cell immersed boundary method (Berthelsen and Faltinsen, 2008). The near-wall effects are accounted through wall functions for the velocities and the variables of the turbulence model.

2.2. Free surface

The interface deformation during the breaking process is complex due to the change in fluid properties such as viscosity and density across the interface. The interface deformation, i.e. free surface changes, are captured by the level set method (Osher and Sethian, 1988) without explicitly tracking the interface. The interface is modeled as the zero set of the smooth signed distance function $\phi(\vec{x},t)$ defined on the entire computational domain. The location and the sign of the zero level set function defines the fluid phase as follows:

$$\phi(\vec{x},t)\begin{cases} >0 \text{ if } \vec{x} \in \text{water} \\ =0 \text{ if } \vec{x} \in \Gamma \\ <0 \text{ if } \vec{x} \in \text{air} \end{cases} \tag{7}$$

The free surface motion is described by the propagation of the zero level set function. The convection equation of the level set function is as follows:

$$\frac{\partial \phi}{\partial t} + U_j \frac{\partial \phi}{\partial x_j} = 0 \tag{8}$$

The Eikonal equation $|\nabla \phi| = 1$ is valid in the computational domain. In the present study, the mass conservation property is improved by reinitializing the level set function after each time step with a PDE based reinitialization equation proposed by Sussman et al. (1994) and Peng et al. (1999). The density and viscosity of the two phases are discontinuous at the interface. Numerical instabilities may occur due to viscosity and density jumps at the interface. This can be eliminated by smoothing out the fluid properties in a transition zone with a Heaviside function $H(\phi)$. The thickness of the transition region is 2ϵ, where $\epsilon = 2.1\,dx$. The density and the viscosity are smoothed at the interface as follows:

$$\begin{aligned} \rho(\phi) &= \rho_{\text{water}} H(\phi) + \rho_{\text{air}}(1 - H(\phi)), \\ \nu(\phi) &= \nu_{\text{water}} H(\phi) + \nu_{\text{air}}(1 - H(\phi)) \end{aligned} \tag{9}$$

and where $H(\phi)$ is a Heaviside function:

$$H(\phi) = \begin{cases} 0 & \text{if } \phi < -\epsilon \\ \frac{1}{2}\left(1 + \frac{\phi}{\epsilon} + \frac{1}{\pi}\sin\left(\frac{\pi\phi}{\epsilon}\right)\right) & \text{if } |\phi| < \epsilon \\ 1 & \text{if } \phi > \epsilon \end{cases} \tag{10}$$

2.3. Numerical wave generation and absorption

The computational experiments are performed in a numerical wave tank. The relaxation method presented by Larsen and Dancy (1983) is employed for wave generation at the inlet of the numerical wave tank. Here the values for the velocities and free surface are ramped up to the values obtained from wave theory. At the outlet of the numerical wave tank, the relaxation method works as a numerical beach. Here, the velocities are set to zero, the pressure to its hydrostatic distribution and the free surface to the still water level.

3. Computational set-up and simulation cases

Numerical experiments are conducted in a wave tank with a 1/35 sloping bed and waves are generated in the region of a flat bed of 0.4 m water depth. The computational set-up follows the experimental conditions reported by Ting and Kirby (1995, 1996) as shown in Fig. 2. It has been reported by Ting and Kirby (1995, 1996) that cnoidal waves were used in the laboratory experiments. In order to reproduce the experimentally measured waves in the numerical simulation, three different wave theories are tested namely, shallow water cnoidal waves, first-order and fifth-order cnoidal waves. Finally, with the fifth-order cnoidal wave theory by Fenton (1999), a very good representation of the measured waves is obtained in the numerical

Please cite this article as: M. Alagan Chella et al., Hydrodynamic characteristics and geometric properties of plunging and spilling breakers over impermeable slopes, Ocean Modelling (2015), http://dx.doi.org/10.1016/j.ocemod.2015.11.011

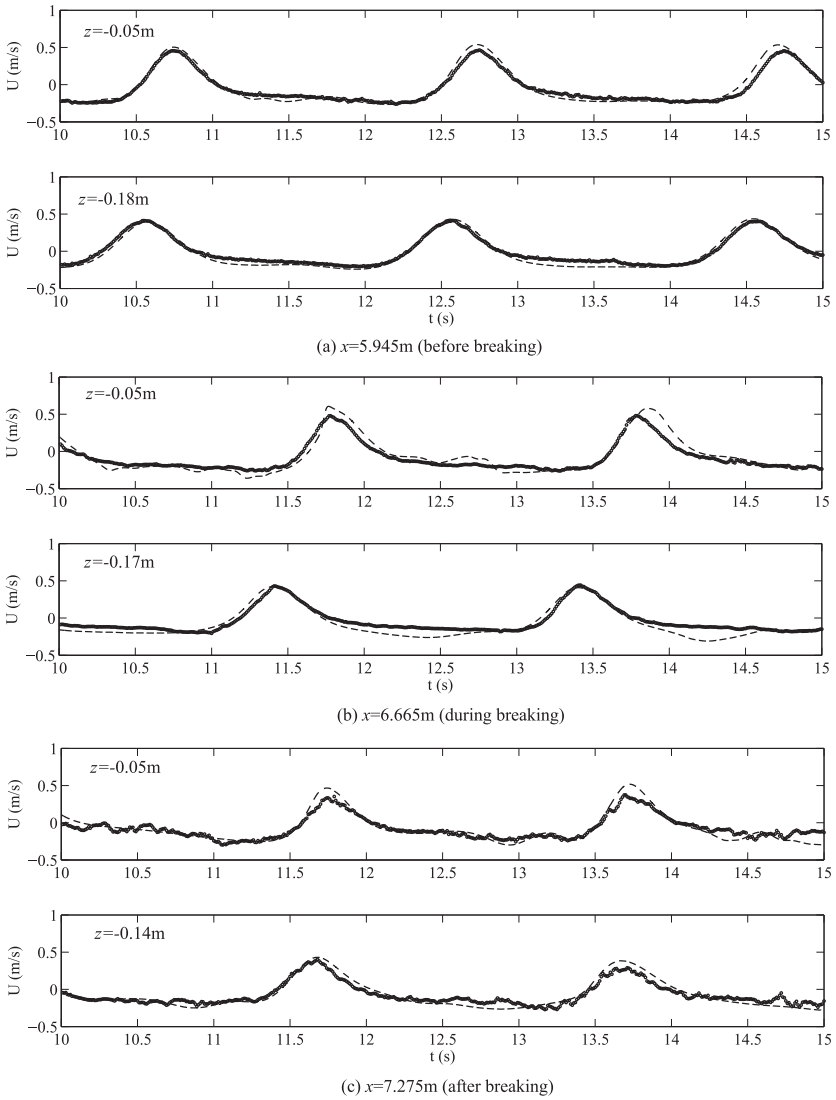

Fig. 16. Comparison of numerical and experimental horizontal component of velocity for the spilling breaker. Dashed lines: present numerical results; circles/full line: experimental results by Ting and Kirby (1996).

simulation. The wave parameters that are used in the simulations are listed in Table 1. The size of the 2D computation domain is $L_x = 30$ m and $L_z = 1.0$ m. A uniform grid is used in both horizontal and vertical directions i.e. $dx = dz$. The length of the numerical simulation is 25 s for spilling breakers and 35 s for plunging breakers. The mean quantities are obtained from the simulated values of last five waves e.g. the breaker height (H_b) and breaking location (x_b).

In order to examine the characteristics and geometric properties of plunging breakers of different offshore wave steepness (H_0/L_0) over different slopes (m), a series of numerical experiments are performed. In the simulation cases, the environment parameters for plunging breakers are chosen based on the surf similarity parameter suggested by Battjes (1974). This also includes a few transitional spilling–plunging breakers, as listed in Table 2.

3.1. Grid sensitivity study

The sensitivity of the numerical results to the grid size (dx) is tested with four different grid sizes, $dx = 0.025$ m, 0.01 m, 0.005 m and 0.0025 m. Fig. 3 presents the comparison of the numerical breaking location (x_b) (Fig. 3(a)) and the breaker height (H_b) (Fig. 3(b)) for different grid sizes for spilling and plunging breakers. It appears that the numerical waves on coarser grids ($dx = 0.025$ m and $dx = 0.01$ m) break later and further up in the wave tank with larger breaker height than the experimental waves. On the other hand, the numerical waves on finer grids ($dx = 0.005$ m and $dx = 0.0025$ m) break at about the same location as that of the experimental waves for both cases. The numerical results at the breaking point on the grid size $dx = 0.005$ match well with the experimental data as presented

Please cite this article as: M. Alagan Chella et al., Hydrodynamic characteristics and geometric properties of plunging and spilling breakers over impermeable slopes, Ocean Modelling (2015), http://dx.doi.org/10.1016/j.ocemod.2015.11.011

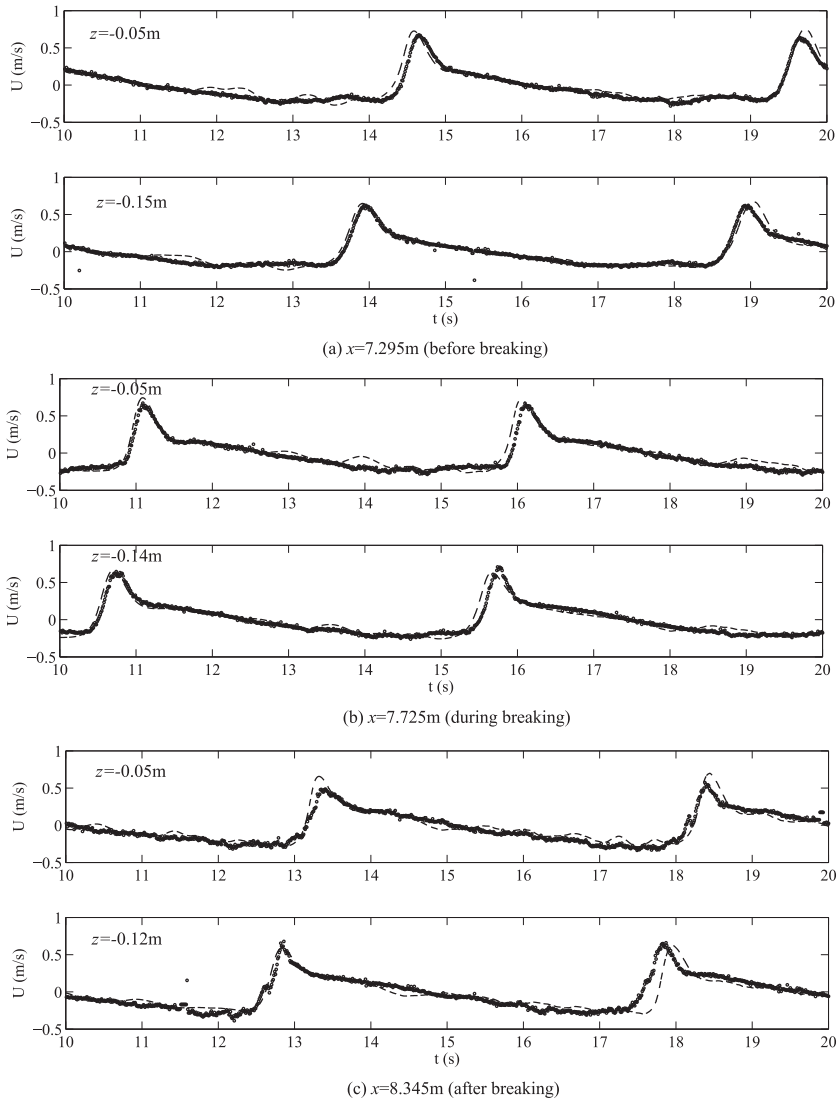

Fig. 17. Comparison of numerical and experimental horizontal component of velocity for the plunging breaker. Dashed lines: present numerical results; circles/full line: experimental results by Ting and Kirby (1995).

in Table 1. In addition, the difference between the results of two fine grid sizes ($dx = 0.005$ m and $dx = 0.0025$ m) is very small. Therefore, the grid size $dx = 0.005$ is considered for the simulations.

3.2. Mass conservation

In order to test the mass conservation during the numerical simulation, the total fluid volume changes in the computational domain are studied for 50 s of simulation time. Fig. 4 shows the total fluid volume in the computational domain versus time. It appears that the total fluid volume in the whole computational domain is constant throughout the simulation with very little fluctuations with the volume error about −0.019%. This error is very small and indicates that volume conservation is satisfied very accurately throughout the simulation time. In addition, the free surface and the horizontal and vertical components of particle velocity are in good agreement with the measured data by Ting and Kirby (1995, 1996) as presented in Figs. 14, 16, 17, 20 and 21. Therefore, the mass is conserved locally and globally for the whole computational domain throughout the simulation time. Specifically, the mass is conserved even after the wave breaks which leads to a complex wave transformation process.

4. Results and discussion

4.1. Wave envelope of spilling and plunging breaker

Figs. 5 and 6 show the comparison of computed and measured maximum (upper curves) and minimum (lower curves) wave surface elevations for the spilling breaker and plunging breaker, respectively. The numerical results of Bradford (2000), Zhao et al. (2004),

Please cite this article as: M. Alagan Chella et al., Hydrodynamic characteristics and geometric properties of plunging and spilling breakers over impermeable slopes, Ocean Modelling (2015), http://dx.doi.org/10.1016/j.ocemod.2015.11.011

Xie (2013) are also presented for comparison as reported in Xie (2013). The computed results of all the numerical models show the same trend as the experimental measurements. The numerical model by Xie (2013) is a two-phase flow model based on the RANS equations together with k–ϵ and the VOF method. Bradford (2000) performed simulations with the commercial software FLOW-3D that uses the RANS equations together with the VOF method and the RNG (Re-Normalized Group) turbulence model. Zhao et al. (2004) used a model based on the space filtered Navier–Stokes equations with the VOF method and the multi-scale turbulence model. In the spilling breaker case (Fig. 5), the computed maximum and minimum wave surface elevations are quite well captured up to the breaking point by the present numerical model and the model by Xie (2013). Zhao et al. (2004) overestimate the wave crest significantly near the breaking point and slightly in the surf zone, whereas Bradford (2000) largely underestimates the wave crest near the breaking point and estimates it reasonably well in the surf zone. The comparison of computed and measured envelope of the water surface elevation for the spilling breaker is also presented in Fig. 8 of Alagan Chella et al. (2015a) using the present numerical model.

For the plunging breaker (Fig. 6), Zhao et al. (2004) overpredict the wave crest height close to the breaking point, but predicts the wave surface quite well in the shoaling and surf zones. The numerical results by Bradford (2000) show a slight overestimation of the wave crest and a significant underestimation of the wave trough. Xie (2013) shows a good comparison with the experimental data for the whole domain for both the breakers. The present numerical model shows a good representation of the wave height evolution during the shoaling and initial breaking region for both cases, but overestimates slightly the wave crest heights after the breaking point in the surf zone. However, the computed wave troughs are in a good agreement with the experimental data. The overprediction of the wave crest heights after breaking is due to the slower dissipation process in the numerical simulation.

4.2. Plunging breakers over slopes

4.2.1. Breaking process

Fig. 7 illustrates the free surface profile evolution with the velocity vectors and their magnitudes variation during the breaking process. The overturning water jet that evolves from the wave crest when the particle velocity becomes larger than the wave celerity is shown in Fig. 7(a). The overturning wave crest then hits the free surface of the preceding wave (Fig. 7(b)) and the splash-up occurs. Further, this leads to the formation of the secondary wave with new flow characteristics which depends on the size of the overturning crest as seen in Fig. 7(c).

4.2.2. Characteristics and geometric properties

Fig. 8 presents the numerical relative breaker depth (d_b/d) versus the surf similarity parameters ($\xi = \frac{m}{\sqrt{H_0/L_0}}$) (Fig. 8(a)) (since H_0/L_0 is constant) for different slopes and offshore wave steepness (H_0/L_0) (Fig. 8(b)). It appears that d_b/d increases as ξ (Fig. 8(a)) and H_0/L_0 (Fig. 8(b)) increase. Waves break offshore at larger water depths over steeper slopes and also waves with larger wave steepness.

Figs. 9 and 10 show the breaker depth index ($\gamma_b = H_b/d_b$) and breaker height index ($\Omega_b = H_b/H_0$) versus the surf similarity parameters (ξ) (Fig. 9) (since H_0/L_0 is constant) for different slopes and offshore wave steepness (H_0/L_0) (Fig. 10). It appears that γ_b and Ω_b decrease as ξ and H_0/L_0 increase. Waves over milder slopes break farther onshore at shallower water depths with larger H_b as the waves deform more during the shoaling process, corresponding to $\xi = 0.381$, $d_b/d = 0.233$ (Fig. 8(a)), $\gamma_b = 2.50$ (Fig. 9(a)) and $\Omega_b = 2.60$ (Fig. 9(b)). In the case of waves over a steeper slope, breaking occurs farther offshore with a lower H_b, with more partial reflections from the slope, corresponding to $\xi = 1.396$, $d_b/d = 0.70$ (Fig. 8(a)), $\gamma_b = 0.77$ (Fig. 9(a)) and $\Omega_b = 2.30$ (Fig. 9(b)). Unlike the variation of Ω_b for the spilling breaking waves with low H_0/L_0 over slopes (Alagan Chella et al., 2015a), Ω_b decreases as the seabed slope increases for the plunging breaker. In the present case, the plunging breaking waves are relatively long waves compared to the spilling breaking waves. The plunging breakers have a deeper wave base, propagate faster, interact more with the slope and break sooner. Waves with lower H_0/L_0 break farther shoreward at shallower water with higher H_b, transform more during the shoaling process, corresponding to $H_0/L_0 = 0.0011$, $d_b/d = 0.405$ (Fig. 8(b)), $\gamma_b = 1.69$ (Fig. 10(a)) and $\Omega_b = 3.05$ (Fig. 10(b)). The variations of the breaker indices versus H_0/L_0 for the plunging breakers are consistent with those for the spilling breakers as shown in Fig. 15(b) of Alagan Chella et al. (2015a).

Fig. 11 shows the changes in the wave profile during the breaking for different combinations of slopes and offshore wave steepnesses. Figs. 12 and 13 show the wave asymmetry parameters versus the surf similarity parameters (ξ) (Fig. 12) (since H_0/L_0 is constant) for different slopes and offshore wave steepness (H_0/L_0) (Fig. 13). It appears that ε and λ increase and μ decreases slightly as ξ increases, while δ nearly constant. When the waves approach breaking over steeper slopes, the front part of the wave becomes steeper without any change in the rear crest steepness and deforms both in vertical and horizontal direction with a shallower trough and an overturning crest (Fig. 11(a) and (b)), according to $\xi = 1.39$, $\varepsilon = 1.19$, $\mu = 0.72$ (Fig. 12(a)) and $\lambda = 15.15$ (Fig. 12(b)). In spite of that both spilling and plunging breakers are found to have similar geometrical features in terms of ε, λ and μ, the rear part of the wave crest does not deform during the interaction with slopes for plunging breakers.

For the waves with larger H_0/L_0 over a given slope, ε and δ increase and λ decreases as H_0/L_0 increases. This implies that the wave front and rear part become steeper without much change in the horizontal and vertical asymmetry. For the waves with lower H_0/L_0 at the breaking point, the rear part of the wave crest becomes wider and smooth with a slightly steeper front part and shallower wave trough (Fig. 11(c) and (d)), corresponding to H_0/L_0=0.0011, $\varepsilon = 0.73$ (Fig. 13(a)) and $\lambda = 12.96$ (Fig. 13(b)). The variation of the crest front steepness (ε) and the vertical asymmetry factor (λ) for the plunging breakers are consistent with those for the spilling breakers. However, for plunging breakers, the crest rear steepness (δ) and horizontal asymmetry factor (μ) are nearly independent of H_0/L_0.

In contrast to the previous results for spilling breakers over slopes (Alagan Chella et al., 2015a), the wave profiles during the breaking do not change much for plunging breakers with different H_0/L_0 over slopes as shown in Fig. 11. However, the computed plunging breaking wave profiles show significant changes in the wave crest front steepness (ε) and vertical asymmetry factor (λ). Though the breaker indices exhibit a similar trend for steeper slopes and waves with larger H_0/L_0, the vertical (λ) and horizontal asymmetry (μ) of the breaking wave profiles show an opposite relationship between H_0/L_0 and steeper slopes. This confirms that the breaking mechanism has distinct geometrical features based on seabed slope and H_0/L_0.

4.3. Comparison of hydrodynamic characteristics of spilling and plunging breakers over a sloping seabed

4.3.1. Free surface evaluation

Fig. 14 shows the comparison of the numerical wave surface elevations with the experimental data for the plunging breakers. When the waves propagate over the slope, the wave length and the wave speed are both reduced with decreasing water depth. Consequently, the kinetic wave energy decreases as the waves approach the shore, giving an increased potential energy, and therefore the wave height increases until breaking. The upper part of the wave tends to move faster than the lower part of the wave, resulting in the wave steepening as shown in Fig. 14(b). A further increase in the wave height results in a significantly steeper wave profile and finally the wave

Please cite this article as: M. Alagan Chella et al., Hydrodynamic characteristics and geometric properties of plunging and spilling breakers over impermeable slopes, Ocean Modelling (2015), http://dx.doi.org/10.1016/j.ocemod.2015.11.011

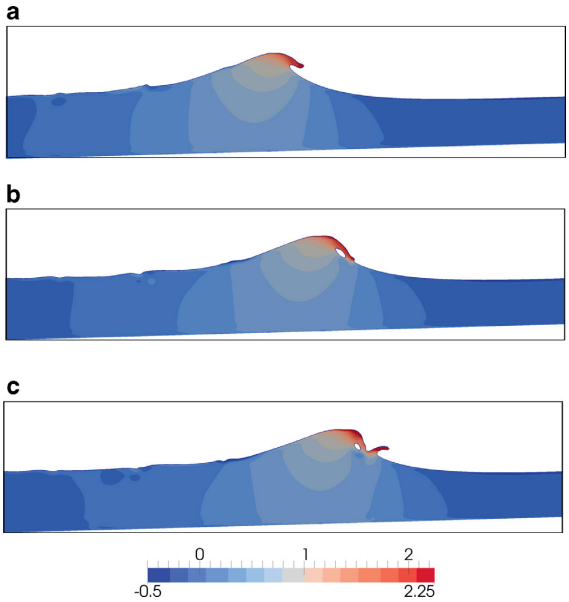

Fig. 18. Variation of horizontal velocity, V_x (m/s) under the spilling breaker at t = 10.35 s (a), 10.45 s (b) and 10.50 s (c).

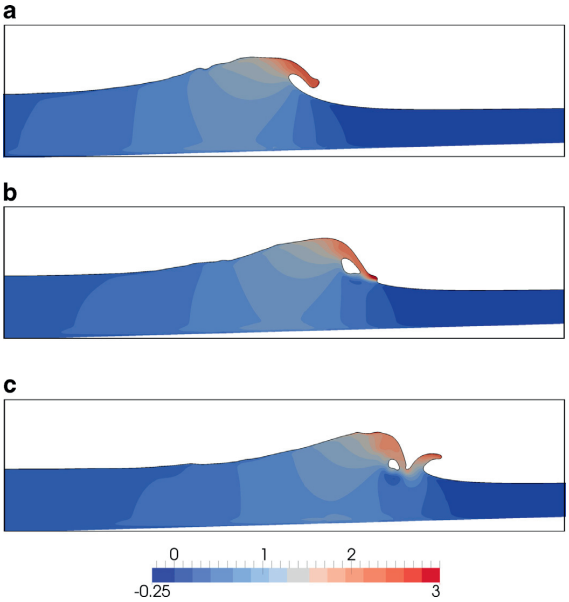

Fig. 19. Variation of horizontal velocity, V_x (m/s) under the plunging breaker at t = 10.85 s (a), 10.95 s (b) and 11.05 s (c).

breaks. As the breaking wave approaches the shore, the potential energy and the wave height decreases. A decrease in the wave height in the inner breaking region due to energy dissipation by wave breaking leads to the changes in the wave characteristics as shown in Fig. 14(d). It should be noted that breaking occurred between Figs. 14(c) and (d) for the plunging breaker. The computed wave surface elevations for the spilling breaker from the results of previous study by (Alagan Chella et al., 2015a) (Fig. 4) show a similar variation trend as the plunging breaker. The numerical wave surface elevations appear to agree well with the experimental data by Ting and Kirby (1995, 1996). The wave height to water depth ratio H/d at wave breaking is a key parameter related to the surf zone turbulence, and it is also useful in categorizing different types of breakers in shallow water (Ting and Kirby, 1995). The computed H/d at the breaking is 1.164 for the plunging breaker, whereas it is 0.775 for the spilling breaker. This implies that plunging breaking occurs farther up on the slope at shallower water depths with larger breaker heights, while spilling breaking occurs farther offshore at larger water depths with a small increase in the breaker height. The computed H/d ratios for both cases are consistent with the experiments and are listed in Table 1.

4.3.2. Wave height evolution and attenuation

Fig. 15 shows the wave height variation before breaking (H/H_0) and after breaking (H/H_b) versus the non-dimensional breaking location ($\hat{x} = x/L$, $x = 0$ at 0.7 m from the toe of the slope and $x = L$ at the shoreline). As can be seen from Fig. 15(a), the plunging breaker undergoes more deformation during shoaling as it advances over the slope than the spilling breaker. Since the plunging breaker has a deeper wave base, it feels the influence of the bed earlier. This intensifies the water particle interaction with the slope, resulting in a larger deformation. The wave height grows over the slope due to the higher shoaling rate and reaches a maximum height of $2.30H_0$ for the plunging breaker. For the spilling breaker it increases less and attains the maximum wave height at the breaking point with $1.35H_0$. Therefore, the initial wave characteristics of the wave approaching over the slope change significantly for the plunging breaker due to a deeper wave base and the higher shoaling rate.

From Fig. 15 (b) it appears that the wave height decreases gradually after breaking for the spilling breaker, whereas a more rapid wave height variation occurs for the plunging breaker which is consistent with the observations by Ting and Kirby (1994), Iwata and Tomita (1992) and Basco (1985). This implies that the potential wave energy decreases gradually for the spilling breaker and rapidly for the plunging breaker in the surf zone by converting some of the potential energy into the kinetic energy plus dissipation by turbulence and bed friction. It is also possible to infer that the amount of energy generated from the plunging breaker is higher and dissipates faster than for the spilling breaker. However, the wave height decreases continuously shoreward as most of the wave energy is dissipated during breaking process.

4.3.3. Horizontal and vertical particle velocity

Figs. 16 and 17 show the comparison of the computed horizontal velocity with the experimental data at three different horizontal locations: before breaking (a), during breaking (b) and after breaking (c), at two elevations; near the free surface and close to the bed. It appears that the horizontal velocity increases shoreward until breaking, with lower velocities at the bed. The motion of water particles close to the sloping bottom is restricted by friction during the shoaling and the breaking process. For both cases, the horizontal velocity depends on the change of the water surface level during the propagation of the wave train. The horizontal velocity distribution under the spilling and plunging breakers is presented in Figs. 18 and 19, respectively. It appears that the variation of the horizontal velocity below the trough of the plunging breaker is almost constant over the depth, but it is changing under the spilling breaker. This is also consistent with the laboratory study by Ting and Kirby (1996). Moreover, the maximum horizontal velocity occurs at the tip of the crest where potential energy is converted into kinetic energy with the formation of the horizontal surface roller. The same type of behavior is also

Please cite this article as: M. Alagan Chella et al., Hydrodynamic characteristics and geometric properties of plunging and spilling breakers over impermeable slopes, Ocean Modelling (2015), http://dx.doi.org/10.1016/j.ocemod.2015.11.011

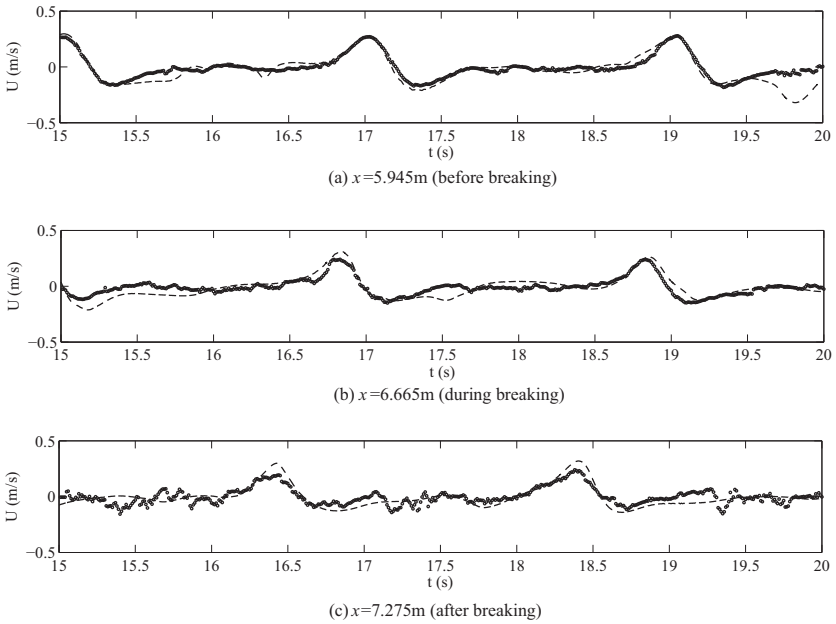

(a) x =5.945m (before breaking)

(b) x =6.665m (during breaking)

(c) x =7.275m (after breaking)

Fig. 20. Comparison of numerical and experimental vertical component of velocity for the spilling breaker. Dashed lines: present numerical results; circles/full line: experimental results by Ting and Kirby (1996).

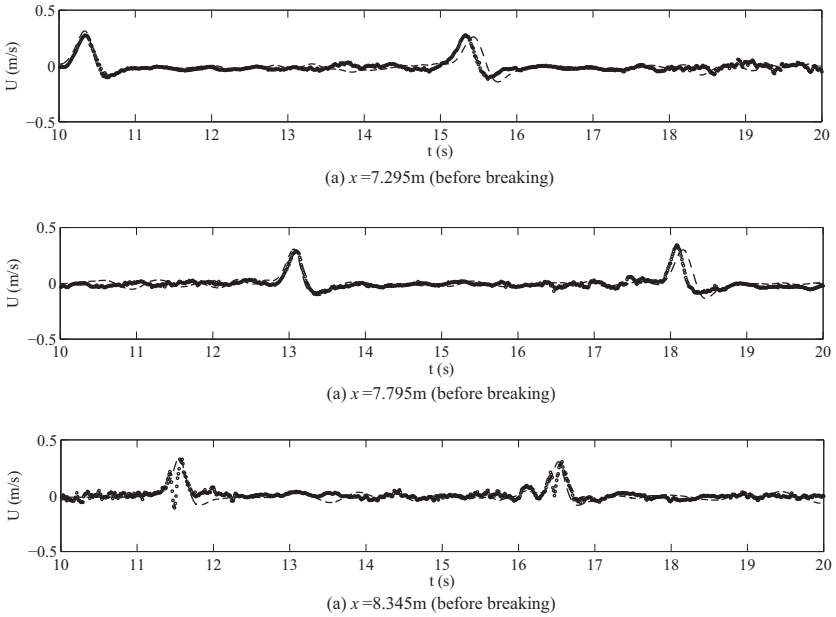

(a) x =7.295m (before breaking)

(a) x =7.795m (before breaking)

(a) x =8.345m (before breaking)

Fig. 21. Comparison of numerical and experimental vertical component of velocity for the plunging breaker. Dashed lines: present numerical results; circles/full line: experimental results by Ting and Kirby (1995).

Please cite this article as: M. Alagan Chella et al., Hydrodynamic characteristics and geometric properties of plunging and spilling breakers over impermeable slopes, Ocean Modelling (2015), http://dx.doi.org/10.1016/j.ocemod.2015.11.011

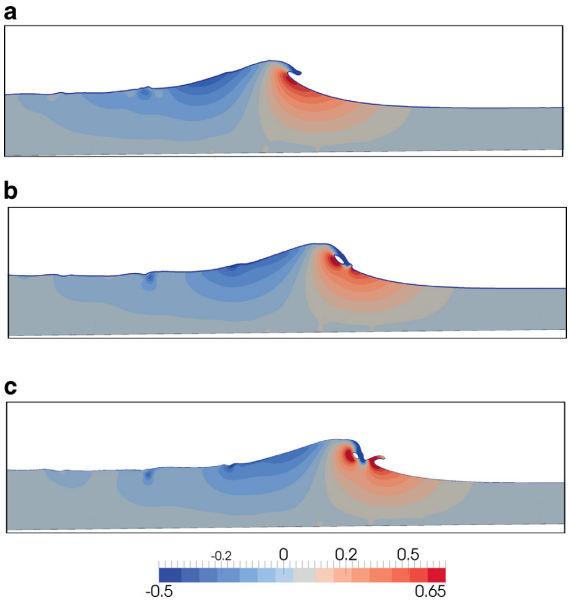

Fig. 22. Variation of vertical velocity, V_z (m/s) under the spilling breaker at $t = 10.35$ s (a), 10.45 s (b) and 10.50 s (c).

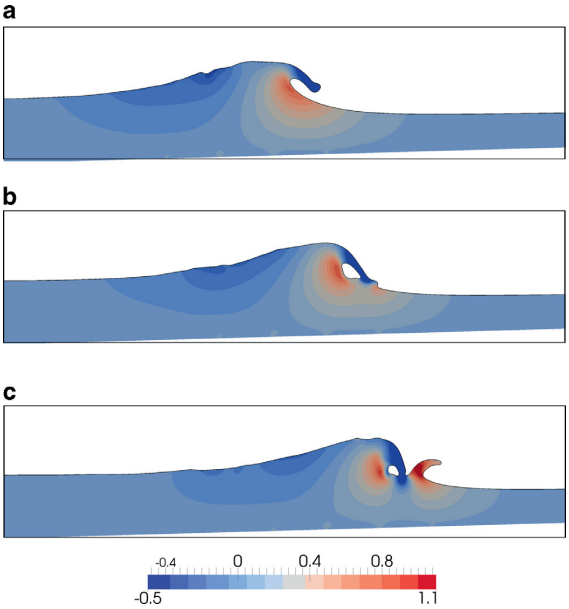

Fig. 23. Variation of vertical velocity, V_z (m/s) under the plunging breaker at $t = 10.85$ s (a), 10.95 s (b) and 11.05 s (c).

observed during the formation of secondary wave during the splash-up phase as shown in Figs. 18(c) and 19(c).

Figs. 20 and 21 show the comparison of the computed vertical velocity near the free surface with the experimental data at three different horizontal locations: before breaking (a), during breaking (b) and after breaking (c). The computed vertical velocity agrees well with the measurements, though it is slightly higher than the experimental data in the outer region of the surf zone for the spilling breaker. A slight increase in the vertical particle velocity can be expected during the formation of small (spilling) and large (plunging) overturning water jets at the wave crest and the splash-up for both the breakers. For the spilling breaker, a slight decrease in the vertical particle velocity near the free surface is observed during the wave breaking. This is due to a stagnation phase in the flow field during the development process of the vertical wave front of the horizontal water jet. This type of behavior is also reported by Mizuguchi (1986). However, the computed vertical velocity clearly follows the experimental trend and it increases continuously until the formation of the secondary wave, while it decreases shoreward for the plunging breaker. Figs. 22 and 23 show the vertical velocity variation during the wave breaking process for the spilling and plunging breaker, respectively. It appears that the vertical particle velocity attains the maximum value at the mean water level near the forward portion of the wave crest. It is evident from Figs. 22 and 23 that the maximum vertical component of velocity moves along the wave front of the propagating wave and becomes larger under the steep wave front. This is also seen in the laboratory experiment by Ting and Kirby (1995, 1996). By comparing Figs. 18 and 22 as well as Figs. 19 and 23, it appears that the velocity distribution at the overturning water jet is dominated by the horizontal velocity component with a small vertical velocity component. Although the kinematics of the secondary wave, that evolves during the splash-up, are still dominated by the horizontal velocity component, the vertical velocity component has a significant contribution in the region as shown in Figs. 22(c) and 23(c). This is consistent with the previous studies by Basco (1985) and Hendrickson (2005). Moreover, the computed horizontal and vertical velocities for both cases are consistent with the laboratory measurements by Ting and Kirby (1995, 1996).

4.3.4. Variation of time-mean turbulent kinetic energy

Fig. 24 shows the comparison of computed and measured square root of the non-dimensional time-mean turbulent kinetic energy versus the non-dimensional water depth after the breaking point at $x =$ 6.665 m, 7.275 m and 7.885 m for the spilling breaker. The numerical results of Bradford (2000) and Xie (2013) are also presented for comparison as reported in Xie (2013). It appears that the variation of time-mean turbulent kinetic energy with the water depth increases gradually as the distance to the free surface decreases. The present numerical results at $x = 6.665$ m is compared only with the numerical results by Xie (2013) as the experimental data is not available. It is observed that the computed results by Xie (2013) are slightly larger than the experimental measurements at $x = 7.275$ m, but they are in good agreement at $x = 7.885$ m. The computed results by Bradford (2000) show a significant underestimation of turbulence intensity at $x = 7.275$ m. With the present numerical model, the variation of turbulence intensity is well represented at $x = 7.275$ m but it is slightly underestimated at $x = 7.885$ m.

Fig. 25 shows the comparison of computed and measured square root of the non-dimensional time-mean turbulent kinetic energy versus the non-dimensional water depth after the breaking point at $x =$ 8.345 m, 8.795 m and 9.295 m for the plunging breaker. The predicted turbulence intensity profile by Xie (2013) agrees well with the experimental data at $x = 8.345$ m and 8.795 m, though this is overestimated slightly at $x = 9.295$ m. The results by Bradford (2000) also show a good prediction at $x = 8.345$ m. Though the present numerical model represents the vertical turbulence profile quiet well at $x = 8.345$ m, the model slightly underestimates the profile at $x = 8.795$ m and 9.295 m. For both cases, the turbulence is generated after the wave breaking when the flow characteristics change significantly leading to the formation of the surface roller. The turbulence intensity increases gradually shoreward until the surface roller dissipates energy completely during the transformation in the surf zone. In addition, the

Please cite this article as: M. Alagan Chella et al., Hydrodynamic characteristics and geometric properties of plunging and spilling breakers over impermeable slopes, Ocean Modelling (2015), http://dx.doi.org/10.1016/j.ocemod.2015.11.011

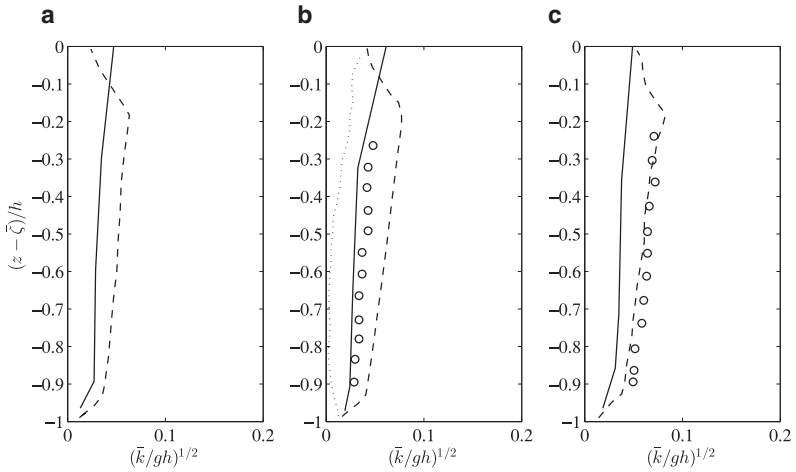

Fig. 24. Comparison of the computed and measured square root of the non-dimensional time-mean turbulent kinetic energy versus the non-dimensional water depth at $x =$ 6.665 m (a), 7.275 m (b) and 7.885 m (c) for the spilling breaker. Solid lines: the present numerical model; circles: experimental data from Ting and Kirby (1994); dotted lines, numerical: Bradford (2000); dashed lines, numerical: Xie (2013).

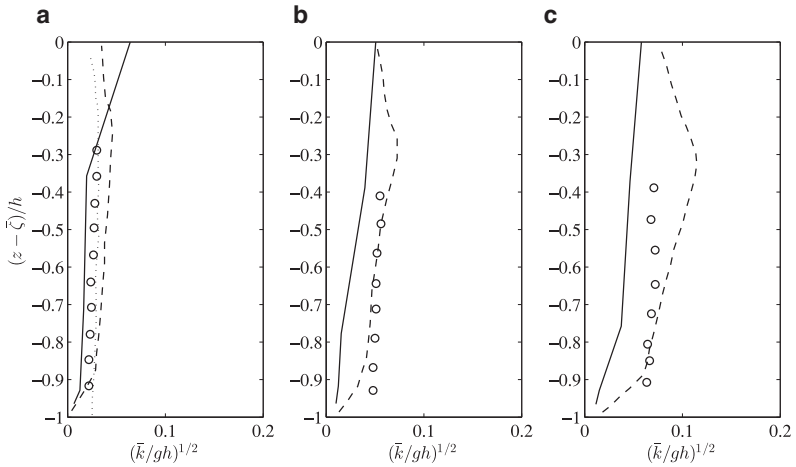

Fig. 25. Comparison of the computed and measured square root of the non-dimensional time-mean turbulent kinetic energy versus the non-dimensional water depth at $x =$ 8.345 m (a), 8.795 m (b) and 9.295 m (c) for the plunging breaker. Solid lines: the present numerical model; circles: experimental data from Ting and Kirby (1994); dotted lines, numerical: Bradford (2000); dashed lines, numerical: Xie (2013).

maximum value of the turbulence intensity occurs near the free surface and decreases gradually with the water depth. It is observed that the turbulence intensity generated by the plunging breaker is much stronger than for the spilling breaker, being consistent with Ting and Kirby (1996).

Overall, the present numerical results are in reasonable agreement with the measured data and the other numerical models. However, the model underestimates the vertical turbulence profile in the surf zone. The detailed investigation on the turbulence characteristics in the surf zone is not considered in present study. In fact, the modeling of the complex turbulent characteristics in the surf zone necessitates the use of more sophisticated turbulence modeling techniques. In addition, these simulations are computationally demanding. Further development of the current numerical model concerning the turbulence modeling is required to capture the detailed surf zone hydrodynamics.

4.3.5. Transformation of free surface profile

Figs. 26 and 27 show the transformation of the free surface profile during the breaking process for spilling and plunging breakers, respectively. It appears that the forward overturning wave crest during the breaking process moves faster than the lower part of the wave with high crest velocity (Figs. 26(a) and 27(a)). Thus, the overturning water jet falls onto the free surface as it propagates over the slope, as seen in Figs. 26(c) and 27(b). When the water jet plunges down on the trough of the preceding wave, a rotating motion with an air pocket inside and a surface roller are created by a combination of the downstream return flow under the preceding wave trough together with the overturning jet and the forward motion of the wave crest. The size of the rotating plunger motion is similar to the initial plunger vortex as shown in Fig. 1(b). Further, a portion of water which is equivalent to the strength of the jet is displaced and pushed forward during the impact of the overturning water jet on the free

Please cite this article as: M. Alagan Chella et al., Hydrodynamic characteristics and geometric properties of plunging and spilling breakers over impermeable slopes, Ocean Modelling (2015), http://dx.doi.org/10.1016/j.ocemod.2015.11.011

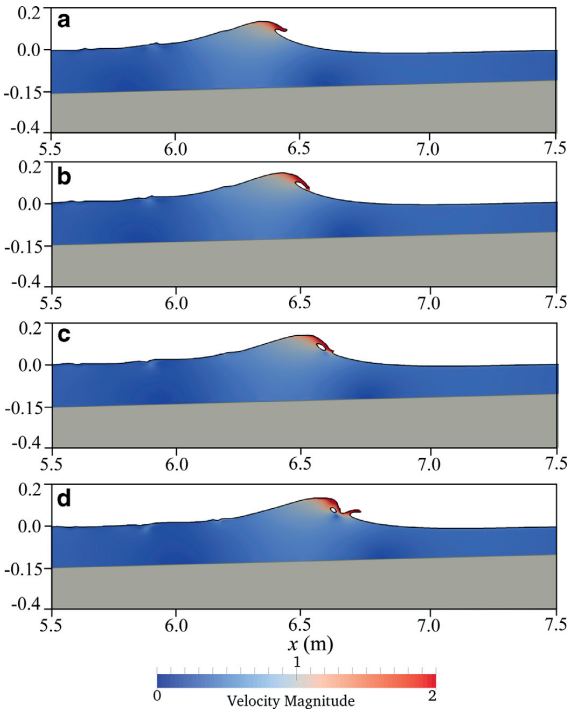

Fig. 26. Simulated velocity variation (m/s) and free surface profile changes during the breaking process at $t = 10.35$ s (a), 10.40 s (b), 10.45 s (c) and 10.50 s (d) for the spilling breaker.

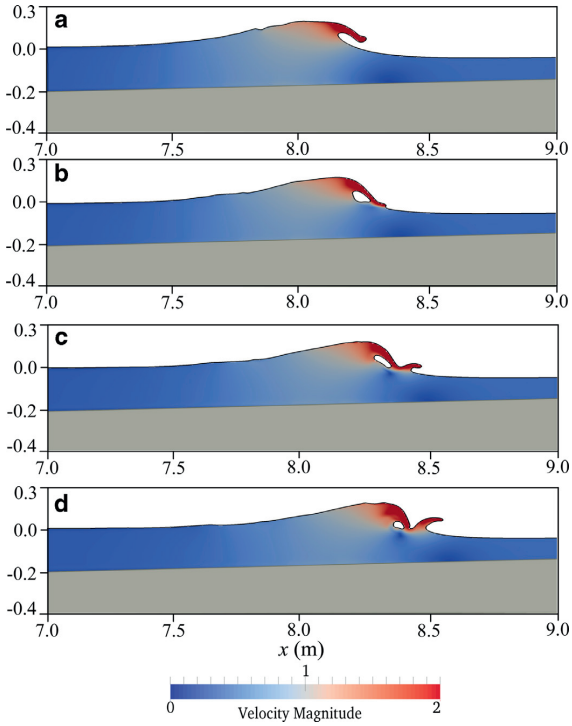

Fig. 27. Simulated velocity variation (m/s) and free surface profile changes during the breaking process at $t = 10.85$ s (a), 10.95 s (b), 11.00 s (c) and 11.05 s (d) for the plunging breaker.

surface and creates a secondary wave in the surf zone as depicted in Figs. 26(d) and 27(c) and (d). Therefore, the main sources of turbulence for the plunging wave are the transformation of rotational motion and the surface roller (Basco, 1985; Peregrine and Svendsen, 1978). The present study shows that both spilling and plunging breakers are found to have similar flow features during the initial breaking process. This has been confirmed experimentally by Miller (1987) and Ting and Kirby (1994). The authors also addressed that in spite of similar flow features between plunging and spilling breakers, turbulence generating mechanism and the characteristics are different.

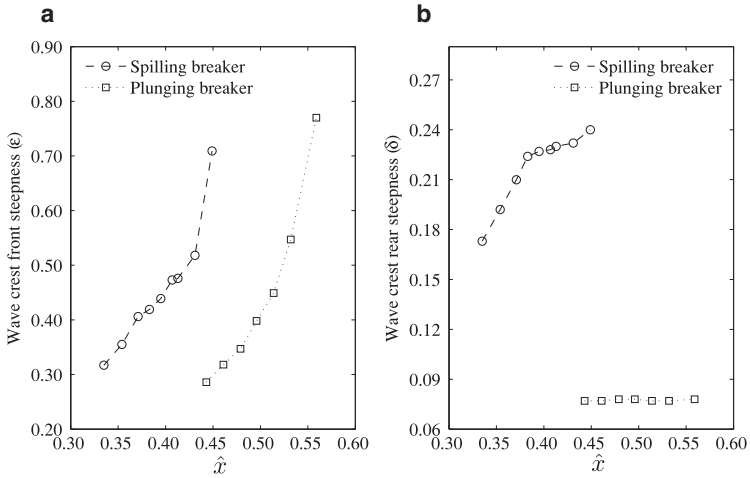

Fig. 28. Simulated development of steepness parameters (a) wave crest front steepness (ε); (b) wave crest rear steepness (δ) versus the non-dimensional breaking location ($\hat{x}$) during the transition to breaking.

Please cite this article as: M. Alagan Chella et al., Hydrodynamic characteristics and geometric properties of plunging and spilling breakers over impermeable slopes, Ocean Modelling (2015), http://dx.doi.org/10.1016/j.ocemod.2015.11.011

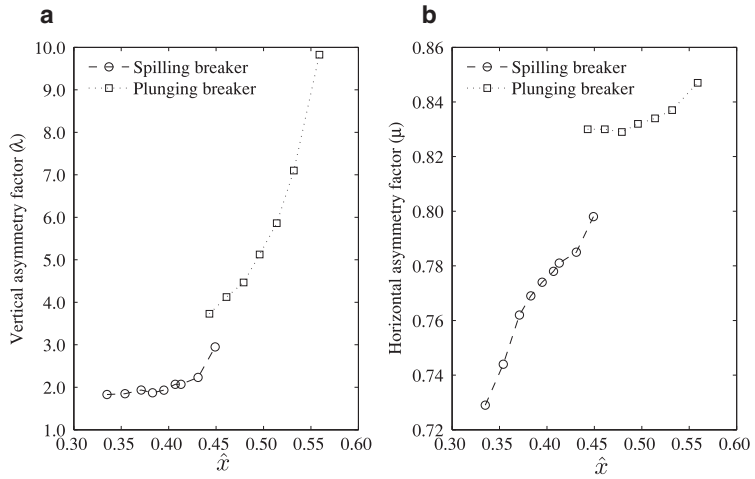

Fig. 29. Simulated development of asymmetry factors (a) vertical asymmetry factor (λ); (b) horizontal asymmetry factor (μ) versus the non-dimensional breaking location ($\hat{x}$) during the transition to breaking.

4.3.6. Wave profile asymmetry properties

Now the steepness and asymmetry parameters defined by Kjeldsen and Myrhaug (1978) are used to describe the geometric properties of the wave profile asymmetry during breaking. In order to investigate the geometric properties of a wave approaching breaking, the steepness and asymmetry parameters of each case are calculated at different locations along the wave tank until the breaking point.

Fig. 28 shows the variation of the wave crest front steepness (ε) and the wave crest rear steepness (δ) for the spilling and plunging breakers. It appears that ε increases as the wave approaches breaking in both cases; the front face of the wave becomes steeper for the plunging breaker than for the spilling breaker (Fig. 28(a)). On the other hand, δ increases as the wave approaches the breaking point for the spilling breaker, whereas it does not change during the transition stage for the plunging breaker.

Fig. 29 shows the vertical asymmetry factor (λ) and the horizontal asymmetry factor (μ) for the spilling and plunging breakers. It appears that λ and μ increase as the wave approaches breaking for both cases. However, λ increases rapidly and μ increases slowly for the plunging breaker, while λ increases slowly and μ increases rapidly for the spilling breaker. For the spilling breaker, the front and rear faces of the wave crest become steeper with a gradual increase of the vertical asymmetry, and the forward wave trough flattens as the wave approaches breaking. For the plunging breaker, the front face of the wave crest becomes very steep without much change in the rear face of the wave crest. The vertical asymmetry becomes larger with small changes in the preceding wave trough. The computed trend of the steepness and asymmetry parameters of waves close to breaking over the slope is consistent with the results from the experimental studies of deep water waves by Bonmarin (1989) and Lader (2002).

5. Conclusions

The two-phase flow model REEF3D has been used to model waves breaking over a sloping seabed. The Reynolds-averaged Navier–Stokes (RANS) equations are solved together with the level set method (LSM) for the free surface and the k–ω turbulence model. Numerical experiments are performed in order to investigate the hydrodynamic characteristics and geometric properties of plunging breakers over slopes. Comparison with similar results obtained for spilling breakers in Alagan Chella et al. (2015a) are also discussed. The results show that the numerical model is capable of describing the prominent physical flow characteristics such as the formation of forward overturning water jet, air pocket, splash-up, and the secondary wave during the breaking process. The numerical model shows a good match with the measurements by Ting and Kirby (1995, 1996) for the free surface elevation, horizontal and vertical particle velocities, wave envelope and turbulence intensity. The hydrodynamic characteristics of spilling and plunging breakers in terms of the wave height evolution and attenuation, horizontal and vertical velocity components, free surface profile evolution, and the geometric properties during the development of the breaking process are presented and discussed. This knowledge allows to learn and to understand more about the physical processes related to wave breaking. This will in turn improve the assessment of the hydrodynamic loads on offshore and coastal structures and the flow characteristics around them. The following main conclusions can be drawn from the numerical investigations:

- The variation of the breaker depth index (γ_b) of plunging breakers over slopes shows a similar trend as for the spilling breakers. On the other hand, the breaker height index (Ω_b) varies opposite to the trend of the spilling breakers, i.e. the breaker height index (Ω_b) increases as the slope becomes steeper. The breaker indices for the plunging breakers over a given slope for different offshore wave steepness (H_0/L_0) are consistent with the spilling breakers.
- For both spilling and plunging breakers over slopes, the wave profile asymmetry properties at the breaking point are found to be similar for the crest front steepness (ε), vertical asymmetry factor (λ) and horizontal asymmetry factor (μ), but different for the crest rear steepness (δ). The rear part of the wave crest of the plunging breakers does not change much during the interaction with slopes, while it does for spilling breakers.
- The crest front steepness (ε) increases and vertical asymmetry factor (λ) decreases as the offshore wave steepness (H_0/L_0) increases for plunging breakers which is consistent with that of spilling breakers. However, the crest rear steepness (δ) and horizontal asymmetry factor (μ) are almost independent of offshore wave steepness (H_0/L_0) for plunging breakers.
- Unlike spilling breakers over slopes, the wave profile asymmetry properties of plunging breakers, except the vertical asymmetry

Please cite this article as: M. Alagan Chella et al., Hydrodynamic characteristics and geometric properties of plunging and spilling breakers over impermeable slopes, Ocean Modelling (2015), http://dx.doi.org/10.1016/j.ocemod.2015.11.011

factor (λ), are less dependent on the seabed slope and the offshore wave steepness (H_0/L_0).

- The wave undergoes more deformation for the plunging breaker than for the spilling breaker as it breaks at a shallower water depth with a larger breaker height. Therefore, the wave height to water depth ratio H/d is larger for the plunging breaker than for the spilling breaker.
- The change in the initial wave characteristics of the wave approaching the breaking point is larger for the plunging breaker as it has a deeper wave base and experiences higher shoaling rate than for the spilling breaker.
- A rapid transition of the wave height occurs after breaking in the surf zone for the plunging breaker, while it is more gradual for the spilling breaker.
- The variation of the horizontal velocity component below the wave trough is almost constant over the water depth for the plunging breaker, while it is significant under the spilling breaker. It is noticed that the maximum horizontal velocity component occurs at the tip of the main wave crest and the secondary wave crest.
- For both spilling and plunging breakers, the maximum vertical particle velocity component becomes larger under the steep wave front. Although the kinematics of the main wave crest and the secondary wave crest are dominated by the horizontal velocity component, the vertical velocity component has a significant contribution in the formation of the secondary wave during splash-up.
- For spilling and plunging breakers, the physical flow process is found to have similar features such as the formation of a forward overturning water jet, air entrainment, splash-up, and the secondary wave during the breaking.
- For the spilling breaker, the wave crest becomes narrower with steeper wave front face and rear face and the wave trough depth flattens as the wave approaches breaking. For the plunging breaker, the wave crest becomes wider with steeper wave front face and broader rear face and small changes in the wave trough depth during the transition to breaking.

Acknowledgments

The authors would like to thank Dr. James Kirby and Dr. Ting Francis for sharing the experimental data. The work was supported by the Norwegian Research Center for Offshore Wind Technology (NOWITECH), Research Council of Norway (Contract no.193823). The authors would also like to thank NOTUR (Project no. NN9240K) for allocation of computational resources provided on the Vilje system at the super computing facilities at NTNU.

References

Adeyemo, M., 1968. Effect of beach slope and shoaling on wave asymmetry. In: Proceedings of the 11th conference on Coastal Engineering, pp. 145–172.
Alagan Chella, M., Bihs, H., Myrhaug, D., Muskulus, M., 2015a. Breaking characteristics and geometric properties of spilling breakers over slopes. Coast. Eng. 95, 4–19.
Alagan Chella, M., Bihs, H., Myrhaug, D., 2015b. Characteristics and profile asymmetry properties of waves breaking over an impermeable submerged reef. Coast. Eng. 100, 26–36.
Alagan Chella, M., Tørum, A., Myrhaug, D., 2012. An overview of wave impact forces on offshore wind turbine substructures. Energy Procedia 20, 217–226.
Banner, M., Peregrine, D.H., 1993. Wave breaking in deep water. Annu. Rev. Fluid Mech. 25, 373–397.
Basco, D.R., 1985. A qualitative description of wave breaking. J. Waterw. Port Coast. Ocean Eng. 3, 171–188.
Battjes, J.A., 1974. Surf similarity. In: Proceedings of the 14th Conference on Coastal Engineering, pp. 466–480.
Berthelsen, P.A., Faltinsen, O.M., 2008. A local directional ghost cell approach for incompressible viscous flow problems with irregular boundaries. J. Comput. Phys. 227, 4354–4397.
Bonmarin, P., 1989. Geometric properties of deep-water breaking waves. J. Fluid Mech. 209, 405–433.
Bradford, S.F., 2000. Numerical simulation of surf zone dynamics. J. Waterw. Port Coast. Ocean Eng. 126, 1–13.
Chorin, A., 1968. Numerical solution of the Navier-Stokes equations. Math. Comput. 22, 745–762.
Christensen, E.D., 2006. Large eddy simulation of spilling and plunging breakers. Coast. Eng. 53, 463–485.
Christensen, E.D., Deigaard, R., 2001. Large eddy simulation of breaking waves. Coast. Eng. 42, 53–86.
Cokelet, E., 1977. Breaking waves. Nature 267, 769–774.
Durbin, P.A., 2009. Limiters and wall treatments in applied turbulence modeling. Fluid Dyn. Res. 41, 1–18.
Emarat, N., Forehand, D.I., Christensen, E.D., Greated, C.A., 2012. Experimental and numerical investigation of the internal kinematics of a surf-zone plunging breaker. Eur. J. Mech. B/Fluids 32, 1–16.
Fenton, J.D., 1999. The cnoidal theory of water waves. In: Herbich, J.B. (Ed.), In: Developments in Offshore Engineering, Gulf, Houston. (Chapter 2)
Galvin, C.J., 1968. Breaker type classification on three laboratory beaches. J. Geophys. Res. 73, 3651–3659.
Griebel, M., Dornseifer, T., Neunhoeffer, T., 1998. Numerical Simulation in Fluid Dynamics, A Practical Introduction. SIAM.
Harlow, F.H., Welch, J.E., 1965. Numerical calculation of time-dependent viscous incompressible flow of fluid with free surface. Phys. Fluids 8, 2182–2189.
Hendrickson, K.L., 2005. Navier-Stokes simulations of steep breaking water waves with a coupled air-water interface. Massachusetts Institute of Technology (Ph.D. thesis).
Hieu, P.D., Katsutoshi, T., Ca, V.T., 2004. Numerical simulation of breaking waves using a two-phase flow model. Appl. Math. Model. 28, 983–1005.
Iversen, H.W., 1952. Laboratory study of breakers. In: Proceedings of the NBS Semicentennial Symposium on Gravity Waves, National Bureau of Standards Circular 521, pp. 9–32.
Iwata, K., Tomita, T., 1992. Variation of potential and kinetic wave energy in the surf zone. In: Proceedings of 23rd Conference on Coastal Engineering, pp. 336–349.
Jacobsen, N.G., Fuhrman, D.R., Fredsøe, J., 2012. A wave generation toolbox for the open-source cfd library: Openfoam. Int. J. Numer. Methods Fluids 70, 1073–1088.
Jiang, G.S., Shu, C.W., 1996. Efficient implementation of weighted ENO schemes. J. Comput. Phys. 126, 202–228.
Kjeldsen, S.P., Myrhaug, D., 1978. Kinematics and dynamics of breaking waves. Technical Report. River and Harbour Laboratory (NHL), The Norwegian Institute of Technology.
Lader, P.F., 2002. Geometry and kinematics of breaking waves. Norwegian University of Science and Technology (Ph.D. thesis)..
Larsen, J., Dancy, H., 1983. Open boundaries in short wave simulations—a new approach. Coast. Eng. 7, 285–297.
Lemos, C.M., 1992. A simple numerical technique for turbulent flows with free surfaces. Int. J. Numer. Methods Fluids 15, 127–146.
Lin, P., Liu, P.L.F., 1998. A numerical study of breaking waves in the surf zone. J. Fluid Mech. 359, 239–264.
Lubin, P., Vincent, S., Abadie, S., Caltagirone, J.P., 2006. Three-dimensional large eddy simulation of air entrainment under plunging breaking waves. Coast. Eng. 53, 631–655.
Ma, G., Shi, F., Kirby, J.T., 2011. A polydisperse two-fluid model for surf zone bubble simulation. J. Geophys. Res. 116, 1978–2012.
Mayer, S., Madsen, P.A., 2000. Simulation of breaking waves in the surf zone using a Navier-Stokes solver. In: Coastal Engineering Proceedings, pp. 928–941.
Miller, R.L., 1987. Role of Vortices in Surf Zone Prediction: Sedimentation and Wave Forces. The Society of Economic Paleontologists and Mineralogists, Special Publications 92–114.
Mizuguchi, M., 1986. Experimental study on kinematics and dynamics of wave breaking. In: Proceedings of 20th Conference on Coastal Engineering, pp. 589–603.
Mo, W., Jensen, A., Liu, P.L.F., 2013. Plunging solitary wave and its interaction with a slender cylinder on a sloping beach. Ocean Eng. 74, 48–60.
Moraga, F., Carrica, P., Drew, D., Lahey Jr, R., 2008. A sub-grid air entrainment model for breaking bow waves and naval surface ships. Comput. Fluids 37, 281–298.
Nadaoka, K., Hino, M., Koyano, Y., 1989. Structure of the turbulent flow field under breaking waves in the surf zone. J. Fluid Mech. 204, 359–387.
Naot, D., Rodi, W., 1982. Calculation of secondary currents in channel flow. J. Hydr. Div., ASCE 108, 948–968.
Osher, S., Sethian, J.A., 1988. Fronts propagating with curvature-dependent speed: algorithms based on Hamilton-Jacobi formulations. J. Comput. Phys. 79, 12–49.
Peng, D., Merriman, B., Osher, S., Zhao, H., Kang, M., 1999. A PDE-based fast local level set method. J. Comput. Phys. 155, 410–438.
Peregrine, D., Svendsen, I., 1978. Spilling breakers, bores and hydraulic jumps. In: Proceedings of the 16th Conference on Coastal Engineering, pp. 540–550.
Peregrine, D.H., 1983. Breaking waves on beaches. Annu. Rev. Fluid Mech. 15, 149–178.
Perlin, M., Choi, W., Tian, Z., 2013. Breaking waves in deep and intermediate waters. Annu. Rev. Fluid Mech. 115–145.
Shi, F., Kirby, J.T., Ma, G., 2010. Modeling quiescent phase transport of air bubbles induced by breaking waves. Ocean Modell. 35, 105–117.
Shu, C.W., Osher, S., 1988. Efficient implementation of essentially non-oscillatory shock capturing schemes. J. Comput. Phys. 77, 439–471.
Smith, E.R., Kraus, N.C., 1990. Laboratory study on macro-features of wave breaking over bars and artificial reefs. Technical Report. Coast. Eng. Research Center.
Stive, M., Wind, H., 1982. A study of radiation stress and set-up in the nearshore region. Coast. Eng. 6, 1–26.
Sussman, M., Smereka, P., Osher, S., 1994. A level set approach for computing solutions to incompressible two-phase flow. J. Comput. Phys. 114, 146–159.
Svendsen, I.A., Madsen, P.A., Hansen, J.B., 1978. Wave characteristics in the surf zone. In: Proceedings of the Coastal Engineering Conference, pp. 520–539.

Please cite this article as: M. Alagan Chella et al., Hydrodynamic characteristics and geometric properties of plunging and spilling breakers over impermeable slopes, Ocean Modelling (2015), http://dx.doi.org/10.1016/j.ocemod.2015.11.011

Ting, F.C., Kirby, J.T., 1994. Observation of undertow and turbulence in a laboratory surf zone. Coast. Eng. 24, 51–80.
Ting, F.C., Kirby, J.T., 1995. Dynamics of surf-zone turbulence in a strong plunging breaker. Coast. Eng. 24, 177–204.
Ting, F.C.K., Kirby, J.T., 1996. Dynamics of surf-zone turbulence in a spilling breaker. Coast. Eng. 27, 131–160.
van der, V.H., 1992. Bi-CGSTAB: a fast and smoothly converging variant of Bi-CG for the solution of nonsymmetric linear systems. SIAM J. Sci. Stat. Comput. 13, 631–644.
Wang, Z., Zou, Q., Reeve, D., 2009. Simulation of spilling breaking waves using a two phase flow cfd model. Comput. Fluids 38, 1995–2005.
Wilcox, D.C., 1994. Turbulence Modeling for CFD. DCW Industries Inc., La Canada, California.
Xie, Z., 2013. Two-phase flow modelling of spilling and plunging breaking waves. Appl. Math. Model. 37, 3698–3713.
Zhao, Q., Armfield, S., Tanimoto, K., 2004. Numerical simulation of breaking waves by a multi-scale turbulence model. Coast. Eng. 51, 53–80.

Please cite this article as: M. Alagan Chella et al., Hydrodynamic characteristics and geometric properties of plunging and spilling breakers over impermeable slopes, Ocean Modelling (2015), http://dx.doi.org/10.1016/j.ocemod.2015.11.011

6.5 Paper 5

Characteristics and profile asymmetry properties of waves breaking over an impermeable submerged reef

Alagan Chella, M., Bihs, H., Myrhaug, D.
Coastal Engineering, 2015, Vol. 100, pp. 26-36
DOI: 10.1016/j.coastaleng.2015.03.008

Paper 5

Coastal Engineering 100 (2015) 26–36

Contents lists available at ScienceDirect

Coastal Engineering

journal homepage: www.elsevier.com/locate/coastaleng

Characteristics and profile asymmetry properties of waves breaking over an impermeable submerged reef

Mayilvahanan Alagan Chella [a,*], Hans Bihs [a], Dag Myrhaug [b]

[a] Department of Civil and Transport Engineering, Norwegian University of Science and Technology (NTNU), NO-7491 Trondheim, Norway
[b] Department of Marine Technology, Norwegian University of Science and Technology (NTNU), NO-7491 Trondheim, Norway

ARTICLE INFO

Article history:
Received 12 September 2014
Received in revised form 18 March 2015
Accepted 19 March 2015
Available online xxxx

Keywords:
Breaking waves
Profile asymmetry properties
Numerical modeling
Breaker indices
Submerged reef

ABSTRACT

In the present study, a 3D two-phase flow CFD model that solves the unsteady, incompressible Reynolds-Averaged Navier–Stokes equations has been used to simulate breaking waves over an impermeable submerged reef. The level set method is used to capture the complex free surface and the turbulence is described by the $k-\omega$ turbulence model. The numerical model was evaluated by comparing the computed results with the experimental data by Blenkinsopp and Chaplin (2008) and the computed results are in good agreement with the measured data. The computed results over the submerged reef clearly depict the flow features associated with the breaking process such as the complex interface deformation, the formation of the plunger vortex and the downstream vortex, the splash-up phenomenon and the movement of the enclosed air pocket. The main aim of the study was to investigate the effect of the offshore wave steepness and the water depth above the reef crest on the characteristics and the profile asymmetric properties of waves breaking over a submerged reef. The computed results suggest that the water depth over the reef crest affects the prominent characteristics of waves breaking over a reef such as breaker type, water depth at breaking, breaker indices and geometric properties.

1. Introduction

Wave breaking is a prominent research subject in coastal and marine engineering. It is a two phase flow phenomenon involving air and water, and it strongly influences the air–sea interaction by enhancing mass, momentum and energy transfer between the phases. It thereby limits the wave steepness, generating vorticity and turbulence, enhancing wave energy dissipation, entraining air and white water formation. Despite a considerable number of experimental, numerical and theoretical studies and field observations have been carried out to investigate the process, the wave breaking mechanism is not completely understood. A comprehensive examination of breaking wave properties is inevitable to understand the mechanism of wave breaking and thus the description of the breaking process. Wave breaking over a submerged reef primarily depends on the tidal level and the characteristics of the incident waves. Moreover, an accurate description of waves breaking over submerged structures has always been a central issue in estimation of hydrodynamic loads on marine structures.

Numerous studies have attempted to explain the wave breaking process and their characteristics, and a detailed literature review on wave breaking in deep and shallow water can be found in Cokelet (1977), Peregrine (1983), Basco (1985), Banner and Peregrine (1993), and Perlin et al. (2013). The characteristics of wave breaking over slopes are strongly affected by the local environmental parameters, water depth (d), offshore wave steepness (H_0/L_0) and sea bed slope (m). On plane slopes, the offshore wave steepness and seabed slope determine the breaker characteristics (Battjes, 1974; Galvin, 1968; Iversen, 1952). In the case of a submerged reef, however, wave breaking is strongly influenced by the water depth and the wave height at the crest of the reef. This has been studied in laboratory experiments by Gourlay (1994), Smith and Kraus (1990), Blenkinsopp and Chaplin (2008), and Yao et al. (2013). They suggested that the application of the surf similarity parameter proposed by Battjes (1974) is inappropriate to categorize the breaker type of waves breaking over submerged structures. Several studies on submerged breakwaters have revealed the role of the water depth at the reef crest and the offshore wave height on the wave transformation properties (Ahrens, 1987; Iwata et al., 1996; Kawasaki and Iwata, 1998; Ting and Kim, 1994). Hence, the wave breaking process over a submerged reef with a fixed crest height is very sensitive to the water depth and the wave height at the crest. During the course of the tidal cycles, the water depth over a submerged reef continuously changes, which has a substantial impact on the wave breaking process and its characteristics. Blenkinsopp and Chaplin (2008) performed a series of experiments to investigate the effect of the water level on the characteristics of the breaking process over a submerged reef with a slope of 1/10. They found that, although the water level does not strongly affect the breaker indices unlike on plane slopes, it influences the breaker type, reflection and transmission characteristics. However, a relationship exists between the asymmetric parameters

* Corresponding author.
E-mail address: acm@ntnu.no (M. Alagan Chella).

http://dx.doi.org/10.1016/j.coastaleng.2015.03.008
0378-3839/

and the breaker type and this has been first reported by Kjeldsen and Myrhaug (1978). They introduced steepness and asymmetry parameters to define the asymmetry of the wave profile: crest front steepness (ε), crest rear steepness (δ), the vertical asymmetry factor (λ) and the horizontal asymmetry factor (μ) as depicted in Fig. 1(a). Additionally, the geometric properties of breaking waves can be related to the breaker type, which plays a key role in estimation of breaking wave forces on marine structures (Alagan Chella et al., 2012). Importantly, the breaker shape influences the size and strength of the breaker vortices. Research has been reported on the geometric parameters of breaking waves in deep water (Babanin et al., 2010; Bonmarin, 1989; Kjeldsen and Myrhaug, 1978; Lader, 2002) and in shallow water (Adeyemo, 1968; Ippen and Kulin, 1954; Iwagaki and Sakai, 1972; Miller and Zeigler, 1964).

Several surface wave theories can only be applied to describe the waves with small fluid accelerations compared to gravity such as Airy's and Stokes theory based on small wave steepness approximations, solitary and cnoidal wave theories based on the nonlinear shallow water equations and the Korteweg-De Vries equations (Babanin, 2011). Longuet-Higgins and Cokelet (1976) first proposed a boundary element method based on two dimensional potential theory and conformal mapping to model periodic breaking waves in deep water. Later the method was modified by Vinje and Brevig (1981), using the physical plane representation to finite water depth. The main flow features of wave transformation over submerged structures are the creation of higher harmonics and vortices. It is possible to model the breaking process using the potential theory prior to the water jet impingement on the water surface by the breaker (Chen et al., 1999; Christensen, 1998). Most studies in the field of submerged breakwater structures have only focused on the prediction of the reflection and transmission characteristics of waves for a given environmental condition. The theoretical and numerical description of the flow problem was based on potential theory which does not account for the rotational flow. Ting and Kim (1994) investigated the wave transformation over a submerged structure and concluded that potential theory cannot be applied to model the flow process such as flow separation and energy dissipation. However, the generation and dissipation of vortices during the breaking process are created by rotational flow (not potential) (Takikawa et al., 1997). In addition to that, viscous fluid forces and associated turbulence become significant during the wave breaking process.

Moreover, measures of incipient breaking of regular waves such as geometric, kinematic and dynamic breaking criteria are connected to the limiting value of wave steepness, horizontal fluid velocity and downward vertical acceleration, respectively. Much uncertainty still exists in defining incipient breaking and breaking onset. Importantly, these criteria are a function of many physical parameters and comprehensive measurements are relatively limited and are still challenging to obtain. Some of the indirect analytical approaches, such as the Boussinesq approximation, are based on the interpretation of the energy dissipation due to breaking with pre-breaking and post-breaking wave properties and cannot describe the breaking process completely (Babanin, 2011). Numerical modeling of wave breaking becomes challenging due to the intricacy in describing the physical processes involved such as air–sea interaction, vorticity generation, overturning motion, and the air entrainment. A straightforward approach to describe the breaking process numerically is to solve the fundamental fluid dynamic equations with Computational Fluid Dynamics (CFD). The method is able to capture the prominent flow properties during breaking without specifying breaking criteria or relying on empirical criteria. CFD models that are based on a single-phase flow which concerns only liquid flow and disregards the air phase during breaking have been presented by e.g. Lin and Liu (1998), Bradford (2000) and Zhao et al. (2004). Computational studies of the breaking process with two-phase flow CFD models have gained much attention in recent years by Chen et al. (1999), Christensen and Deigaard (2001), Hieu et al. (2004), Christensen (2006), Wang et al. (2009a, 2009b), Bakhtyar et al. (2013), Jacobsen et al. (2012) and Alagan Chella et al. (2015). Two-phase flow CFD models account for the interaction of air above the free surface, density difference at the interface and entrapped air during breaking.

The main objective of the present numerical study is to investigate the effects of offshore wave steepness and water depth on the characteristics and geometry properties of waves breaking over a submerged reef. A three-dimensional (3D) numerical wave tank based on two-phase flow CFD model is used in a two-dimensional (2D) setup to model waves breaking over a submerged reef. The present numerical model is validated by comparing the numerical results to experimental data by Blenkinsopp and Chaplin (2008), and the computed results agree well with the experimental data. The wave breaking characteristics such as the incipient breaker height and water depth at breaking, incipient breaker indices and wave profile asymmetry properties are investigated in detail to understand the physical features associated with the breaking process. Moreover, the present numerical investigation is limited to the wave transformation up to the inner breaking region (Svendsen et al., 1978).

2. Computational method

2.1. Governing equations

In the present 3D numerical model, the incompressible Reynolds-Averaged Navier–Stokes equations are used to describe the two-phase viscous flow. The governing equations are:

$$\frac{\partial U_i}{\partial x_i} = 0 \tag{1}$$

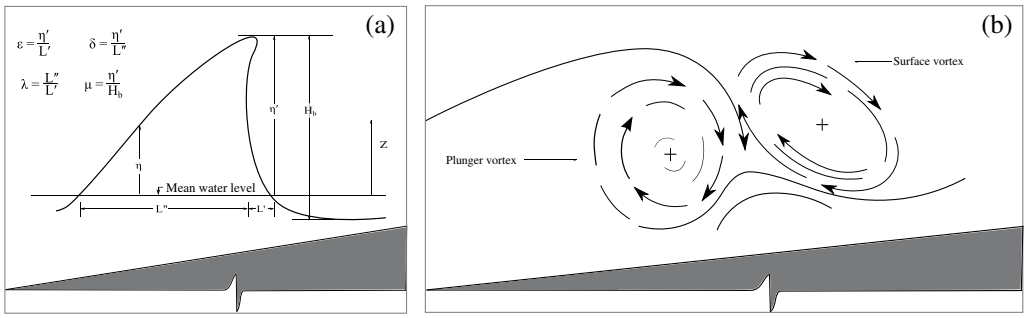

Fig. 1. (a) Definition sketch of local wave profile asymmetry parameters following Kjeldsen and Myrhaug (1978) and (b) schematic of generation of plunger vortex and surface roller during breaking following Basco (1985).

$$\frac{\partial U_i}{\partial t} + U_j \frac{\partial U_i}{\partial x_j} = -\frac{1}{\rho}\frac{\partial P}{\partial x_i} + \frac{\partial}{\partial x_j}\left[(\nu + \nu_t)\left(\frac{\partial U_i}{\partial x_j} + \frac{\partial U_j}{\partial x_i}\right)\right] + g_i. \quad (2)$$

U is the velocity averaged over time t, ρ is the fluid density, P is the pressure, ν is the kinematic viscosity, ν_t is the eddy viscosity and g is the gravity term. Since the numerical model is used as a numerical wave tank, higher order schemes are employed to avoid the unphysical excessive damping of free surface waves. The discretization of the convection term of the RANS equations is accomplished by the 5-th order Weighted Essentially Non-Oscillatory (WENO) scheme in the conservative finite difference version (Jiang and Shu, 1996). This WENO scheme consists of three substensils that are weighted based on the local smoothness of the discretized function. Moreover, this scheme provides very robust numerical stability without causing numerical oscillations.

Time discretization is performed with a third-order accurate total variation diminishing (TVD) Runge–Kutta scheme consisting of three Euler substeps (Shu and Osher, 1988). The velocities at each Euler substep are obtained by solving the pressure term with the projection method. The BiCGStab algorithm (van der Vorst, 1992) with Jacobi preconditioning calculates the pressure from the Poisson equation. It is well known that a large amount of wave energy is dissipated as turbulence in the free surface layer during the breaking process. The turbulence is modeled with the RANS equations coupled with the $k-\omega$ model. A ghost-cell immersed boundary method based upon the local directional by Berthelsen and Faltinsen (2008) is employed to account for the solid boundaries of the fluid domain. In addition to that, complex geometries can be represented without specifying the boundary conditions explicitly.

2.2. Free surface

One of the major challenges in the modeling of the breaking process is to describe the free surface changes i.e. interface deformation. Here, the level set method (Osher and Sethian, 1988) is chosen since the free surface changes can be obtained without any special treatments at the interface. The level set method is an Eulerian method and represents the interface between the two phases water and air. The interface is the zero level set of the smooth signed distance function $\phi\left(\vec{x},t\right)$. At any point on the computational domain, the level set function gives the distance from the interface and the sign of the function marks the fluid phase as follows:

$$\phi\left(\vec{x},t\right)\begin{cases} > & 0 \ if \ \vec{x} \in \text{water} \\ = & 0 \ if \ \vec{x} \in \Gamma \\ < & 0 \ if \ \vec{x} \in \text{air} \end{cases}. \quad (3)$$

Table 1
List of computational cases.

Simulation cases	Simulation no.	Offshore wave steepness, H_0/L_0	Reference water depth, d (m)
Based on offshore wave steepness (H_0/L_0): Case (A)	1	0.02	0.7
	2	0.03	
	3	0.04	
	4	0.05	
	5	0.06	
	6	0.07	
Based on reference water depth (d): Case (B)	7	0.033	0.65
	8		0.68
	9		0.69
	10		0.70
	11		0.71
	12		0.72

Also the Eikonal equation $|\nabla\phi| = 1$ is valid. When the interface is moved under an externally generated velocity field $\vec{v}$, a convection equation for the level set function is obtained:

$$\frac{\partial \phi}{\partial t} + U_j \frac{\partial \phi}{\partial x_j} = 0. \quad (4)$$

The fluid properties such as the density ρ and the viscosity ν can be defined for the computational domain with the level set method. However, the discontinuity in the fluid properties across the interface can cause numerical instabilities in the solution. This discontinuity is removed by smoothing the fluid properties over a small distance in the region close to the interface with a Heaviside function $H(\phi)$. This region is 2ϵ thick, with ϵ being proportional to the grid spacing dx. The density and the viscosity from the level set function can be written as:

$$\begin{aligned} \rho(\phi) &= \rho_{water}H(\phi) + \rho_{air}(1-H(\phi)), \\ \nu(\phi) &= \nu_{water}H(\phi) + \nu_{air}(1-H(\phi)) \end{aligned} \quad (5)$$

and the Heaviside function:

$$H(\phi) = \begin{cases} 0 & \text{if } \phi < -\epsilon \\ \frac{1}{2}\left(1 + \frac{\phi}{\epsilon} + \frac{1}{\Pi}sin\left(\frac{\Pi\phi}{\epsilon}\right)\right) & \text{if } |\phi| < \epsilon \\ 1 & \text{if } \phi > \epsilon \end{cases} \quad (6)$$

2.3. Numerical wave generation and absorption

The present numerical model is used as a numerical wave tank. Wave generation is performed at the inflow boundary and waves are absorbed at the outflow boundary using the relaxation method

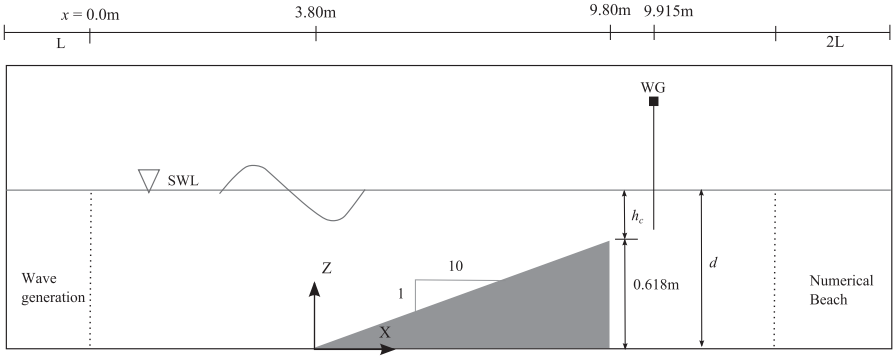

Fig. 2. Computational domain.

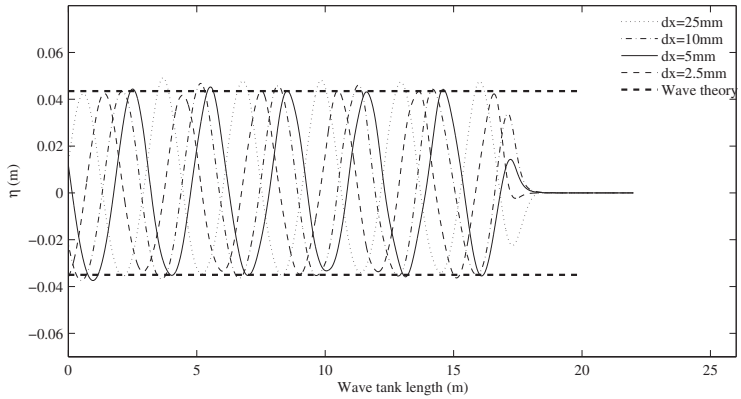

Fig. 3. Grid sensitivity study on computed free surface elevations.

presented by Larsen and Dancy (1983). With the relaxation method, reflected waves from the reef face are absorbed at the inlet boundary of the wave tank. If a nonlinear analytical solution is known, it can be used as the imposed solution to moderate the computational solution. This is a relatively straightforward approach for the wave generation in a numerical wave tank and proves to be efficient, as this has been presented by Mayer et al. (1998), Engsig-Karup (2006) and Jacobsen et al. (2012). Waves are absorbed at the outlet boundary with a relaxation zone where the velocity components are gradually reduced to zero and the water surface and the pressure follows the hydrostatic distribution at the still water level.

3. Computational domain, cases and parameters

In order to validate the present numerical model, the numerical results are compared with the experimental data measured by Blenkinsopp and Chaplin (2008). The numerical wave tank consists of a submerged reef with a height of 0.62 m and a slope of 1/10, located 3.8 m from the wave generation zone as shown in Fig. 2. The numerical set-up, incident wave parameters and the coordinate system are the same as the experimental conditions presented in Blenkinsopp and Chaplin (2008). The computed results of two experiment cases with different reef crest submergences, $h_c = 0.032$ m and 0.102 m ($d = 0.65$ m and 0.72 m) are compared to the experimental measurements. The free surface elevations are obtained using a wave gauge 0.115 m after the crest of the reef. The computational domain is discretized with a uniform grid size in both directions x and y. In the numerical simulations, five waves are generated for each run.

The present numerical cases explore the breaking characteristics and geometric properties of waves breaking over the submerged reef and their dependence on offshore wave steepness, (H_0/L_0, H_0 and L_0 are deep water wave height and wave length, respectively, case A) and water depth (d, case B) as listed in Table 1. Case A tests six different offshore wave steepnesses ranging from 0.02 to 0.07 at a fixed water depth, and case B examines a wave with a fixed offshore wave steepness of 0.033 at six different water depths from 0.65 m to 0.72 m.

Most of the previous studies have been conducted to establish relationships between the characteristics of waves at the breaking point. The breaking point is assessed in the present study as the point where part of the wave front becomes vertical. Thus, the computed water depth (d_b) and wave height (H_b) at the breaking point are used to calculate the breaker indices. The breaker depth index, γ_b, is the ratio of the breaker height H_b to the water depth at breaking d_b:

$$\gamma_b = \frac{H_b}{d_b}. \tag{7}$$

The breaker height index, Ω_b is the ratio of the breaker height H_b to offshore wave height H_0:

$$\Omega_b = \frac{H_b}{H_0}. \tag{8}$$

It is well known that the wave profile becomes asymmetric as it approaches the breaking point and cannot be described by the wave steepness (H/L). Hence, additional parameters are required to describe the asymmetric shape of the wave at breaking. Four additional geometric parameters proposed by Kjeldsen and Myrhaug (1978) are used in this study to describe the asymmetry of the wave profile as shown in Fig. 1(a).

3.1. Grid dependence study

Since the numerical model uses a uniform Cartesian grid, the computational domain is discretized with a uniform grid size in both directions x and y. In order to investigate the effect of grid sizes (dx) on the simulation results, four different grid sizes, $dx = 25$ mm, 10 mm, 5 mm and 2.5 mm, are examined. Fifth-order Stokes waves with $H = 0.12$ m and $T = 1.5$ s are simulated in the numerical wave tank without any structure. The free surface elevations for the different grid sizes are compared with the maximum and minimum values of the theoretical result as shown in Fig. 3. It appears that the difference between the

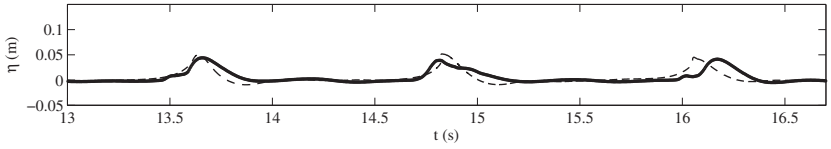

Fig. 4. Comparison of simulated and measured wave surface elevation for the numerical case at $d = 0.65$ m. Dashed lines: present numerical model; Solid lines: experimental data from Blenkinsopp and Chaplin (2008).

numerical results and the theoretical result decreases as the grid size decreases, showing that the wave surface elevations for $dx = 5$ mm and 2.5 mm, agree well with the theoretical results. However, the grid size $dx = 2.5$ mm with 1248 cells per wave length demands more computation time than $dx = 5$ mm with 624 cells. Therefore, in order to perform efficient simulations within a reasonable computing time, the grid size $dx = 5$ mm is selected for the present study.

4. Results and discussion

4.1. Numerical model evaluation

The computed wave surface elevation of two experimental cases with different water depths are compared with the experimental measurements by Blenkinsopp and Chaplin (2008). Figs. 4 and 5 show the comparison of computed and measured wave surface elevation for the simulation case with $d = 0.65$ m and $d = 0.72$ m, respectively. The wave surface elevation is computed 0.115 m behind the reef crest, which is an inner breaking region of the surf zone as defined in Svendsen et al. (1978). Although the numerical results are in reasonable agreement with the experimental data for both the cases, the computed wave crests are slightly higher for $d = 0.65$ and slightly lower for $d = 0.72$ than the experimental data. The reason is unclear but this might be related to the energy dissipation in the inner breaking region where the large deterministic flow structures disintegrate into smaller flow structures with extreme chaotic and turbulent behavior. It is therefore difficult to predict the free surface elevation in this region. However, the present numerical model is capable of calculating the free surface elevation in the inner breaking region with satisfactory accuracy.

4.2. Waves breaking over the reef

The characteristics of waves breaking over a submerged reef solely depend on the wave height and the water depth at the reef crest unlike over a sloping seabed. Hence, the breaker types cannot be described by the surf similarity parameter which is more appropriate for plane slopes. During the breaking process, the return flow is created seaward in order to balance the shoreward mass flux created in the overturning wave crest. The interaction between the incoming breaker in the upstream side and the seaward return flow of the preceding wave from the downstream side strongly influences the breaking process and thus the characteristics of breaking waves. This effect has been studied in detail by Smith and Kraus (1990) and Blenkinsopp and Chaplin (2008). It is highly challenging to capture the seaward return flow that is generated during the breaking process experimentally and numerically since the flow pattern becomes complex during the extreme changes in the gross mass flux distribution. The initial evolution of the overturning wave crest also causes drastic changes in the free surface. Moreover, Blenkinsopp and Chaplin (2008) have not measured the return flow in the experimental investigation and therefore, the experimental data is not available to compare against the numerical results.

Fig. 6 shows the changes in the wave surface profile and the velocity during the breaking process for the wave with $H_0/L_0 = 0.033$ at $d = 0.65$ m. The wave profile changes with velocity variation during the breaking process clearly depict that a portion of the wave crest with higher velocity moves forward faster than the rest of the wave.

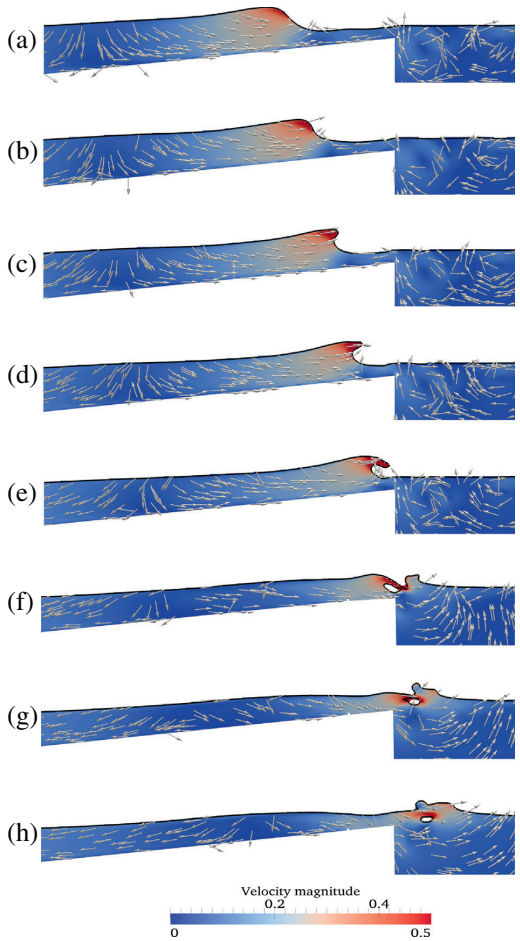

Fig. 6. Simulated free surface profile with velocity (m/s) variation during wave breaking over the reef from 9.5 s to 9.9 s with a time step of 0.05 s (a to h) for the simulation case $H_0/L_0 = 0.033$ and $d = 0.65$ m.

Initially, the wave reaches the breaking point as most of the wave front becomes vertical (Fig. 6(a) and (b)). Then the wave propagates further and the wave crest overturns with an ejecting water jet emanating a plunger vortex as seen in Fig. 6(c) to (e). When the overturned and ejected wave front hits the free surface at the base of the wave, it almost falls over the wave trough of the preceding wave and generates a surface roller. Then water splashes up causing a rise in the water surface with an air pocket inside the water as shown in Fig. 6(f) to (h). The two main turbulence zones addressed by Basco (1985) are the toe of the surface roller due to interfacial shear and the outermost part of the plunging vortex as shown in Fig. 1(b). An extreme changeover

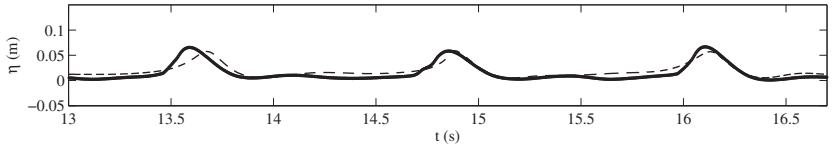

Fig. 5. Comparison of simulated and measured wave surface elevation for the numerical case at $d = 0.72$ m. Dashed lines: present numerical model; Solid lines: experimental data from Blenkinsopp and Chaplin (2008).

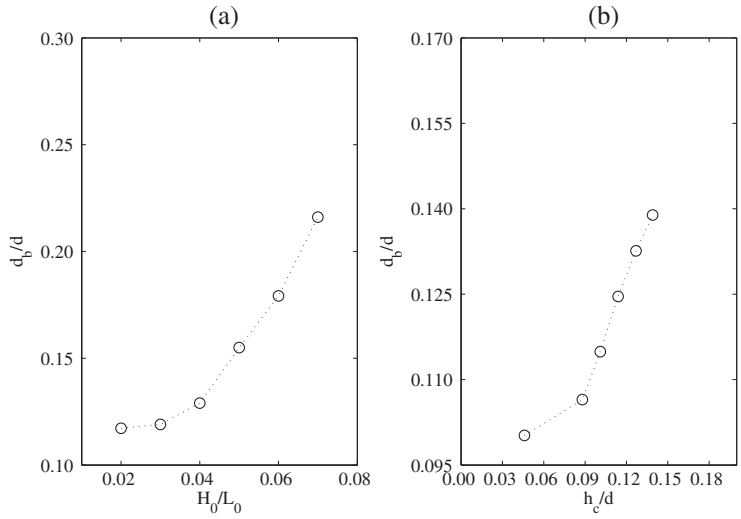

Fig. 7. Simulated non-dimensional water depth at breaking (d_b/d) as a function of (a) offshore wave steepness (H_0/L_0) and (b) relative water depth (h_c/d).

from irrotational flow to rotational flow leads to increased vorticity and turbulence as the wave approaches the beach and eventually violent mixing of air and water occurs. It is worth to notice that the impingement of the rotating plunging vortex is causing a secondary wave with new wave characteristics that propagates shoreward as shown in Fig. 6(f) to (h). Moreover, the numerical prediction of the flow pattern and the wave profile changes are very similar to the observation of the flow features of plunging breakers over plane slopes by Basco (1985).

As Fig. 6(a) to (e) shows, a clockwise vortex is created behind the reef during the breaking process. Initially the size of the vortex is small and it increases as the wave propagates over the reef in order to balance the upstream energy rise in the form of a plunging jet. When the wave trough propagates in the vicinity of the reef crest, the return flow is established around the corner of the reef which opposes the upstream flow. Therefore the wave breaking occurs early further offshore due to the combined effect of the reef face friction and the return flow. The vortex further rises up and the size diminishes as the plunger vortex at the wave crest develops. Finally, the downstream vortex weakens and decays rapidly due to the interaction with the plunger vortex upstream. In addition, the downstream vortex size becomes larger as the water depth over the reef crest is increased. This is consistent with those of Iwata et al. (1996), Ting and Kim (1994), and Chang et al. (2005) who reported the return flow due to the vortex formation behind the submerged structures. Hence, the numerical model is able to capture the complex interface changes and flow features during breaking process with reasonable accuracy. However, it should be noted that the details of the flow need to be verified against data in order to check the validity of the simulations.

4.3. Characteristics of waves breaking over the reef

The breaking characteristics such as breaker water depth, breaker depth index and breaker height index are examined for different offshore wave steepnesses (case A) and different water depths (case B) as listed in Table 1.

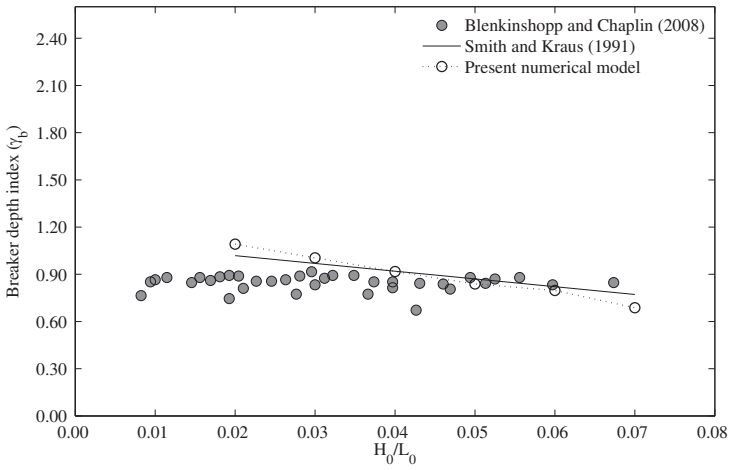

Fig. 8. Breaker depth index (γ_b) as a function of offshore wave steepness (H_0/L_0).

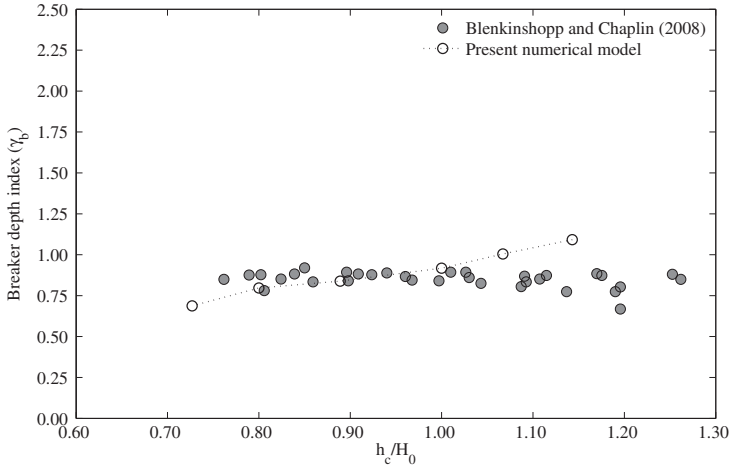

Fig. 9. Breaker depth index (γ_b) as a function of relative crest submergence (h_c/H_0).

4.3.1. Incipient wave breaking

Fig. 7 shows the non-dimensional breaker depth (d_b/d) versus the offshore wave steepness (H_0/L_0) and the relative water depth (h_c/d). It appears that d_b/d increases with increasing H_0/L_0 and increasing h_c/d. Therefore, waves over the reef break further offshore at larger water depth (d_b) as H_0/L_0 and h_c become larger, corresponding to $H_0/L_0 = 0.07$, $d_b/d = 0.216$ and $h_c/d_0 = 0.14$, $d_b/d = 0.14$ in Fig. 7. This means that waves with larger H_0/L_0 reaches the breaking point sooner with smaller crest deformation than waves with lower H_0/L_0, which follows the same trend of results on plane slopes. But the crest submergence (h_c) strongly affects the breaker depth (d_b). This suggests that waves propagating over the submerged reef with larger h_c experience more partial reflections, return flow and break further offshore at larger d_b. This also agrees with the experimental observation by Blenkinsopp and Chaplin (2008) and the theoretical study by Battjes (1974). Moreover, the present results appear to be different from the behavior of waves over plane slopes (Rattanapitikon and Shibayama, 2006) and submerged breakwaters (Kawasaki and Iwata, 1998), where d_b decreases as the water depth increases. It seems possible that waves breaking over the submerged reef are strongly influenced by the return flow due to the downstream clockwise vortex, which continues to grow with increasing water depth over the reef crest as presented in Section 4.2. Therefore, waves break further offshore as the reef crest submergence increases.

4.3.2. Breaker depth index (γ_b) and breaker height index (Ω_b)

Fig. 8 presents the comparison of the computed and the measured breaker depth index (γ_b) for different offshore wave steepnesses (H_0/L_0). It appears that γ_b decreases with increasing H_0/L_0, although the experimental data by Blenkinsopp and Chaplin (2008) do not vary much versus H_0/L_0. However, the computed results are in good agreement with experimental data for H_0/L_0 in the range of 0.03 to 0.06. In particular, the computed results are slightly higher and slightly lower than the experimental results for $H_0/L_0 < 0.03$ and $H_0/L_0 > 0.06$, respectively. Moreover, the numerical prediction follows the experimental trend for waves breaking on plane slopes of 1/10 reported by Smith and Kraus (1990).

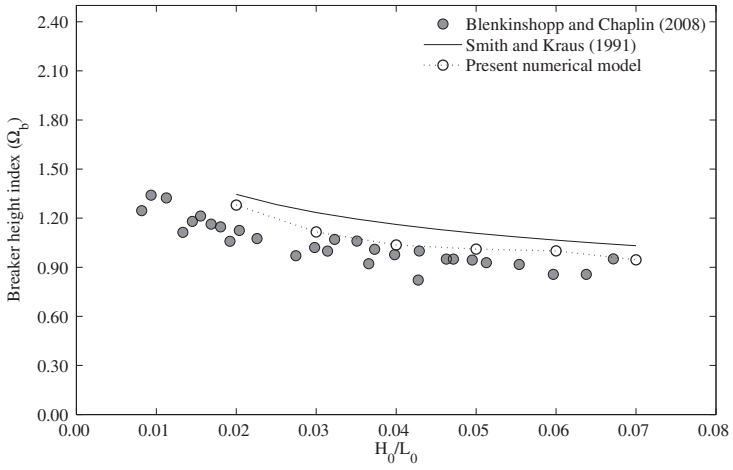

Fig. 10. Breaker height index (Ω_b) as a function of offshore wave steepness (H_0/L_0).

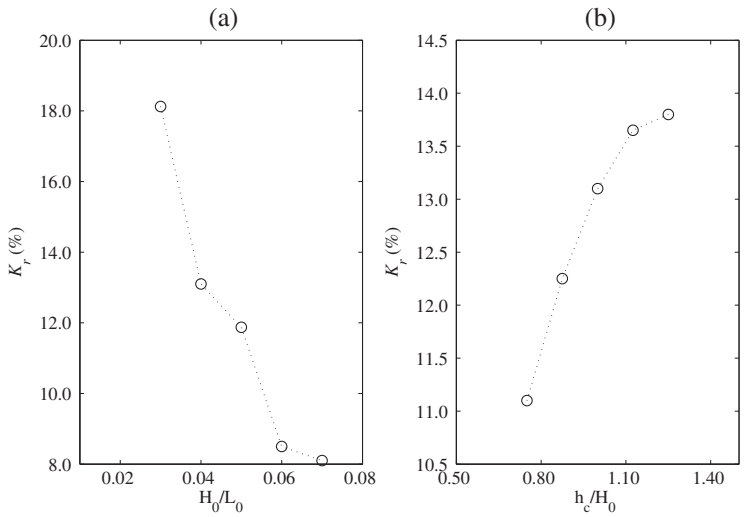

Fig. 11. Measured reflection coefficient (K_r) by Blenkinsopp and Chaplin (2008) as a function of (a) offshore wave steepness (H_0/L_0) and (b) relative water depth (h_c/H_0).

Fig. 9 shows the comparison of the computed and measured breaker depth index (γ_b) for different relative crest submergence h_c/H_0. It appears that γ_b increases slightly as h_c/H_0 increases for the computations, while γ_b seems to be invariant with h_c/H_0 in the experiments. The computed results are slightly higher and slightly lower than the experiments for $h_c/H_0 > 1.0$ and $h_c/H_0 < 0.8$, respectively. Moreover, the computed results agree well with the experimental data for h_c/H_0 in the range of 0.8 to 1.0. It is possible that waves over larger h_c/H_0 break further onshore at higher d_b with larger H_b, corresponding to $h_c/H_0 = 1.143$ and $\gamma_b = 1.09$ (Fig. 9), and $\Omega_b = 1.28$ (Fig. 12).

Fig. 10 presents comparison of the computed and the measured breaker height index (Ω_b) for different offshore wave steepnesses (H_0/L_0), showing that Ω_b decreases as H_0/L_0 increases for both computations and experiments. This is also the case for the Smith and Kraus (1990) experimental results on plane slopes. It appears that the present computations represent an upper bound of the Blenkinsopp and Chaplin (2008) data.

Fig. 11 shows the measured reflection coefficient for different offshore wave steepnesses (H_0/L_0) and different relative water depths (h_c/H_0). It appears that the reflection coefficient (K_r) decreases as H_0/L_0 increases and increases as (h_c/H_0) increases. This suggests that the wave with small H_0/L_0 experiences more reflections from the reef face, undergoing more deformation during shoaling than the waves with larger H_0/L_0, and reaches the maximum height before it breaks. Similar results have been found by Smith and Kraus (1990), Battjes (1974), and Blenkinsopp and Chaplin (2008).

Fig. 12 shows comparison of the computed and the measured breaker height index (Ω_b) for different relative crest submergence h_c/H_0. It appears that Ω_b increases slightly as h_c/H_0 increases, which agrees well with the experimental data by Blenkinsopp and Chaplin (2008). However, the computed dependence of Ω_b on h_c/H_0 increases slightly more for $h_c/H_0 > 1.0$ than for the experiments. Moreover, Blenkinsopp and Chaplin (2008) reported that there is a strong dependence of reflection coefficient on h_c/H_0. It can be seen from Fig. 11(b) that the waves

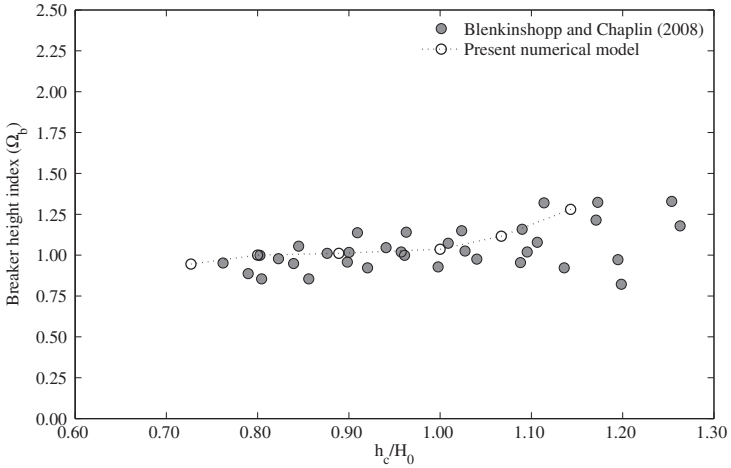

Fig. 12. Breaker height index (Ω_b) as a function of relative crest submergence (h_c/H_0).

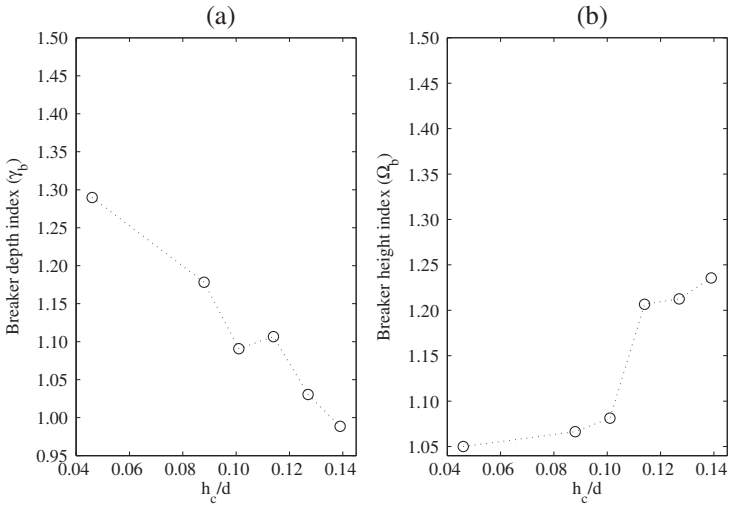

Fig. 13. Simulated breaker depth index (γ_b) and breaker height index (Ω_b) as a function of relative depth (h_c/d).

propagating over the reef with larger h_c experience more reflection from the reef face. This implies that the waves break at larger d_b with larger H_b, corresponding to $h_c/H_0 = 1.15$, $\Omega_b = 1.26$ in Fig. 12 and $h_c/d = 0.14$, $d_b/d = 0.14$ in Fig. 7(b).

Fig. 13 shows the breaker depth index (γ_b) and the breaker height index (Ω_b) versus the relative water depth (h_c/d). It appears that γ_b decreases and Ω_b increases as h_c/d increases. The computed γ_b follows the same trend as observed on plane slopes (Smith and Kraus, 1990; Tsai et al., 2005) but the computed Ω_b is different from the trend on plane slopes. It is seen from Fig. 11(b) that the value of the reflection coefficient increases as the crest submergence increases. Therefore, the present results suggest that waves advancing over larger h_c break further offshore at higher d_b with larger H_b, corresponding to $h_c/d = 0.14$ and $d_b/d = 0.14$ (Fig. 7(b)), $\Omega_b = 1.24$ (Fig. 13(b)). In addition to the partial reflection, the return flow due to the vortex formation behind the crest of the reef could also have an influence on the breaking characteristics as mentioned in Section 4.2. It is therefore likely that a moderate relationship may exist between breaker indices and h_c.

4.4. Profile asymmetry parameters

Fig. 14 shows the crest front steepness (ε), the crest rear steepness (δ), the horizontal asymmetry factor (μ) and the vertical asymmetry factor (λ) versus the offshore wave steepness (H_0/L_0). It appears that ε, δ, and μ increase and λ decreases for waves with larger H_0/L_0. This suggests that the geometric profile of waves with large values of H_0/L_0 at breaking have a steep wave crest front steepness and wave crest rear steepness and shallower trough without much change in the vertical asymmetry. Meanwhile, waves with lower H_0/L_0 break further onshore with higher crest deformation, corresponding to $H_0/L_0 = 0.02$, $d_b/d = 0.117$ in Fig. 7(a) and $H_0/L_0 = 0.02$, $\Omega_b = 1.28$ in Fig. 10. Therefore, the breaking wave profile has an ejected wave front with wide rear

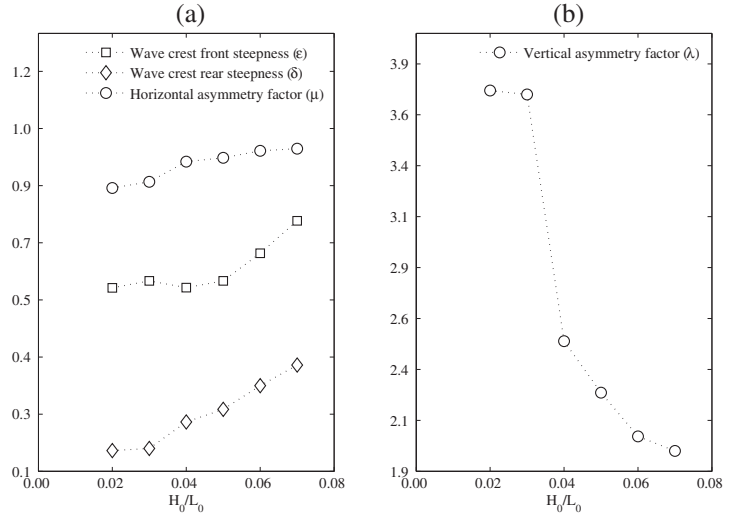

Fig. 14. Simulated wave profile asymmetry parameters as a function of offshore wave steepness (H_0/L_0).

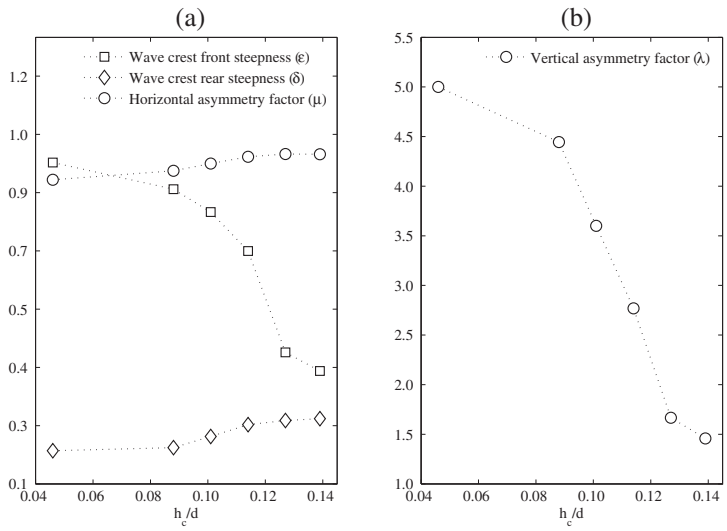

Fig. 15. Simulated wave profile asymmetric parameters as a function of relative depth (h_c/d).

part without much change in the wave trough and crest front and crest rear steepnesses. It is also observed from Fig. 11(a) that the effect of reflection is predominant for waves with larger steepness. This deformation is due to the combination of higher partial reflections from the reef face and the slower shoaling process.

Fig. 15 shows the crest front steepness (ε), the crest rear steepness (δ), the horizontal asymmetry factor (μ) and the vertical asymmetry factor (λ) versus the relative water depth (h_c/d). It appears that ε and λ decreases and δ and μ increases with increasing reef crest submergence. As the wave propagates over the reef from the larger d it breaks further seaward with larger breaker height index (Ω_b), corresponding to $h_c/d = 0.14$, $d_b/d = 0.14$ in Fig. 7(b) and $h_c/d = 0.14$, $\Omega_b = 1.23$ in Fig. 13(b). This implies that the wave profile does not change much from the initial wave shape with a small increase in rear steepness. At the same time, the wave profile becomes more asymmetric when h_c/d decreases. The wave front becomes steep and ejects forward at the breaking point when h_c/d decreases, which is similar to the development of a plunging breaker. However, for larger values of h_c/d the waves break over the reef as spilling breakers. Moreover, the present results are consistent with those of Sayce et al. (1999) and Blenkinsopp and Chaplin (2008) who state that the breaker type over a submerged reef depends strongly on wave height and water depth.

5. Conclusions

The numerical simulations of waves breaking over a reef have been carried out using a two-phase flow CFD model based on the RANS equation together with the level set method and the $k-\omega$ turbulence model. The computed results show good agreement with the experimental data by Blenkinsopp and Chaplin (2008). It has been shown that the numerical model can provide detailed information about the flow features associated with the breaking process such as the complex interface deformation, formation of plunger vortex and the downstream vortex, the splash-up phenomenon and the movement of the enclosed air pocket. The purpose of the present study was to investigate the effects of offshore wave steepness and water depth on the characteristics and profile asymmetry parameters of waves breaking over a submerged reef. The present work confirms results of previous studies and enhances the understanding of the characteristics and asymmetry properties of waves breaking over the reef. The main conclusions from the numerical study are:

- A clockwise vortex is generated downstream close to the reef crest due to the formation of a plunger vortex upstream above the reef face. It seems that the downstream vortex is responsible for the return flow.
- The dependence of the offshore wave steepness and the water depth on the breaker water depth is observed. The main factors that affect the wave breaking over the reef are the partial reflection from the reef face and the return flow.
- The computed breaker depth index decreases slightly as the offshore wave steepness increases, and it increases slightly as the water depth above the reef crest increases. For the water depth above the reef crest the most results agree well with those measured by Blenkinsopp and Chaplin (2008), while they found that the breaker depth index was nearly independent of wave steepness.
- The computed breaker height index over the reef matches well with the experimentally measured data and it shows significant dependence on offshore wave steepness and water depth.
- Waves with larger offshore wave steepnesses have a steep wave crest and a shallow trough without much change in the vertical asymmetry, and thus it breaks as a spilling breaker. Waves with small offshore wave steepnesses have an ejected wave front with a wide rear part without significant change in the wave trough and crest front and crest rear steepnesses, and thus it breaks as a plunging breaker.
- A strong dependence of the breaker type on the water depth over the reef crest is clearly observed from the profile asymmetry properties. Waves breaking over the reef have similar features to a plunging breaker for shallower water depth, whereas for a larger water depth waves break similar to a spilling breaker. The degree of asymmetry increases with decreasing water depth above the reef crest.

Acknowledgment

The first author wishes to express his gratitude to late Prof. Geir Moe and late Prof. Alf Tørum for their support. The authors would like to thank Dr. Chris Blenkinsopp and Prof. John Chaplin for sharing the experimental data. The work was supported by the Norwegian Research

Center for Offshore Wind Technology (NOWITECH), Research council of Norway (Contract no. 193823). The authors would also like to thank NOTUR (Project no. NN9240K) for allocation of computational resources provided on the Vilje system at the super computing facilities at NTNU.

References

Adeyemo, M., 1968. Effect of beach slope and shoaling on wave asymmetry. Proceedings of the 11th Conference on, Coastal Engineering, pp. 145–172.

Ahrens, J.P., 1987. Characteristics of reef breakwaters. Technical Report. Coastal Engineering Research Center.

Alagan Chella, M., Tørum, A., Myrhaug, D., 2012. An overview of wave impact forces on offshore wind turbine substructures. Energy Procedia 20, 217–226.

Alagan Chella, M., Bihs, H., Myrhaug, D., Muskulus, M., 2015. Breaking characteristics and geometric properties of spilling breakers over slopes. Coast. Eng. 95, 4–19.

Babanin, A.V., 2011. Breaking and Dissipation of Ocean Surface Waves. Cambridge University Press.

Babanin, A.V., Chalikov, D., Young, I.R., Savelyev, I., 2010. Numerical and laboratory investigation of breaking of steep two-dimensional waves in deep water. J. Fluid Mech. 644, 433.

Bakhtyar, R., Razmi, A.M., Barry, D.A., Kees, C.E., 2013. Two-phase flow modeling of the influence of wave shapes and bed slope on nearshore hydrodynamics. J. Coast. Res. 159–164.

Banner, M., Peregrine, D.H., 1993. Wave breaking in deep water. Annu. Rev. Fluid Mech. 373–397.

Basco, D.R., 1985. A qualitative description of wave breaking. J. Waterw. Port Coast. Ocean Eng. 3, 171–188.

Battjes, J.A., 1974. Surf similarity. Proceedings of the 14th Conference on, Coastal Engineering, pp. 466–480.

Berthelsen, P.A., Faltinsen, O.M., 2008. A local directional ghost cell approach for incompressible viscous flow problems with irregular boundaries. J. Comput. Phys. 227, 4354–4397.

Blenkinsopp, C., Chaplin, J., 2008. The effect of relative crest submergence on wave breaking over submerged slopes. Coast. Eng. 55, 967–974.

Bonmarin, P., 1989. Geometric properties of deep-water breaking waves. J. Fluid Mech. 209, 405–433.

Bradford, S.F., 2000. Numerical simulation of surf zone dynamics. J. Waterw. Port Coast. Ocean Eng. 126, 1–13.

Chang, K.A., Hsu, T.J., Liu, P.L.F., 2005. Vortex generation and evolution in water waves propagating over a submerged rectangular obstacle Part II: cnoidal waves. Coast. Eng. 52, 257–283.

Chen, G., Kharif, C., Zaleski, S., Li, J., 1999. Two-dimensional Navier–Stokes simulation of breaking waves. Phys. Fluids 11, 121–133.

Christensen, E.D., 1998. Turbulence in Breaking Waves — A Numerical Investigation. Ph.D. thesis. Technical University of Denmark.

Christensen, E.D., 2006. Large eddy simulation of spilling and plunging breakers. Coast. Eng. 53, 463–485.

Christensen, E.D., Deigaard, R., 2001. Large eddy simulation of breaking waves. Coast. Eng. 42, 53–86.

Cokelet, E., 1977. Breaking waves. Nature 267, 769–774.

Engsig-Karup, A.P., 2006. Unstructured Nodal DG-FEM Solution of High-order Boussinesq-type Equations. Ph.D. thesis. Technical University of Denmark, Lyngby.

Galvin, C.J., 1968. Breaker type classification on three laboratory beaches. J. Geophys. Res. 73, 3651–3659.

Gourlay, M.R., 1994. Wave transformation on a coral reef. Coast. Eng. 23, 17–42.

Hieu, P.D., Katsutoshi, T., Ca, V.T., 2004. Numerical simulation of breaking waves using a two-phase flow model. Appl. Math. Model. 28, 983–1005.

Ippen, A.T., Kulin, G., 1954. The shoaling and breaking of the solitary wave. Proceedings of the 5th conference on, Coastal Engineering, pp. 27–47.

Iversen, H.W., 1952. Laboratory study of breakers. Proceedings of the NBS Semicentennial Symposium on Gravity Waves. National Bureau of Standards Circular 521, pp. 9–32.

Iwagaki, Y., Sakai, T., 1972. Shoaling of finite amplitude long waves on a beach of constant slope. Proceedings of the 13th Conference on Coastal Engineering, pp. 347–364.

Iwata, K., Kawasaki, K., Kim, D.S., 1996. Breaking limit, breaking and post-breaking wave deformation due to submerged structures. Proceedings of the 24th Conference on Coastal Engineering, pp. 2338–2351.

Jacobsen, N.G., Fuhrman, D.R., Fredsøe, J., 2012. A wave generation toolbox for the open-source CFD library: OpenFoam. Int. J. Numer. Methods Fluids 70, 1073–1088.

Jiang, G.S., Shu, C.W., 1996. Efficient implementation of weighted ENO schemes. J. Comput. Phys. 126, 202–228.

Kawasaki, K., Iwata, K., 1998. Numerical analysis of wave breaking due to submerged breakwater in three-dimensional wave field. Proceedings of the 26th conference on, Coastal Engineering, pp. 853–866.

Kjeldsen, S.P., Myrhaug, D., 1978. Kinematics and dynamics of breaking waves. Technical Report. River and Harbour Laboratory (NHL), The Norwegian Institute of Technology.

Lader, P.F., 2002. Geometry and Kinematics of Breaking Waves. Ph.D. thesis. Norwegian University of Science and Technology.

Larsen, J., Dancy, H., 1983. Open boundaries in short wave simulations — a new approach. Coast. Eng. 7, 285–297.

Lin, P., Liu, P.L.F., 1998. A numerical study of breaking waves in the surf zone. J. Fluid Mech. 359, 239–264.

Longuet-Higgins, M.S., Cokelet, E.D., 1976. The deformation of steep surface waves on water I — a numerical method of computation. Proceedings of the Royal Society of London. Series A, Mathematical and Physical Sciences, pp. 1–26.

Mayer, S., Garapon, A., Sørensen, L.S., 1998. A fractional step method for unsteady free surface flow with applications to non linear wave dynamics. Int. J. Numer. Methods Fluids 28, 293–315.

Miller, R., Zeigler, J., 1964. The internal velocity field in breaking waves. Proceedings of the 9th conference on Coastal Engineering, pp. 103–122.

Osher, S., Sethian, J.A., 1988. Fronts propagating with curvature-dependent speed: algorithms based on –Hamilton-Jacobi formulations. J. Comput. Phys. 79, 12–49.

Peregrine, D.H., 1983. Breaking waves on beaches. Annu. Rev. Fluid Mech. 149–178.

Perlin, M., Choi, W., Tian, Z., 2013. Breaking waves in deep and intermediate waters. Annu. Rev. Fluid Mech. 115–145.

Rattanapitikon, W., Shibayama, T., 2006. Breaking wave formulas for breaking depth and orbital to phase velocity ratio. Coast. Eng. 48, 395–416.

Sayce, A., Black, K., Gorman, R., 1999. Breaking wave shape on surfing reefs. Proceedings of Coasts and Ports'99, Perth, Australia, pp. 596–603.

Shu, C.W., Osher, S., 1988. Efficient implementation of essentially non-oscillatory shock capturing schemes. J. Comput. Phys. 77, 439–471.

Smith, E.R., Kraus, N.C., 1990. Laboratory study on macro-features of wave breaking over bars and artificial reefs. Technical Report. Coastal Engineering Research Center.

Svendsen, I.A., Madsen, P.A., Hansen, J.B., 1978. Wave characteristics in the surf zone. Proceedings of the 16th conference on Coastal Engineering, pp. 520–539.

Takikawa, K., Yamada, F., Matsumoto, K., 1997. Internal characteristics and numerical analysis of plunging breaker on a slope. Coast. Eng. 31, 143–161.

Ting, F.C.K., Kim, Y.K., 1994. Vortex generation in water waves propagating over a submerged obstacle. Coast. Eng. 24, 23–49.

Tsai, C.P., Chen, H.B., Hwung, H.H., Huang, M.J., 2005. Examination of empirical formulas for wave shoaling and breaking on steep slopes. Ocean Eng. 32, 469–483.

van der Vorst, H., 1992. Bi-CGSTAB: a fast and smoothly converging variant of Bi-CG for the solution of nonsymmetric linear systems. SIAM J. Sci. Stat. Comput. 13, 631–644.

Vinje, T., Brevig, P., 1981. Numerical simulation of breaking waves. Adv. Water Resour. 4, 77–82.

Wang, Z., Yang, J., Koo, B., Stern, F., 2009a. A coupled level set and volume-of-fluid method for sharp interface simulation of plunging breaking waves. Int. J. Multiphase Flow 35, 227–246.

Wang, Z., Zou, Q., Reeve, D., 2009b. Simulation of spilling breaking waves using a two phase flow cfd model. Comput. Fluids 38, 1995–2005.

Yao, Y., Huang, Z., Monismith, S.G., Lo, E.Y., 2013. Characteristics of monochromatic waves breaking over fringing reefs. J. Coast. Res. 29, 94–104.

Zhao, Q., Armfield, S., Tanimoto, K., 2004. Numerical simulation of breaking waves by a multi-scale turbulence model. Coast. Eng. 51, 53–80.

6.6 Paper 6

Energy transfer due to shoaling and decomposition of breaking and non-breaking waves over a submerged bar

Kamath, A., Alagan Chella, M., Bihs, H., Arntsen, Ø. A.
Submitted to *Engineering Applications of Computational Fluid Mechanics*, 2015 - under review

Paper 6

Energy Transfer due to Shoaling and Decomposition of Breaking and Non-Breaking Waves over a Submerged Bar

Arun Kamath[1], Mayilvahanan Alagan Chella, Hans Bihs, Øivind A. Arntsen

Department of Civil and Transport Engineering, Norwegian University of Science and Technology, 7491 Trondheim, Norway

Abstract

Wave propagation over a submerged bar is simulated using the open source CFD model REEF3D with various incident wave heights to study shoaling, wave breaking features and the process of wave decomposition into higher harmonics for long waves of $T = 2.5$s. The computed free surface elevations are compared with experimental data and a good agreement is obtained for both non-breaking and spilling breaking waves. The differences in the mode of wave shoaling over the weatherside slope and the wave decomposition over the leeside slope of the submerged bar are discussed. The evolution of spilling breakers and plunging breakers over the bar crest is also studied. It is found that the free surface elevation continuously increases due to shoaling in the case of non-breaking waves, whereas breaking waves propagate with much lower free surface elevations after breaking over the bar crest. The power spectra of the free surface elevations at various locations indicate that the wave energy in the fundamental frequency is reduced by 76% for the lowest incident wave and by about 90% for all the other cases due to energy dissipation and energy transfer to higher harmonic components as the wave propagates over the submerged bar.

Keywords: wave decomposition, wave breaking, shoaling, submerged bar, numerical wave tank, CFD, REEF3D

1. Introduction

Wave propagation in shallow waters is influenced by the sea bottom topography and wave transformation processes such as diffraction, shoaling and wave breaking are observed. Wave shoaling refers to the phenomenon where the incident wave height is changed as the deep water wave propagates to water depths less than half the wavelength. Shoaling results in asymmetry in the wave profile with sharper crests and shallower troughs, creating an imbalance in the local wave energy distribution and leading to wave deformation.

[1]Corresponding Author, Email: arun.kamath@ntnu.no, Ph: (+47) 73 59 46 40, Fax: (+47) 73 59 70 21

The wave crest heights reach a limiting value, beyond which the wave breaks to balance the local increase in the wave energy. The additional challenge in wave propagation over a submerged obstacle is the wave decomposition process which occurs behind the obstacle, in the region of increasing water depth, leading to the evolution of higher-order harmonics and rapidly varying waveforms. These processes can only be represented in a numerical model, which accounts for for nonlinearity and has good dispersion characteristics [Beji and Battjes, 1994].

The accurate evaluation of the wave kinematics in the near-shore area is important due to their impact on hydrodynamic properties such as wave forces, wave run-up and sediment transport. The mode of wave breaking is generally classified using the surf similarity parameter, $\xi = \frac{tan\alpha}{\sqrt{H/L_0}}$, where α is the angle of the slope, H is the incident wave height over the toe of the slope and $L_0 = \frac{g}{2\pi}T^2$ is the deep water wavelength where T is the wave period. Battjes [1974] presented the relationships between ξ and various flow parameters, and also the classification of breaker types on emergent plane sloping beaches. Gourlay [1994] carried out experiments on waves breaking on a submerged reef and Blenkinsopp and Chaplin [2008] on a submerged slope and found out that the classification presented by Battjes [1974] for emergent sloping beaches is not directly applicable for submerged structures. Wave propagation over submerged structures has been studied through experimental investigations on a submerged bar [Beji and Battjes, 1993], a rectangular obstacle [Chang et al., 2001] and processes such as wave decomposition and vortex generation have been identified. Numerical modeling of wave propagation over a submerged obstacle has been carried out using Boussinesq equations [Beji and Battjes, 1994; Bosboom et al., 1996; Brocchini et al., 1992] and shallow water equations [Kobayashi et al., 1987] with good results for the wave shoaling process. According to Lemos [1992], the drawback of these methods is that they cannot account for the wave breaking process and was the first to present simulations of breaking waves using the Reynolds Averaged Navier-Stokes (RANS) equations. Lin and Liu [1998] and Zhao et al. [2004] employed single-phase CFD (Computational Fluid Dynamics) models to simulate breaking waves, which could not provide the complete picture on wave breaking as they cannot account for the air-water interaction responsible for the complex free surface deformations.

The knowledge of wave transformation and transmission across submerged structures finds its application in coastal protection measures such as submerged breakwaters, ecological conservation and recreational measures such as artificial reefs. The wave decomposition process modifies the waves transmitted over the submerged structure and this can

be usefully exploited in a combined submerged bar- floating breakwater coastal protection measure. For the design of recreational artificial reefs and bars, it is essential to have a better idea regarding the breaking wave characteristics on the crest of the bar to provide sufficient breaker heights for surfing. It has been presented in previous studies on wave breaking that the wave breaking characteristics vary significantly under different breaking conditions [Battjes, 1974; Gourlay, 1994; Blenkinsopp and Chaplin, 2008]. In addition, the many existing numerical and theoretical models for wave transformation over submerged breakwaters are based on the potential flow assumption, which cannot describe the rotational flow that occurs during the breaking process [Takikawa et al., 1997]. CFD modeling solves the fluid flow problem by solving the Navier-Stokes equations, accounting for most of the fluid physics with few assumptions. This method has been previously applied to the simulation of breaking waves over a slope by Hieu et al. [2004] and Jacobsen et al. [2012] using a Volume of Fluids (VoF) -based interface capturing method and Alagan Chella et al. [2015] using the level set method to obtain the interface. Alagan Chella et al. [2015] obtained good agreement to experimental data, with a sharp representation of the breaking wave and the formation air pockets, due to the higher order discretization schemes used in the model along with the level set method, compared to the lower order schemes used in previous studies. Numerical modeling with a two-phase CFD model resolves all the physics involved in the wave breaking process with few assumptions. Along with higher order discretization schemes and sharp interface capturing, it can account for the complex free surface process involved during wave transformation including breaking and decomposition. These processes can be evaluated in a more detailed manner compared to models based on the Boussinesq and shallow water equations.

In the current study, the open source CFD model REEF3D [Alagan Chella et al., 2015] is used to simulate wave propagation over a submerged bar. The numerical results are compared with the experimental data from Beji and Battjes [1993]. Several previous studies regarding this have numerically calculated the wave propagation only for the non-breaking wave cases [Morgan et al., 2010; Roeber et al., 2010; Stelling and Zijlema, 2003]. The breaking wave case was modeled by Tissier et al. [2012], but they reported deviations from the experimental observations from the point of wave breaking. Thus, numerical models accounting for both breaking and non-breaking waves over a submerged bar [Beji and Battjes, 1993] with good agreement to experimental data for both the free surface elevation and the wave phase have not been presented in current literature. This is especially true for the longer wave with $T = 2.5$ s, where the wave decomposition process

is seen to be much stronger in the experiments compared to the shorter waves with $T = 1$ s, which have been presented by several authors. An initial study for only non-breaking wave shoaling on a submerged bar was presented with comparison to experimental data [Kamath et al., 2015]. In this paper, the study is significantly extended to cover the evolution of spilling and plunging breakers on the bar crest, with comparison of the free surface elevation in the spilling case. In addition, the shoaling process for the different incident waves is examined through the comparison of the relative wave crest elevations, evaluation of the maximum wave crest steepness and the relative phase differences between the primary wave crests of the transformed waves in the different cases. The decomposition process with transfer of wave energy to higher harmonics is also examined using the power spectral density computed from the free surface elevations and the redistribution of the wave energy amongst the harmonics is discussed. The effect of wave breaking on the wave propagation and decomposition process is also discussed.

2. Numerical Model

2.1. Governing equations

The numerical model uses the Reynolds Averaged Navier Stokes (RANS) equations along with the continuity equation to evaluate the fluid flow:

$$\frac{\partial u_i}{\partial x_i} = 0 \tag{1}$$

$$\frac{\partial u_i}{\partial t} + u_j \frac{\partial u_i}{\partial x_j} = -\frac{1}{\rho}\frac{\partial p}{\partial x_i} + \frac{\partial}{\partial x_j}\left[(\nu + \nu_t)\left(\frac{\partial u_i}{\partial x_j} + \frac{\partial u_j}{\partial x_i}\right)\right] + g_i \tag{2}$$

where u_i is the time averaged velocity, ρ is the density of the fluid, p is the pressure, ν is the kinematic viscosity, ν_t is the eddy viscosity, t is time and g is the acceleration due to gravity. The projection method [Chorin, 1968] is used for pressure treatment and the resulting Poisson pressure equation is solved using a preconditioned BiCGStab solver [van der Vorst, 1992]. Turbulence modeling is carried out using the two-equation $k - \omega$ model proposed by Wilcox [1994]. Wave propagation is characterized by large gradients in the velocities resulting in a highly strained flow. Since, the production of turbulence in the $k - \omega$ model depends on the gradients in the velocity field, this results in unphysical overproduction of turbulence in a numerical wave tank. A stress limiter in the definition of eddy viscosity using assumption by Bradshaw et al. [1967] as shown by Durbin [2009] is

implemented to avoid this. The free surface is a natural boundary for the turbulent eddies which is not accounted for in the k-ω model, resulting in an overproduction of turbulence at the free surface in a two-phase CFD model, due to the large strain caused by the large difference in the density of air and water. Free surface turbulence damping using a limiter around the interface as shown by Naot and Rodi [1982] is carried out to avoid the overproduction of turbulence at the interface. The limiter is activated only around the interface using the Dirac delta function.

2.2. Discretization schemes

The fifth-order conservative finite difference Weighted Essentially Non Oscillatory (WENO) scheme [Jiang and Shu, 1996] is used for the discretization of the convective terms in the RANS equations and the level set function, the turbulent kinetic energy and the specific turbulence dissipation rate are discretized using the Hamilton-Jacobi formulation of the WENO scheme [Jiang and Peng, 2000]. Time advancement is carried out using a four-step scheme proposed by Choi and Moin [1994] with implicit treatment of convective and viscous terms. An adaptive time stepping approach is used to satisfy the Courant-Frederich-Lewy (CFL) condition for numerical stability. The numerical model uses a uniform Cartesian grid for spatial discretization facilitating an easy implementation of higher order schemes. The staggered grid approach is used with pressure at the cell centers and velocities at the cell faces, providing a tight coupling between the pressure and the velocity. A local directional ghost cell immersed boundary method [Berthelsen and Faltinsen, 2008] extended to three dimensions is employed to handle complex geometries. The numerical model completely parallelized using the MPI library and can be executed on high performance computing systems.

2.3. Free surface

The free surface in the numerical wave tank is captured using the level set method [Osher and Sethian, 1988]. Here, the interface is represented by the zero level set of the signed distance level set function . The level set function provides the least distance of each point in the domain from the interface. The different fluids are distinguished by the sign of the level set function as shown in Eq. (3):

$$\phi(\vec{x},t)\begin{cases} > 0 & if\ \vec{x}\ is\ in\ phase\ 1 \\ = 0 & if\ \vec{x}\ is\ at\ the\ interface \\ < 0 & if\ \vec{x}\ is\ in\ phase\ 2 \end{cases} \tag{3}$$

The definition of the level set function makes it smooth across the interface and provides a sharp representation of the interface. The level set function is convected by the velocity field in the numerical wave tank. The signed distance property is lost on convection and is restored by re-initializing the level set function after every iteration with the partial differential equation re-initialization procedure by Peng et al. [1999].

2.4. Numerical wave tank

The numerical wave tank uses the relaxation method [Larsen and Dancy, 1983] for wave generation and absorption. In this method, relaxation functions are used to moderate the computational values to the expected values from wave theory to generate and absorb waves. This requires certain zones of the wave tank to be reserved as relaxation zones for wave generation and absorption. The numerical model uses the relaxation functions proposed by Jacobsen et al. [2012] presented in Eq. (4):

$$\Gamma(x) = 1 - \frac{e^{(1-x)^{3.5}} - 1}{e - 1} \tag{4}$$

where $\Gamma(x)$ is the relaxation function and x is the coordinate along the x-axis scaled to the length of the relaxation zone. The relaxation functions prescribe the required values for free surface elevation and velocity from wave theory to the wave tank using Eq. (5):

$$\begin{aligned} u_{relaxed} &= \Gamma(x) u_{analytical} + (1 - \Gamma(x)) u_{computational} \\ \phi_{relaxed} &= \Gamma(x) \phi_{analytical} + (1 - \Gamma(x)) \phi_{computational} \end{aligned} \tag{5}$$

The relaxation function also absorbs reflections from the objects placed in the numerical wave tank, so that it does not affect wave generation and simulates a wavemaker with active absorption. At the numerical beach, the computational values from the wave tank are reduced to zero to smoothly absorb wave energy without spurious reflections from the beach.

3. Results

A grid refinement study is carried out first to select the grid size to be used for the simulations in the study. Then, wave propagation over a submerged bar are simulated for different incident wave heights and the numerical results are compared to experimental data. The wave transformation over the submerged bar is studied using the data obtained from the wave gages at different locations along the length of the bar. The evolution of

spilling and plunging breakers on the bar crest in the simulation is also presented. The shoaling process for the different incident waves is examined through the variation of the relative wave crest elevations. The decomposition process with transfer of wave energy to higher harmonics is examined by calculating the power spectral densities of the computed free surface elevations at the different locations in the wave tank.

3.1. Grid refinement study

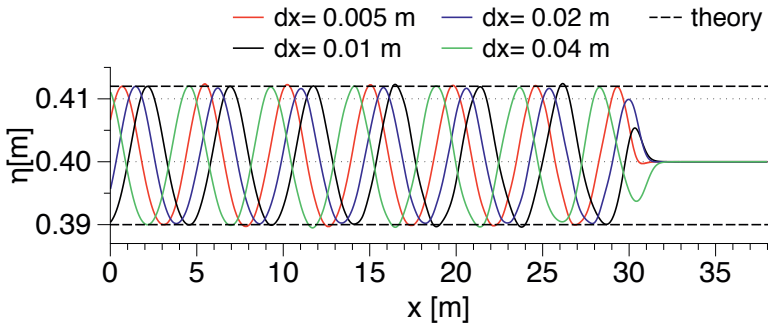

Figure 1: Grid refinement study with 2*nd*-order Stokes waves of T=2.525 s and $H_1 = 0.022$ m

Accurate wave generation and propagation in the numerical wave tank is verified by carrying out a grid refinement study. A two-dimensional wave tank of length 38 m and height 0.8 m is used to generate second-order Stokes waves with wave period $T = 2.5$ s, wavelength $L = 4.74$ m and wave height $H_1 = 0.022$ m in a water depth of $d = 0.4$ m. Grid sizes $dx = 0.04$ m, 0.02 m, 0.01 m and 0.005 m are used. The results presented in Fig. (1) show that the free surface elevations converge to the required values from a grid size of $dx = 0.02$ m onwards. Due to the high order discretization schemes used in the model and the relatively low wave steepness in the study, there is no significant difference in the wave heights obtained at the different grid sizes. But, in order to capture the evolution of wave shoaling and breaking in this study, a grid size of $dx = 0.005$ m is used for the simulations.

3.2. Numerical wave tank setup

The simulations of wave propagation over a submerged bar are carried out based on the experimental studies by Beji and Battjes [1993]. The submerged bar has a weatherside slope of 1 : 20, a leeside slope of 1 : 10 and a crest height of 0.3 m. The wave tank has a water depth of $d = 0.4$ m resulting in a depth of 0.1 m on the crest of the bar and incident waves of heights $H_1 = 0.022$ m, $H_2 = 0.035$ m, $H_3 = 0.042$ m and $H_4 = 0.052$ m are

simulated. Wave gages are placed at various locations along the bar to evaluate the wave propagation over the bar as shown in Fig. (2). A two-dimensional numerical wave tank 38 m long and 0.8 m high with a grid size of 0.005 m is used, resulting in a total of 1.216 million cells. A wave generation relaxation zone of length 5 m and a numerical beach of length 9.5 m are used at the beginning and the end of the wave tank respectively to ensure good wave generation and absorption. The $x-$coordinate in the wave tank begins at the end of the wave generation relaxation zone and the same distances as in the experiments by Beji and Battjes [1993] are maintained.

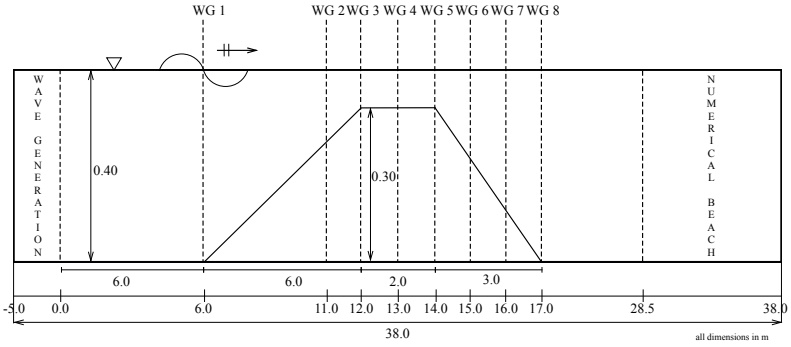

Figure 2: Schematic diagram of the setup used in the numerical simulations, all dimensions in m

3.3. Non-breaking wave propagation over a submerged bar

A simulation is carried out with second-order Stokes waves of wave height $H_1 = 0.022$ m, wave period $T = 2.5$ s and wavelength $L = 4.74$ m. The free surface elevations are computed at several locations along the submerged bar and are compared with the measured experimental data in Fig. (3) and a good agreement is seen in both the phase and amplitude of the transformed waves. As the waves propagate along the reducing water depth along the upward slope of the bar, the wave profile is seen to be slightly deformed with the development of a saw-toothed profile at $x = 11.0$ m in Fig. (3b), which becomes prominent at $x = 12.0$ m in Fig. Fig. (3c). As a result of wave shoaling, high and sharp wave crests are formed over the bar crest $x = 13.0$ m in Fig. (3d). The decomposition of the wave with the development of higher harmonic components is also observed from $x = 14.0$ m (Fig. 3e) onwards, as the wave propagates over the end of the bar crest. As the wave propagates along the leeside slope of the bar, the water depth increases and a process opposite to wave shoaling takes place[Beji and Battjes, 1993]. The free surface elevation begins to reduce compared to the elevations on the upward slope and the crest.

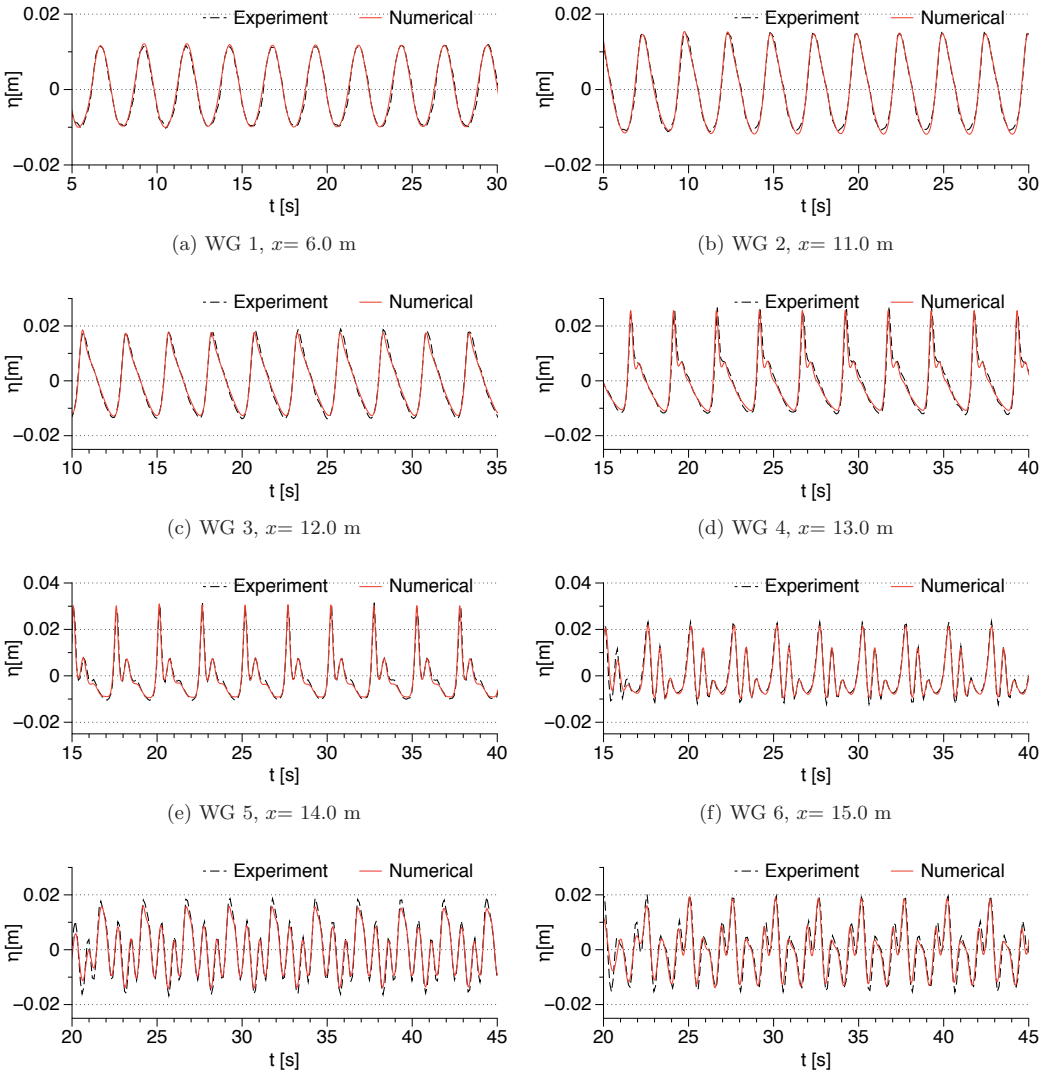

(a) WG 1, x= 6.0 m

(b) WG 2, x= 11.0 m

(c) WG 3, x= 12.0 m

(d) WG 4, x= 13.0 m

(e) WG 5, x= 14.0 m

(f) WG 6, x= 15.0 m

(g) WG 7, x= 16.0 m

(h) WG 8, x= 17.0 m

Figure 3: Free surface elevations at various locations along the wave flume for $H_1 = 0.022$ m

The wave decomposition results in the formation of secondary and tertiary waves after the bar crest as seen in Figs. 3f, 3g, 3h.

3.4. Breaking wave propagation over a submerged bar

The incident wave height is further increased to $H_3 = 0.042$ m to simulate spilling breakers and the computed free surface elevations are compared with experimental data in Fig. (4). The computed results show a good agreement with the experimental data at most of the locations but some differences are seen in the amplitudes computed at $x = 13.0$ m, 14.0 m and 15.0 m, though the wave phases are in good agreement. This is due to the fact that the wave breaks over the crest of the bar, between $x = 13.0$ m and $x = 14.0$ m. The average difference between the primary wave crest heights in the numerical results and the experimental data are found to be about 0.012 m over a 25 s window which is 24% of the local wave height. The complex flow scenario due to small scale wave breaking over very shallow water ($d = 0.1$ m) over the bar crest results in instantaneous changes in the pattern of the free surface elevations in this region. It is challenging to capture these free surface effects resulting from violent mixing of air and water, both experimentally and numerically in the near post-breaking region. This accounts for the difference observed in the free surface elevations at $x = 13.0$ m and $x = 14.0$ m in Fig. (4d) and (4e). The difference in the wave crest height reduces to 0.0036 m over a 25 s window at WG 7 at $x = 16.0$ m and the numerical results for WG 8 at $x = 17.0$ m match the experimental results again.

The evolution of the wave profile in the region of wave breaking in the simulation is presented in Fig. (5) to obtain further insight into the breaking process in this case. The shoaling of the wave due to the reducing water depth leads to a sharp wave crest on the bar crest as seen in Fig. (5a). The bar crest acts as a flat bottom with very low water depth and the wave propagates over the crest without much change to its amplitude, but with reduced wave celerity. The reduction in wave celerity combined with an increase in wave crest elevation due to shoaling leads to a local imbalance in the wave energy with wave crest particle velocities higher than the wave celerity. This increases the asymmetry of the wave and the appearance of a steep wave crest. The steep wave crest then stretches away from the main wave crest in Fig. (5b). Due to lack of further excess energy, the wave crest then begins to spill forward onto the main wave crest in Figs. (5c) and (5d), resulting in a small scale spilling breaker. The velocity contours in the figures demonstrate the large increase in the horizontal water particle velocity in the overturning crest compared to

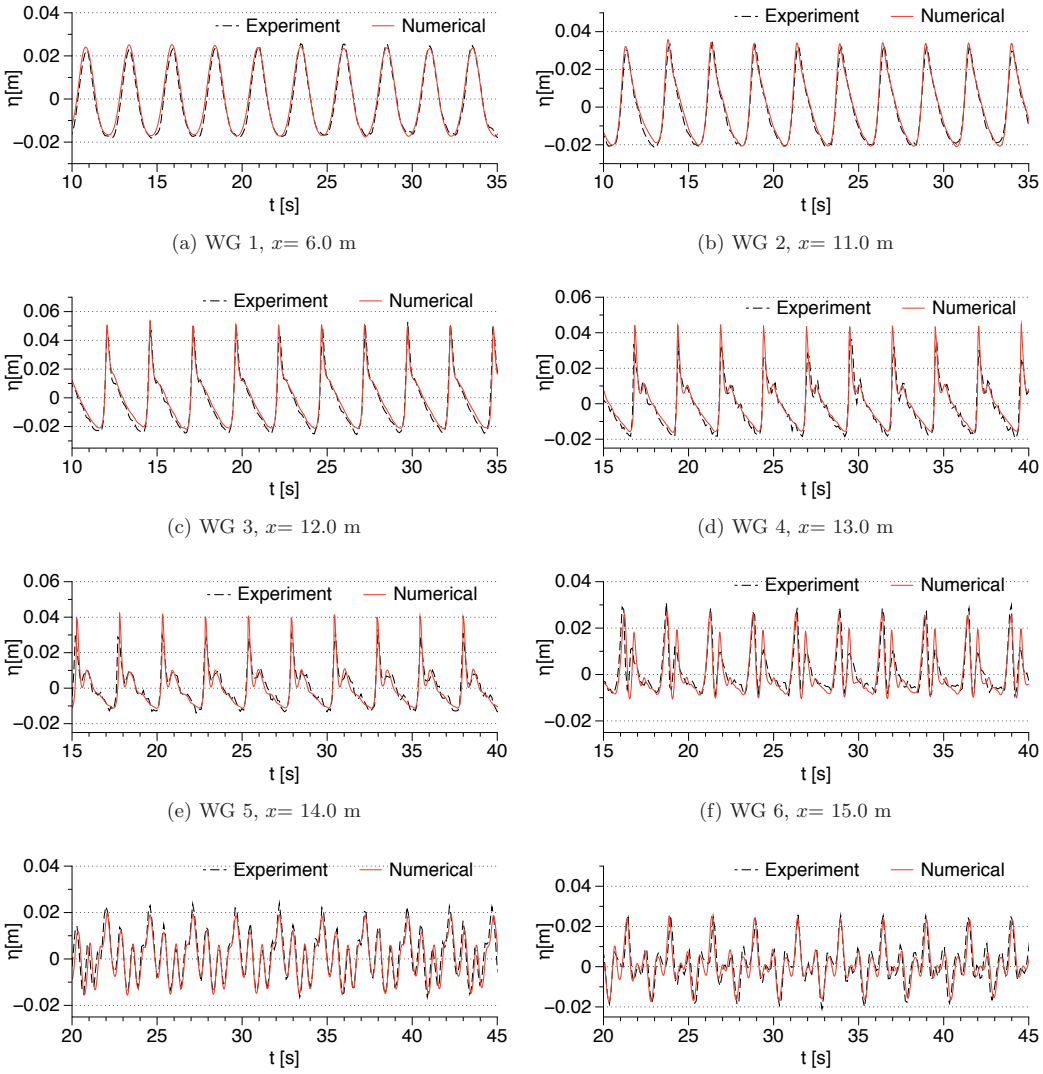

(a) WG 1, x= 6.0 m

(b) WG 2, x= 11.0 m

(c) WG 3, x= 12.0 m

(d) WG 4, x= 13.0 m

(e) WG 5, x= 14.0 m

(f) WG 6, x= 15.0 m

(g) WG 7, x= 16.0 m

(h) WG 8, x= 17.0 m

Figure 4: Free surface elevations at various locations along the wave flume for $H_3 = 0.042$ m

the rest of the free surface, signifying the complex hydrodynamics involved in the spilling breaking wave. The total duration from the near vertical wave crest profile until the wave crest rejoins the preceding trough is only $0.1T$, signifying the rapid and small scale nature of the spilling breaker in this case.

The wave transformation over the submerged bar is further investigated with an incident wave height of $H_4 = 0.052$ m and the wave elevations computed along the submerged bar are presented in Fig. (6). Since there was no experimental data available for this

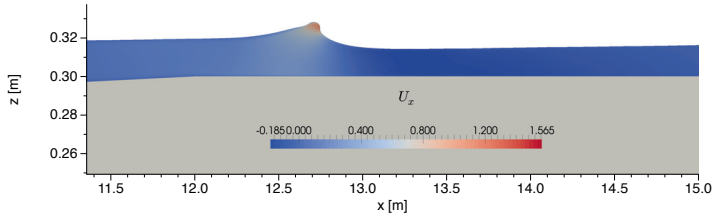

(a) t/T=8.89

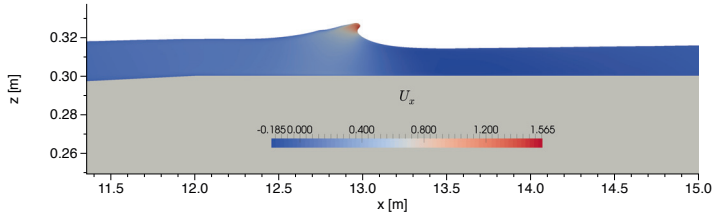

(b) t/T=8.93

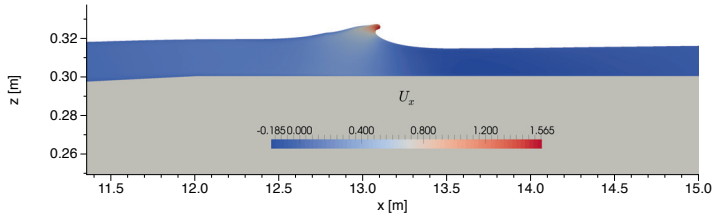

(c) t/T=8.95

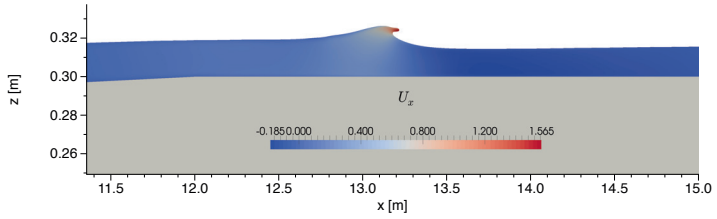

(d) t/T=8.97

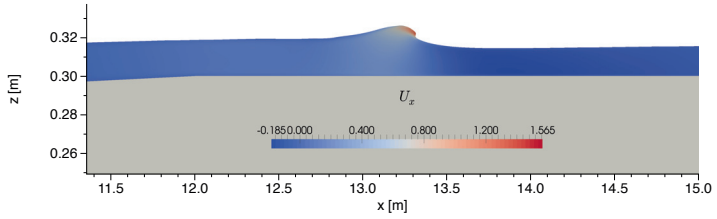

(e) t/T=8.99

Figure 5: Process of spilling wave breaking over the bar crest for $H_3 = 0.042$ m

case, only the numerical results are presented. The effect of shoaling with saw-toothed asymmetry in the wave profile appears sooner than in the previous cases at $x = 11.0$ m in Fig. (6b). The wave profile then undergoes similar transformations as seen for the previous cases at $x = 12.0$ m, $x = 13.0$ m and $x = 14.0$ m with even more sharper wave crests, due to stronger shoaling of the higher incident wave. At $x = 15.0$ m, the decomposed waves consist of the primary crest and a secondary wave crest of similar magnitude, which further decompose to produce a tertiary wave crest at $x = 16.0$ m and a quaternary crest at $x = 17.0$ m. The free surface deformation over the crest of the submerged bar are presented in Fig. (7) and the wave breaking process in this case is studied. The steep wave crest formed as a result of wave shoaling on the upward slope enters the shallow

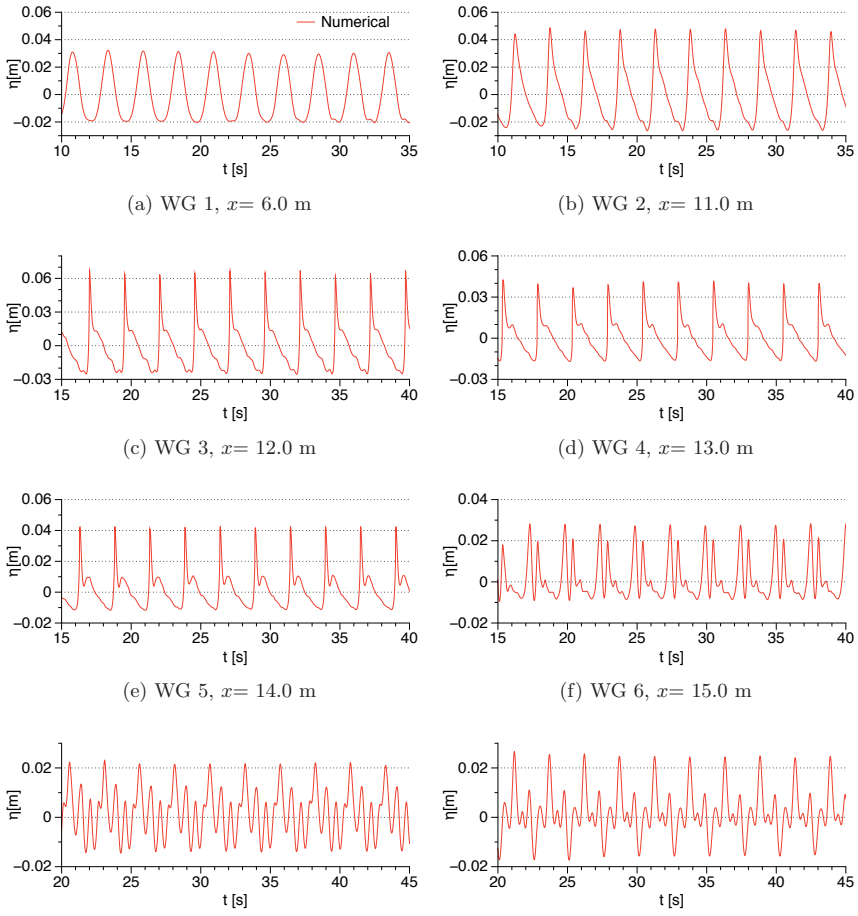

(a) WG 1, x= 6.0 m

(b) WG 2, x= 11.0 m

(c) WG 3, x= 12.0 m

(d) WG 4, x= 13.0 m

(e) WG 5, x= 14.0 m

(f) WG 6, x= 15.0 m

(g) WG 7, x= 16.0 m

(h) WG 8, x= 17.0 m

Figure 6: Free surface elevations at various locations along the wave flume for $H_4 = 0.052$ m

Table 1: Summary of the results from the different simulations in the study

Test	T (s)	H (m)	ξ	ϵ_{max}	breaking type
1.	2.5	0.022	1.4678	0.1275	non-breaking
2.	2.5	0.035	1.1637	0.2008	non-breaking
3.	2.5	0.042	1.0623	0.0526	spilling
4.	2.5	0.052	0.9547	0.0641	plunging

water region on the bar crest is observed in Fig. (7a). The steep crest stretches away from the main wave crest to form an overturning wave crest in Fig. (7b). The overturning wave crest then forms a plunging jet to rejoin with the free surface slightly in front of the primary wave crest, resulting in the formation of an air pocket in Fig. (7c). The splash up of the free surface after the plunging wave breaking is seen Fig. (7d). The horizontal velocity contours in Fig. (7) show the increase in the horizontal velocity at the free surface that leads to the formation of the overturning wave crest and eventually the plunging breaker. The wave crest goes from a near vertical profile to reconnection to the preceding wave crest in $0.12T$, which is slightly slower than the spilling breaker.

A grid refinement study for the plunging breaking wave obtained for $H_4 = 0.052$ m is carried with additional simulations at grid sizes $dx = 0.01$ m, $dx = 0.02$ m and $dx = 0.04$. From the free surface profiles in Fig. (8), it can be concluded that the breaker location has converged to $x = 17.2$ m from $dx = 0.01$ m onwards, but the vertical profile of the breaking wave crest is best represented by $dx = 0.005$ m. This confirms that the choice of $dx = 0.005$ m as the grid size for the simulations is justified. The very fine grid required to represent the wave breaking in this study arises from the fact that the incident waves are of low steepness and they undergo large and rapid changes in their wave steepness during propagation over the bar. This follows the conclusions by **?**, that incident waves with lower steepnesses undergo larger deformations than waves with larger incident steepnesses. An overview of the results obtained for the different simulations is presented in Table 1.

3.5. Wave transformation process

The variation in the relative wave crest elevations computed at the different wave gages is studied to gain a comparative perspective of the wave transformation process for both non-breaking and breaking waves. The incident waves at $x = 6.0$ m in Fig. (9a) show the small horizontal asymmetry in the wave profile with shallower troughs and sharper crests, which is characteristic of second-order Stokes waves. The breaking and non-breaking waves show certain differences in the transformation properties. In the case of the non-breaking waves with $H_1 = 0.022$ m and $H_2 = 0.035$ m, shoaling leads to saw-toothed asymmetry in

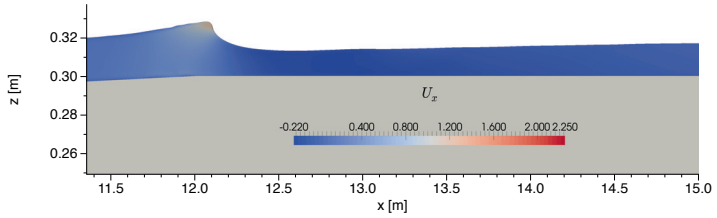

(a) t/T=7.74

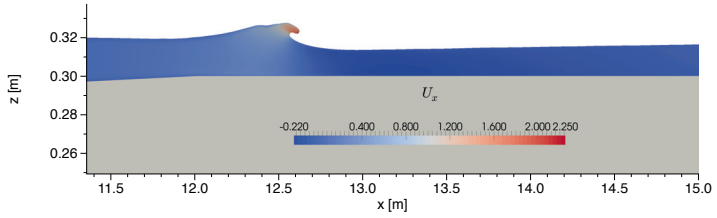

(b) t/T=7.82

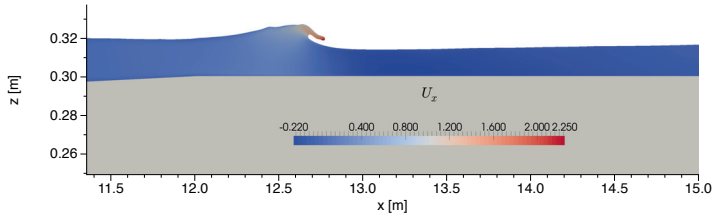

(c) t/T=7.84

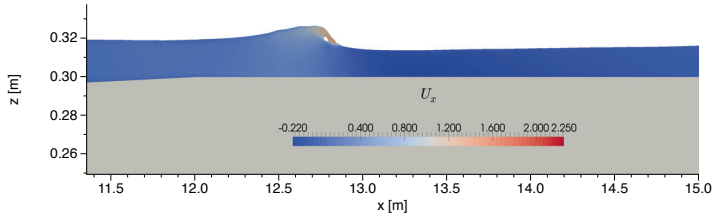

(d) t/T=7.86

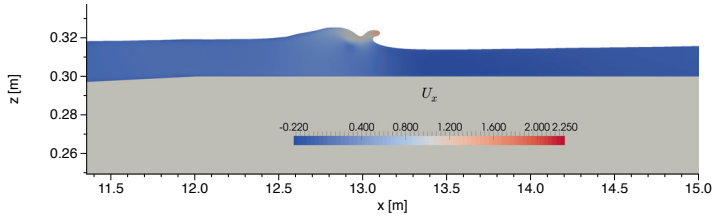

(e) t/T=7.90

Figure 7: Process of plunging wave breaking over the bar crest for $H_4 = 0.052$ m

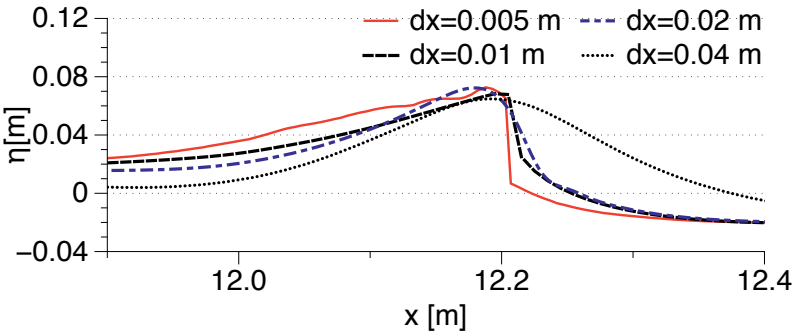

Figure 8: Grid refinement study for plunging breaker location for $H_4 = 0.052$ m

the wave profile. The higher incident wave H_2 undergoes a higher increase in the relative crest elevation and attains a sharper saw-toothed asymmetry in Fig. (9b) at $x = 11.0$ m. As the wave reaches the crest of the bar at $x = 12.0$ m, the relative crest elevation is higher for H_2 compared to H_1 in Fig. (9c). In the region over the bar crest at $x = 13.0$ m and $x = 14.0$ m, the higher incident wave maintains a higher relative crest elevation in Figs. (9d) and (9e). The maximum wave crest steepness [Kjeldsen and Myrhaug, 1978] $\epsilon = \eta'/L'$, where η' is the wave crest height and L' the distance from the wave crest to the wave zero-crossing location, can be used to quantify the crest steepness. In the case of $H_2 = 0.035$ m, the maximum wave crest steepness $\epsilon_{max} = 0.2008$ is calculated for WG 4 at $x = 13.0$ m. The maximum wave crest steepness $\epsilon_{max} = 0.1275$ for $H_1 = 0.022$ m is obtained at $x = 14.0$ m at WG 5. Also, the higher incident wave (H_2) moves faster than the lower incident wave (H_1). This follows from shallow water wave propagation, where a higher wave propagates faster for a given wave period and water depth. The higher incident wave attains the highest crest elevation during its propagation over the upward slope and thus propagates faster over the shallow water depth over the crest.

The submerged bar crest ends at $x = 14.0$ m and the initiation of wave decomposition is seen in Fig. (9e), with the appearance of secondary crests. As the wave propagates further, the water depth increases over the downward slope of the submerged bar. This change in the water depth begins a process of de-shoaling [Beji and Battjes, 1993], where the waves reduce in amplitude as they propagate over gradually increasing water depths. Well-developed secondary wave crests are seen at $x = 15.0$ m in Fig. (9f). It is also observed that the reduction in the relative crest elevation is lower for the lower incident wave. The higher non-breaking wave H_2, which had the highest crest elevation at $x = 13.0$ m has a lower primary crest elevation and a higher secondary crest elevation compared to

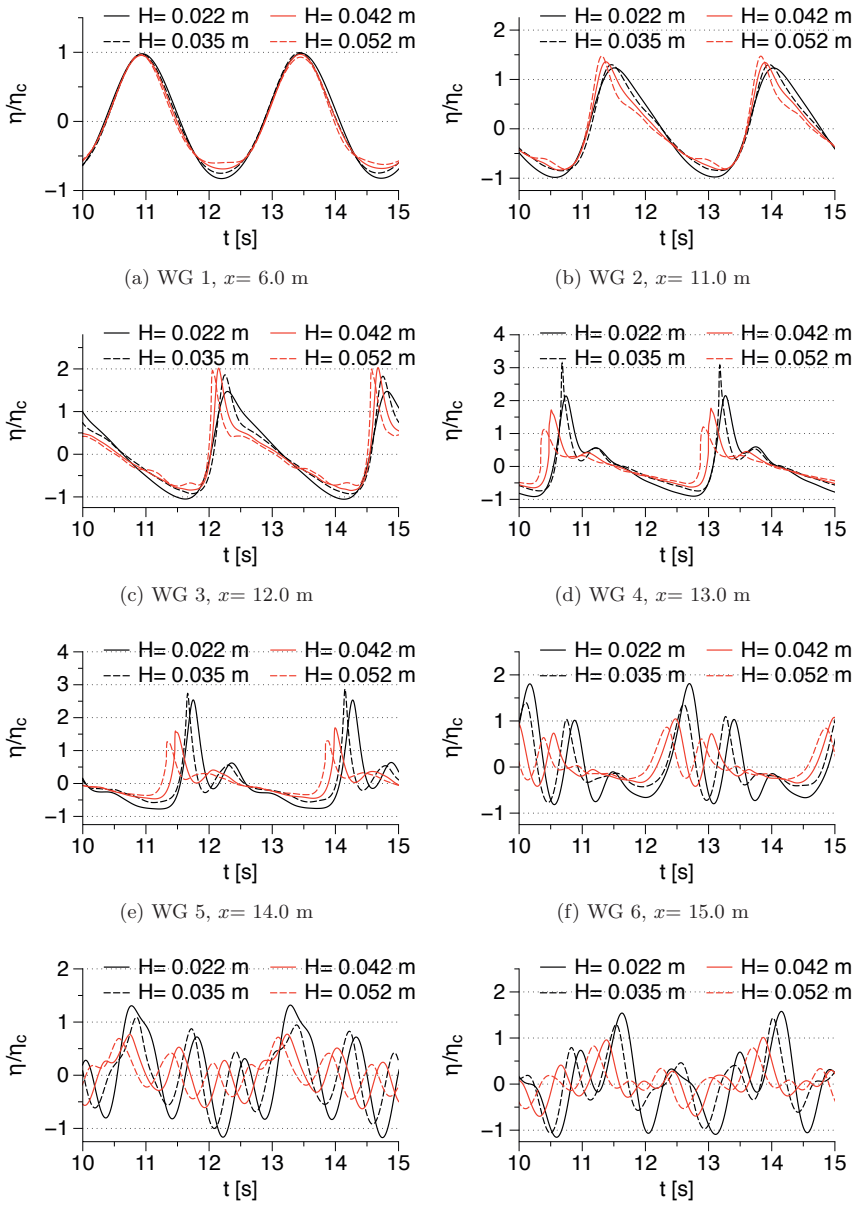

(a) WG 1, x= 6.0 m

(b) WG 2, x= 11.0 m

(c) WG 3, x= 12.0 m

(d) WG 4, x= 13.0 m

(e) WG 5, x= 14.0 m

(f) WG 6, x= 15.0 m

(g) WG 7, x= 16.0 m

(h) WG 8, x= 17.0 m

Figure 9: Relative free surface elevations at various locations along the wave flume for the different wave heights simulated

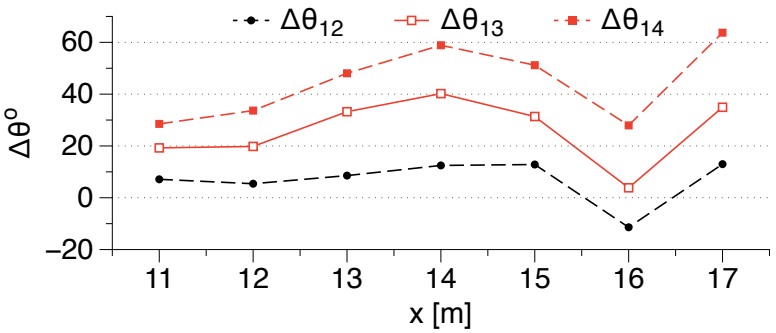

Figure 10: Relative phase difference between primary wave crests in the different cases simulated in the study with respect to the lowest incident wave with $H_1 = 0.022$ m

H_1, indicating that H_2 transfers a larger amount of wave energy to a higher frequency. In Figs. (9g) and (9h), the formation of a secondary and a tertiary wave crest is seen for both the non-breaking waves. The lower wave (H_1) continues to maintain a higher primary relative crest elevation throughout the wave decomposition process, whereas the higher wave has slightly higher secondary and tertiary relative crest elevations.

In the case of $H_3 = 0.042$ m and $H_4 = 0.052$ m spilling and plunging wave breaking is observed between $x = 12.0$ m and $x = 13.0$ m. During the shoaling process from $x = 6.0$ m to $x = 12.0$ m shown in Figs. (9b) and (9c), the waves have similar relative elevations. The breaking waves attain their maximum wave crest steepness of $\epsilon_{max} = 0.0526$ for H_3 and $\epsilon_{max} = 0.0641$ for H_4 at WG 3 at $x = 12.0$ m. At the wave gages after the breaking region, $x = 13.0$ m to $x = 17.0$ m, H_3 maintains a higher relative crest elevation in Figs. (9d)-(9h). This is justified by the fact that H_4 evolves into a plunging breaking wave and dissipates a larger part of its energy in the process compared to the spilling breaking wave formed by H_3. It is also noticed that the surf similarity number is $\xi = 1.0623$ for H_3 and $\xi = 0.9547$ for H_4. According to the classification by Battjes [1974], these correspond to plunging wave breaking on an emergent plane slope, but the results in this study show a spilling breaker for H_3 and plunging breaker for H_4. This indicates that the wave breaking on a bar crest has different breaker characteristics and the original classification for wave breaking on emergent plane slopes can not be directly applied to wave breaking over a submerged bar. In order to further understand the wave transformation process for the different cases simulated, the phase difference between the different waves during their propagation over the bar is analysed at the various gage locations. The relative phase difference $\delta\theta$ between the primary wave crests for $H_2 = 0.035$ m, $H_3 = 0.042$ and $H_4 = 0.052$ m with respect

to $H_1 = 0.022$ m is presented in Fig. (10). It can be concluded that the higher waves propagate faster and keep gaining on the lower incident waves until the bar crest ends. The phase differences between the free surface elevations show that H_4 leads H_1 by a maximum $\delta\theta_{14} = 60^\circ$ at $x = 14.0$ m. Over the leeside of the bar, the primary wave crests undergo a sudden reduction in their celerity during the decomposition process with H_2 lagging H_1 by $\delta\theta_{12} = 11.46^\circ$ and H_4 leading H_1 by only $\delta\theta_{14} = 27.94^\circ$ at $x = 16.0$ m (WG 7). As the waves propagate further to $x = 17.0$ m (WG 8), the phase differences return to the values obtained at the end of the bar crest at $x = 14.0$ m (WG 5).

Thus, the wave transformation process for all the incident waves is similar up to the region of wave breaking, with a higher incident wave attaining a higher relative crest elevation. After the region of wave breaking, the transformation of the breaking waves depends on the type of wave breaking, whereas the non-breaking waves continue with the trend seen on the weatherside slope. In the region of increasing water depth after the bar crest, the lower non-breaking wave maintains a higher primary relative crest elevation compared to the secondary relative crest elevation. The breaking waves show similar relative crest amplitudes. The higher incident waves are also seen to propagate faster and increase in celerity over the bar up to the end of the bar crest.

3.6. Wave decomposition process

The wave decomposition process is examined by calculating the power spectral densities for the different incident waves using the free surface elevations at the different locations. The frequencies to which the wave energy is transferred resulting in the evolution of the secondary and tertiary wave crests are identified. The normalized power spectra at the different wave gage locations along the bar are presented in Fig. (11). The power spectra for all the cases are normalized with the spectral amplitude at the primary wave frequency, $f_0 = 0.4$ Hz, S_{max} in Fig. (11a). The process of shoaling results in an increase of the energy content at the primary frequency and the first harmonic of the non-breaking waves. The lowest incident wave, H_1, adds $0.25S_{max}$ to its fundamental frequency f_0 whereas H_2 and H_3 gain 0.12 and 0.16 S_{max} respectively at the first harmonic at $x = 11.0$ m. On the other hand, the spectral power density for the highest incident wave H_4 is reduce by $0.05S_{max}$ at f_0 and increased by $0.14S_{max}$ at the first harmonic f_1. At $x = 12.0$ m, the waves reach the bar crest, and significant spectral densities are obtained up to the fourth harmonic f_4 with $0.024S_{max}$ for H_4. Wave breaking occurs between $x = 12.0$ m and $x = 13.0$ m for H_3 and H_4. This corresponds with a reduction of the spectral power density to $0.368S_{max}$ for

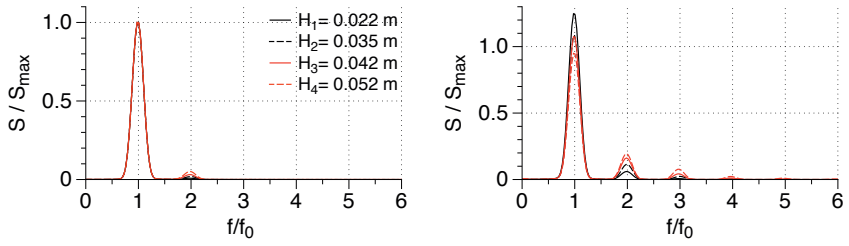

(a) WG 1, $x = 6.0$ m

(b) WG 2, $x = 11.0$ m

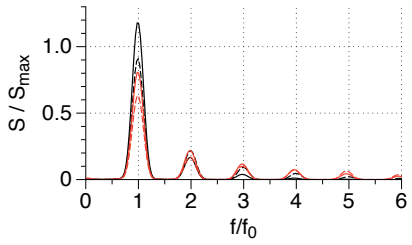

(c) WG 3, $x = 12.0$ m

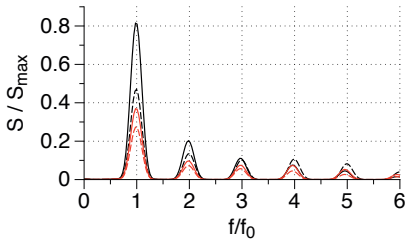

(d) WG 4, $x = 13.0$ m

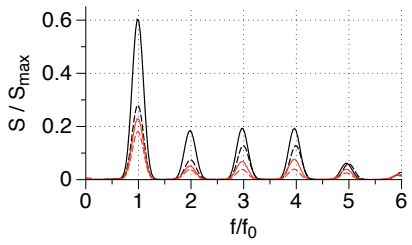

(e) WG 5, $x = 14.0$ m

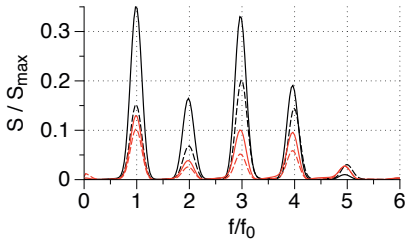

(f) WG 6, $x = 15.0$ m

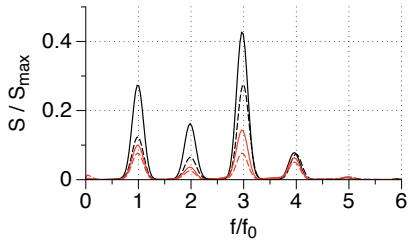

(g) WG 7, $x = 16.0$ m

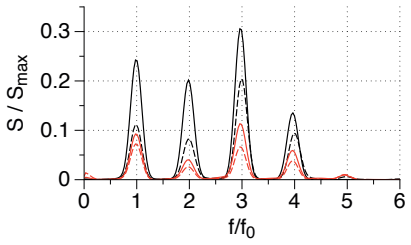

(h) WG 8, $x = 17.0$ m

Figure 11: Normalized spectra for the simulated waves showing decomposition of the incident wave into higher harmonics

H_3 and $0.272S_{max}$ for H_4 at f_0 at $x = 13.0$ m. In the case of the non-breaking waves, H_1 retains $0.82S_{max}$ at f_0 and transfers $0.20S_{max}$ and $0.11S_{max}$ to f_1 and f_2 respectively. As the waves propagate across the bar crest and in the region of increasing water depth at $x = 15.0$ m, the major portion of the energy is distributed between f_0 and f_2 for H_1. For H_2, H_3 and H_4 the major portion of the energy is distributed amongst f_0, f_2 and f_3 at $x = 15.0$ m in Fig. (11f). At $x = 16.0$ m, the spectral power density for all the four waves is mainly concentrated at f_0 and f_2 in Fig. (11g). As the waves reach a water depth of $d = 0.4$ m again at $x = 17.0$ m, H_1 similar power densities of $0.24S_{max}$ and $0.20S_{max}$ at f_0 and f_1 respectively and $0.31S_{max}$ at f_2. For the higher incident waves, the power spectra show a similar distribution as at $x = 16.0$ m, but with lower magnitudes.

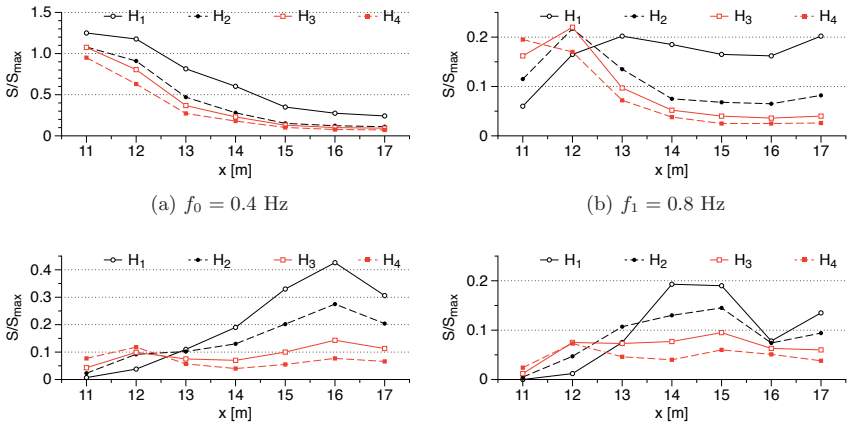

(a) $f_0 = 0.4$ Hz (b) $f_1 = 0.8$ Hz

(c) $f_2 = 1.2$ Hz (d) $f_3 = 1.6$ Hz

Figure 12: Variation of the normalized power density spectra at the first four harmonics for the different incident waves along the submerged bar

The variation of the spectral power density in the first four harmonics over the submerged bar for all the four waves is presented in Fig. (12. The power spectral density at f_0 is reduced significantly at $x = 17.0$ m to $0.24S_{max}$, $0.11S_{max}$, $0.09S_{max}$ and $0.09S_{max}$ for H_1, H_2, H_3 and H_4 respectively in Fig. (12a). From Fig. (12b), it is seen that the first harmonic f_1 initially gains energy for all the cases, but loses its energy gradually for all the cases except H_1. The second harmonic f_2 gradually gains energy as the propagate over the bar, with a maximum of $0.42S_{max}$ at $x = 16.0$ m for H_1 in Fig. (12c). The maximum spectral power in the third harmonic f_3 is presents itself between $x = 14.0$ m and $x = 15.0$ m. The following distinct pattern emerges regarding the energy transfer between the different harmonics. The fundamental frequency gradually loses most of its

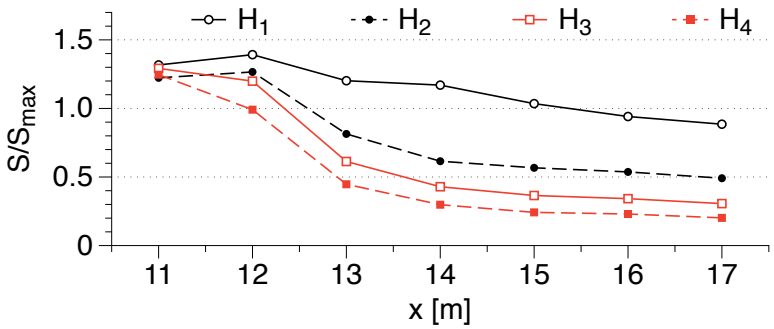

Figure 13: Variation of the total normalized power spectral density for the different incident waves along the submerged bar

energy as the wave propagates over the bar. The first harmonic gains energy initially on the weatherside slope, but loses this energy gradually. The second harmonic gains energy steadily and holds most of the wave energy towards the end of the bar. The third harmonic contains significant amounts of energy in the intermediate stages between $x = 13.0$ m and $x = 15.0$ m. Finally, the variation of the total energy in the first four harmonics over the length of the bar for all the cases is presented in Fig. (13). It is clear that all the waves lose significant amounts of energy except for H_1, with total spectral power densities of $0.89S_{max}$, $0.49S_{max}$, $0.31S_{max}$ and $0.30S_{max}$ for H_1, H_2, H_3 and H_4 respectively at $x = 17.0$ m, losing $12.5S_{max}$, $0.53S_{max}$, $0.73S_{max}$ and $0.85S_{max}$ during propagation of the bar.

4. Conclusion

The open-source CFD model, REEF3D is used to simulate wave propagation over a submerged bar including wave shoaling, breaking and decomposition for regular long waves with $T = 2.5$ s. The computed free surface elevations at several locations along the length of the flume are compared with experimental data and a general good agreement is seen both in terms of the phase and the elevation of the free surface variation for both non-breaking and spilling breaking waves. A good representation of the wave shoaling and decomposition during the propagation of the wave on the weatherside and leeside slopes respectively is obtained in the simulations. The high order discretization schemes in the model result in realistic modeling of the non-linear wave interactions and the dispersion characteristics of the decomposing waves for the more challenging case with long waves with $T = 2.5$ s, showing strong decomposition on the leeside of the bar. Spilling breakers

are observed on the bar crest for an incident wave height of 0.042 m ($\xi = 1.0623$) and on further increase of the incident wave height to 0.052 m ($\xi = 0.9547$), plunging breakers are observed. The wave transformation and decomposition is thoroughly analysed and the following conclusions are made regarding the wave transformation process along the bar:

- Non-breaking waves with higher incident amplitude increase in crest elevation until the end of the bar crest.
- Breaking waves with higher incident amplitude increase in crest elevation until the breaking region on the bar crest.
- Breaker classification using the surf similarity numbers based on emergent sloping beaches can not be applied directly in this scenario.
- Higher incident waves keep increasing their celerity and gain in wave phase over the lower wave heights until end of the bar crest.

The power spectra of the free surface elevations along the bar provided the following results regarding the wave decomposition process:

- Significant reduction in the wave energy at the fundamental frequency is seen for all the cases simulated and higher incident waves transfer a larger amount of energy to their higher harmonics on the weatherside slope.
- Non-breaking waves preserve most of their energy throughout the wave tank, whereas a large amount of wave energy is lost due to the breaking process for the breaking waves.
- A distinct pattern is observed in energy transfer amongst the harmonics with the first, second and third harmonics containing their maximum energies at the initial, the final and in the intermediate stages over the bar respectively.

Acknowledgements

The authors are grateful to Prof. Serdar Beji, Istanbul Technical University for providing the experimental data. This study has been carried out under the OWCBW project (No. 217622/E20) and the authors are grateful to the grants provided by the Research Council of Norway. This research was supported in part with computational resources at the Norwegian University of Science and Technology (NTNU) provided by NOTUR, http://www.notur.no (No. NN2620K).

References

Alagan Chella, M., Bihs, H., Myrhaug, D., Muskulus, M., 2015. Breaking characteristics and geometric properties of spilling breakers over slopes. Coastal Engineering 95, 4–19.

Battjes, J.A., 1974. Surf similarity, in: Proc., 14th International Conference on Coastal Engineering, Copenhagen, Denmark, pp. 466–480.

Beji, S., Battjes, J.A., 1993. Experimental investigation of wave propagation over a bar. Coastal Engineering 19, 151–162.

Beji, S., Battjes, J.A., 1994. Numerical simulation of nonlinear wave propagation over a bar. Coastal Engineering 23, 1–16.

Berthelsen, P.A., Faltinsen, O.M., 2008. A local directional ghost cell approach for incompressible viscous flow problems with irregular boundaries. Journal of Computational Physics 227, 4354–4397.

Blenkinsopp, C.E., Chaplin, J.R., 2008. The effect of crest submergence on wave breaking over submerged slopes. Coastal Engineering 55, 967–974.

Bosboom, J., Klopman, G., Roelvink, J., Battjes, J., 1996. Wave kinematics computations using boussinesq models, in: Proc. 25th International Conference on Coastal Engineering, Orlando, USA, pp. 109–122.

Bradshaw, P., Ferriss, D.H., Atwell, N.P., 1967. Calculation of boundary layer development using the turbulent energy equation. Journal of Fluid Mechanics 28, 593–616.

Brocchini, M., Drago, M., Iovenitti, L., 1992. The modelling of short waves in shallow water. comparison of numerical methods based on boussinesq and serre equations, in: Proc. 23rd International Conference on Coastal Engineering, New York, USA.

Chang, K.A., Hsu, T.J., Liu, P.L.F., 2001. Vortex generation and evolution of water waves propagating over a submerged rectangular obstacle. part i. solitary waves. Coastal Engineering 44, 13–36.

Choi, H., Moin, P., 1994. Effects of the computational time step on numerical solutions of turbulent flow. Journal of Computational Physics 113, 1–4.

Chorin, A., 1968. Numerical solution of the Navier-Stokes equations. Mathematics of Computation 22, 745–762.

Durbin, P.A., 2009. Limiters and wall treatments in applied turbulence modeling. Fluid Dynamics Research 41, 1–18.

Gourlay, M.R., 1994. Wave transformation on a coral reef. Coastal Engineering 23, 17–42.

Hieu, P.D., Katsutoshi, T., Ca, V.T., 2004. Numerical simulation of breaking waves using a two-phase flow model. Applied Mathematical Modeling 28, 983–1005.

Jacobsen, N.G., Fuhrman, D.R., Fredsøe, J., 2012. A wave generation toolbox for the open-source CFD library: OpenFOAM. International Journal for Numerical Methods in Fluids 70, 1073–1088.

Jiang, G.S., Peng, D., 2000. Weighted ENO schemes for Hamilton-Jacobi equations. SIAM Journal on Scientific Computing 21, 2126–2143.

Jiang, G.S., Shu, C.W., 1996. Efficient implementation of weighted ENO schemes. Journal of Computational Physics 126, 202–228.

Kamath, A., Alagan Chella, M., Bihs, H., Arntsen, Ø.A., 2015. Cfd simulations of wave propagation and shoaling over a submerged bar. Aquatic Procedia 4, 308–316.

Kjeldsen, S., Myrhaug, D., 1978. Kinematics and dynamics of breaking waves. River and Harbour Laboratory (NHL) The Norwegian Institute of Technology.

Kobayashi, N., Otta, A., Roy, I., 1987. Wave reflection and runup on rough slopes. Journal of Waterway, Port, Coastal and Ocean Engineering 3, 282–298.

Larsen, J., Dancy, H., 1983. Open boundaries in short wave simulations - a new approach. Coastal Engineering 7, 285–297.

Lemos, C.M., 1992. A simple numerical technique for turbulent flows with free surfaces. International Journal of Numerical Methods in Fluids 15, 127–146.

Lin, P., Liu, P.L.F., 1998. A numerical study of breaking waves in the surf zone. Journal of Fluid Mechanics 359, 239–264.

Morgan, G.C.J., Zang, J., Greaves, D., Heath, A., Whtilow, C.D., Young, J.R., 2010. Using the rasinterfoam CFD model for wave transformation and coastal modeling, in: Proc., Coastal Engineering Conference, Shanghai, China, pp. 1–9.

Naot, D., Rodi, W., 1982. Calculation of secondary currents in channel flow. Journal of the Hydraulic Division, ASCE 108, 948–968.

Osher, S., Sethian, J.A., 1988. Fronts propagating with curvature- dependent speed: algorithms based on Hamilton-Jacobi formulations. Journal of Computational Physics 79, 12–49.

Peng, D., Merriman, B., Osher, S., Zhao, H., Kang, M., 1999. A PDE-based fast local level set method. Journal of Computational Physics 155, 410–438.

Roeber, V., Cheung, K., Kobayashi, M., 2010. Shock-capturing boussinesqtype model for nearshore wave processes. Coastal Engineering 57, 407–423.

Stelling, G., Zijlema, M., 2003. An accurate and effcient fnite-difference algorithm for non-hydrostatic free-surface fow with application to wave propagation. International Journal for Numerical Methods in Fluids 43, 1–23.

Takikawa, K., Yamada, F., Matsumoto, K., 1997. Internal characteristics and numerical analysis of plunging breaker on a slope. Coastal Engineering 31, 143–161.

Tissier, M., Bonneton, P., Marche, F., Chazel, F., Lannes, D., 2012. A new approach to handle wave breaking in fully non-linear boussinesq models. Coastal Engineering 67, 54–66.

van der Vorst, H., 1992. BiCGStab: A fast and smoothly converging variant of Bi-CG for the solution of nonsymmetric linear systems. SIAM Journal on Scientific and Statistical Computing 13, 631–644.

Wilcox, D.C., 1994. Turbulence modeling for CFD. DCW Industries Inc., La Canada, California.

Zhao, Q., Armfield, S., Tanimoto, K., 2004. Numerical simulation of breaking waves by a multi-scale turbulence model. Coastal Engineering 51, 53–80.

6.7 Paper 7

Breaking solitary waves and breaking wave forces on a vertically mounted slender cylinder over an impermeable sloping seabed

Alagan Chella, M., Bihs, H., Myrhaug, D., Muskulus, M.
Submitted to *Journal of Ocean Engineering and Marine Energy*, 2015 - Revised version under review

Paper 7

Journal of Ocean Engineering and Marine Energy manuscript No.
(will be inserted by the editor)

Breaking Solitary Waves and Breaking Wave Forces on a Vertically Mounted Slender Cylinder over an Impermeable Sloping Seabed

Mayilvahanan Alagan Chella · Hans Bihs · Dag Myrhaug · Michael Muskulus

the date of receipt and acceptance should be inserted later

Abstract In the present study, breaking solitary waves over a sloping seabed and breaking wave forces on a vertically mounted cylinder are simulated with the three-dimensional CFD model REEF3D. The numerical model uses the Reynolds-Averaged Navier-Stokes (RANS) equations together with the level set method (LSM) for the free surface and the $k-\omega$ for the turbulence. The numerical model is validated for simulating breaking solitary waves and breaking wave forces against the experimentally measured free surface profiles and vertical and horizontal velocities by Mo et al. (2013) and the experimentally measured free surface elevation and breaking wave force by Chakrabarti et al. (1997). The main purpose of the paper is to examine the effects of the breaking characteristics, the geometric properties, the relative cylinder positions and the incident wave heights on the breaking wave force characteristics. A total of 21 simulations are performed to investigate the characteristics and the geometric properties of solitary waves breaking over a slope and the associated breaking wave forces on a cylinder. First, the characteristics and geometric properties of breaking solitary waves are investigated with two-dimensional simulations. Further, the study

Mayilvahanan Alagan Chella
Department of Civil and Transport Engineering
Norwegian University of Science and Technology
E-mail: acm@ntnu.no

Hans Bihs
Department of Civil and Transport Engineering
Norwegian University of Science and Technology

Dag Myrhaug
Department of Marine Technology
Norwegian University of Science and Technology

Michael Muskulus
Department of Civil and Transport Engineering
Norwegian University of Science and Technology

explores the effect of the relative distance between the breaking point and the cylinder on breaking wave forces. Finally, the study examines breaking solitary wave forces for different incident waves. This also includes the analysis of breaking wave force characteristics such as the impact duration and rise time, the peak force, the average slamming coefficient, and the force impulse. The results of the numerical simulations show that the relative distance between the cylinder and the breaking point plays an important role in obtaining the maximum force. In addition, the numerical model is capable of representing the most important physical flow features related to the breaking solitary waves and the interaction with the vertical slender cylinder.

Keywords Solitary waves · wave structure interaction · breaking waves · geometric properties · breaking characteristics · breaking wave forces

1 Introduction

The wave transformation process in shallow waters is strongly influenced by seabed interaction. As a result, the wave height increases with a steeper wave front, gains forward momentum and the wave front becomes nearly vertical at the breaking point. When the vertical wave front hits the surface of a structure, a sudden drop in the forward momentum leads to an impact force of large magnitude with short duration. The wave impact characteristics are determined by the breaker type and breaker point. The breaker types can be grouped into four types: spilling, plunging, surging and collapsing, and are determined by the incident wave characteristics and beach slope (Galvin, 1968). The knowledge of the wave impact loads from the steep and breaking waves is important for an understanding of the global load characteristics on structures deployed in shallow waters; e.g. substructures for offshore wind turbines (Alagan Chella et al., 2012).

The solitary wave theory is appropriate for describing the propagation of long-period oscillatory waves in shallow waters. Moreover, the propagation and interaction of tsunami waves with coastal structures can be well represented with an appropriate solitary wave theory. Solitary breaking waves exert huge hydrodynamic loads on support structures in shallow waters. Goring (1978) performed numerical and experimental investigations on the wave propagation of long waves in shallow waters. Different theoretical approaches such as linear and nonlinear dispersive and linear and nonlinear nondispersive wave theories were considered. The author also investigated the transmission and reflection properties of solitary and cnoidal waves, which are relevant for the propagation of tsunami waves from deep waters to shallow coastal waters. Losada et al. (1989) examined the propagation of non-breaking solitary waves over a step. The various aspects of solitary wave characteristics were investigated. The shoaling and the breaking characteristics of solitary waves over plane slopes have been extensively studied by Camfield and Street (1979); Grilli et al. (1995, 1997); Ippen and Kulin (1954); Miles (1980); Munk (1949).

An analytical model for predicting impact pressures on vertical walls due to breaking

waves was proposed by Cooker and Peregrine (1990, 1995) based on the pressure-impulse theory. The peak pressure distribution and the kinematics during the impact process were investigated for liquid-solid and liquid-liquid impact problems . It was found that the wave pressure impulse field is strongly influenced by the local wave characteristics during the impact. More detailed discussion on wave impact on walls can be found in Kortenhaus et al. (1999), and Peregrine (2003). Cuomo et al. (2011, 2010) investigated wave impact loads from breaking waves on vertical walls and caisson breakwaters experimentally and analytically. Based on the analysis, the authors proposed a set of new formulae for estimating both horizontal quasi-static and impact forces and overturning moments on vertical face coastal structures. The estimated wave forces were in good agreement with experimental data and the predicted forces with the pressure-impulse theory (Cooker and Peregrine, 1990, 1995). Further, Cuomo et al. (2007) examined the characteristics of wave loads on offshore jetties experimentally. The force mechanism of impulsive loading process was studied with the wavelet analysis. The authors also proposed dimensionless equations to estimate wave forces on deck and beam elements.

According to Goda et al. (1966), the total wave force on a vertical pile due to breaking

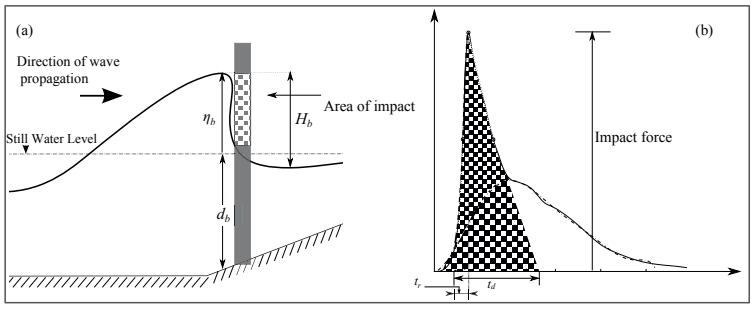

Fig. 1 Definition sketch for characteristics of (a) breaking waves and (b) impact force; t_d and t_r are the duration and rise time of the impact, respectively. The area of the shaded portion in (b) represents the force impulse (I_{td}).

waves is composed of two parts. The first part is associated with a fluid force which can be represented well by the Morison equation. The other part is associated with the wave impact force arising from the complex interaction of fluid velocities and accelerations with the structure. The hydrodynamics related to the wave impact force due to breaking waves are extremely complicated. The shape of the water surface at the instant of the wave impact plays a significant role in estimating the impact force as shown in Fig. 1 (b). In the case of a nearly breaking wave in shallow water, the maximum particle velocity occurs at the crest, thus the force contribution from the crest

is larger than the contribution from the rest of the wave. Therefore, the mechanism of the wave impact force mainly depends on the shape of the wave front and the wave celerity at breaking.

Kjeldsen and Myrhaug (1978) raised a concern about the geometrical description

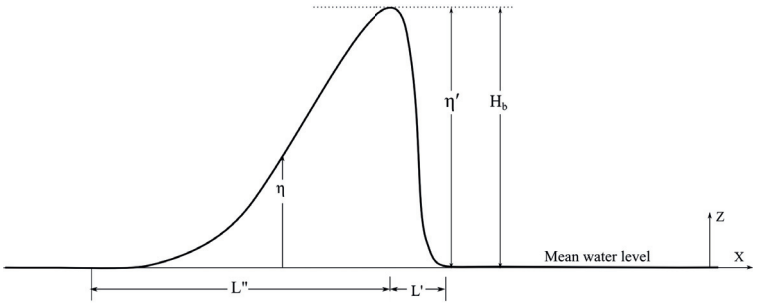

$$\varepsilon = \frac{\eta'}{L'} \qquad \delta = \frac{\eta'}{L''} \qquad \lambda = \frac{L''}{L'}$$

Fig. 2 Definition sketch for crest front steepness (ε), crest rear steepness (δ) and vertical asymmetry factor (λ) following Kjeldsen and Myrhaug (1978)

of the breaker profile in deep water since the local wave steepness is inadequate to represent it. They suggested steepness and asymmetry parameters to categorize the breaker profiles: crest front steepness (ε), crest rear steepness (δ) and vertical asymmetry factor (λ) as defined in the Fig. 2. With these parameters, the geometry of the wave profile at breaking can be defined. There has been some discussion about the geometrical properties of periodic waves in shallow water, see e.g. Adeyemo (1968); Alagan Chella et al. (2015a,c); Hwang (1984). However, to the knowledge of the authors, a study on the geometric properties has not been carried out for solitary waves breaking over slopes.

Laboratory experiments have contributed to the knowledge about waves breaking over beaches and the associated wave impact forces on structures; e.g. breaking waves on slopes by Adeyemo (1968); Stive and Wind (1982); Ting and Kirby (1994), and breaking wave forces by Arntsen et al. (2011); Chaplin et al. (1992); Goda et al. (1966); Sawaragi and Nochino (1984); Wienke and Oumeraci (2005). The application of the theoretical models (e.g. Sawaragi and Nochino (1984); Wienke and Oumeraci (2005)) for determining breaking wave forces is confined to the use of force and slamming coefficients. Since these coefficients are mostly obtained from physical experiments, they are subjected to the specific laboratory conditions.

The theoretical breaking criterion in deep water is always related to the physical properties of the highest steady wave, which limits the wave growth. Whereas shallow water waves deform as they propagate into decreasing water depth, the seabed friction is included as an additional effect in defining the breaking criterion in shallow water. Computational fluid dynamics (CFD) models based on the Navier-Stokes equations are capable of describing the wave transformation process including wave breaking and their non-linear interaction with structures (Lemos, 1992). CFD models can describe the breaking process without defining an empirical breaking criterion. In addition, the non-linear wave impact forces can be obtained without determining the force and slamming coefficients and curling factors . Lemos (1992) proposed a numerical model for simulating breaking waves in shallow waters based on the RANS equations, the $k-\epsilon$ model and the volume of fluid (VOF) method.

Many numerical studies have been carried out to model breaking waves in shallow waters (e.g. Alagan Chella et al. (2015a,c); Hieu et al. (2004); Jacobsen et al. (2012); Lin and Liu (1998); Xie (2013); Zhao et al. (2004)) and associated breaking wave forces (e.g. Choi et al. (2015); Mo et al. (2013); Xiao and Huang (2014)). It is challenging to model the interaction between breaking waves and structures in the breaking zone. More recently, Mo et al. (2013) performed both experimental and numerical investigations on breaking solitary waves and its interaction with a slender cylinder over a slope. The free surface elevation and velocity at different locations were measured using PIV (Particle Image Velocimetry). They modelled the three-dimensional (3D) wave-structure interaction numerically with the filtered Navier-Stokes equations together with the Large Eddy Simulations (LES) model. Xiao and Huang (2014) modelled breaking solitary waves and breaking wave forces on a cylindrical pile using the Reynolds-Averaged Navier-Stokes (RANS) equations, the $k-\epsilon$ model and the VOF method. They studied solitary wave run-up, breaking on a slope and the breaking wave force on a vertical pile at different locations. Although the aforementioned studies reported many interesting results, little work has been carried out to study the relationship between the characteristics and geometric properties of breaking solitary waves and the resulting impact forces on structures.

The main purpose of this paper is to investigate the characteristics and geometric properties of breaking solitary waves over a slope and their interaction with a vertical circular cylinder using the two-phase flow CFD model, REEF3D (Alagan Chella et al., 2015a). The numerical model uses the RANS equations together with the level set method for the free surface and the $k-\omega$ model for turbulence. Compared to previous studies, the present study focuses on different aspects of breaking solitary wave forces on a structure in connection with the characteristics and geometric properties at breaking. The connection between the maximum total force and the cylinder location relative to the breaking point is examined.

The paper is divided into four parts. The first part deals with the validation of the numerical model. The second part examines the breaking characteristics and geometric properties of solitary waves over a sloping seabed without any structure for different

incident waves with two-dimensional (2D) simulations. The third part evaluates the relative distance between the cylinder and the breaking point which significantly influences the wave impact force characteristics using 3D simulations. This has been investigated by placing a cylinder over a slope at different locations from the non-breaking zone to the post-breaking zone. In part four the effect of the incident wave height on the total force characteristics is investigated. The 3D simulations are carried out by maintaining the relative distance between the cylinder and the breaking point for different incident wave heights based on the results obtained from the second and third part. The effect of the breaking characteristics, the geometric properties, the relative cylinder positions and the incident wave heights on the the total breaking wave force characteristics are presented and discussed. Finally, conclusions are given in Part 5. Overall, the present work provides new insight into the assessment of the hydrodynamic loads on vertical cylinders and flow characteristics around them due to breaking solitary waves.

2 Numerical model

The model proposed in this paper uses numerical approaches to enable the implementation of higher order schemes for the spatial and temporal discretization. With the higher order discretization schemes, good numerical accuracy and stability is achieved. The present numerical model has been successfully used to simulate spilling and plunging breakers over slopes (Alagan Chella et al., 2015a,c), waves breaking over an impermeable slope (Alagan Chella et al., 2015b), non-breaking wave forces on large cylinders (Kamath et al., 2015, 2016), and breaking wave forces on slender cylinders (Bihs et al., 2016).

A viscous incompressible two-phase flow for water and air is considered and this is described by the RANS equations. The governing equations are the continuity equation:

$$\frac{\partial U_i}{\partial x_i} = 0 \tag{1}$$

and the momentum equation:

$$\frac{\partial U_i}{\partial t} + U_j \frac{\partial U_i}{\partial x_j} = -\frac{1}{\rho}\frac{\partial P}{\partial x_i} + \frac{\partial}{\partial x_j}\left[(\nu + \nu_t)\left(\frac{\partial U_i}{\partial x_j} + \frac{\partial U_j}{\partial x_i}\right)\right] + g_i \tag{2}$$

Here U is the velocity averaged over time t, ρ is the fluid density, P is the pressure, ν is the kinematic viscosity, ν_t is the eddy viscosity, and g the gravity term.

A 5th-order Weighted Essentially Non-Oscillatory (WENO) scheme is used to discretize the non-linear convective term of the RANS equations (Jiang and Shu, 1996). Time discretization is performed by a 3rd-order total variation diminishing (TVD) Runge-Kutta scheme (Shu and Osher, 1988) which preserves numerical stability and temporal accuracy. This method involves three Euler sub-steps. Due to the lack of

correlation in the pressure field (p) obtained by the solution of the Navier-Stokes equations, the pressure is modeled separately with Chorinś projection method. First, an intermediate velocity (u^*) is determined by omitting the pressure term in the momentum equations. By taking the divergence of the intermediate velocity (u^*), the Poisson equation for the pressure is obtained as follows:

$$\frac{\partial}{\partial x_i}\left(\frac{1}{\rho\left(\phi^n\right)}\frac{\partial p}{\partial x_i}\right) = -\frac{1}{\Delta t}\frac{\partial U_i^*}{\partial x_i} \tag{3}$$

Then the pressure is determined by solving the Poisson equation with the BiCGStab algorithm (van der Vorst H., 1992) with Jacobi preconditioning. After solving the Poisson equation for pressure, the velocity field is updated with the projection method (Chorin, 1968) at each time step:

$$u_i^{n+1} = u_i^* - \frac{\Delta t}{\rho\left(\phi^n\right)}\frac{\partial p}{\partial x_i} \tag{4}$$

The staggered grid arrangement is implemented in the numerical model to achieve a strong pressure-velocity coupling. Turbulence in the breaking waves is described by the $k-\omega$ model together with the standard RANS turbulence closure. An accurate representation of the interface for time-dependent free-surface flow problems is highly demanding as this involves the capturing of discontinuities in the material properties such as density and viscosity. The two-fluid interface is modelled with the level set method (Osher and Sethian, 1988) which is an Eulerian front capturing scheme. Simulations are carried out in a 3D numerical wave tank. The relaxation method is used to describe the wave generation (Jacobsen et al., 2012; Larsen and Dancy, 1983). The total wave forces on a structure are directly obtained by integrating the pressure and the normal component of the viscous stress tensor τ over the surface of the structure as follows:

$$F = \int_{\Omega}(-\mathbf{n}p + \mathbf{n}.\tau)d\Omega \tag{5}$$

where $\mathbf{n}$ is the unit normal vector to the surface, pointing into the fluid domain and Ω is the surface of the structure. More detailed information concerning the numerical model can be found in Alagan Chella et al. (2015a,c) and Kamath et al. (2015).

3 Characteristics of breaking waves and impact force

In the present study, the breaking point is identified when most of the wave front becomes vertical and the breaker height (H_b) and water depth at breaking (d_b) are calculated as defined in Fig. 1 (a). The breaking characteristics are evaluated based on the location of the breaking point (x_b), water depth at breaking (d_b), the breaker depth index ($\gamma_b = H_b/d_b$), and the breaker height index ($\Omega_b = H_b/H_0$, where H_0 is the deep water wave height). The waves considered in the present study are plunging

breaking waves as listed in Table 1. The breaker type is classified based on the slope parameter (S_0) defined by Grilli et al. (1997):

$$S_0 = 1.521 \frac{m}{\sqrt{(H_0/d_0)}} \tag{6}$$

The values of slope parameter (S_0) for different breaker types:

Spilling : S_0<0.025
Plunging: 0.025<S_0<0.30
Surging: 0.3<S_0<0.37.

A force impulse is a most common design parameter for coastal structures especially; it governs the global response of a structure (Kortenhaus et al., 1999). The force impulse (I_{td}) is described by the peak force (F_{peak}), the impact duration (t_d), and the impact rise time (t_r), and it is the area under the peak force of a force-time curve over an impact duration as defined in Fig. 1. In order to evaluate the wave impact force contribution to the total breaking wave force, the average slamming coefficient $\overline{C_s}$ proposed by Sarpkaya and Isaacson (1981) is used and it is defined as follows:

$$\overline{C_s} = \frac{F_{maxt}}{0.5 \rho A_{sub} C_b^2} \tag{7}$$

where F_{maxt} is the maximum total force, D is the diameter of the cylinder, A_{sub} is the submerged projected area, and C_b is the wave celerity at the breaking point.

Simulation cases	Normalized wave height, H_0/d_0	Normalized relative distance between the cylinder and the breaking point, $L_c = (H_b x_c/d_b D)$	Slope parameter, S_0	Breaker type
Case A	0.33	-12.72 -8.48 -4.24 0.000 4.24 8.48 12.72 16.96 21.20	0.236	PL
Case B 2D and 3D simulations	0.257 0.281 0.305 0.330 0.354 0.378 0.403	4.24	0.21 0.22 0.23 0.24 0.25 0.26 0.27	PL PL PL PL PL PL PL

Table 1: List of the 2D and 3D computational cases; PL: Plunging breaker.

4 Results and discussion

4.1 Benchmark case

4.1.1 Experimental and simulation conditions

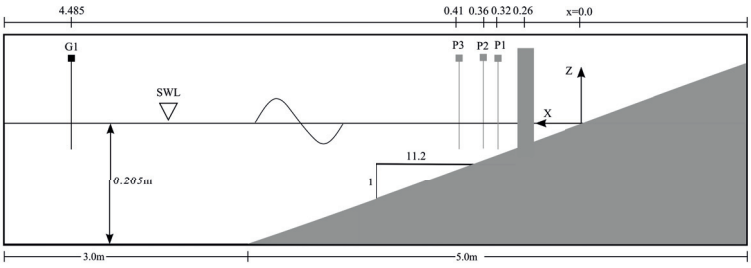

Fig. 3 Computational set-up

To validate the numerical model, the simulated results are compared with the experimental results reported by Mo et al. (2013). They performed a series of laboratory experiments in a 25m long, 0.3m wide and 1.0m deep wave tank. In the present numerical study, the computation domain starts with a 3.0m long flat bed portion with a water depth of 0.205m connected to a slope of 1/11.2. The computational domain is of length L_x=12.0m, width L_y=0.01m and height $L_z = 0.50m$ for the 2D set-up (Fig. 3) and of length L_x=12.0m, width L_y=0.40m and height $L_z = 0.50m$ for the 3D set-up. At first, the 2D simulations are carried out to examine the characteristics and geometry of breaking solitary waves over a slope. The results from these 2D simulations such as the breaking point and the breaker height serve as input to the 3D simulations for case B as listed in Table 1. Since the 3D flow features are insignificant before the wave breaking, the 2D simulations are used to determine the incipient breaker characteristics and geometric properties. Further, the 3D simulations are performed with a cylinder of diameter D=0.06m placed over a slope at x=0.260m from the shoreline. The interaction of breaking waves with the cylinder and the resulting breaking wave forces are investigated. Therefore, the 3D simulations are performed to obtain the breaking wave forces and 3D flow features around the cylinder. Though the experiments were carried out in a wave tank with a flat 5.0m long bed, the numerical wave tank is reduced to 3.0m as the reduction in the flat bed part does not affect the incident wave characteristics in the flat bed region. Except for that, the coordinate system and wave parameters of the numerical simulations are the same as that of the laboratory measurements.

4.1.2 Grid dependence study

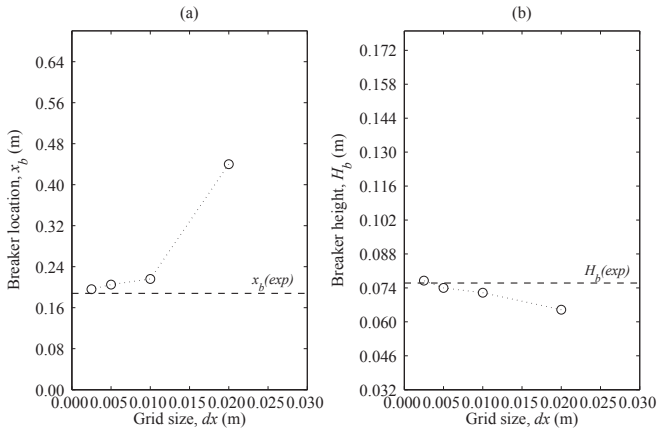

Fig. 4 Grid dependency study on numerical breaking location (x_b) and breaker height (H_b); $x_b(exp)$ and $H_b(exp)$ are the experimentally measured values of x_b and H_b by Mo et al. (2013).

The sensitivity of the grid size on the computational results is investigated with four different uniform grid sizes, dx=0.0025m, 0.005m, 0.010m and 0.020m. Fig. 4 shows the breaker location (x_b) and the breaker height (H_b) for these grid sizes. In contrast to cnoidal waves on slopes (Alagan Chella et al., 2015a), the simulated waves with the coarsest grid (dx=0.020m) reach the breaking point sooner with lower H_b than that of the waves with finer grids, corresponding to dx=0.02, x_b=0.44m (Fig. 4 (a)) and H_b=0.065m (Fig. 4 (b)). The numerical results for dx=0.0025m, 0.005m and 0.010m are close to the laboratory breaking location x_b=0.188m and the breaker height H_b=0.076m as shown in Fig. 4. In addition, the 3D simulations are computationally quite expensive. Therefore, the grid size dx=0.010m is used for the following simulations with 55981 number of cells for 2D simulations and 1648400 number of cells for 3D simulations.

4.1.3 Solitary wave generation and breaking over a sloping seabed

In the wave generation zone, the free surface elevation and the kinematics are described using the third-order solitary wave theory proposed by Grimshaw (1971). The solitary wave with the normalized wave height of H_0/d_0=0.33 is generated for the constant water depth of d_0=0.205m. The comparison of the numerical wave surface

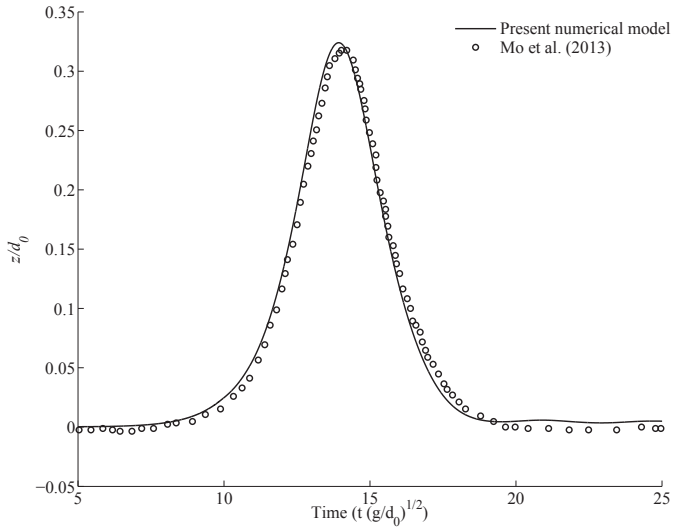

Fig. 5 Comparison of numerical and experimental free surface elevation at x=4.485m, circles: experimental data by Mo et al. (2013); solid lines: present numerical results;

elevation at x=4.485m shows a good agreement with the experimental data by Mo et al. (2013) as presented in Fig. 5. This confirms that the laboratory waves are well represented by the numerically generated waves. Figs. 6 and 7 show the comparison of the 2D numerical wave profiles at $t\sqrt{g/d_0}$=31.35 and 31.77, respectively, and the corresponding normalized horizontal velocity profiles at x=0.32m, 0.36m and 0.41m with the experimental results. The velocity profiles at different locations are computed from the seabed up to the free surface in the numerical simulations while the laboratory profiles are measured up to a point little above the free surface in the air phase. The computed and measured horizontal component of velocity increase as the distance from the bottom increases. At the crest, the horizontal component of velocity increases with increasing wave surface elevation (Fig. 6). It is noticed that the computed velocity profiles have large gradients close to the seabed due to the boundary layer effect. However, the spatial resolution of the numerical results are not sufficiently small to account for the boundary layer effects close to the seabed; strictly it should approach zero at the bed. It was reported by Mo et al. (2013) that the boundary layer effects near the seabed was not captured well in the laboratory experiments due to the low resolution in the measurements.

Fig. 8 shows the evolution of the free surface profiles of the wave approaching

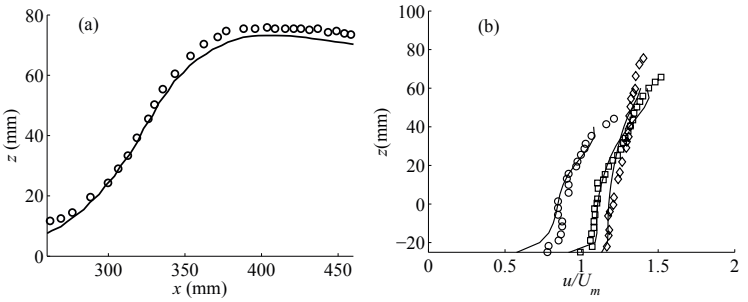

Fig. 6 Comparison of numerical (solid lines) and experimental results for (a) wave surface elevation at $t\sqrt{g/d_0}$=31.35 (circles: experimental data) and (b) horizontal velocity profiles at x=0.32m (circles: experimental data), 0.36m (squares: experimental data) and 0.41m (diamonds: experimental data); U_m is the computed mean horizontal velocity and the value is 726 mm/s.

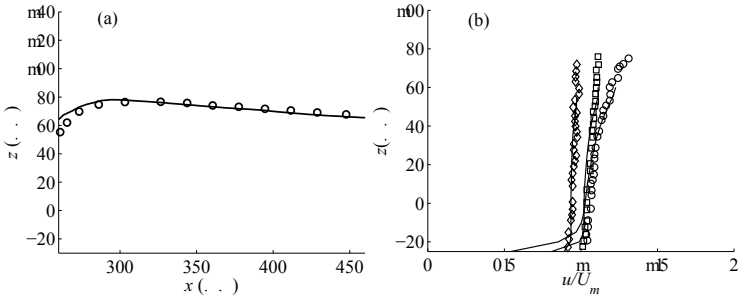

Fig. 7 Comparison of numerical (solid lines) and experimental results for (a) wave surface elevation at $t\sqrt{g/d_0}$=31.77 (circles: experimental data) and (b) horizontal velocity profiles at x=0.32m (circles: experimental data), 0.36m (squares: experimental data) and 0.41m (diamonds: experimental data); U_m=768 mm/s

breaking and the comparison with the experimental data. The simulated free surface profiles are in good agreement with those measured by Mo et al. (2013). The wave front becomes steep as the wave propagates over the slope due to the shoaling and the wave front becomes vertical and breaks at x=0.216m which is very close to the laboratory breaking (x_b=0.188m). Further, the wave crest overturns with a forward ejected water jet due to high velocities at the wave crest in the proximity of the interface. The

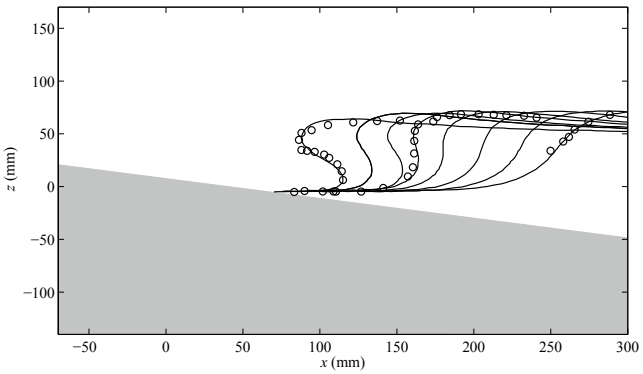

Fig. 8 Comparison of numerical and experimental free surface profiles at different time instants. circles: experimental data; solid line: present numerical results

wave height decreases as the wave approaches the shore after the breaking point. This implies that the overturned wave crest falls over the free surface in order to balance the change in the local momentum during the wave breaking process. Moreover, the numerical results agree well with the measured data for the changes in the wave profile and the horizontal velocity.

4.1.4 Solitary wave interaction with a slender circular cylinder

In order to validate the numerical model performance for simulating the solitary breaking wave interaction with a slender circular cylinder, the numerical results are compared with the experimental data. Figs. 9 and 10 show the numerical and laboratory wave profiles at $t\sqrt{g/d_0}$=31.70 and 32.18 and the corresponding normalized horizontal component of velocity profiles at x=0.32m, 0.36m and 0.41m, respectively. A rise in the water level along the upstream surface of the cylinder is observed as the wave interacts with the cylinder as shown in Fig. 10 (b). As mentioned in Section 4.1.3, the computed horizontal velocity profiles close to the seabed is strongly influenced by the boundary layer effect.

Fig. 11 shows the simulated horizontal and vertical components of velocity variation under the solitary wave during the initial interaction with the cylinder. The horizontal velocity profiles at different locations for $t\sqrt{g/d_0}$=31.70 and 32.18 show an increasing trend from the sea bottom towards the free surface as seen in Fig. 11 (a). However, the vertical velocity profiles show an increasing trend to the free surface for $t\sqrt{g/d_0}$=31.70

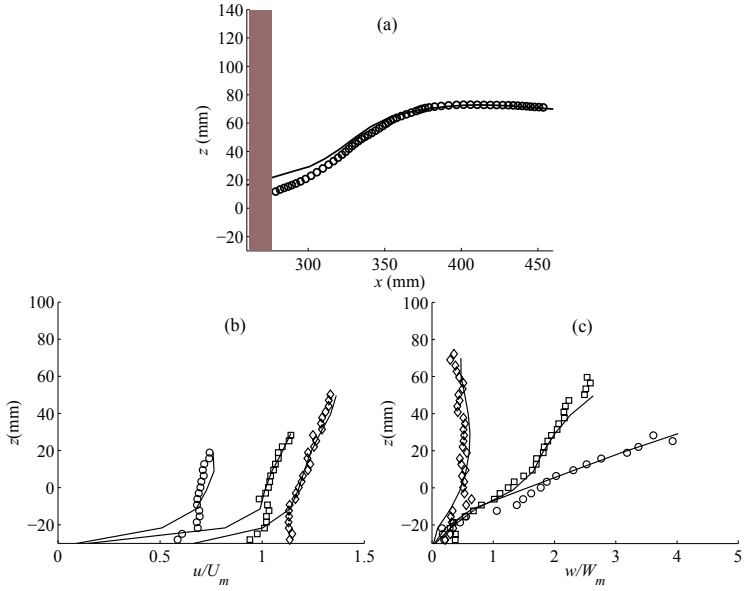

Fig. 9 Comparison of numerical (solid lines) and experimental results for (a) wave surface elevation at $t\sqrt{g/d_0}$=31.70 (circles: experimental data), (b) horizontal velocity profiles and (c) vertical velocity profiles at x=0.32m (circles: experimental data), 0.36m (squares: experimental data) and 0.41m (diamonds: experimental data); U_m=605 mm/s and W_m=105 mm/s, W_m is the computed mean vertical velocity.

at x=0.32m and 0.36m (Fig. 9 (c)) and for $t\sqrt{g/d_0}$=32.18 at x=0.32m (10 (c)) and a decreasing trend for $t\sqrt{g/d_0}$=31.70 at x=0.41m (Fig. 9 (c)) and for $t\sqrt{g/d_0}$=32.18 at x=0.36m and 0.41m (Fig. 10 (c)). The vertical component of the velocity near the sea bottom is larger than close to the free surface as seen in Fig. 11 (b). The simulated wave surface profile and the horizontal and vertical velocities match well with the laboratory measurements. The simulated horizontal and vertical velocities (Fig. 11) exhibit a similar variability as that of laboratory experiments.

Fig. 12 shows the comparison of the computed breaking force by the present numerical model and the numerical model by Mo et al. (2013). Though the present results match overall well with the results from Mo et al. (2013), the details near the secondary peak after the maximum load are not well captured in the numerical simulation. The upper part of the total force variation obtained from the present study shows a sharp and narrow pattern with a small secondary hump. It should be noted that Mo et al. (2013) modelled only half of the computational domain along the x-direction based on the symmetric flow field assumption, while the full computational domain is modelled

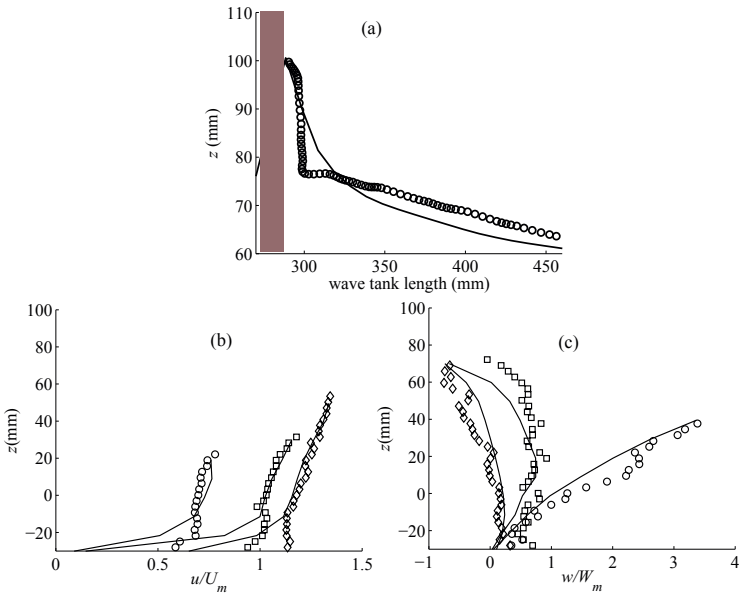

Fig. 10 Comparison of numerical (solid lines) and experimental results for (a) wave surface elevation at $t\sqrt{g/d_0}$=32.18 (circles: experimental data), (b) horizontal velocity profiles and (c) vertical velocity profiles at x=0.32m (circles: experimental data), 0.36m (squares: experimental data) and 0.41m (diamonds: experimental data); U_m=644 mm/s and W_m=65 mm/s.

in the present study. It seems likely that the flow features and the dynamic pressure gradient in the wake of the cylinder are not symmetric. Fig. 13 shows the velocity magnitude and the free surface changes of the wave interacting with the cylinder at different times. In the beginning, the water surface in front of the cylinder increases drastically (Fig. 13 (a)). The undisturbed upstream wave then separates into nearly two symmetric waves passing around the cylinder and the water level rises continuously until the flow around the cylinder is established (Fig. 13 (b)). As a result, the free surface deformation occurs along the surface of the cylinder and the water level decreases as the wave passes the cylinder. This is due to the reflection of the water column in front of the cylinder. Moreover, the water level rises with increase of the height of the water column that leads to the run-up effect (Fig. 13 (b)). This causes the early submergence of the cylinder and this in turn strongly influences the duration (t_d) of the impact and the maximum upstream pressure. Further, the deformed free surface around the cylinder reconnects at the downstream side of the cylinder (Fig.

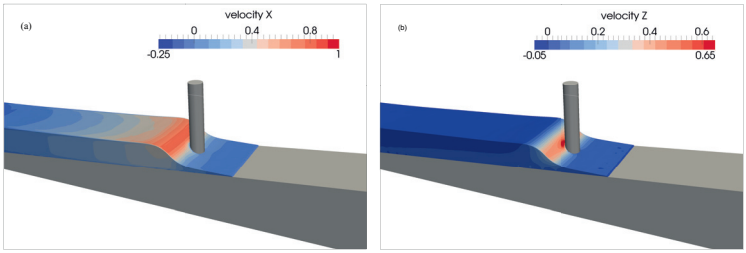

Fig. 11 Simulated horizontal (V_x (m/s)) and vertical (V_z (m/s)) velocity variation at $t\sqrt{g/d_0}$=32.18 during the interaction.

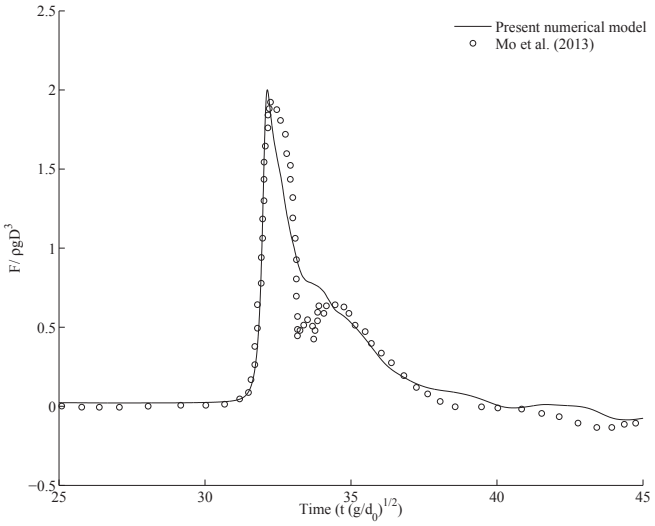

Fig. 12 Comparison of present numerical and computational results by Mo et al. (2013) for total force on the cylinder

13 (c)). This evolves into a forward moving water jet behind the cylinder with high velocities near the free surface (Fig. 13 (d)).

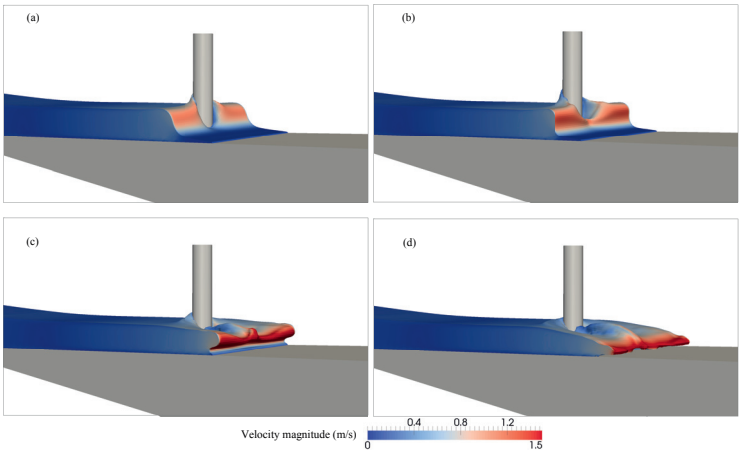

Fig. 13 Simulated free surface changes with velocity magnitude variation for the benchmark case at t=7.50s (a), 7.55s (b), 7.65s (c) and 7.70s (d)

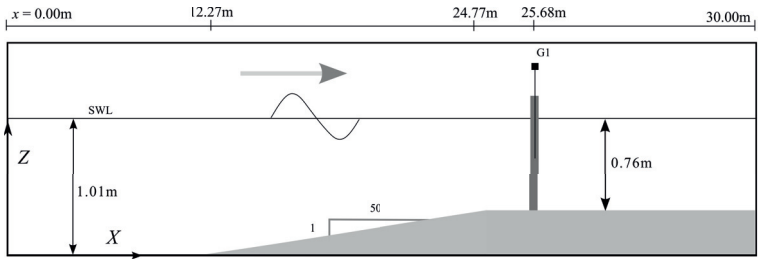

Fig. 14 Numerical set-up.

4.1.5 Breaking solitary wave force on a slender circular cylinder

The numerical model for simulating breaking wave forces is validated by comparing the experimentally measured breaking wave force on a vertical cylindrical pile by Chakrabarti et al. (1997). The authors investigated the wave loads from depth-limited breaking waves on a vertical single pile caisson. In the physical experiments, the cylinder has a uniform diameter D=0.046m up to 0.460m below the free surface and it is tapered over a distance of 0.08m to a uniform diameter D=0.052m. Whereas in the numerical simulation, a uniform diameter D=0.046m throughout its legnth is considered as the breaking wave force is strongly influenced by the free surface

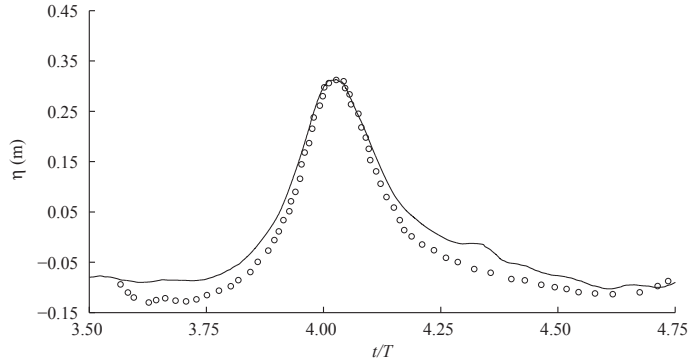

Fig. 15 Comparison of present numerical and experimental results by Chakrabarti et al. (1997) for wave surface elevation close to the cylinder.

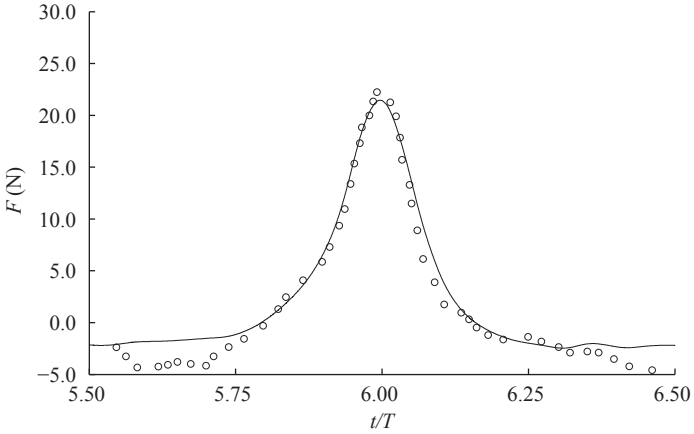

Fig. 16 Comparison of present numerical and experimental results by Chakrabarti et al. (1997) for total force on the cylinder.

deformations around the cylinder. The computational set-up consists of a 4m long flat bed connected to a 1/50 slope followed by a 0.25m high flat bed as shown in Fig. 14. A cylinder with D=0.046m is placed at x=25.68m over a flat bed portion (Fig. 14). The size of the numerical wave tank is L_x=30m, L_y=0.30m, and L_z=1.80m and it is descretized into 13.80 million uniform cells with a grid size dx=0.01m.

Fifth-order Stokes waves (Fenton, 1985) with H_0= 0.406m and T=3.0s are used in the numerical simulation. The water surface elevation is calculated at x=25.68m close to the cylinder (G1, Fig. 14). Figs. 15 and 16 show the comparison of the computed and measured results for the water surface elevation (η) at x=25.68m (Fig. 14) and the breaking wave force (F), respectively. It appears that the computed η and F match well with the experimentally measured results by Chakrabarti et al. (1997). The breaking wave force on the cylinder is evaluated when the wave breaks at the cylinder. Though the computed wave crest is in good agreement with the experimental data, the wave trough is slightly over-predicted (Fig. 15). The development of the breaking wave force on a single pile caisson is well captured and the computed peak force distribution matches well with the measured one. However, the force emerged from the wave trough interaction with the cylinder is slightly under-predicted as seen in Fig. 16, but in general, the wave surface elevation (η) and the breaking wave force (F) are well represented in the numerical simulation.

4.2 Characteristics and geometric properties of solitary waves breaking over a sloping seabed

In this part the characteristics and geometric properties of solitary waves breaking over a slope are investigated for different H_0/d_0 (case B) with the 2D simulations. Fig. 17 (a) shows the relative breaker depth (d_b/d_0) versus the normalized wave heights (H_0/d_0) for different offshore wave heights (H_0) (since d_0 is fixed). It appears that d_b/d_0 increases with increasing H_0/d_0. As anticipated, waves with larger H_0/d_0 break earlier offshore at larger water depths as the shoaling rate increases with increasing wave heights. The range of d_b/d_0 for solitary waves in the present case is much lower than for periodic waves on slopes (Fig. 14 of Alagan Chella et al. (2015a)). Fig. 17 (b) and (c) show the breaker depth index (γ_b) and breaker height index (Ω_b) versus H_0/d_0 for different incident wave heights (H_0). It appears that γ_b and Ω_b decrease as H_0/d_0 increases. Waves with larger H_0/d_0 break seaward at larger water depths with relatively small increase in the incident wave height, corresponding to H_0/d_0=0.403, d_b/d_0=0.12 (Fig. 17 (a)), γ_b=3.63 (Fig. 17 (b)) and Ω_b=1.05 (Fig. 17 (c)). Waves with smaller H_0/d_0 shoal more over the slope and break farther shoreward at a smaller water depth with a relatively large change from the incident wave height, corresponding to H_0/d_0=0.257, d_b/d_0=0.051 (Fig. 17 (a)), γ_b=5.77 (Fig. 17 (b)) and Ω_b=1.136 (Fig. 17 (c)). In the present case, the range of γ_b is varied from 3.50 to 5.77, which are much larger than the typical values of periodic waves on slopes as presented in Fig. 16 of Alagan Chella et al. (2015a). This also suggests that in the case of solitary waves, the absence of the wave trough interaction with the slope cause the waves to propagate further up the slope, breaking at shallower water depths.

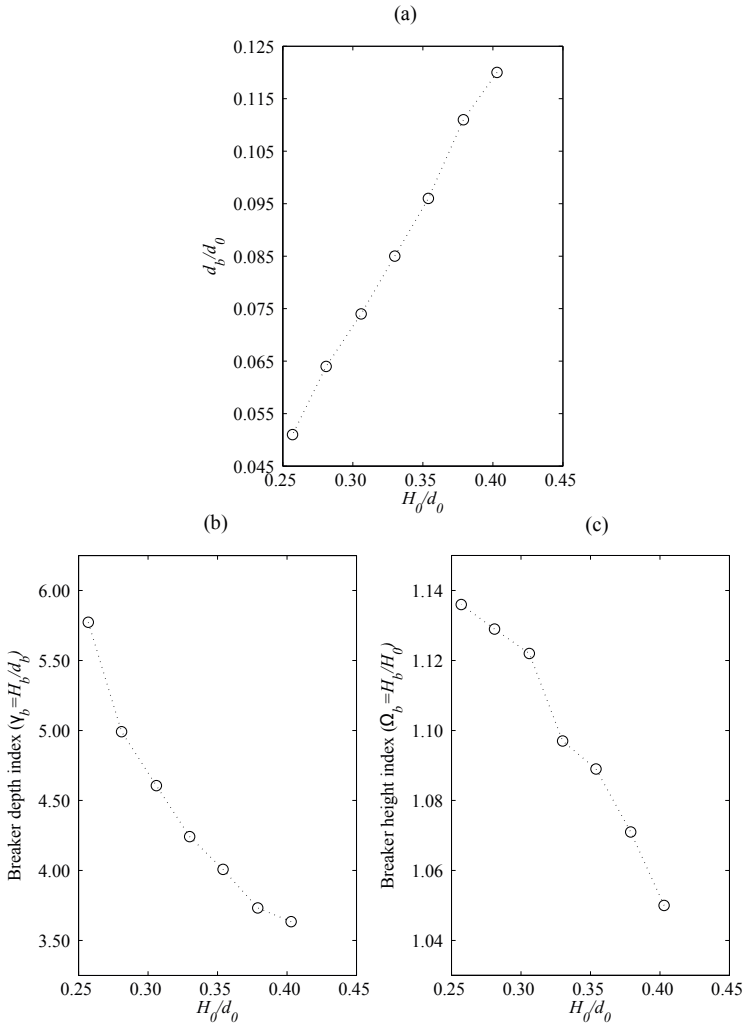

Fig. 17 Computed (a) relative breaker depth (d_b/d_0), (b) breaker depth index (γ_b), and (c) breaker depth index (Ω_b) versus normalized wave height (H_0/d_0)

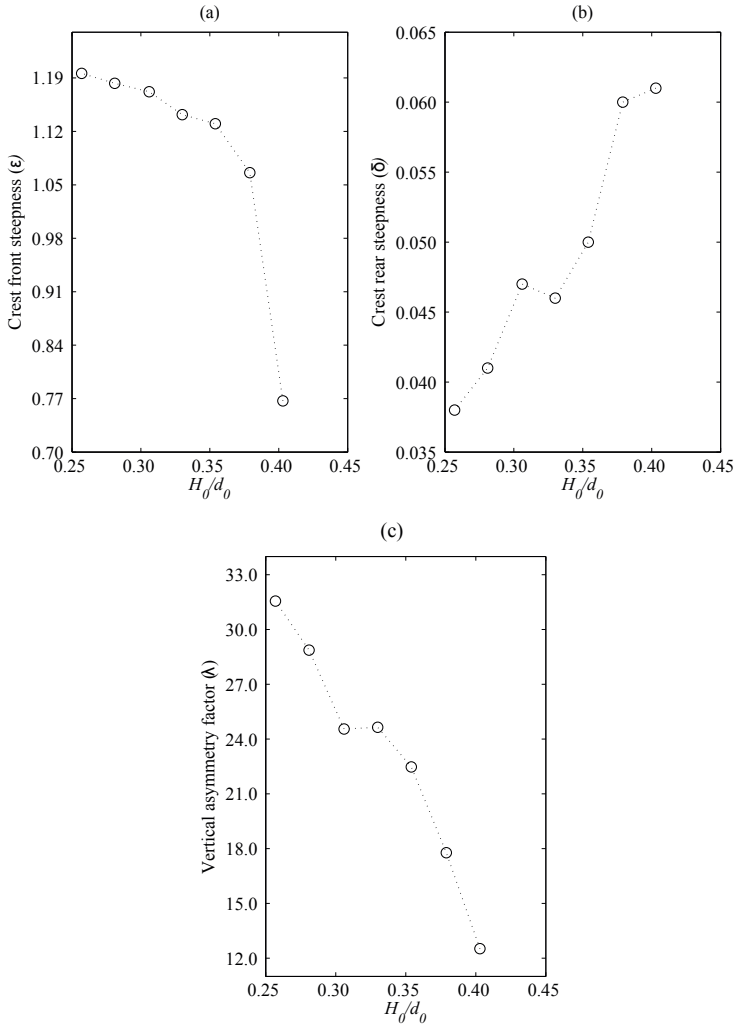

Fig. 18 Computed (a) crest front steepness (ε), (b) crest rear steepness (δ) and (c) vertical asymmetry factor (λ) versus normalized wave height (H_0/d_0)

The geometric properties at breaking are calculated based on the wave crest front steepness (ε), the wave crest rear steepness (δ) and the vertical asymmetry factor (λ) proposed by Kjeldsen and Myrhaug (1978) as defined in Fig. 2. Moreover, the relationship between the wave characteristics and the geometric properties as well as the breaking force characteristics are discussed in Section 4.3.2. Fig. 18 shows ε, δ and λ versus the normalized wave height (H_0/d_0) for different offshore wave heights (H_0) (since d_0 is fixed). It appears that ε (Fig. 18 (a)) and λ (Fig. 18 (c)) decrease and δ (Fig. 18 (b)) increases as H_0/d_0 increases. Waves with larger H_0/d_0 do not undergo much deformation when compared to waves with smaller H_0/d_0. As seen from Fig. 18 (c), waves with smaller H_0/d_0 approaching the breaking point experience more deformation as smaller waves propagate longer over the slope than waves with larger H_0/d_0. This is consistent with the findings of Grilli et al. (1997) who investigated the characteristics of solitary waves over slopes. The front face of the wave steepens and the rear face of the wave becomes milder as the incident wave height increases, corresponding to H_0/d_0=0.257, ε=1.20 (Fig. 18 (a)), δ=0.038 (Fig. 18 (b)) and λ=31.56 (Fig. 18 (c)). The range of λ from 12.0 to 31.56 is larger than that of periodic waves in shallow water as shown in Fig. 24 of Alagan Chella et al. (2015a).

Simulation cases	Normalized wave height, H_0/d_0	Normalized relative distance, $L_c = (H_b x_c/d_b D)$	Peak force, F_{peak} (N)	Impact duration, t_d (s)	Impact rise time, t_r (s)
1	0.33	-12.72	3.56	0.068	0.021
2		-8.48	3.68	0.081	0.021
3		-4.24	2.67	0.107	0.023
4		0.00	3.36	0.184	0.056
5		4.24	4.35	0.259	0.058
6		8.48	2.85	0.320	0.099
7		12.72	2.95	0.428	0.142
8		16.96	2.98	0.464	0.175
9		21.20	2.92	0.63	0.214

Table 2: Computed force peak (F_{peak}), Impact duration (t_d), and Impact rise time (t_r) for different normalized distances (L_c).

4.3 Breaking solitary wave forces on a vertically mounted slender circular cylinder

4.3.1 Breaking wave force variation for different cylinder positions

In this part the effect of the relative distance between the cylinder and the breaking point on the breaking wave forces is examined for different cylinder positions. The cylinder is placed at different locations based on the normalized relative cylinder distance $L_c = H_b x_c / d_b D$, where x_c is the distance between the cylinder and the breaking point. The normalized relative cylinder distance (L_c) describes the relationship between the breaker depth index ($\gamma_b = H_b/d_b$), the diameter (D) and the distance between the breaking point and the cylinder (x_c). A total of 9 simulations are carried out for the L_c values listed in Table 1 (case A). Fig. 19 depicts the velocity variation and the free surface changes at the selected positions of the cylinder during the breaking process. For a given wave, the variation of the maximum force for non-breaking, breaking and post-breaking waves is evaluated by placing the cylinder at different normalized relative distances corresponding to L_c=0.0 (at breaking, Fig. 19 (f)), L_c=4.24, 8.48, 12.72, 16.96 and 21.20 (before breaking, Figs. 19 (a) to (e)) and L_c=-4.24, -8.48 and -12.72 (after breaking, Figs. 19 (g) to (i)) as listed in Table 1.

Figs. 20 and 21 show the normalized wave force ($F_{norm} = F/\rho g D^3$) versus time for different normalized relative distances (L_c) before and after the breaking point. The maximum normalized force occurs when the cylinder is placed just before the breaking point at L_c=4.24 (Fig. 19 (e) and Fig. 20 (e)), which is larger than the wave force experienced by the cylinder when it is placed at the breaking point (L_c=0.0) (Fig. 19 (f) and Fig. 21 (a)). It appears that the wave with the inclined wave front is less steep leading to a larger submergence of the cylinder, causing a larger force than the force caused by a steeper wave with a smaller submergence of the cylinder. Table 2 presents the computed peak force (F_{peak}), impact duration (t_d), and rise time (t_r) for different normalized relative distances (L_c). It appears that the impact duration (t_d) and rise time (t_r) increase as L_c increases (from L_c=21.20 (before breaking) to L_c=-12.72 (after breaking)). The corresponding cylinder locations are presented in Fig. 19. The impact duration (t_d) and rise time (t_r) are 0.259s and 0.059s, respectively, for L_c=4.24, and 0.184s and 0.056s, respectively, for L_c=0.00. Although the impact duration (t_d) is larger for L_c=4.24 (Fig. 20 (e)) than for L_c=0.0 (Fig. 21 (a)), the rise time (t_r) is almost the same for both cases. The main differences between the case with L_c=0.0 (Fig. 19 (f)) and L_c=4.24 (Fig. 19 (e)) are the local steepness of the wave front, larger impact duration (t_d), and the submergence of the cylinder during the impact. Therefore, a certain combination of the cylinder submergence and the deformed wave shape causes the maximum horizontal force. It is also found that the wave height at which the maximum horizontal force occurs is almost the same as that of the wave height at the breaking point. This also implies that the relative distance between the cylinder and the breaking point plays a crucial role in obtaining the maximum force. The steepness of the wave front and the crest particle velocity increases as the wave

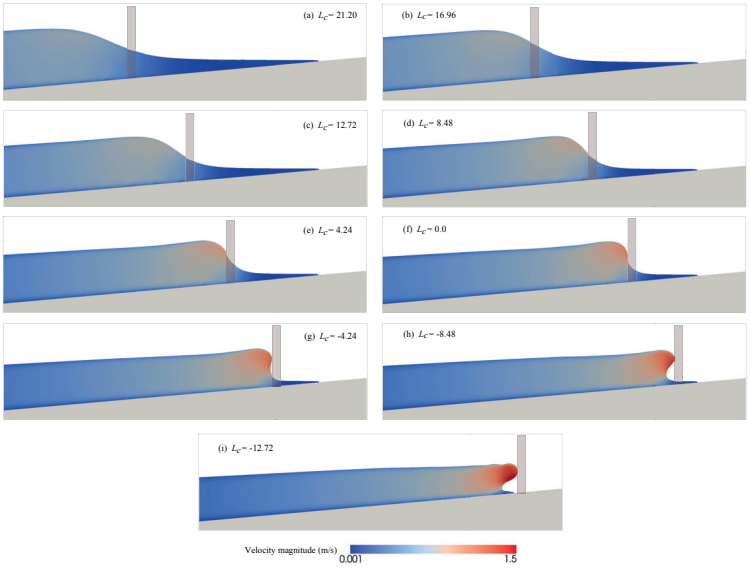

Fig. 19 Simulated free surface profiles with velocity magnitude (m/s) variation at t=5.38s (a), 5.51s (b), 5.57s (c), 5.67s (d), 5.74s (e), 5.80s (f), 5.87s (g), 5.94s (h), and 6.00s (i) and the corresponding cylinder positions, see case A in Table 1.

propagates over the slope. Thus, a portion of wave crest propagates faster than the rest of the wave with an ejected forward water jet as presented in Fig. 19 (h) and (i). Therefore, the overturned wave crest impinges onto the surface of the cylinder causing a very short duration impact, corresponding to Fig. 21 (c) and (d) and Fig. 19 (h) and (i). It is noticed that the development of the overturned wave crest after breaking is associated with a smoothly ejected water jet (Fig. 19 (h) and (i)) and the velocity distribution under the wave crest is almost constant. The impact duration (t_d) and rise time (t_r) are 0.081s and 0.021s, respectively, for L_c=-8.48, and 0.068s and 0.021s , respectively, for L_c=-12.72. The peak force (F_{peak}) and impact rise time (t_r) are almost the same for both cases; however, the impact duration (t_d) is larger for L_c=-8.48.

When the wave breaks just before the cylinder, the maximum force on the cylinder computed at L_c=-4.24 (Figs. 19 (g) and 21 (b)) is smaller than the non-breaking wave force. This may be due to the interaction of an overturned wave crest including an air pocket evolved during the breaking process with the cylinder as shown in Fig. 19 (g). In the case of L_c=-8.48 (Fig. 19 (h)) and L_c=-12.72 (Fig. 19 (i)), the wave breaks far

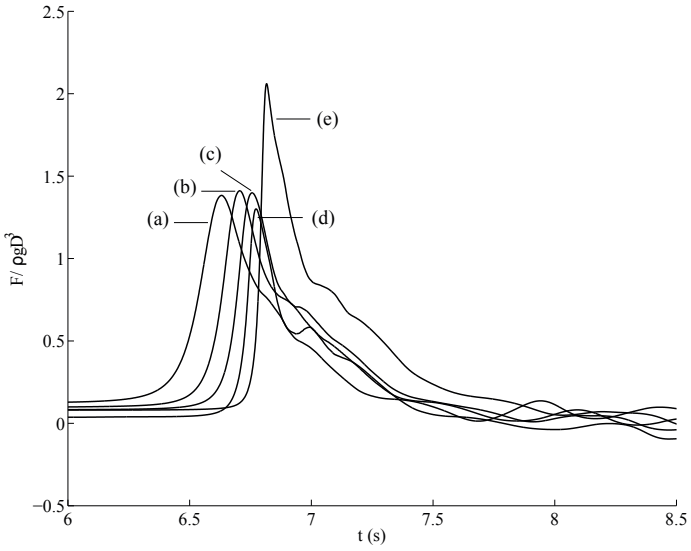

Fig. 20 Computed normalized force ($F_{norm} = F/\rho g D^3$) versus time for different normalized relative distances $L_c = (H_b x_c / d_b D)$ (before breaking): (a) 21.20, (b) 16.96, (c) 12.72, (d) 8.48 and (e) 4.24

before the cylinder and it experiences the maximum force from the impingement of the wave crest with the ejected water jet on the cylinder. Therefore, the total forces acting on the cylinder at L_c=-8.48 (Fig. 21 (c)) and -12.72 (Fig. 21 (d)) are larger than for the non-breaking wave forces for L_c=0.0, (Fig. 19 (f)), L_c=4.24 (Fig. 19 (e)).

As can be seen from Fig. 19, the slope of the wave front increases as L_c increases. During the wave impact, the rise time (t_r) mainly depends on the local slope of the wave front (Sawaragi and Nochino, 1984). The computed results indicate that t_r decreases as the front shape of the wave becomes steeper. Moreover, the present numerical results confirm the experimetally measured characteristics reported by Sawaragi and Nochino (1984) who investigated wave impact forces on a vertical slender cylinder experimentally. Finally, Fig. 22 presents the normalized maximum force ($F_{maxn} = F_{max}/\rho g D^3$) versus L_c for different cylinder positions, i.e. showing the peak values of the curves shown in Figs. 20 and 21 versus L_c. The corresponding peak forces (F_{peak}) for each L_c case are listed in Table 2. The results demonstrate that L_c plays an important role in determining the maximum force. This is also consistent

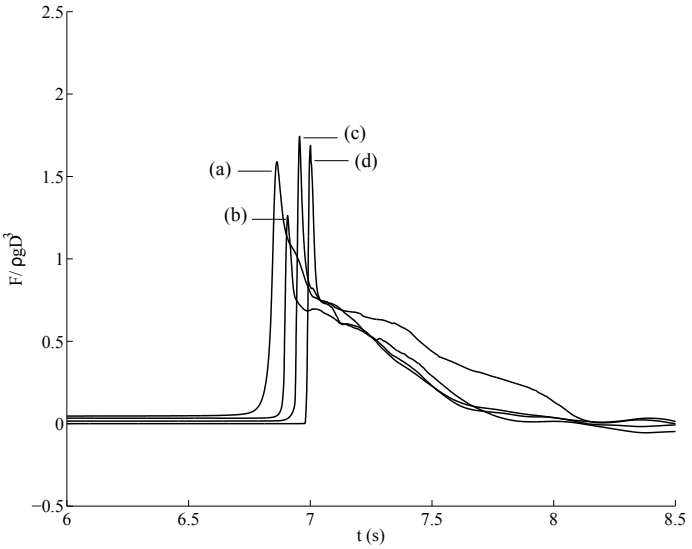

Fig. 21 Computed normalized force ($F_{norm} = F/\rho g D^3$) versus time for different normalized relative distances $L_c = (H_b x_c / d_b D)$ (after breaking): (a) 0.0, (b) -4.24, (c) -8.48, and (d) -12.72.

with the experimental observations by Wienke et al. (2000) and Irschik et al. (2002) who investigated the breaking wave forces on a slender cylinder.

4.3.2 Breaking wave force variation for different incident waves

Further, a total of seven simulations are carried out to study the characteristics of breaking wave forces for different incident waves as seen in Table 1 (case B). The cylinder is placed based on the normalized relative distance $L_c = H_b x_c / d_b D$=4.24 corresponding to the maximum total force for each case. The breaking locations obtained from the 2D simulations are used to determine the appropriate relative cylinder position. Fig. 23 shows the normalized wave force (F_{norm}) versus time for different normalized incident wave heights (H_0/d_0). As expected, the results show that F_{norm} increases as H_0/d_0 increases for larger incident waves. Table 3 presents the computed peak force (F_{peak}), impact duration (t_d), rise time (t_r), and force impulse (I_{td}, Fig. 1) over the impact duration for different normalized incident wave heights (H_0/d_0). It appears that t_d, t_r, and I_{td} decrease and F_{peak} increases as H_0/d_0 increases. It is noticed that the area under the primary peak of the normalized total force curve be-

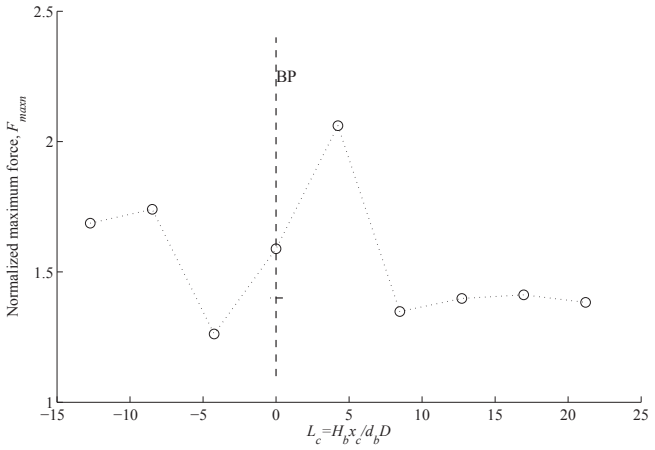

Fig. 22 Computed normalized maximum force ($F_{maxn} = F_{max}/\rho g D^3$) as a function of $L_c = H_b x_c / d_b D$, BP is the breaking point.

comes larger and the shape of the primary peak becomes narrower as H_0/d_0 increases.

Simulation cases	Normalized wave height, H_0/d_0	Normalized relative distance, $L_c = (H_b x_c/d_b D)$	Peak force, F_{peak} (N)	Impact duration, t_d (s)	Impact rise time, t_r (s)	Force impulse, I_{td} (Ns)
1	0.257		3.14	0.440	0.095	0.690
2	0.281		3.82	0.352	0.062	0.692
3	0.305		4.31	0.328	0.062	0.697
4	0.33	4.24	4.36	0.300	0.060	0.690
5	0.354		4.53	0.255	0.059	0.544
6	0.378		5.12	0.240	0.052	0.620
7	0.403		5.25	0.118	0.042	0.442

Table 3: Computed force peak (F_{peak}), Impact duration (t_d), Impact rise time (t_r), and force impulse (I_{td}) for different normalized wave heights (H_0/d_0).

On the one hand, the cylinder experiences a larger peak force (F_{peak}) of a shorter rise time (t_r) with a lower force impulse (I_{td}) from a larger incident wave, corresponding to H_0/d_0=0.403, F_{peak}=5.25N, t_r=0.042s, and I_{td}=0.442 Ns in Table 3. Further, the crest front steepness (ε) and the vertical asymmetry factor (λ) become lower, implying that the wave front does not deform much during the shoaling, corresponding to H_0/d_0=0.403, ε=0.76 (Fig. 18 (a)), λ=12.0 (Fig. 18 (c)), Ω_b=1.048 (Fig. 17 (c)). On the other hand, for smaller incident waves, F_{peak} decreases and t_r and I_{td} increase, corresponding to H_0/d_0=0.257, F_{peak}=3.14N, t_r=0.085s, and I_{td}=0.69 Ns in Table 3. Then, ε=1.20 (Fig. 18 (a)) and λ=31.56 (Fig. 18 (c)) increase as H_0/d_0 decreases. This also suggest that the forces due to smaller incident waves rise slowly for longer duration with larger force impulses.

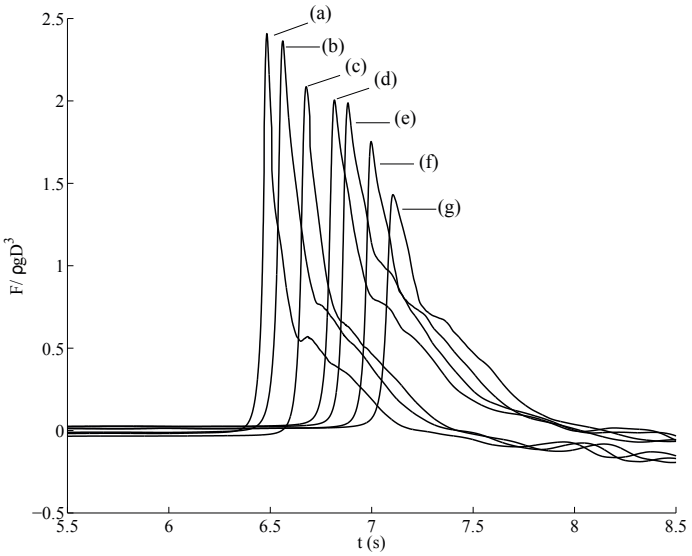

Fig. 23 Computed normalized total force (F_{norm}) versus time for different H_0/d_0: (a) 0.403, (b) 0.378 (c) 0.354 (d) 0.330, (e) 0.305, (f) 0.281 and (g) 0.257

As reported by Hattori et al. (1994) who studied breaking wave impact pressure on a vertical wall experimentally, the force impulse increases as the rise time (t_r) increases. The authors also pointed out that a larger load on a vertical wall is always associated with a lower peak force and a larger force impulse. Overall, the computed variations of F_{peak} versus t_r and F_{peak} versus I_{td} are quite consistent with the previous studies on vertical walls (Cuomo et al., 2011, 2010; Hattori et al., 1994; Kortenhaus et al., 1999).

Though a larger incident wave does not undergo more deformation during the shoaling, i.e. the wave front is not steeper than for a smaller incident wave at breaking, the impact rise time (t_r) is smaller with the lower force impulse (I_{td}). However, the slope of the wave front always determines the rise time (Sawaragi and Nochino, 1984). The computed geometric properties indicate that larger incident waves have sharper rear parts, whereas smaller incident waves have smoother rear parts. It is therefore likely that the large crest particle velocity changes occur rapidly when a larger incident wave interacts with the cylinder, causing a sudden rise of the impact force, i.e. lower impact rise time (t_r).

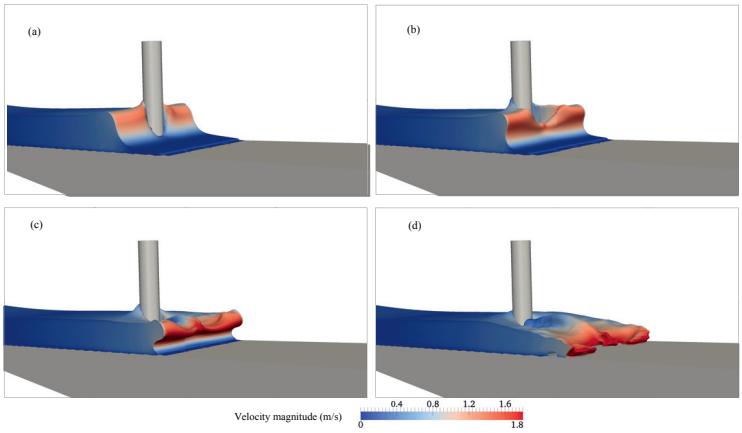

Fig. 24 Simulated free surface changes with velocity magnitude (m/s) variation during the interaction of the larger solitary wave (H_0/d_0=0.403) with the cylinder at t=6.37s (a), 6.56s (b), 6.75s (c) and 6.94s (d)

Fig. 24 shows the velocity magnitude and free surface variation at different stages for the interaction of the largest solitary wave (H_0/d_0=0.403, Fig. 23 (a)) with the cylinder. The free surface deformation around the cylinder becomes wider and larger for larger solitary waves (Fig. 24 (a) and (b)) when compared to the interaction with relative smaller solitary waves (Fig. 13 (a) and (b)). This creates a larger pressure gradient downstream and the run-up upstream (Fig. 24 (a) and (b)). In addition to that, the high crest velocity can cause the wave to pass the cylinder more quickly with a large pressure gradient resulting in a larger impact force. The size of the downstream water jet formed during the reconnection of the free surface behind the cylinder (Fig. 24 (c) and (d)) grows larger and wider as H_0/d_0 increases. This also implies that the free surface deformation in the vicinity of the cylinder increases as the incident wave height increases.

Fig. 25 shows the average slamming coefficient ($\overline{C_s}$) as defined in Eq. 7 versus the normalized wave height (H_0/d_0) for different offshore wave heights (H_0) (since d_0 is fixed). The variation of $\overline{C_s}$ shows a decreasing trend as H_0/d_0 increases which is opposite to the variation of F_{norm} versus H_0/d_0 (see Fig. 23) and similar to the variation of I_{td} and t_r versus H_0/d_0 (Table 3). Waves with larger H_0/d_0 break farther offshore at shallower water depths with small changes in the wave crest, corresponding to H_0/d_0=0.403, d_b/d_0=0.12 (Fig. 17 (a)), γ_b=3.63 (Fig. 17 (b)) and Ω_b=1.05 (Fig. 17 (c)). Therefore, the cylinder exposed to smaller incident waves experiences larger force impulse and larger force from the deformed wave above the still water level, corresponding to H_0/d_0=0.257, γ_b=5.77 (Fig. 17 (b)), ε=1.196 (Fig. 18 (a)), λ=31.56

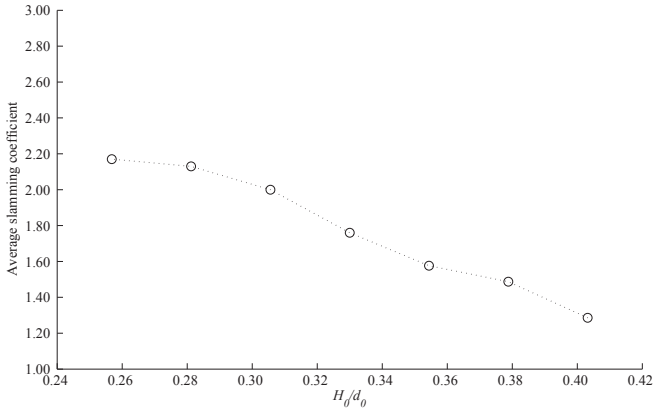

Fig. 25 Computed average slamming coefficients ($\overline{C_s}$) versus normalized wave height (H_0/d_0)

(Fig. 18 (c)), and I_{td}=0.690Ns (Table 3). On the other hand, $\overline{C_s}$, I_{td}, and t_r decrease and F_{peak} increases as H_0/d_0 increases. In addition to that the submerged projected area (Eq. 7) of the cylinder and the crest velocity increase with the increase of H_0. An implication of this is the possibility that the force contribution from the wave above the still water level to the total force increases as the incident wave becomes smaller. Consequently, the average slamming coefficient ($\overline{C_s}$) decreases as H_0 increases. The present results suggest that $\overline{C_s}$ and I_{td} represent an important part of the force contribution from the wave above the still water level to the total force.

5 Conclusions

Numerical simulations have been carried out with the CFD model, REEF3D to study breaking solitary waves and the associated wave impact forces on a slender cylinder over a sloping seabed. The perfomance of the numerical model is evaluated against the experimental data for the wave generation, wave surface elevation, free surface profile, horizontal and vertical velocity profiles reported by Mo et al. (2013) and breaking wave forces reported by Chakrabarti et al. (1997).

The main purpose of the present study is to investigate the characteristics and geometric properties of breaking solitary waves and their relationship with the breaking wave forces on a cylinder over a sloping seabed. Further, the study investigates the significance of the relative distance between the breaking point and the cylinder on the breaking wave forces on the cylinder. The breaking wave force characteristics such as the peak impact force, the impact duration and rise time, the average slamming coef-

ficient, and the force impulse are also examined to understand the underlying physical processes. However, to the authors′ knowledge no data to compare this second part with are available in the open literature, but the results suggest that the numerical model can represent important flow features related to breaking solitary waves and the interaction with a vertical cylinder. The main results are:

- The breaker depth index and the breaker height index for solitary waves on slopes have a similar trend as breaking periodic waves on slopes. However, the breaker depth index for solitary waves is much larger than typical values for periodic waves. This suggests that for a given slope, a solitary wave propagates further up on the slope and breaks in a shallower water depth than periodic waves.
- Solitary waves with smaller incident wave heights deform more during the shoaling and break at shallower water depth with larger breaker height due to the longer interaction time with the slope. Consequently, the crest front steepness and the vertical asymmetry factor increase. Overall, the degree of asymmetry of solitary wave profile at breaking increases as the offshore wave height decreases.
- In accordance with previous findings, the relative distance between the cylinder and the breaking point plays a prominent role in obtaining the maximum force. The impact duration and rise time increases as the distance between the cylinder and the breaking point increases. The maximum total force occurs when the wave hits the cylinder just before breaking. The wave height and the rise time during the impact are almost equivalent to the one at the breaking.
- As smaller solitary waves undergo more deformation over a slope before they break, the force contribution from the deformed wave above the still water level to the total force becomes larger. In addition, the forces on the cylinder rise slowly with longer duration, resulting in larger force impulses. It is found that the average slamming coefficient decreases as the incident wave height increases.

Acknowledgment

The authors wish to thank Prof. Atle Jansen and Prof. Phillip L.-F.Liu for providing the experimental data. The research for this paper was supported by the Norwegian Research Center for Offshore Wind Technology (NOWITECH), Research council of Norway (Contract no.193823). The authors also wish to thank NOTUR (Project no. NN9240K) for the allocation of computational resources provided on the Vilje system at the super computing facilities at NTNU.

References

Adeyemo, M. (1968), Effect of beach slope and shoaling on wave asymmetry, *in* ‘Proceedings of the 11-th Conference on Coastal Engineering’, pp. 145–172.

Alagan Chella, M., Bihs, H. and Myrhaug, D. (2015b), 'Characteristics and profile asymmetry properties of waves breaking over an impermeable submerged reef', *Coast. Eng.* **100**, 26–36.

Alagan Chella, M., Bihs, H., Myrhaug, D. and Muskulus, M. (2015a), 'Breaking characteristics and geometric properties of spilling breakers over slopes', *Coast. Eng.* **95**, 4–19.

Alagan Chella, M., Bihs, H., Myrhaug, D. and Muskulus, M. (2015c), 'Hydrodynamic characteristics and geometric properties of plunging and spilling breakers over impermeable slopes', *Ocean Modelling* . http://dx.doi.org/10.1016/j.ocemod.2015.11.011.

Alagan Chella, M., Tørum, A. and Myrhaug, D. (2012), 'An overview of wave impact forces on offshore wind turbine substructures', *Energy Procedia* **20**, 217–226.

Arntsen, Ø. A., Ros, X. and Tørum, A. (2011), Impact forces on a vertical pile from plunging breaking waves, *in* 'Proceedings of the 24-th Conference on Coastal structures'.

Bihs, H., Kamath, A., Alagan Chella, M. and Arntsen, Ø. A. (2016), 'Breaking wave interaction with tandem cylinders under different impact scenarios', *J. Waterw. Port Coast. Ocean Eng.* . DOI: 10.1061/(ASCE)WW.1943-5460.0000343.

Camfield, F. and Street, R. (1979), 'Shoaling of solitary waves on small slopes', *Journal of the Waterway Port Coastal and Ocean Division* **95**, 1–22.

Chakrabarti, S. K., Kriebel, D. and Berek, E. (1997), 'Forces on a single pile caisson in breaking waves and current', *Appl Ocean Res* **19**, 113–140.

Chaplin, J.and Flintham, T., Greated, C. and Skyner, D. (1992), Breaking wave forces on a vertical cylinder, Technical report, Health and Safety Executive, London, UK.

Choi, S., Lee, K. and Gudmestad, O. (2015), 'The effect of dynamic amplification due to a structures vibration on breaking wave impact', *Ocean Eng.* **96**, 8–20.

Chorin, A. (1968), 'Numerical solution of the Navier-Stokes equations', *Math. Comput.* **22**, 745–762.

Cooker, M. J. and Peregrine, D. H. (1990), A model for breaking wave impact pressures, *in* 'Proceedings of the 22nd Conference on Coastal Engineering', pp. 1473–1486.

Cooker, M. J. and Peregrine, D. H. (1995), 'Pressure-impulse theory for liquid impact problems', *J. Fluid Mech.* **297**, 193–214.

Cuomo, G., , Piscopia, R. and Allsop, W. (2011), 'Evaluation of wave impact loads on caisson breakwaters based on joint probability of impact maxima and rise times', *Coast. Eng.* **58**, 9–27.

Cuomo, G., , Tirindelli, M. and Allsop, W. (2007), 'Breaking wave loads at vertical seawalls and breakwaters', *Coast. Eng.* **54**, 657–679.

Cuomo, G., Allsop, W., Bruce, T. and Pearson, J. (2010), 'Breaking wave loads at vertical seawalls and breakwaters', *Coast. Eng.* **57**, 424–439.

Fenton, J. (1985), 'A fifth-order stokes theory for steady waves', *J. Waterw. Port Coast. Ocean Eng.* **111**(2), 216–234.

Galvin, C. J. (1968), 'Breaker type classification on three laboratory beaches', *J. Geophys. Res.* **73**(12), 3651–3659.

Goda, Y., Haranaka, S. and Kitahata, M. (1966), Study of impulsive breaking wave forces on piles, Technical report, Port and Harbor Research Institute, Ministry of

Transport.
Goring, D. G. (1978), Tsunamis–the propagation of long waves onto a shelf, PhD thesis, California Institute of Technology.
Grilli, S. T., Subramanya, R., Svendsen, I. A. and Veeramony, J. (1995), 'Shoaling of solitary waves on plane beaches', *J. Waterw. Port Coast. Ocean Eng.* **120**(6), 609–628.
Grilli, S. T., Svendsen, I. A. and Subramanya, R. (1997), 'Breaking criterion and characteristics for solitary waves on slopes', *J. Waterw. Port Coast. Ocean Eng.* **123**(3), 102–112.
Grimshaw, R. (1971), 'The solitary wave in water of variable depth. Part 2.', *J. Fluid Mech.* **46**, 611–622.
Hattori, M., Arami, A. and Yui, T. (1994), 'Wave impact pressure on vertical walls under breaking waves of various types', *Coast. Eng.* **22**, 79–114.
Hieu, P. D., Katsutoshi, T. and Ca, V. T. (2004), 'Numerical simulation of breaking waves using a two-phase flow model', *Appl. Math. Model.* **28**(11), 983–1005.
Hwang, P. A. (1984), Profile asymmetry of shoaling waves on a mild slope, *in* 'Proceedings of the 19-th Conference on Coastal Engineering', pp. 1016–1027.
Ippen, A. T. and Kulin, G. (1954), The shoaling and breaking of the solitary wave, *in* 'Proceedings of the 5-th Conference on Coastal Engineering', pp. 27–47.
Irschik, K., Sparboom, U. and Oumeraci, H. (2002), Breaking wave characteristics for the loading of a slender pile, *in* 'Proceedings of the 28-th Conference on Coastal Engineering', pp. 1341–1352.
Jacobsen, N. G., Fuhrman, D. R. and Fredsøe, J. (2012), 'A wave generation toolbox for the open-source CFD library : OpenFoam', *Int. J. Numer. Methods Fluids* **70**(November), 1073–1088.
Jiang, G. S. and Shu, C. W. (1996), 'Efficient implementation of weighted ENO schemes', *J. Comput. Phys.* **126**, 202–228.
Kamath, A., Alagan Chella, M., Bihs, H. and Arntsen, Ø. A. (2015), 'CFD investigations of wave interaction with a pair of large tandem cylinders', *Ocean Eng.* **108**, 734–748.
Kamath, A., Bihs, H., Alagan Chella, M. and Arntsen, Ø. A. (2016), 'Upstream-cylinder and downstream-cylinder influence on the hydrodynamics of a four-cylinder group', *J. Waterw. Port Coast. Ocean Eng.* . DOI: 10.1061/(ASCE)WW.1943-5460.0000339.
Kjeldsen, S. P. and Myrhaug, D. (1978), Kinematics and dynamics of breaking waves, Technical report, River and Harbour Laboratory (NHL), The Norwegian Institute of Technology.
Kortenhaus, A., Oumeraci, H., Allsop, N., McConnell, K., Van Gelder, P., Hewson, P., Walkden, M., Müller, G., Calabrese, M. and Vicinanza, D. (1999), Wave impact loads-pressures and forces, *in* 'Final Proceedings, MAST III, PROVERBS-Project: Vol. IIa: Hydrodynamic Aspects'.
Larsen, J. and Dancy, H. (1983), 'Open boundaries in short wave simulations - a new approach', *Coast. Eng.* **7**, 285–297.
Lemos, C. M. (1992), 'A simple numerical technique for turbulent flows with free surfaces', *Int. J. Numer. Methods Fluids* **15**, 127–146.

Lin, P. and Liu, P. L.-F. (1998), 'A numerical study of breaking waves in the surf zone', *J. Fluid Mech.* **359**, 239–264.

Losada, M. A., Vidal, C. and Medina, R. (1989), 'Experimental study of the evolution of a solitary wave at an abrupt junction', *J. Geophys. Res.* **94**, 14557–14566.

Miles, J. W. (1980), 'Solitary waves', *Annu. Rev. Fluid Mech.* (12), 11–43.

Mo, W., Jensen, A. and Liu, P. L.-F. (2013), 'Plunging solitary wave and its interaction with a slender cylinder on a sloping beach', *Ocean Eng.* **74**, 48–60.

Munk, W. H. (1949), 'The solitary wave theory and its application to surf problems', *Annals of the New York Academy of Sciences* **3**, 376–424.

Osher, S. and Sethian, J. A. (1988), 'Fronts propagating with curvature-dependent Speed: Algorithms based on Hamilton-Jacobi formulations', *J. Comput. Phys.* **79**, 12–49.

Peregrine, D. H. (2003), 'Water-wave impact on walls', *Annu. Rev. Fluid Mech.* **35**, 23–43.

Sarpkaya, T. and Isaacson, M. (1981), *Mechanics of Wave Forces on Offshore Structures*, Van Nostrand Reinhold Company.

Sawaragi, T. and Nochino, M. (1984), 'Impact forces of nearly breaking waves on a vertical circular cylinder', *Coastal Engineering Journal* **27**, 249–263.

Shu, C. W. and Osher, S. (1988), 'Efficient implementation of essentially non-oscillatory shock capturing schemes', *J. Comput. Phys.* **77**, 439–471.

Stive, M. and Wind, H. (1982), 'A study of radiation stress and set-up in the nearshore region', *Coast. Eng.* **6**, 1–26.

Ting, F. C. K. and Kirby, J. T. (1994), 'Observation of undertow and turbulence in a laboratory surf zone', *Coast. Eng.* **24**(1-2), 51–80.

van der Vorst H. (1992), 'Bi-CGSTAB: A fast and smoothly converging variant of Bi-CG for the solution of nonsymmetric linear systems', *SIAM Journal on scientific and Statistical Computing* **13**, 631–644.

Wienke, J. and Oumeraci, H. (2005), 'Breaking wave impact force on a vertical and inclined slender pile-theoretical and large-scale model investigations', *Coast. Eng.* **52**, 435–416.

Wienke, J., Sparboom, U. and Oumeraci, H. (2000), Breaking wave impact on a slender cylinder, *in* 'Proceedings of the 27th Conference on Coastal Engineering', pp. 1787–1798.

Xiao, H. and Huang, W. (2014), 'Three-dimensional numerical modeling of solitary wave breaking and force on a cylinder pile in a coastal surf zone', *J. Eng. Mech. - ASCE* **141(8)**.

Xie, Z. (2013), 'Two-phase flow modelling of spilling and plunging breaking waves', *Appl. Math. Model.* **37**, 3698–3713.

Zhao, Q., Armfield, S. and Tanimoto, K. (2004), 'Numerical simulation of breaking waves by a multi-scale turbulence model', *Coast. Eng.* **51**(1), 53–80.

6.8 Paper 8
Breaking wave interaction with a vertical cylinder and the effect of breaker location

Kamath, A., Alagan Chella, M., Bihs, H., Arntsen, Ø. A.
Submitted to *Ocean Engineering*, 2015 - under review

Paper 8

Breaking Wave Interaction with a Vertical Cylinder and the Effect of Breaker Location

Arun Kamath[1], Mayilvahanan Alagan Chella, Hans Bihs, Øivind A. Arntsen

Department of Civil and Transport Engineering, Norwegian University of Science and Technology (NTNU), 7491 Trondheim, Norway

Abstract

The open-source CFD model REEF3D is used to simulate plunging breaking wave forces on a vertical cylinder. The numerical results are compared with data from the experiments carried out at the Large Wave Channel, Hannover, Germany to validate the model. Further, the location of the cylinder is changed so that the breaking wave impacts the cylinder at different stages of wave breaking and the resulting wave forces are evaluated. The different locations for the cylinder placement based on the breaker location are determined from the results obtained for the wave breaking process in a two-dimensional numerical wave tank. Maximum wave forces are found to occur when the breaking wave tongue impacts the cylinder just below the wave crest in all the cases simulated and the lowest wave forces are generally obtained when the wave breaks behind the cylinder. Several wave features such as the splashing on impact, the splitting and rejoining of the wave around the cylinder resulting in a chute-like jet formation are identified. The model provides a good representation of the breaking wave process and can be a useful tool to evaluate breaking wave forces on structures.

Keywords: breaking wave, wave forces, wave impact, vertical cylinder, Computational Fluid Dynamics, REEF3D

1. Introduction

A lot of research work has been carried out in the past on the evaluation of wave forces on structures exposed to waves due to their importance in coastal and offshore engineering. The wave forces on cylinders at higher KC numbers (KC > 2) and cylinder diameter to wavelength ratio $D/L < 0.2$ are generally determined using the Morison formula (Morison et al., 1950) to account for inertial and drag component of the wave forces using empirical force coefficients. In the case of breaking wave forces, Morison formula cannot be directly applied because

[1]Corresponding Author, Email: arun.kamath@ntnu.no, Ph: (+47) 73 59 46 40, Fax: (+47) 73 59 70 21

breaking waves are associated with impact forces of very high magnitudes acting over a short duration. In order to describe the total force from breaking waves with the Morison equation, an impact force term is considered in addition to the quasi-static forces (Goda et al., 1966). Present knowledge concerning the breaking wave forces is gained from experiments by Goda et al. (1966), Wienke and Oumeraci (2005), Arntsen et al. (2011) to name a few, but the measurement of velocity and acceleration under breaking waves and their interaction with structures is very demanding. The theoretical description of the impact force involves the use of several parameters such as slamming coefficients, curling factor, breaker shape and wave kinematics at breaking which have to be determined experimentally. Previous studies on breaking wave forces such as Chan and Melville (1988), Bullock et al. (2007), Wienke and Oumeraci (2005) have indicated that breaking wave impact characteristics depend on several parameters such as the depth inducing breaking, breaker type and the distance of the structure from the breaker location.

The modelling of breaking waves in shallow waters is challenging due to the complex nature of the physical processes including highly non-linear interactions. A considerable amount of numerical studies have been attempted to model wave breaking over plane slopes (Lin and Liu, 1998; Zhao et al., 2004; Alagan Chella et al., 2015b). These studies have helped extend the knowledge regarding breaking wave characteristics and the geometric properties of breaking waves. The quantification of these breaking wave parameters are an important input to improve the empirical coefficients used for the evaluation of breaking wave forces. Though many extensive numerical studies exist in current literature that study the wave breaking process, not many have been extended to study the forces due to breaking waves and the effect of breaker types on the wave forces. Bredmose and Jacobsen (2010) studied breaking wave impact forces due to focussed waves with the Jonswap wave spectrum for input and carried out computations for half the domain assuming lateral symmetry of the problem using OpenFOAM. Mo et al. (2013) measured and modelled solitary wave breaking and its interaction with a slender cylinder over a plane slope for a single case using the filtered Navier-Stokes equations with large eddy simulation (LES) turbulence modeling, also assuming lateral symmetry and showed that their numerical model sufficiently captured the important flow features. Choi et al. (2015) investigated breaking wave impact forces on a vertical cylinder and two cases of inclined cylinders for one incident wave using the modified Navier-Stokes equations with the volume of fluid (VOF) method for interface capturing to study the dynamic amplification factor due to structural response.

The study of breaking wave forces using computational fluid dynamics (CFD) can provide a very detailed description of the physical processes as the fluid physics are calculated with few assumptions. With high-order discretization schemes for the convection and time advancement, sharp representation of the free surface and tight velocity-pressure coupling in the model, the wave transformation, wave hydrodynamics and flow features can be represented very accurately and in a realistic manner. In the complex case of breaking wave interaction with structures, CFD simulations can be used to capture the details of the flow field that are challenging to capture in experimental studies due to various factors including cost, instrumentation and structural response. Different wave loading scenarios can be analysed as the breaker locations are easier to analyse and maintain in the simulations.

In the current study, the open source CFD model REEF3D (Alagan Chella et al., 2015b) is used to simulate periodic breaking wave forces on a slender cylinder in a three-dimensional wave tank without assuming lateral symmetry. The model has been previously used to simulate the wave breaking process under different conditions (Alagan Chella et al., 2015a,b) and the wave breaking kinematics were fully represented including the motion of the jet, air pocket formation and the reconnection of the jet with the preceding wave trough. The model provides a detailed representation of the free surface and is numerically stable for various problems related to wave hydrodynamics. It is fully parallelised, has shown very good scaling on the high performance computing system at NTNU provided by NOTUR (2012) and can be used to carry out complex simulations efficiently on a large number of processors.

This paper presents the breaking wave interaction with a vertical cylinder. Three different wave heights are simulated and the evolution of wave breaking over a $1:10$ slope is studied using two-dimensional simulations. The locations for the placement of the cylinder to investigate five different wave loading cases based on Irschik et al. (2002) are identified from these two-dimensional studies. Next, the wave forces in the different scenarios for the three different incident wave heights are evaluated in a three-dimensional numerical wave tank. The numerical model is validated by comparing the calculated wave forces and the free surface with experimental data from experiments carried out in the Large Wave Channel (GWK), Hannover, Germany. The wave interaction with the vertical cylinder in selected two different scenarios is investigated and the effect of the cylinder placement with respect to the breaker location on the free surface features is presented.

2. Numerical Model

The open-source CFD model REEF3D solves the fluid flow problem using the incompressible Reynolds-Averaged Navier-Stokes (RANS) equations along with the continuity equation:

$$\frac{\partial u_i}{\partial x_i} = 0 \tag{1}$$

$$\frac{\partial u_i}{\partial t} + u_j \frac{\partial u_i}{\partial x_j} = -\frac{1}{\rho}\frac{\partial p}{\partial x_i} + \frac{\partial}{\partial x_j}\left[(\nu + \nu_t)\left(\frac{\partial u_i}{\partial x_j} + \frac{\partial u_j}{\partial x_i}\right)\right] + g_i \tag{2}$$

where u is the velocity averaged over time t, ρ is the fluid density, p is the pressure, ν is the kinematic viscosity, ν_t is the eddy viscosity and g is the acceleration due to gravity.
The pressure is determined using Chorin's projection method (Chorin, 1968) and the resulting Poisson pressure equation is solved with a preconditioned BiCGStab solver (van der Vorst, 1992). Turbulence modeling is handled using the two-equation $k - \omega$ model proposed by Wilcox (1994), where the transport equations for the turbulent kinetic energy, k and the specific turbulent dissipation rate, ω are:

$$\frac{\partial k}{\partial t} + U_j \frac{\partial k}{\partial x_j} = \frac{\partial}{\partial x_j}\left[\left(\nu + \frac{\nu_t}{\sigma_k}\right)\frac{\partial k}{\partial x_j}\right] + P_k - \beta_k k\omega \tag{3}$$

$$\frac{\partial \omega}{\partial t} + U_j \frac{\partial \omega}{\partial x_j} = \frac{\partial}{\partial x_j}\left[\left(\nu + \frac{\nu_t}{\sigma_\omega}\right)\frac{\partial \omega}{\partial x_j}\right] + \frac{\omega}{k}\alpha P_k - \beta\omega^2 \tag{4}$$

$$\nu_t = \frac{k}{\omega} \tag{5}$$

where, P_k is the production rate and closure coefficients $\sigma_k = 2$, $\sigma_\omega = 2$, $\alpha = 5/9$, $\beta_k = 9/100$, $\beta = 3/40$.

The highly strained flow due to the propagation of waves in the tank results in an overproduction of turbulence in the numerical wave tank as the eddy viscosity is determined from the strain in the convective terms. The Bradshaw et al. (1967) assumption is used to limit the eddy viscosity as shown by Durbin (2009):

$$\nu_t \leq \sqrt{\frac{2}{3}}\frac{k}{|\mathbf{S}|} \tag{6}$$

where $\mathbf{S}$ stands for the source terms in the transport equations. In a two-phase CFD model, the large difference between the density of air and water leads to a large strain at the interface,

which leads to an overproduction of turbulence at the free surface. In reality, the free surface is a boundary at which eddy viscosity is damped naturally. The standard $k-\omega$ model does not account for this and the specific turbulence dissipation at the free surface is defined using the empirical relationship presented by Naot and Rodi (1982) is used at the interface.

The discretization of the convective terms of the RANS equations are discretized using the fifth-order conservative finite difference Weighted Essentially Non-Oscillatory (WENO) scheme (Jiang and Shu, 1996). The Hamilton-Jacobi formulation of the WENO scheme (Jiang and Peng, 2000) is used to discretize the level set function ϕ, turbulent kinetic energy k and the specific turbulent dissipation rate ω. The WENO scheme is a minimum third-order accurate in the presence of large gradients and provides the accuracy required to model complex free surface flows. The time advancement of the momentum equation, the level set function and the reinitialisation equation is treated with a Total Variation Diminishing (TVD) third-order Runge-Kutta explicit time scheme (Shu and Osher, 1988). The Courant-Frederick-Lewis (CFL) criterion is maintained at a constant value throughout the simulation using an adaptive time stepping strategy to determine the time steps. A first-order implicit scheme for the time advancement of k and ω removes the large source term contributions from these variables for the evaluation of the CFL criterion. This is reasonable, as these variables are largely driven by source terms and have a low influence from the convective terms. The diffusion terms of the velocities are also handled using an implicit scheme, removing them from the CFL criterion and the maximum velocities in the domain are used to determine the time steps to maintain the numerical stability of the simulation.

The model uses a Cartesian grid for spatial discretization and high-order finite difference schemes can be implemented in a straight forward manner. A ghost cell immersed boundary method (GCIBM) (Berthelsen and Faltinsen, 2008) is used to account for the complex geometric solid-fluid boundaries. The code is fully parallelised using the MPI library and the numerical model can be executed on high performance computing systems with very good scaling.

2.1. Level Set Method

The level set method (Osher and Sethian, 1988) is an interface capturing method in which the the zero level set of a signed distance function, $\phi(\vec{x},t)$ represents the interface between two phases. For the rest of the domain, $\phi(\vec{x},t)$ gives the closest distance of each point in the domain from the interface and the sign distinguishes the two phases across the interface. The

level set function is continuous across the interface and is defined as:

$$\phi(\vec{x},t)\begin{cases} > 0 & if\ \vec{x}\ is\ in\ phase\ 1 \\ = 0 & if\ \vec{x}\ is\ at\ the\ interface \\ < 0 & if\ \vec{x}\ is\ in\ phase\ 2 \end{cases} \tag{7}$$

The level set function provides a sharp representation of the interface. A partial differential equation based reinitialisation procedure presented by Peng et al. (1999) is used to maintain the signed distance property of the function, which can be lost on convecting the function under an external velocity field.

2.2. Numerical Wave Tank

The two-dimensional numerical wave tank has symmetry conditions on the side walls and the top of the tank. The bottom wall of the tank and boundaries of objects placed in the tank are treated with a no-slip or wall boundary condition. In a three-dimensional wave tank, the side walls are also subjected to wall boundary conditions. Wave generation is handled using the relaxation method (Larsen and Dancy, 1983), with the relaxation function presented by Jacobsen et al. (2012):

$$\Gamma(x) = 1 - \frac{e^{(1-x)^{3.5}} - 1}{e - 1} \tag{8}$$

where $\Gamma(x)$ is the relaxation function and $x \in [0,1]$ is the length scale along the relaxation zone and ensures a smooth transition of the still water to a wave. The relaxation function also absorbs any waves reflected from the objects placed in the wave tank, travelling towards the wave generation zone. This prevents the reflected waves from affecting the wave generation and simulates a wave generator with active absorption. The numerical beach is implemented using the active absorbing beach formulated by Schäffer and Klopman (2000).

3. Results and Discussion

3.1. Setup for the numerical simulations

The experiments (Irschik et al., 2002) at the Large Wave Channel (GWK), Hannover are carried out in a wave channel 309 m long, 5 m wide and 7 m high with a 23 m long 1 : 10 slope reaching a height of 2.3 m placed at 180 m from the wavemaker. A flat bed extends from the end of slope with a height of 2.3 m. A vertical cylinder of diameter $D = 0.7$ m is placed with its central axis at the top of the slope and incident waves with heights H between

$1.15 - 1.60$ m and periods T between $4.0 - 9.0$ s are generated. In the current study, the case with incident wave period $T = 4.0$ s, wave height $H_B = 1.30$ m and water depth $d = 3.8$ m presented in Choi et al. (2015) is chosen for comparison with the numerical results. The three-dimensional numerical wave tank is 54 m long, 5 m wide and 7 m high with a grid size of $dx = 0.05$ m resulting a total of 15.12 million cells. In order to study the wave breaking process for the different cases simulated in the study, a two-dimensional wave tank with the same dimensions is used as illustrated in Fig. (1). Waves with incident wave steepnesses $H_0/L_0 = 0.070, 0.063, 0.059$, corresponding to wave heights of $H_A = 1.44$ m, $H_B = 1.30$ m and $H_C = 1.23$ m are generated to study the breaking wave forces on a vertical cylinder.

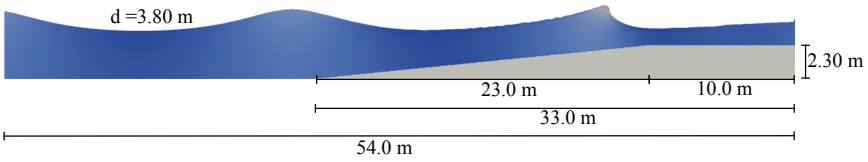

Figure 1: Dimensions of the two-dimensional numerical wave tank to determine breaking wave characteristics

3.2. Breaking wave characteristics

The process of wave breaking for incident waves with period $T = 4.0$ s, wavelength $L = 20.5$ m and heights $H_A = 1.44$ m $H_B = 1.30$ m and $H_C = 1.23$ m is studied in a two-dimensional wave tank to identify the various stages of wave breaking. The results are used to select the locations to place the cylinder in order to analyse the effect of the wave breaker location on the wave force acting on the cylinder.

Figure (2) depicts the free surface deformation and the evolution of the overturning wave crest of the plunging breaking waves produced over the slope along with the horizontal velocity contours for $H_B = 1.30$ m. As a result of wave shoaling over the slope, the wave crest becomes steeper and the wave crest approaches a near-vertical profile in Fig. (2a). Due to increasing water particle velocities at the wave crest and reducing particle velocities towards the bed, the wave becomes asymmetrical and a part of the wave crest develops into an overturning crest seen in Fig. (2b). On further propagation, the overturning crest develops into a plunging jet which impinges the preceding wave trough, creating an air pocket, splash-up and secondary waves shorewards. The breaking characteristics vary depending on the incident wave characteristics, which determine the size and flow features of the overturning wave crest

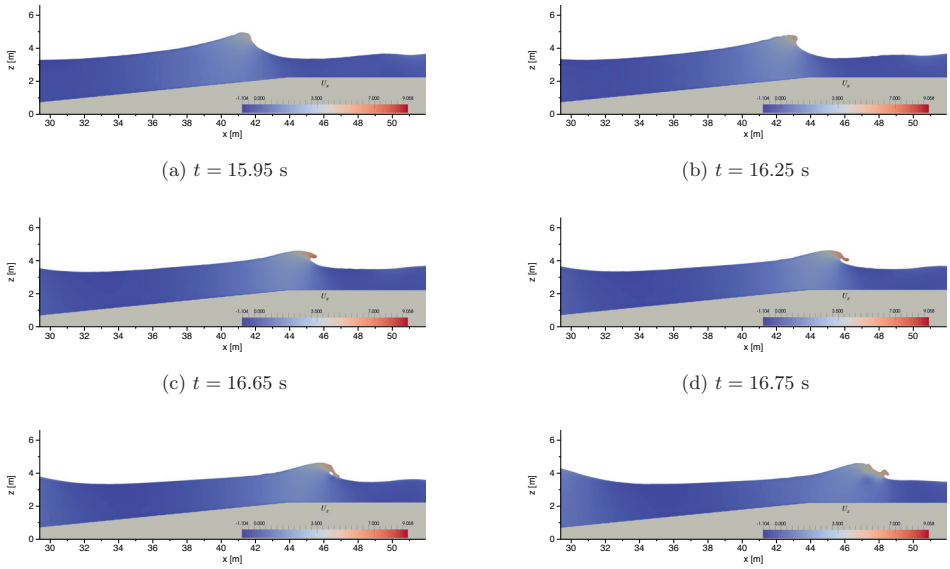

(a) $t = 15.95$ s (b) $t = 16.25$ s

(c) $t = 16.65$ s (d) $t = 16.75$ s

(e) $t = 16.90$ s (f) $t = 17.25$ s

Figure 2: Evolution of the breaking wave for $H_B = 1.30$ m with horizontal velocity contours

as seen in Figs. (2d-2f).

Similarly, simulations are carried out for incident waves with $H_A = 1.44$ m and $H_C = 1.23$ m and $T = 4.0$ s. It is observed that the breaker location moves shorewards as the incident wave height is reduced. The breaking locations for H_A, H_B and H_C are identified to be $x_b = 42.10$m, 43.65 m and 43.85 m with breaking heights of $h_b = 1.55$ m, 1.44 m and 1.32 m respectively. The information regarding the breaking process obtained from the two-dimensional simulations is used in further sections to determine the cylinder placement location to investigate various wave loading scenarios.

3.3. Validation of the numerical model for breaking wave force calculation

The numerical results for breaking wave forces and the free surface elevation along the frontline of the cylinder ($x = 43.65$ m) near the tank wall for $H_B = 1.30$ m are compared to the experimental data to validate the numerical model. The cylinder is placed with its axis at the top of the slope ($x = 44.00$ m), such that the front surface of the cylinder is directly at the breaking point and the vertical breaking wave crest impacts the cylinder front surface. A grid size of $dx = 0.05$ m is used. The filtered and Empirical Mode Decomposition (EMD)-treated experimental data from the experiments carried out at GWK, Hannover (Irschik et al., 2002),

presented by Choi et al. (2015) is used for the comparison with the numerical results for the wave force. Figure (3a) shows that the numerical model provides a good prediction of the breaking wave force and the calculated wave force is consistent over several wave periods. Since the wave impact is very sensitive to the wave breaking location, the consistent results indicate that the model simulates successive breaking waves at the same location consistently. The numerically calculated free surface elevation along the frontline of the cylinder at $x = 43.65$ m also presents a good agreement with the experimental data in Fig. (3b) showing that the model provides a good representation of the wave propagation in the wave tank.

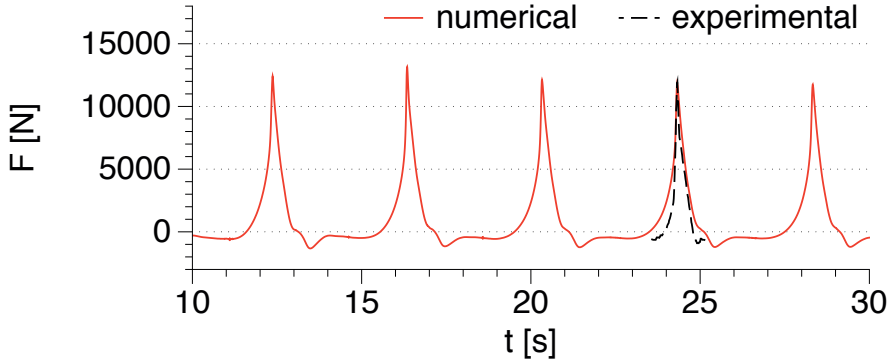

(a) wave force on the cylinder

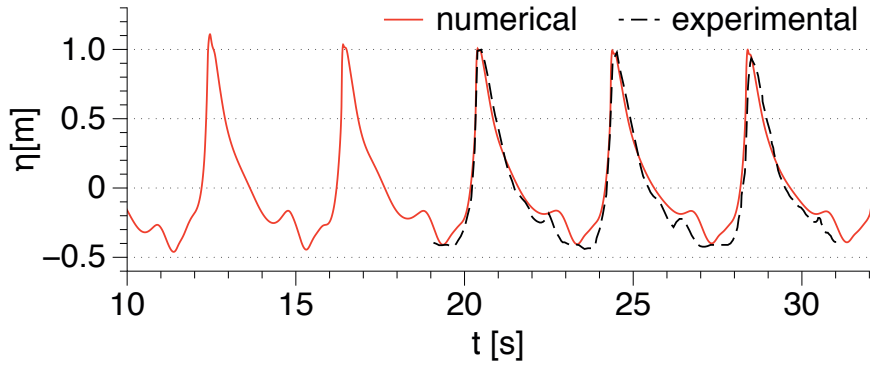

(b) free surface elevation at the tank wall, along the frontline of the cylinder

Figure 3: Comparison of numerical results with experimental data

A grid convergence study is carried out by repeating the above simulation with grid sizes of $dx = 0.20$ m, 0.15 m, 0.10 m and compared to the results at $dx = 0.05$ m and experimental

data for the wave force in Fig. (4). The results in Fig. (4a) show that the numerical values for the wave force converge to the experimental value at $dx = 0.05$ m, confirming the choice of the grid for the study. Figure (4b) shows the free surface elevation evaluated for the different grid sizes and for $dx = 0.15$ m and 0.20 m, neither the breaking location nor the vertical breaking crest is represented with sufficient accuracy. The wave forces calculated at these grid sizes is subsequently much lower as seen in Fig. (4a). At a grid size of $dx = 0.10$ m, the free surface differs slightly with regards to the breaking wave height but the corresponding difference in the calculated wave force is large. The vertical profile of the wave crest at breaking and the breaker location at $t = 24.2$ s is best represented by $dx = 0.05$ m. From the grid convergence studies, the grid size $dx = 0.05$ m is selected for all the simulations in this study.

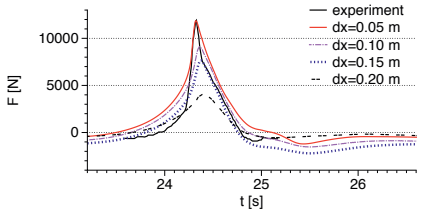

(a) calculated wave force

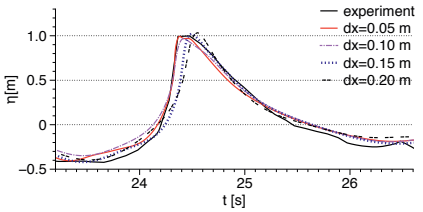

(b) calculated free surface elevation at $x = 43.65$ m

Figure 4: Grid convergence study for wave forces and free surface elevation near the wall along the frontline of the cylinder

3.4. Influence of cylinder location with respect to the breaker location

From the study about the breaking wave process for the three incident waves in section 3.2, five different locations at different stages of wave breaking are selected, similar to the loading cases identified in Irschik et al. (2002), as follows:

1. the wave breaks behind the cylinder, the crest is not yet vertical at impact.
2. the wave breaks exactly on the cylinder, the crest is vertical at impact.
3. the wave breaks just in front of the cylinder, the breaker tongue impacts the cylinder at crest level
4. the wave breaks in front of the cylinder, the breaker tongue impacts the cylinder slightly below the crest level
5. the wave breaks much before the cylinder, the breaker tongue impacts the cylinder much below the crest level.

The different scenarios are illustrated in Fig. (5) using case A with incident height $H_A = 1.44$ m as an example. An overview of the simulations carried out for the three different incident heights and the five different wave impact scenarios is listed in Table (1).

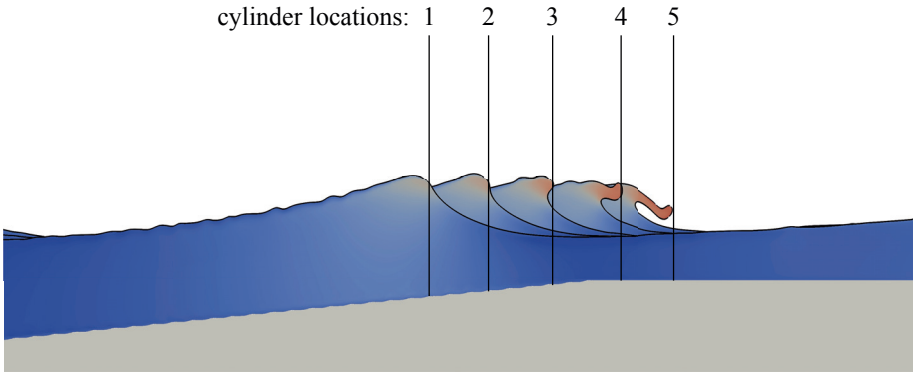

Figure 5: Location of the cylinder front surface for various wave loading cases

No.	H (m)	h_b (m)	x_b (m)	Cylinder axis (m)	Impact scenario
A1	1.44	1.55	42.10	40.95	before breaking
A2				42.45	vertical wave crest impact
A3				42.75	breaker tongue at crest level
A4				44.85	breaker tongue just below crest level
A5				46.25	breaker tongue much below crest level
B1	1.30	1.44	43.65	42.70	before breaking
B2				44.00	vertical wave crest impact
B3				44.60	breaker tongue at crest level
B4				46.35	breaker tongue just below crest level
B5				47.35	breaker tongue much below crest level
C1	1.23	1.32	43.85	42.85	before breaking
C2				44.20	vertical wave crest impact
C3				45.15	breaker tongue at crest level
C4				46.60	breaker tongue just below crest level
C5				47.85	breaker tongue much below crest level

Table 1: Overview of the simulations carried out to investigate the effect of different breaking wave impact scenarios

The calculated wave force on the cylinder in the different wave impact scenarios A1-A5 is presented in Fig. (6). The highest wave force $F = 16400$ N is calculated for scenario A4, where the breaker tongue impacts the cylinder just below the wave crest level. The lowest wave force $F = 11000$ N is calculated in scenario A1, where the wave breaks behind the cylinder. A small secondary force peak appears in scenario A5 representing the second impact from the wave crest behind the breaker tongue. Due to the small change of 0.3 m in the cylinder location between scenarios A2 and A3 and forces peaks in these two cases appear very close to each other and a slight difference is seen in the force magnitudes. The lowest force in this case in scenario A1 is about 33% lower than the highest force calculated in A4.

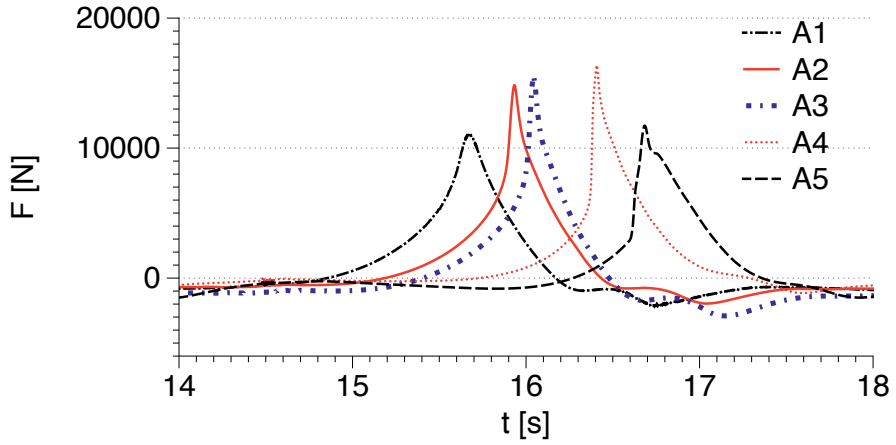

Figure 6: Calculated wave forces for $H_A = 1.44$ m for different wave impact scenarios

The wave forces calculated in scenarios B1-B5 is presented in Fig. (7) and the highest wave force is calculated for scenario B4 with $F = 14000$ N. The lowest force in this scenario is calculated for scenario B5 where the breaker tongue impacts the cylinder much below the wave crest level. A double peak in the force due to the first impact of the breaker tongue and the second impact of the wave crest is also clearly recognised for scenario B5. The wave forces calculated in scenarios B2 and B3 are similar, with a slightly higher force for B3. The wave force in scenario B1 with $F = 9800$ N is similar to scenario B5 with $F = 9400$ N. The lowest force calculated in B5 is about 33% lower than the highest force calculated in B4.

Figure (8) presents the wave forces calculated in scenarios C1-C5 with the highest force calculated in scenario C4 with $F = 12350$ N and the lowest force $F = 8380$ N for scenario C1. The difference between the highest and the lowest wave forces is 3970 N with about

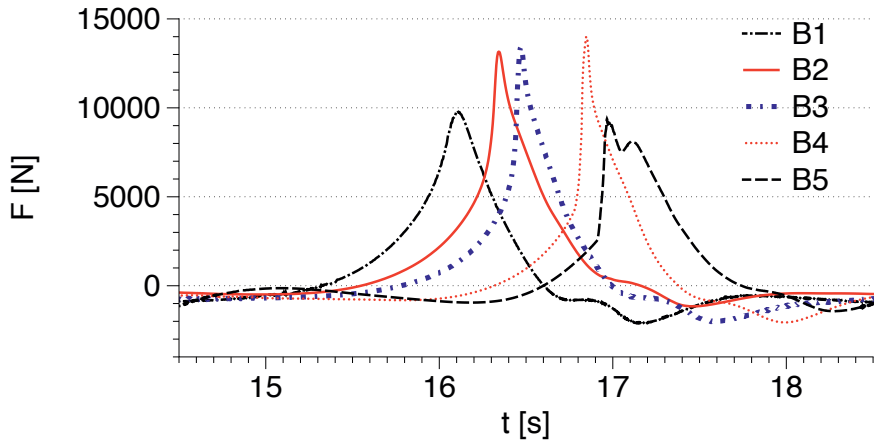

Figure 7: Calculated wave forces for $H_B = 1.30$ m for different wave impact scenarios

32% lower force in C1 compared to C4. The wave forces in the other scenarios simulated show a similar trend to that seen in the other two cases, where the wave force reduces as the cylinder is moved towards the wavemaker or towards the beach from the location resulting in the maximum wave force.

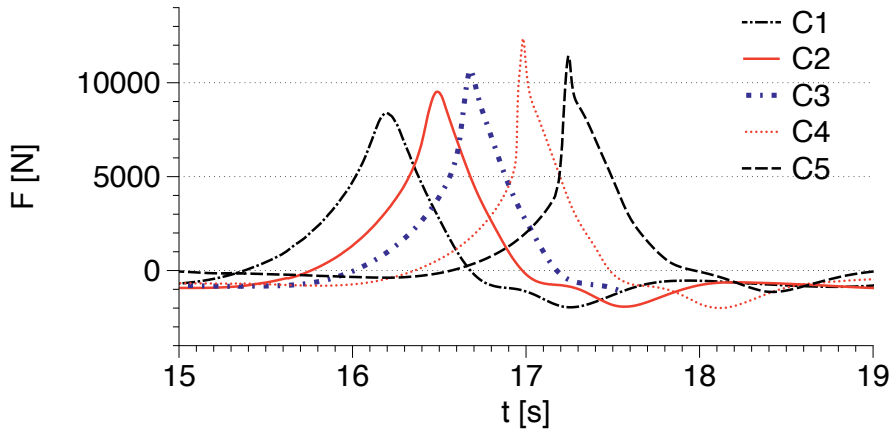

Figure 8: Calculated wave forces for $H_C = 1.23$ m for different wave impact scenarios

The results for the wave forces on the cylinder in the different scenarios for different wave heights show that the maximum force is obtained in wave impact scenario 4, where the breaker tongue impacts the cylinder just below the wave crest. The lowest breaking wave

force is generally obtained when the wave impacts the cylinder before its breaking point in scenario 1. These findings are in agreement with previous studies for focussed waves and periodic waves (Wienke et al., 2000; Irschik et al., 2002).

In order to obtain more insight into the difference in the physical free surface features in two varying wave impact scenarios, the breaking wave interaction with the cylinder in B2 and B5 are presented and the free surface features are discussed. Figure (9) presents the interaction process for scenario B2, where the wave impacts the cylinder at the breaker location with both isometric view of the tank and the top view around the cylinder. The vertical wave crest profile incident on the cylinder front surface is seen in Fig. (9a). The wave crest begins to overturn as it passes the cylinder in Figs. (9c). The separation of the incident wavefront by the cylinder and the generation of semi-circular waves meeting in the shadow zone behind the cylinder is seen in Fig. (9d). The meeting of the semi-circular wavefronts behind the cylinder and the formation of a chute-like jet is seen in Fig. (9f). The chute-like jet originates in the region of low horizontal velocities behind the cylinder and has a maximum horizontal velocities at the tip, where it meets the broken wave crest. Figure (9g) shows the fully developed chute-like jet and is seen to extend up to just behind the broken wave crest in Fig. (9h). The chute-like jet appears after the peak force is observed for the cylinder and thus may not have a significant effect on the forces experienced by the cylinder. The importance of the chute-like jet may be more apparent in the case of neighboring cylinders placed in the zone of influence of the chute-like jet behind the first cylinder. The chute-like jet can lead to a large wave run-up on the downstream cylinder. It can also result in interaction effects between the cylinders based on the distance between the two cylinders, influencing the wave forces on both cylinders.

Wave impact scenario B5 presented in Fig. (10) shows the interaction of a broken wave with the cylinder. The highly curled breaker tongue impacts the cylinder much below the wave crest level in Fig. (10a). Figure (10c) shows the separation of the incident wavefront. The formation of semi-circular wavefronts meeting behind the cylinder is absent in Fig. (10d). The broken wave separated around the cylinder propagates further with a region of low velocity in the shadow region behind the cylinder in Fig. (10e). There are no major free surface features at this stage in Fig. (10f). A mildly developed chute-like jet is seen in Fig. (10g) which is close to its collapse state and this weakly developed chute wave is seen to rejoin the free surface at some distance behind the broken wave crest in Fig. (10h).

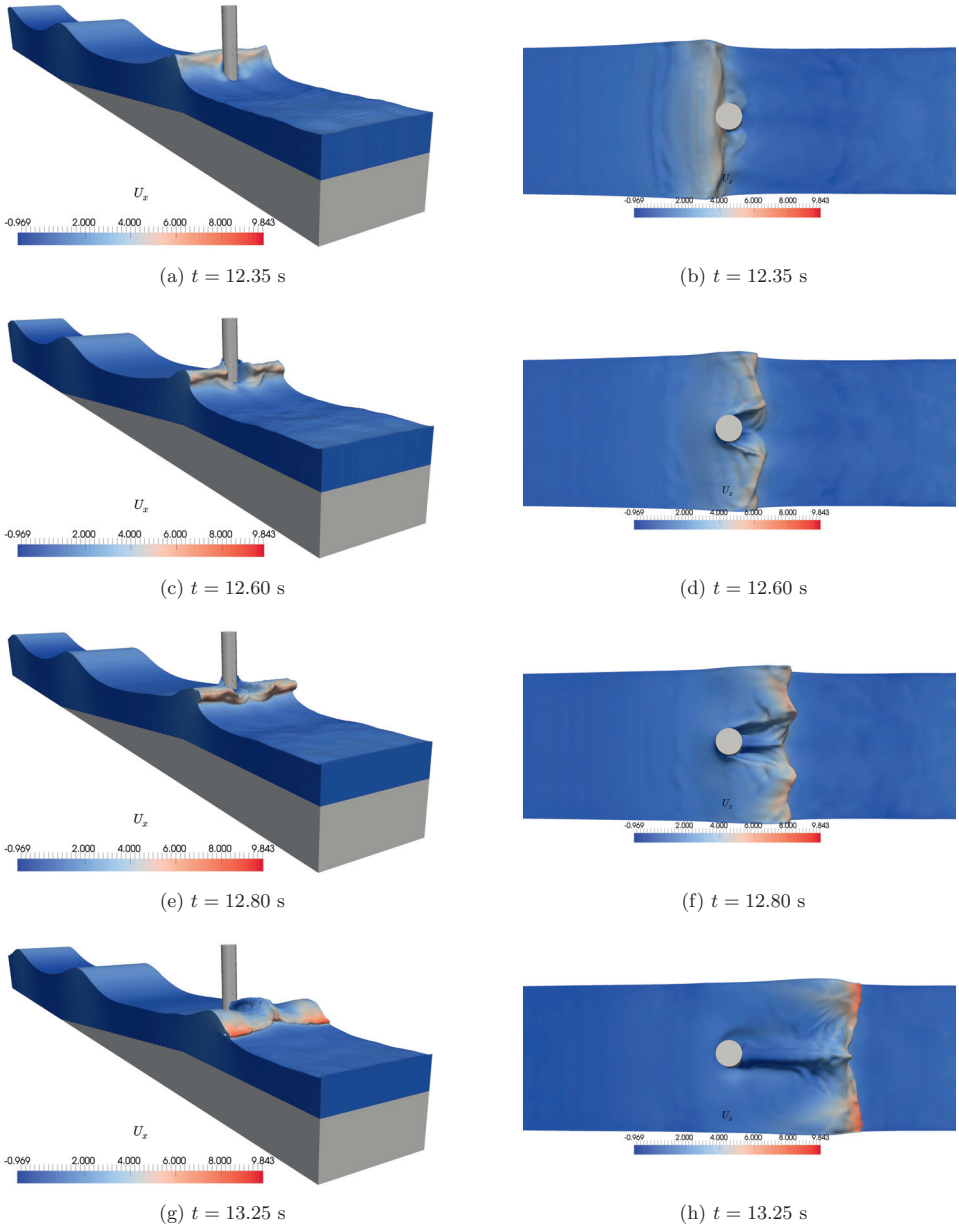

(a) $t = 12.35$ s (b) $t = 12.35$ s

(c) $t = 12.60$ s (d) $t = 12.60$ s

(e) $t = 12.80$ s (f) $t = 12.80$ s

(g) $t = 13.25$ s (h) $t = 13.25$ s

Figure 9: Isometric and corresponding top views of breaking wave interaction with the cylinder for $H_B = 1.30$ m for scenario B2

From the two different wave impact scenarios presented, the wave interaction process with the cylinder varies for the two cases in terms of free surface features and the velocities around

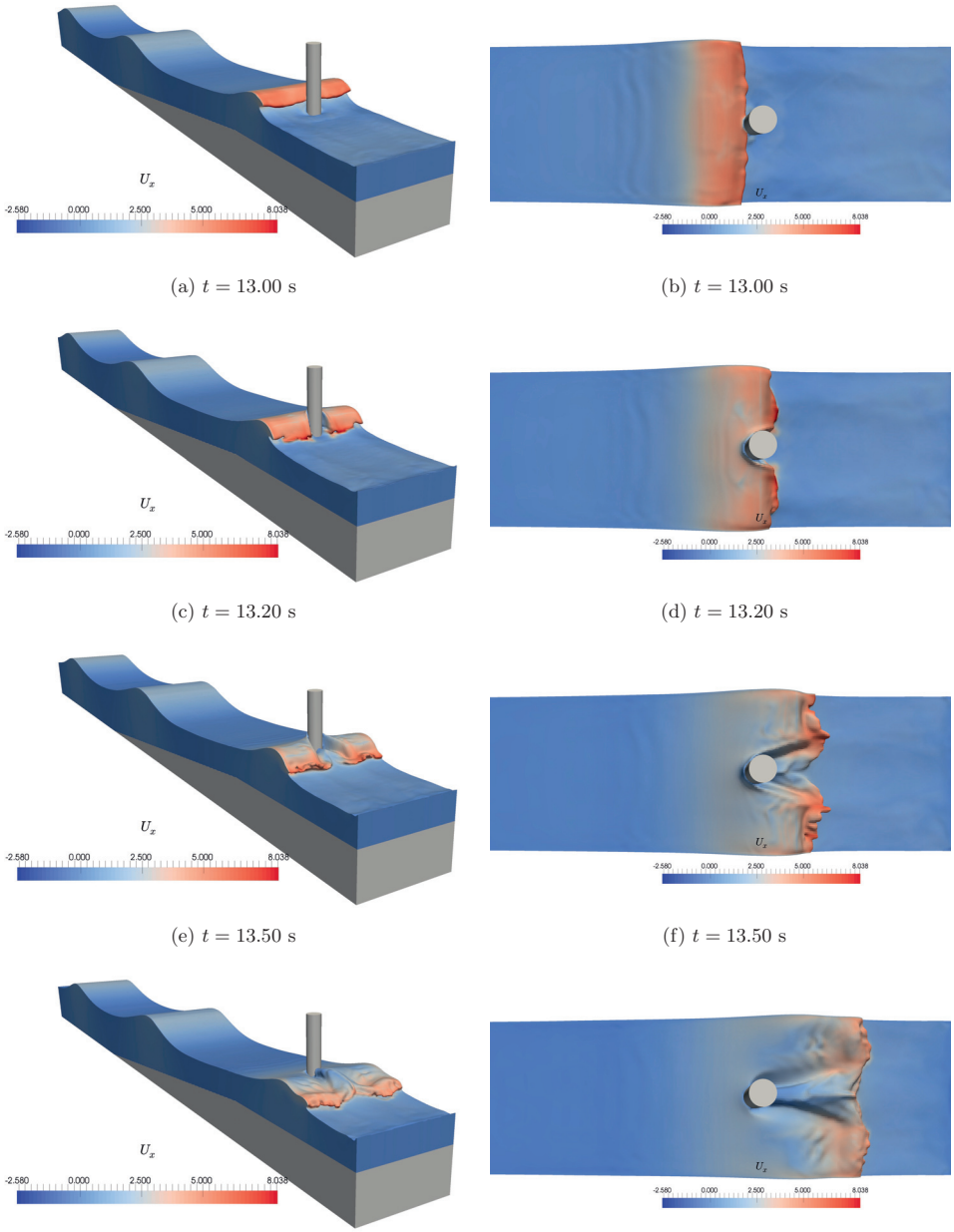

(a) $t = 13.00$ s (b) $t = 13.00$ s

(c) $t = 13.20$ s (d) $t = 13.20$ s

(e) $t = 13.50$ s (f) $t = 13.50$ s

(g) $t = 13.85$ s (h) $t = 13.85$ s

Figure 10: Isometric and corresponding top views of breaking wave interaction with the cylinder for $H_B = 1.30$ m for scenario B5

the cylinder. When the wave impacts the cylinder at its breaking point, in scenario B2, major free surface features are noticed in the shadow region behind the cylinder, with the development of a strong chute-like jet which extends up to the broken wave crest. Semi-circular waves are formed in front of the breaking wavefront around the cylinder, which meet in the shadow region and result in the chute-like jet. When the overturning wave impacts the cylinder with the breaker tongue much below the wave crest in scenario B5, the separation of the wavefront occurs without major free surface features in the region behind the cylinder. The chute-like jet is developed at a late stage is also seen to be weaker than in the previous scenario with regards to both the velocity of the chute tip and the length of extension.

4. Conclusions

The open-source CFD model REEF3D is used to simulate breaking wave interaction with a vertical cylinder. The effect of different incident wave heights and different wave impact scenarios for each incident wave height is studied by changing the location of the cylinder. The process of wave breaking is first studied using two-dimensional simulations. The cylinder locations for different wave impact scenarios are identified from these simulations. The numerical results for the wave force and the free surface elevation are compared to experimental data from large scale tests carried out at the Large Wave Channel, Hannover, Germany and a good agreement is obtained. The following conclusions can be drawn from the studies carried out in this study:

- Cylinder location with respect to the wave breaking location has a large influence on the wave forces exerted on the vertical cylinder. The highest force is seen in the case where the breaker tongue impacts the cylinder just below the wave crest level and the lowest force obtained when the wave breaks behind the cylinder.

- The difference between the highest and the lowest forces among the different scenarios evaluated for each incident wave is about $30\% - 33\%$.

- Different free surface features are observed in the different scenarios presented. The formation of a chute-like jet is seen in the shadow region behind the cylinder, where the wavefront split by the cylinder partly reunites. The chute-like jet is less developed and extends to a smaller distance when the wave impacts the cylinder at a later stage of breaking.

Acknowledgements

This study has been carried out under the OWCBW project (No. 217622/E20) and the authors are grateful to the grants provided by the Research Council of Norway. This study was supported in part with computational resources at the Norwegian University of Science and Technology (NTNU) provided by NOTUR, http://www.notur.no (NN2620K).

References

Alagan Chella, M., Bihs, H., Myrhaug, D., 2015a. Characteristics and profile asymmetry properties of waves breaking over an impermeable submerged reef. Coastal Engineering 100, 26–36.

Alagan Chella, M., Bihs, H., Myrhaug, D., Muskulus, M., 2015b. Breaking characteristics and geometric properties of spilling breakers over slopes. Coastal Engineering 95, 4–19.

Arntsen, Ø.A., Ros, X., Tørum, A., 2011. Impact forces on a vertical pile from plunging breaking waves, in: Coastal Structures.

Berthelsen, P.A., Faltinsen, O.M., 2008. A local directional ghost cell approach for incompressible viscous flow problems with irregular boundaries. Journal of Computational Physics 227, 4354–4397.

Bradshaw, P., Ferriss, D.H., Atwell, N.P., 1967. Calculation of boundary layer development using the turbulent energy equation. Journal of Fluid Mechanics 28, 593–616.

Bredmose, H., Jacobsen, N.G., 2010. Breaking wave impacts on offshore wind turbine foundations: focused wave groups and CFD. Proc., 29th International Conference on Ocean, Offshore and Arctic Engineering, Shanghai, China .

Bullock, G.N., Obhrai, C., Peregrine, D.H., Bredmose, H., 2007. Violent breaking wave impacts. part 1: Results from large-scale regular wave tests on vertical and sloping walls. Coastal Engineering 54, 602–617.

Chan, E.S., Melville, W.K., 1988. Deep-water plunging wave pressures on a vertical plane wall, in: Proc. of the Royal Society of London. A. Mathematical and Physical Sciences, pp. 95–131.

Choi, S.J., Lee, K.H., Gudmestad, O.T., 2015. The effect of dynamic amplification due to a structure s vibration on breaking wave impact. Ocean Engineering 96, 8–20.

Chorin, A., 1968. Numerical solution of the Navier-Stokes equations. Mathematics of Computation 22, 745–762.

Durbin, P.A., 2009. Limiters and wall treatments in applied turbulence modeling. Fluid Dynamics Research 41, 1–18.

Goda, Y., Haranaka, S., Kitahata, M., 1966. Study on impulsive breaking wave forces on piles. Report Port and Harbour Technical Research Institute 6, 1–30.

Irschik, K., Sparboom, U., Oumeraci, H., 2002. Breaking wave characteristics for the loading of a slender pile, in: Proc. 28*th* International Conference on Coastal Engineering.

Jacobsen, N.G., Fuhrman, D.R., Fredsøe, J., 2012. A wave generation toolbox for the open-source CFD library: OpenFOAM. International Journal for Numerical Methods in Fluids 70, 1073–1088.

Jiang, G.S., Peng, D., 2000. Weighted ENO schemes for Hamilton-Jacobi equations. SIAM Journal on Scientific Computing 21, 2126–2143.

Jiang, G.S., Shu, C.W., 1996. Efficient implementation of weighted ENO schemes. Journal of Computational Physics 126, 202–228.

Larsen, J., Dancy, H., 1983. Open boundaries in short wave simulations - a new approach. Coastal Engineering 7, 285–297.

Lin, P., Liu, P.L.F., 1998. A numerical study of breaking waves in the surf zone. Journal of Fluid Mechanics 359, 239–264.

Mo, W., Jensen, A., Liu, P.L.F., 2013. Plunging solitary wave and its interaction with a slender cylinder on a sloping beach. Ocean Engineering 74, 48–60.

Morison, J.R., O'Brien, M.P., Johnson, J.W., Schaaf, S.A., 1950. Force exerted by surface waves on piles. Journal of Petroleum Technology 2, 149–154.

Naot, D., Rodi, W., 1982. Calculation of secondary currents in channel flow. Journal of the Hydraulic Division, ASCE 108, 948–968.

NOTUR, 2012. The Norwegian Metacenter for Computational Science. http://www.notur.no/hardware/vilje .

Osher, S., Sethian, J.A., 1988. Fronts propagating with curvature- dependent speed: algorithms based on Hamilton-Jacobi formulations. Journal of Computational Physics 79, 12–49.

Peng, D., Merriman, B., Osher, S., Zhao, H., Kang, M., 1999. A PDE-based fast local level set method. Journal of Computational Physics 155, 410–438.

Schäffer, H.A., Klopman, G., 2000. Review of multidirectional active wave absorption methods. Journal of Waterway, Port, Coastal, and Ocean Engineering 126, 88–97.

Shu, C.W., Osher, S., 1988. Efficient implementation of essentially non-oscillatory shock capturing schemes. Journal of Computational Physics 77, 439–471.

van der Vorst, H., 1992. BiCGStab: A fast and smoothly converging variant of Bi-CG for the solution of nonsymmetric linear systems. SIAM Journal on Scientific and Statistical Computing 13, 631–644.

Wienke, J., Oumeraci, H., 2005. Breaking wave impact force on a vertical and inclined slender piletheoretical and large-scale model investigations. Coastal Engineering 52, 435–462.

Wienke, J., Sparboom, U., Oumeraci, H., 2000. Breaking wave impact on a slender cylinder, in: Coastal Engineering Conference, pp. 1787–1798.

Wilcox, D.C., 1994. Turbulence modeling for CFD. DCW Industries Inc., La Canada, California.

Zhao, Q., Armfield, S., Tanimoto, K., 2004. Numerical simulation of breaking waves by a multi-scale turbulence model. Coastal Engineering 51, 53–80.

6.9 Paper 9

Breaking wave interaction with tandem cylinders under different impact scenarios

Bihs, H., Kamath, A., Alagan Chella, M., Arntsen, Ø. A.
Journal of Waterway, Port, Coastal, and Ocean Engineering, 2016,
DOI: 10.1061/(ASCE)WW.1943-5460.0000343

Paper 9

Breaking wave interaction with tandem cylinders under different impact scenarios

Hans Bihs [1], Arun Kamath [2] Mayilvahanan Alagan Chella[3], and and Øivind A. Arntsen [4]

ABSTRACT

The interaction of plunging breaking waves with a pair of cylinders placed in tandem is investigated using the open-source computational fluid dynamics (CFD) model REEF3D. The model is validated using experimental data for total wave forces and free surface elevations for breaking wave interaction with a single cylinder. Wave interaction with tandem cylinders is investigated for four different wave impact scenarios on the first cylinder and six different distances between the cylinders in each scenario. Wave forces on the upstream cylinder are generally found to be less than the forces on a single cylinder for a particular scenario. The force on the downstream cylinder is lower than the force on the upstream cylinder when the breaker tongue impacts the first cylinder. Under conditions where the breaker tongue impacts the downstream cylinder around the wave crest level, the wave force on the downstream cylinder is higher than the force on the upstream cylinder. The wave forces experienced by the tandem cylinders is highly influenced by the location of the breaking point with respect to the cylinders and the distance between the cylinders.

Keywords: breaking wave forces, vertical cylinder, tandem cylinders, CFD, computational fluid dynamics

[1]Associate Professor, Dept. of Civil and Transport Engineering, Norwegian University of Science and Technology, Trondheim, 7491, Norway. E-mail: hans.bihs@ntnu.no

[2]Post Doctoral Fellow, Dept. of Civil and Transport Engineering, Norwegian University of Science and Technology, Trondheim, 7491, Norway.

[3]PhD candidate, Dept. of Civil and Transport Engineering, Norwegian University of Science and Technology, Trondheim, 7491, Norway

[4]Associate Professor, Dept. of Civil and Transport Engineering, Norwegian University of Science and Technology, Trondheim, 7491, Norway.

INTRODUCTION

The interaction of breaking wave forces on structures involves complex two-phase air-water interaction, rapid free surface deformations and an impulsive force. The short duration over which these interactions occur, pose several challenges to the evaluation of breaking wave forces. In shallow waters, the hydrodynamic loading on structures such as offshore wind turbine substructures is mostly governed by the loading due to plunging breaking waves (Alagan Chella et al., 2012). The theoretical description of breaking waves in shallow waters is rather limited up to the transition region close to breaking. The evolution of the breaking process and the underlying flow physics can not be described theoretically. This is due to the simplifying assumptions of single-phase and two-dimensional flow, irrotational motion, no return flow and hydrostatic pressure made in obtaining analytical solutions (Cokelet, 1977).

The current knowledge on breaking wave kinematics is mainly based on experimental investigations. Deep water breaking waves were studied by Kjeldsen and Myrhaug (1978); Battjes and Sakai (1981); Bonmarin (1989); Rapp and Melville (1990) and Duncan (2001). Wave breaking on plane beaches was studied by Stive and Wind (1982); Miller (1987); Nadaoka et al. (1989) and Ting and Kim (1994) while wave breaking over submerged structures was studied by Gourlay (1994); Smith and Kraus (1990) and Blenkinsopp and Chaplin (2008). While these studies focussed on the kinematics and dynamics of breaking waves, several other researchers experimentally investigated breaking wave forces on cylinders, e.g. Goda et al. (1966); Watanabe and Horikawa (1974); Apelt and Piorewicz (1986); Chan and Melville (1988); Sawaragi and Nochino (1984); Chaplin et al. (1992); Wienke et al. (2000) and Arntsen et al. (2011). However, the measurement of the quantities related to the wave breaking and their interaction with structures is challenging.

Theoretically, the total breaking wave force on a vertical slender cylinder can be expressed in terms of a slowly varying quasi-static force and an impulsive wave impact force. Goda et al. (1966) proposed the use of an impact force term in addition to the

quasi-static force predicted by the Morison formula (Morison et al., 1950) to evaluate breaking wave forces. The impact force characteristics are mainly determined by the geometric properties and kinematics at breaking, such as the shape of the wave and the distribution of water particle velocities under the wave crest (Goda et al., 1966).

Watanabe and Horikawa (1974) investigated breaking wave forces on a large cylinder and proposed a formula that includes the phase difference between the water particle acceleration and the inertia force. They also pointed out that empirical coefficients used to calculate breaking wave forces are not universal and depend on breaking wave characteristics. Apelt and Piorewicz (1986) carried out experiments to study interference effects of breaking wave forces on rows of two or three vertical cylinders placed along and normal to the direction of wave propagation. Their results suggested that both the distance between the cylinders and the incident wave steepness are important factors when in a row is arranged normal to the direction of wave propagation. They further concluded that the separation distance does not significantly influence the wave forces when the row is along the direction of wave propagation. Sparboom et al. (2005) studied breaking wave forces due to freak waves on two and three cylinder arrays and found that breaking wave forces are reduced significantly along the array due to a sheltering effect from upstream cylinders.

Wienke et al. (2000) carried out large-scale studies on breaking wave impact on a single slender cylinder and presented different wave loading cases that considered the position of the cylinder with respect to the wave breaking point. Irschik et al. (2002) extended this work and presented the Empirical Mode Decomposition (EMD) method to separate the slowly varying quasi-static loading and the dynamic response of the cylinder from the measured breaking wave force history. Based on their large-scale investigations, Wienke and Oumeraci (2005) proposed a theoretical model to calculate breaking wave forces on a single slender cylinder using the wave celerity and curling factor as inputs.

The curling factor (λ) is a parameter used to determine the contribution of the

wave crest to the wave impact force during breaking. The values for λ are determined experimentally for different bottom slopes and water depths, and these values depend on the breaker type. According to Wienke and Oumeraci (2005), the wave impact scenario is different for different distances between the cylinder surface and the breaking point. While calculating λ, the assumption of instantaneous wave impact on the cylinder can also lead to overestimating the breaking wave force. Hildebrandt and Schlurmann (2012) investigated breaking wave forces on a tripod structure in large-scale experiments to study the detailed temporal and spatial variations in the wave slamming loads. They concluded that the curling factors, vertical position of impact and maximum slamming coefficients increase as the distance between the cylinder and the point of wave breaking decreases. Their results agreed with the theoretical slamming coefficients given by Goda et al. (1966).

Most of the current approaches to evaluate breaking wave forces strongly depend on experimentally determined coefficients. However, the measuring various parameters such as velocity and acceleration during breaking is a challenging task (Arntsen et al., 2011). Also, the coefficients are valid only for cases that are similar to the experiments used to obtain them and cannot be applied with multiple cylinders and different arrangements of the cylinders. In addition, the distance from the cylinder to the breaking point results in several breaking wave interaction scenarios that have to be studied in detail to gain useful insights into the breaking wave-structure interaction problem.

Computational fluid dynamics (CFD) models can evaluate breaking waves with few assumptions about the fluid physics to obtain detailed insights into the breaking wave-structure interaction (Christensen, 1998). Many numerical studies have been carried out to investigate the breaking process in shallow waters with single-phase CFD models (Lin and Liu, 1998; Bradford, 2000; Christensen and Deigaard, 2001; Zhao et al., 2004). Hieu et al. (2004) showed that a two-phase CFD model better resolves the breaking wave kinematics. Thus, two-phase CFD models in recent literature include the air-water interaction in the modeling (Chen et al., 1999; Christensen, 2006; Wang et al., 2009;

Jacobsen et al., 2012; Xie, 2013; Alagan Chella et al., 2015b). In addition, results from Alagan Chella et al. (2015b) and Alagan Chella et al. (2015a) show that higher order discretization schemes, tight velocity-pressure coupling and a sharp representation of the free surface provide a more realistic description of the breaking waves. These studies have advanced the knowledge in current literature regarding breaking wave kinematics.

Bredmose and Jacobsen (2010) carried out simulations of focussed wave breaking forces on a slender cylinder using the open-source CFD model OpenFOAM without an explicit turbulence model, using half of the computational domain and assuming lateral symmetry in the flow field. Mo et al. (2013) investigated solitary wave breaking over a slope and its interaction with a slender cylinder with experiments and a CFD model assuming lateral symmetry. For the free surface elevations and particle velocities, the experimental and numerical results showed good agreement. Choi et al. (2015) studied the free surface elevation and breaking wave forces on vertical and inclined single cylinders using a CFD model. Good agreement was obtained between the computed results and the filtered experimental data. However, numerical investigations of breaking wave forces on tandem cylinders, the effect of neighboring cylinders on breaking wave forces, and the complex free surface deformations associated with this interaction has not been presented in current literature to our knowledge.

The interaction between breaking waves and a cylinder involves several important free surface features such as runup on the cylinder, separation of the breaking wavefront around the cylinder, formation of a water jet behind the cylinder and the rejoining of the separated wavefront behind the cylinder. In the presence of neighboring cylinders, the scenario is further relevant as it represents coastal and offshore constructions. In this study, the open-source CFD model REEF3D is used to evaluate breaking wave forces on tandem cylinders placed at different distances from each other in a three-dimensional numerical wave tank. The model has been previously used to investigate breaking wave kinematics (Alagan Chella et al., 2015b) and to calculate non-breaking wave forces on tandem cylinders (Kamath et al., 2015). Several free surface features and

wave impact scenarios associated with breaking waves interacting with a single cylinder and the resulting forces on the cylinder have been discussed in current literature. This paper investigates the case of two cylinders placed in tandem, focussing on how the distance between the cylinders influences the wave forces and the flow features around the cylinders. Four different wave impact scenarios and six separation distances between cylinders are considered. The numerical model is validated using experimental results from the Large Wave Flume (GWK) (Irschik et al., 2002) for breaking wave interaction with a single cylinder.

NUMERICAL MODEL

Governing equations

The numerical wave tank REEF3D solves the incompressible three-dimensional Reynolds-Averaged Navier-Stokes (RANS) equations:

$$\frac{\partial u_i}{\partial x_i} = 0 \tag{1}$$

$$\frac{\partial u_i}{\partial t} + u_j \frac{\partial u_i}{\partial x_j} = -\frac{1}{\rho}\frac{\partial p}{\partial x_i} + \frac{\partial}{\partial x_j}\left[(\nu + \nu_t)\left(\frac{\partial u_i}{\partial x_j} + \frac{\partial u_j}{\partial x_i}\right)\right] + g_i \tag{2}$$

where u is the velocity, ρ is the density of the fluid, p is the pressure, ν is the kinematic viscosity, ν_t is the eddy viscosity and g the acceleration due to gravity.

The fifth-order conservative finite difference Weighted Essentially Non-Oscillatory (WENO) scheme proposed by Jiang and Shu (1996) is applied to discretize the convective terms of the RANS equation. Time is advanced using a Total Variation Diminishing (TVD) third-order Runge-Kutta explicit time scheme (Shu and Osher, 1988). The time step size is controlled with adaptive time stepping based on the Courant-Friedrichs-Lewy (CFL) criterion; this results in an optimal time step value for numerical stability and accuracy. Diffusion is treated with an implicit time scheme to exclude it from the CFL criterion. Pressure is treated with the projection method (Chorin, 1968).

The Poisson equation for pressure is solved with the preconditioned BiCGStab solver (van der Vorst, 1992). The domain decomposition strategy and MPI (Message Passing Interface) is used for parallelization. A Cartesian grid with a staggered arrangement is used in the numerical model. Complex geometries are taken into account with the ghost cell immersed boundary method (Berthelsen and Faltinsen, 2008).

The k-ω model is employed for turbulence closure (Wilcox, 1994) with transport equations for the turbulent kinetic energy k and the specific turbulence dissipation ω shown in Eqs. (3) and (4) respectively. Wall functions are used for k and ω.

$$\frac{\partial k}{\partial t} + u_j \frac{\partial k}{\partial x_j} = \frac{\partial}{\partial x_j}\left[\left(\nu + \frac{\nu_t}{\sigma_k}\right)\frac{\partial k}{\partial x_j}\right] + P_k - \beta_k k\omega \tag{3}$$

$$\frac{\partial \omega}{\partial t} + u_j \frac{\partial \omega}{\partial x_j} = \frac{\partial}{\partial x_j}\left[\left(\nu + \frac{\nu_t}{\sigma_\omega}\right)\frac{\partial \omega}{\partial x_j}\right] + \frac{\omega}{k}\alpha P_k - \beta\omega^2 \tag{4}$$

where, eddy viscosity $\nu_t = k/\omega$, P_k is the production rate, and the closure coefficients $\sigma_k = 2$, $\sigma_\omega = 2$, $\alpha = 5/9$, $\beta_k = 9/100$, $\beta = 3/40$. Eddy viscosity limiters (Durbin, 2009) are used to control the overproduction of turbulence, often occurring in highly unsteady free surface flows. In addition, because the turbulence length scales cannot pass the water-air interface, a free surface turbulence damping scheme is considered (Naot and Rodi, 1982).

Free Surface

The complex wave hydrodynamics are modeled with a two-phase flow approach, calculating the flows for water and air. The interface between the two fluids is captured with the level set method (Osher and Sethian, 1988). The zero level set of the signed distance function $\phi(\vec{x}, t)$ represents the location of the free surface. With its signed distance property, it gives the shortest distance from the interface to all the points in the flow domain. Based on the sign of the level set function, the phases can be

distinguished as follows:

$$\phi(\vec{x},t)\begin{cases} > 0 & if\ \vec{x}\ is\ in\ phase\ 1 \\ = 0 & if\ \vec{x}\ is\ at\ the\ interface \\ < 0 & if\ \vec{x}\ is\ in\ phase\ 2 \end{cases} \tag{5}$$

The flow velocities calculated from Eq. (2) are used to convect the level set function:

$$\frac{\partial \phi}{\partial t} + u_j \frac{\partial \phi}{\partial x_j} = 0 \tag{6}$$

During computation, reinitialization is carried out after every iteration using a partial differential equation by Peng et al. (1999) in order to maintain the signed distance property of the level set function. The level set function is discretized with the Hamilton-Jacobi formulation of the WENO scheme by Jiang and Peng (2000).

Wave generation and absorption

The numerical wave tank uses the relaxation method (Larsen and Dancy, 1983) for the wave generation. To moderate the velocity and the free surface, a relaxation function is used in the relaxation zones:

$$\begin{aligned} u_{relaxed} &= \Gamma(x) u_{analytical} + (1-\Gamma(x)) u_{computational} \\ \phi_{relaxed} &= \Gamma(x) \phi_{analytical} + (1-\Gamma(x)) \phi_{computational} \end{aligned} \tag{7}$$

where $\Gamma(x)$ is the relaxation function and $x \in [0,1]$ is the x-coordinate scaled to the length of the relaxation zone. The relaxation function shown in Eq. (8) is used in the current numerical model (Jacobsen et al., 2012):

$$\Gamma(x) = 1 - \frac{e^{(1-x)^{3.5}} - 1}{e-1} \tag{8}$$

To avoid reflections from the downstream boundary, an active wave absorption

method is employed. Here, waves opposite to the reflected ones are generated, canceling out the reflections. Based on shallow water theory (Schäffer and Klopman, 2000), the following horizontal velocity is prescribed on the downstream boundary:

$$u\left(t\right) = -\sqrt{\frac{g}{h}}\,\xi\left(t\right) \tag{9}$$

where

$$\xi\left(t\right) = \eta\left(t\right) - h \tag{10}$$

Here, $\eta\left(t\right)$ is the actual free surface location along the downstream boundary and h the still water level. The method is applied in vertical strips as wide as one grid cell along the downstream boundary. This way, different free surface elevations along the boundary can be taken into account (Higuera et al., 2013). Also, the handling of oblique waves is also implemented in the current model.

Numerical evaluation of wave forces

The breaking wave forces on the cylinders is calculated by integrating the pressure p and the surface normal component of the viscous shear stress tensor τ on the surface of the solid objects:

$$F = \int_{\Omega} (-\mathbf{n}p + \mathbf{n} \cdot \tau) d\Omega \tag{11}$$

where $\mathbf{n}$ is the unit normal vector pointing into the fluid and Ω is the surface of the object.

RESULTS AND DISCUSSION

Validation of the numerical model

The breaking wave force on a single vertical cylinder is calculated numerically and compared to experimental data to validate the numerical model. The experiments were carried out at the Large Wave Flume (GWK) in Hannover, Germany (Irschik et al., 2002) on a vertical cylinder of diameter $D = 0.7$ m in a water depth of 3.80 m with

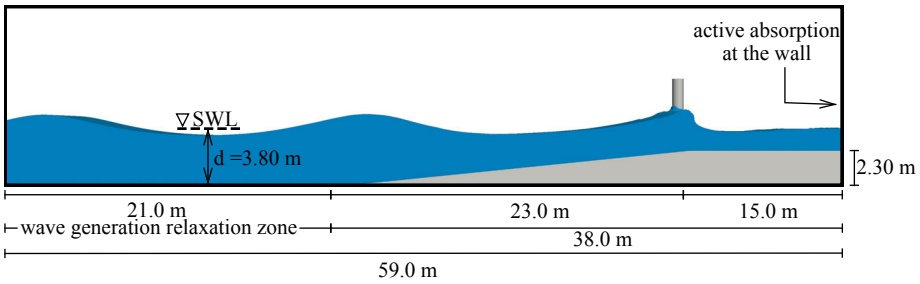

(a) numerical wave tank showing the dimensions of the tank and wave generation and absorption zones

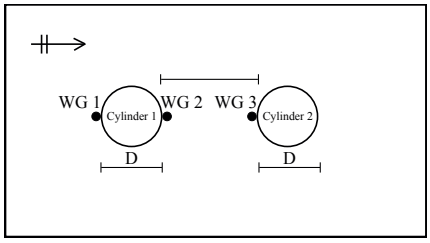

(b) schematic diagram showing the wave gage locations around the cylinders

Fig. 1. Numerical wave tank setup used in the study

incident waves of period $T = 4.0$ s. The cylinder is placed at the top of a 23 m long $1 : 10$ slope, such that the still water depth at the cylinder is 1.50 m. In the numerical setup, the wave tank is 59 m long, 5 m wide and 7 m high with a grid size of $dx = 0.05$ m, resulting in a total of 16.52 million cells. A cylinder with $D = 0.7$ m is placed with its center at 44.0 m, and incident waves of period $T = 4.0$ s break exactly on the front surface of the cylinder. The complete numerical setup is illustrated in Fig. (1a). The definition sketch for tandem cylinders in the wave tank shows the location of the wave gages and the separation distance in Fig. (1b).

The numerically calculated wave force is compared to the EMD (Empirical Mode Decomposition) treated experimental data from Choi et al. (2015) to filter out the dynamic amplification of the wave forces due to vibration of the cylinder as shown in Fig. (2a). Good agreement is seen between the numerical and experimental wave forces. The numerical results are also similar over several wave periods, showing that the

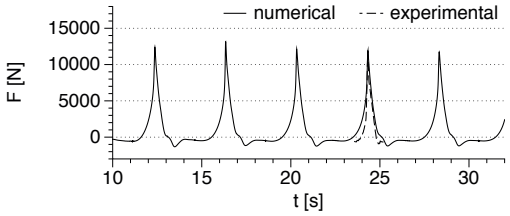

(a) wave force on the cylinder

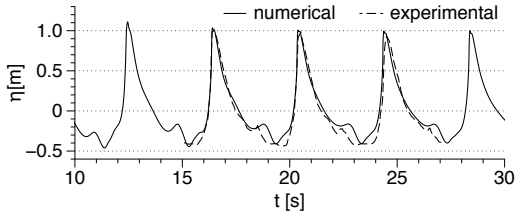

(b) free surface near the wall along the frontline of the cylinder

Fig. 2. Comparison of the numerical and experimental results

numerical model predicts the the wave breaking location and consequently the breaking wave forces consistently. The free surface elevation near the wall along the frontline of the cylinder provides a representation of the incident wave on the cylinder. Comparison of the numerical and experimental free surface elevations shows good agreement in Fig. (2b). The vertical wavefront in the figure shows that the wave breaks on the front surface of the cylinder.

Effect of wave impact scenario and distance between tandem cylinders on the wave forces

The wave forces on tandem cylinders placed at different distances from each other are studied for different wave breaking scenarios. The different scenarios are determined by the location of the wave breaking point with respect to the front surface of the first cylinder. The scenarios considered in this study are:

- scenario A: overturning wave crest impacts cylinder 1 just below the wave crest level

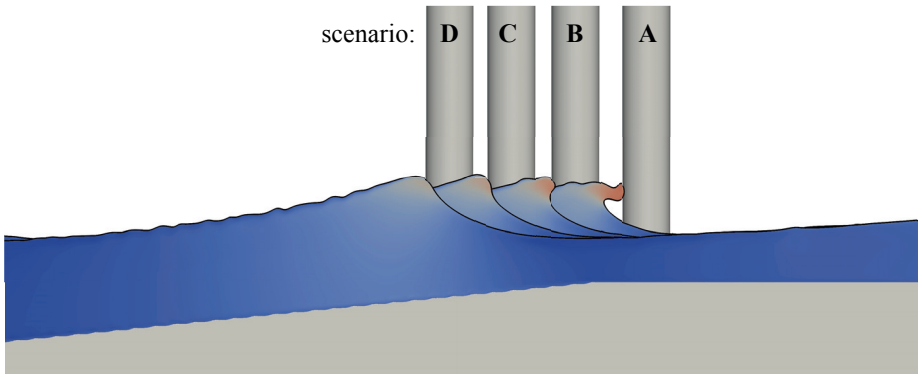

Fig. 3. Four different locations of cylinder 1 with respect to the wave breaking point considered in the study

- scenario B: overturning wave crest impacts cylinder 1 at the wave crest level
- scenario C: wave breaks exactly at cylinder 1 with a vertical wavefront
- scenario D: wave breaks just behind cylinder 1

The various scenarios are illustrated in Fig. (3). Simulations are carried out to determine the breaking wave force for a single cylinder F_0 in each scenario. Previous studies dealing with breaking waves on a single slender cylinder have presented that the mode of wave impact on the cylinder due to the distance between the breaking point and the cylinder significantly impacts the wave forces acting on the cylinder. According to Irschik et al. (2002), scenarios A and B result in the highest and the second highest total wave forces on a single cylinder respectively. The lowest wave forces on a single cylinder are obtained in scenario D. In the context of tandem cylinders, the wave impact on cylinder 1 and the separation distance between the two cylinders can influence in the wave forces experienced by both cylinders. This is investigated in this study by placing the second cylinder at separation distances of $S = 1D$, $S = 2D$, $S = 3D$, $S = 4D$, $S = 5D$ and $S = 6D$. The resulting 24 different cases are listed in Table (1) along with the numerical forces calculated for a single cylinder in each of the wave breaking scenarios, F_0. Table (1) also lists the maximum force on each cylinder with respect to F_0 for each case (F_1/F_0 and F_2/F_0) and the maximum wave crest elevations in front of

Table 1. Details of the setups used in the different simulations

Case	H (m)	T (s)	S (m)	scenario	F_0 (N)	F_1/F_0	F_2/F_0	η_{cyl1}/η_0	η_{cyl2}/η_0
A1			1D	overturning		0.92	0.59	1.58	1.69
A2			2D	wave crest		0.95	0.58	1.64	1.75
A3	1.30	4.00	3D	impact on	14000	0.91	0.45	1.57	1.58
A4			4D	cylinder 1 just		0.90	0.48	1.56	1.62
A5			5D	below wave		0.88	0.55	1.59	1.70
A6			6D	crest level		0.88	0.52	1.68	1.58
B1			1D	overturning		0.74	0.58	1.76	1.71
B2			2D	wave crest		0.93	0.85	1.70	1.72
B3	1.30	4.00	3D	impact on	13400	0.61	0.80	1.75	1.58
B4			4D	cylinder 1 at		0.75	0.57	1.69	1.56
B5			5D	wave crest level		0.83	0.61	1.69	1.45
B6			6D			0.86	0.60	1.70	1.37
C1			1D			0.89	0.66	1.82	1.77
C2			2D	wave breaking		0.90	0.84	1.70	1.84
C3	1.30	4.00	3D	exactly at	11850	0.92	0.97	1.82	1.70
C4			4D	cylinder 1		0.86	0.92	1.76	1.63
C5			5D			0.83	0.71	1.70	1.44
C6			6D			0.83	0.61	1.76	1.32
D1			1D			0.90	0.81	1.83	1.79
D2			2D	wave breaking		0.89	0.99	1.94	1.89
D3	1.30	4.00	3D	just behind	9800	0.90	1.03	1.70	1.76
D4			4D	cylinder 1		0.88	1.04	1.78	1.59
D5			5D			0.85	1.18	1.83	1.45
D6			6D			0.85	1.02	1.78	1.37

the cylinders with respect to the incident wave crest elevation $\eta_0 = 0.789$ m (η_{cyl1}/η_0 and η_{cyl2}/η_0). In the following sections, results from selected cases are presented to obtained detailed insights into the breaking wave interaction, free surface features and wave forces on the cylinders. The selected cases present the prominent breaking wave hydrodynamics for different separation distances in different wave impact scenarios.

Scenario A1: overturning wave crest impacting cylinder 1 just below the wave crest level with $S = 1D$

The breaking wave force and free surface elevations around the cylinders calculated for scenario A1 are presented in Fig. (4). The breaking wave force on a single cylinder in this wave impact scenario is $F_0 = 14000$ N. The breaking wave forces (F) on cylinders

1 and 2 are calculated to be $0.92F_0$ and $0.59F_0$ respectively as shown in Fig. (4a). In this case, the incident wave on the second cylinder is a broken wave that has dissipated most of its energy during the breaking process and with the first cylinder. Thus, the breaking wave force on the second cylinder is significantly lower than that on the first cylinder. The free surface elevations (η) calculated in front of (WG 1) and behind (WG 2) the first cylinder and in front of the second cylinder (WG 3) are presented in Fig. (4b). The free surface elevation in front of cylinder 2, placed $S = 1D$ away is $\eta/\eta_0 = 1.69$, higher than the free surface elevation in front of cylinder 1, $\eta/\eta_0 = 1.58$. The higher free surface elevation is attributed to the large runup on cylinder 2 due to the close placement of the cylinders.

Further insight into the wave interaction problem is obtained from the free surface around the cylinders for case A1, presented in Fig. (5) with horizontal velocity contours. The incident wave impacts cylinder 1 with the breaker tongue just below the wave crest level in Fig. (5a). The overturned wavefront is separated around cylinder 1 in Fig. (5b). This phenomenon of separation of the wave crest around the first cylinder and spreading of the water mass around the sides of the cylinder is also reported by Sparboom et al. (2006) in large-scale experiments. Figure (5c) shows how the separated broken wavefront incident on cylinder 2 reconnects with the free surface. As the broken wave crest propagates past cylinder 2 in Fig. (5d), high runup is observed on the front

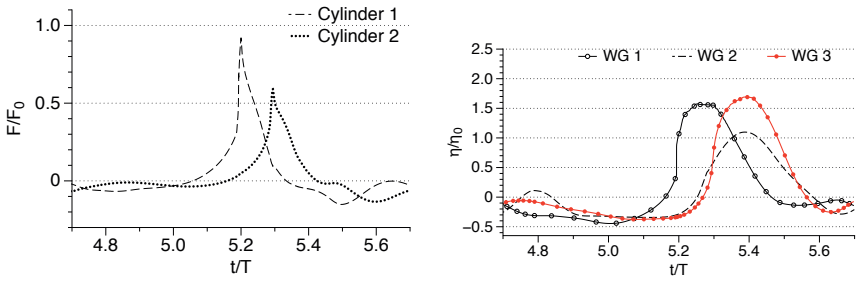

(a) breaking wave forces on the cylinders (b) free surface elevations around the cylinders

Fig. 4. Wave forces on and free surface elevations around the cylinders for scenario A1: breaker tongue impacting cylinder just below wave crest level with $S = 1D$

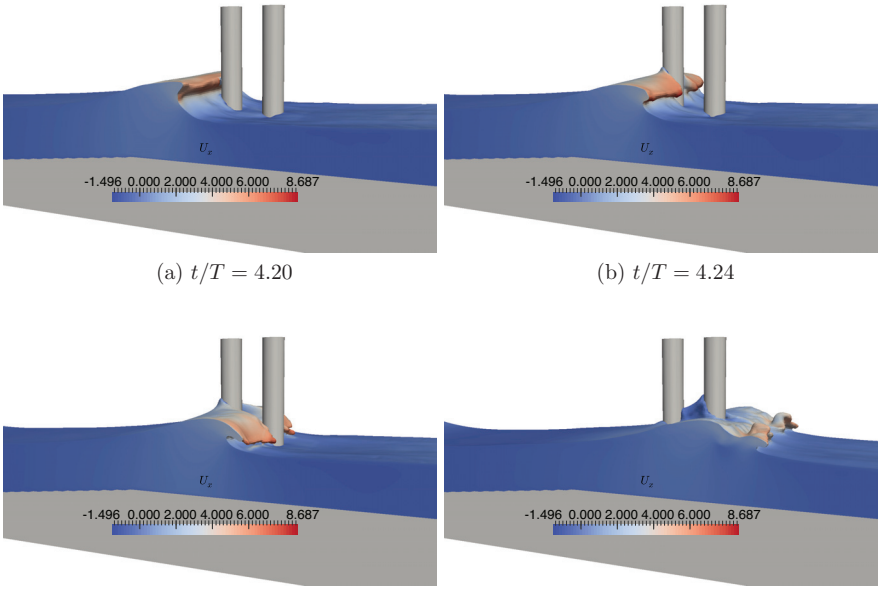

(a) $t/T = 4.20$ (b) $t/T = 4.24$

(c) $t/T = 4.29$ (d) $t/T = 4.40$

Fig. 5. Free surface around the cylinders in scenario A1 ($S = 1D$) with horizontal velocity contours

surface of cylinder 2. This runup results in a higher free surface elevation in front of cylinder 2 compared to cylinder 1 seen for WG 3 in Fig. (4b). Figure (5) also shows that in scenario A, cylinder 2 is always exposed to an already broken wave, which exerts lower wave forces on the cylinder.

Scenario B2: overturning wave crest impacting cylinder 1 at the wave crest level with $S = 2D$

Figure (6) shows the breaking wave forces on and the free surface elevations around the two cylinders in scenario B2. A single cylinder in the same impact scenario experiences a force of $F_0 = 13400$ N. The breaking wave force on cylinder 1 is $0.93F_0$, and on cylinder 2 it is $0.85F_0$, as shown in Fig.(6a). In Fig. (6b) the free surface elevations in front of cylinders 1 and 2 are $\eta/\eta_0 = 1.70$ and $\eta/\eta_0 = 1.72$ respectively. The slopes of the wavefront at the moment of impact on the cylinders are similar, and the wave forces on the two cylinders are comparably similar.

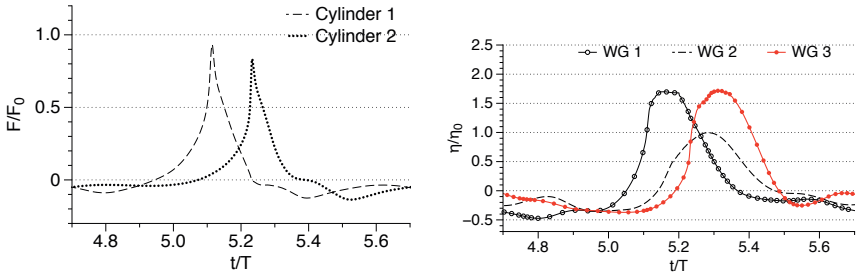

(a) breaking wave forces on the cylinders (b) free surface elevations around the cylinders

Fig. 6. Wave forces on and free surface elevations around the cylinders for scenario B2: breaker tongue impacting cylinder at wave crest level with $S = 2D$

Fig. (7) shows the free surface around the cylinders with horizontal velocity contours for scenario B2. The overturning wave crest impacts cylinder 1 at the wave crest level in Fig. (7a). The incident wave crest shows that it interacts with previous waves reflected off the cylinders. The separation of the overturning wave crest around cylinder 1 is seen in Fig. (7b). In Fig. (7c), the overturning wave crest and the water jet formed behind cylinder 1 impact cylinder 2 below the wave crest level. The high runup on the second cylinder due to the water jet originating behind cylinder 1 and the small separation distance is seen in Fig. (7d). In this scenario, although cylinder 1 separates the wavefront, the sheltering effect on cylinder 2 is seen to be reduced. This is due to the water jet that forms behind cylinder 1 and impacts cylinder 2 along with the breaking wave. This results in comparably similar forces on the two cylinders in this scenario, with the upstream cylinder experiencing a slightly higher force.

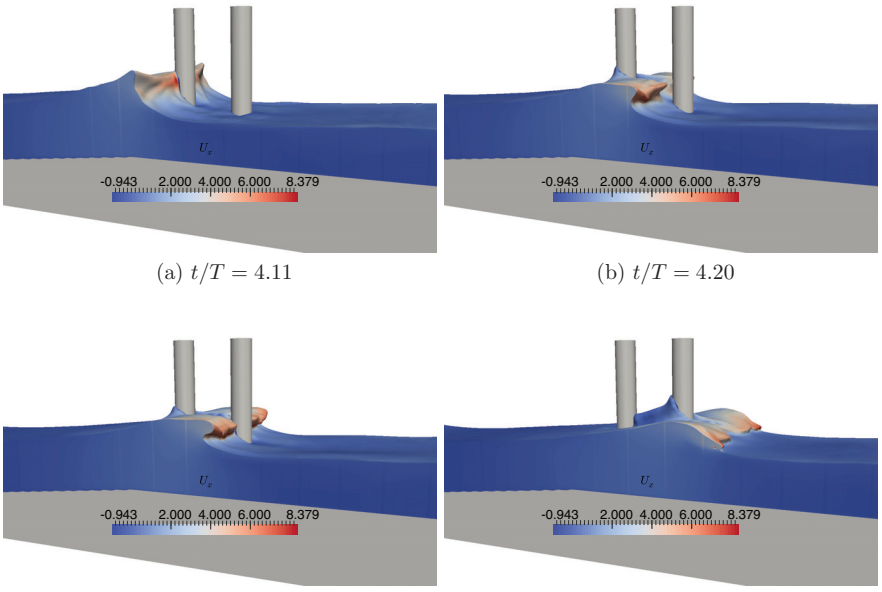

(a) $t/T = 4.11$ (b) $t/T = 4.20$

(c) $t/T = 4.23$ (d) $t/T = 4.31$

Fig. 7. Free surface around the cylinders in scenario B2 ($S = 2D$) with horizontal velocity contours

Scenario C3: wave breaking exactly at cylinder 1 with $S = 3D$

The breaking wave forces on and the free surface elevations around the cylinders in scenario C3 are shown in Fig. (8). The breaking wave force on a single cylinder in this scenario is $F_0 = 11850$ N. Here, cylinder 1 experiences a force of $0.92F_0$ and cylinder 2 a force of $0.97F_0$. The breaking wave force on the downstream cylinder 2 is slightly higher than the force on the upstream cylinder 1. The free surface elevation in front of cylinder 2 is $\eta/\eta_0 = 1.70$, which is slightly lower when compared to $\eta/\eta_0 = 1.82$ in front of cylinder 1.

The wave interaction in scenario C3 is further studied using the free surface around the cylinders and horizontal velocity contours shown in Fig. (9). The incident wave impacts cylinder 1 with a vertical wavefront as seen in Fig. (9a). The incident wave separates around cylinder 1 in Fig. (9b), and the wave crest also begins to overturn just behind the cylinder. The breaker tongue and the water jet originating behind cylinder

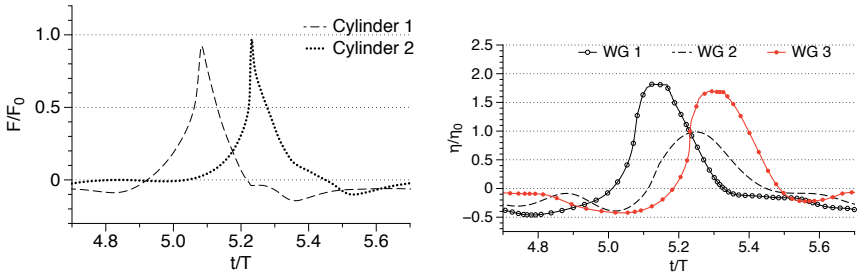

(a) breaking wave forces on the cylinders (b) free surface elevations around the cylinders

Fig. 8. Wave forces on and free surface elevations around the cylinders for scenario C3: wave breaking exactly at the first cylinder with $S = 3D$

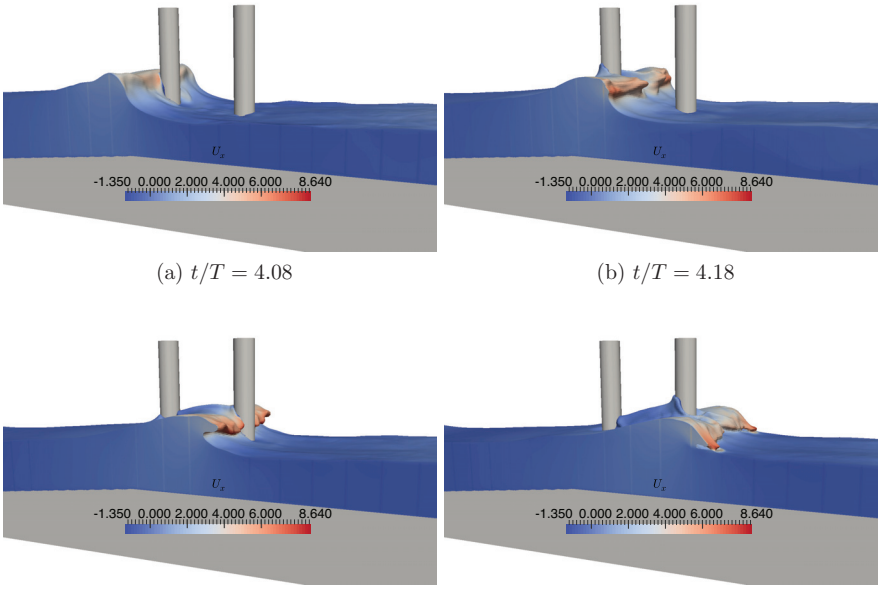

(a) $t/T = 4.08$ (b) $t/T = 4.18$

(c) $t/T = 4.25$ (d) $t/T = 4.32$

Fig. 9. Free surface around the cylinders in scenario C3 ($S = 3D$) with horizontal velocity contours

1 impact cylinder 2 in Fig. (9c). The breaking wave incident on cylinder 2 impacts the cylinder just below the wave crest level; this breaking wave and the water jet result in higher forces on the cylinder. The runup of the trapped water between the cylinders is seen in Fig. (9d), and the overturning wave crest rejoins the preceding wave crest after passing cylinder 2.

Scenario D4: wave breaking just behind cylinder 1 with $S = 4D$

The waves force on a single cylinder in this wave impact scenario is calculated to be $F_0 = 9800$ N. In Fig. (10a), the calculated breaking wave forces on cylinders 1 and 2 are $0.88F_0$ and $1.04F_0$ respectively. In this scenario, the upstream cylinder 1 is exposed to very steep incident waves that approach the wave breaking point. Cylinder 2 is exposed to an overturning wave crest, and the breaking wave impact force contributes to the total wave force on the cylinder; this results in a higher wave force on the downstream cylinder compared to the upstream cylinder. The free surface elevations in Fig. (10b) show that $\eta/\eta_0 = 1.78$ in front of cylinder 1 (WG 1) and that $\eta/\eta_0 = 1.59$ in front of cylinder 2 (WG 3) for this case.

To further understand the wave interaction with the cylinders in scenario D4, the free surface around the cylinders is presented in Fig. (11) along with the horizontal velocity contours. Figure (11a) shows the steep unbroken wave incident on cylinder 1. The wave breaks just behind cylinder 1; the overturning wave crest, along with the water jet originating behind cylinder 1, is seen in Fig. (11b). The overturning wave crest and the water jet then impact the second cylinder just below the wave crest level in Fig. (11c). The breaker tongue reconnects with the preceding wave trough behind cylinder 2 in Fig. (11d). The higher forces on the second cylinder result from the mode of wave impact on each cylinder. Figure (11) clearly shows that the upstream cylinder

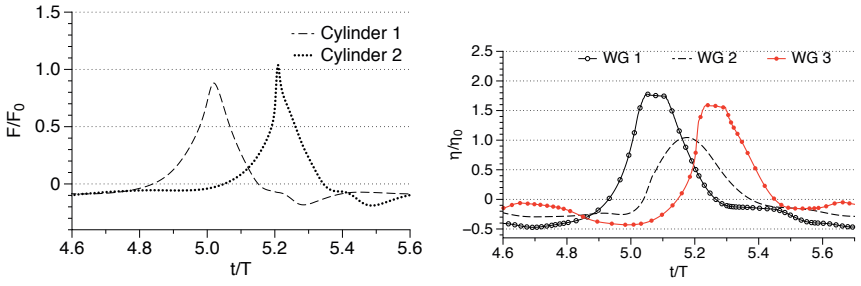

(a) breaking wave forces on the cylinders (b) free surface elevations around the cylinders

Fig. 10. Wave forces on and free surface elevations around the cylinders for scenario D4: wave breaking just behind the first cylinder with $S = 4D$

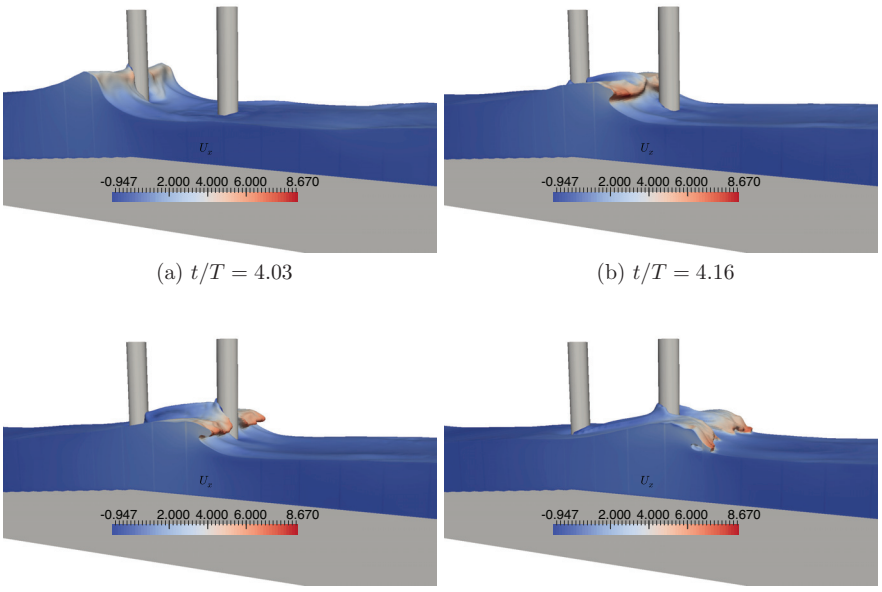

(a) $t/T = 4.03$ (b) $t/T = 4.16$

(c) $t/T = 4.21$ (d) $t/T = 4.30$

Fig. 11. Free surface around the cylinders in scenario D4 ($S = 4D$) with horizontal velocity contours

1 is exposed to a steep non-breaking wave, whereas the overturning wave crest impacts the downstream cylinder 2 just below the wave crest level.

Scenario D6: wave breaking just behind cylinder 1 with $S = 6D$

The wave forces on cylinders 1 and 2 for this case are calculated to be $0.85F_0$ and $1.03F_0$ respectively as shown in Fig. (12a). The wave force on cylinder 2 is significantly higher than the force on cylinder 1 in this scenario. The free surface elevation in front of cylinder 1, $\eta/\eta_0 = 1.78$, is higher than the free surface in front of cylinder 2, which is $\eta/\eta_0 = 1.37$ in Fig. (12b). The runup on cylinder 2 is less for this scenario ($\eta/\eta_0 = 1.37$) when compared to scenario D4 ($\eta/\eta_0 = 1.59$).

The free surface around the cylinders and the horizontal velocity contours are presented in Fig. (13). The steep unbroken wave incident on cylinder 1 is seen in Fig. (13a), similar to that in Fig. (11a). Figure (13b) shows the overturning crest and the water jet originating behind cylinder 1 in between the two cylinders. Fig. (13c) shows the water

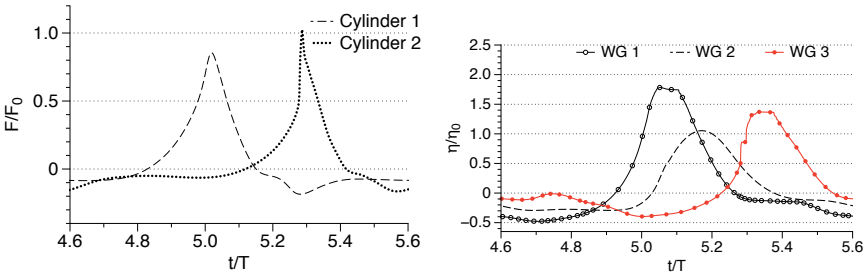

(a) breaking wave forces on the cylinders (b) free surface elevations around the cylinders

Fig. 12. Wave forces on and free surface elevations around the cylinders for scenario D6: wave breaking just behind the first cylinder with $S = 6D$

jet impact on cylinder 2 after the overturning wave crest has impacted the cylinder is seen in . The runup on cylinder 2 in this scenario is lower due to the longer separation distance between the cylinders. The overturning wave crest and the water jet impact the cylinder close to the point where the breaking wave crest reconnects with the preceding wave trough. The broken wave and the water jet formed behind cylinder 2 are seen in Fig. (13d).

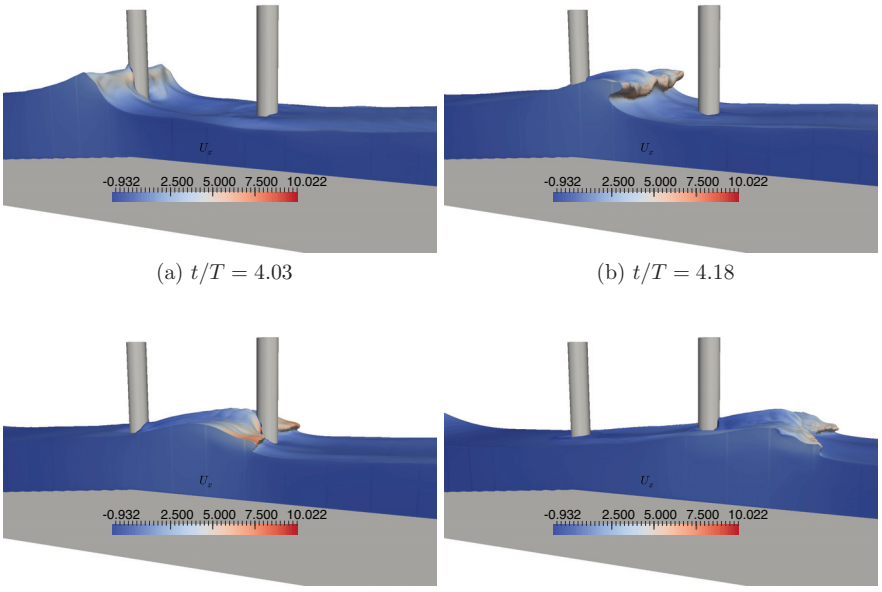

(a) $t/T = 4.03$ (b) $t/T = 4.18$

(c) $t/T = 4.28$ (d) $t/T = 4.46$

Fig. 13. Free surface around the cylinders in scenario D6 ($S = 6D$) with horizontal velocity contours

Variation of the breaking wave forces with separation distance in the different wave impact scenarios

The variation of the total breaking wave forces on each of the cylinders in the different wave impact scenarios and separation distances is presented in Fig. (14). The following sections correlate the variation of the forces with the separation distance with the free surface features associated with the wave impact scenario.

Scenario A

The total wave force on cylinder 1 varies over a small range, between $0.95F_0$-$0.88F_0$ for scenario A in Fig. (14a). For cylinder 2, the total wave force varies significantly with a lowest value of $0.45F_0$ when $S = 3D$ to a highest value of $0.59F_0$ when $S = 1D$. Cylinder 2 is always exposed to a broken wave and the water jet originating behind cylinder 1; the free surface features behind cylinder 1 have a significant effect on the total wave force on cylinder 2. For small separation distances of $S = 1D$ and $2D$,

a separated broken wave crest is incident on cylinder 2, as seen in Fig. (5c). The water jet originating behind cylinder 1, which develops in the small region between the cylinders, is mainly responsible for the force on cylinder 2. The resulting forces for $S = 1D$ and $2D$ are seen to be around $0.58F_0$ in Fig. (14a). When the separation distance increases to $S = 3D$, the force resulting from the impact of the water jet is reduced, and the minimum force is calculated for this scenario. On further increasing the separation distance to $S = 4D$ and $5D$, the wave crest separated by cylinder 1 rejoins the preceding wave trough, undergoes secondary breaking and impacts cylinder 2 along with the water jet. This results in a slight increase in the force on cylinder 2. For $S = 6D$, cylinder 2 is mainly exposed to the post-breaking splash up, and the force on cylinder 2 decreases. Further increases in the separation distance S would result in further reductions in the wave force on cylinder 2.

Scenario B

The total wave forces on both cylinders are significantly affected by the separation distances between the cylinders in this scenario, as seen in Fig. (14b). The total wave force on cylinder 1 is highest for $S = 2D$ with a value of $0.93F_0$ and lowest for $S = 3D$ with a value of $0.61F_0$. For cylinder 2, the total wave force has a maximum value of $0.85F_0$ for $S = 2D$, and a minimum value of $0.57F_0$ for $S = 4D$. For this case, the waves reflected from the cylinders interact with the incident overturning wave crest as seen in Fig. (7a). This results in significant changes in wave forces on both cylinders as the separation distance between the cylinders is varied. When $S = 1D$, the incident wave is separated by cylinder 1, and cylinder 2 is impacted mainly by the water jet. This results in lower forces on cylinder 2. As S increases to $2D$, the separated wave crest rejoins just before impacting cylinder 2, and the force on the cylinder increases. The interaction between the incident wave crest and the reflected waves from the cylinders for $S = 3D$ results in reduced forces on cylinder 1. At the same time, the wave incident on cylinder 2 rejoins the preceding wave trough just in front of the cylinder. The force on the cylinder is reduced, but it is higher than the force on cylinder 1. Further

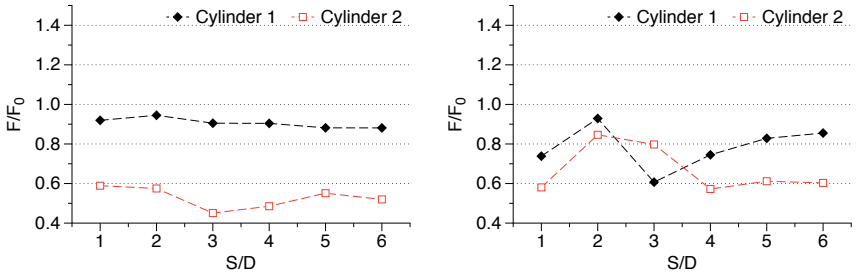

(a) scenario A: breaker tongue impact on cylinder 1 just below wave crest level

(b) scenario B: breaker tongue impact on cylinder 1 at wave crest level

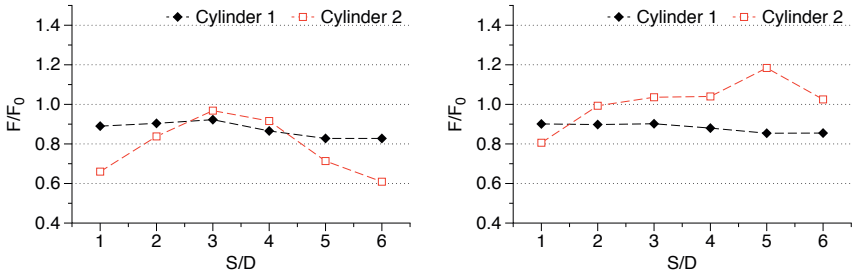

(c) scenario C: wave breaking exactly at cylinder 1

(d) scenario D: wave breaking just behind cylinder 1

Fig. 14. Variation of the maximum wave force on the cylinders with distance of separation S in different wave impact scenarios

increases in S result in lower forces on cylinder 2, since the incident wave has rejoined the preceding wave trough and the cylinder is exposed to splash up. The forces on cylinder 1 increase and nearly reach the value calculated for $S = 1D$ following the interaction between the incident and reflected waves. Hildebrandt et al. (2008) found through large-scale experiments with non-breaking waves on groups of slender cylinders that for certain distances of separation, the forces on the upstream cylinder are influenced by the wave interaction between the cylinders and waves reflected by the cylinders. Their observations are applicable in this case with a strong interaction between the incident wave and the reflected waves when the overturning wave crest impacts cylinder 1 at wave crest level.

Scenario C

In scenario C the front surface of cylinder 1 is at the wave breaking point, and the peak breaking wave force on the cylinder varies between $0.92F_0$ ($S = 3D$) and $0.83F_0$ ($S = 6D$) in Fig. (14c). The peak wave force on cylinder 2 varies significantly with the separation distance, with a maximum of $0.97F_0$ for $S = 3D$ and a minimum of $S = 0.61F_0$ for $S = 6D$. When $S = 3D$ and $4D$, the breaking wave force on downstream cylinder 2 is slightly higher than on upstream cylinder 1. In this scenario, the variation in the forces on cylinder 2 can be attributed to the wave breaking process and the resulting free surface features seen between the cylinders. For $S = 1D$, the incident wave is separated by cylinder 1, and the water jet originating behind the cylinder impacts cylinder 2, leading to a lower force on the cylinder. The separated wave crest rejoins before impacting cylinder 2; this impact and the water jet increases the wave force when $S = 2D$. On further increasing S to $3D$ and $4D$, the breaker tongue impacts the cylinder around the wave crest level along with the water jet as seen in Fig. (9c), resulting in a higher force on cylinder 2 than on cylinder 1. For $S = 5D$ and $6D$, cylinder 2 is exposed mainly to the splash up along with the water jet. The impact of the broken wave on cylinder 2 results in a lower force for $S = 5D$ and $6D$; further increases in S would result in a lower force.

Scenario D

The total wave force on cylinder 1 in scenario D varies over a small range between $0.84F_0$-$0.90F_0$ in Fig. (14d). The peak wave force on cylinder 2 is the lowest for $S = 1D$ ($0.81F_0$) and the highest for $S = 5D$ ($1.18F_0$). Due to the wave breaking just behind the upstream cylinder 1, cylinder 2 is exposed to breaking wave impact and generally experiences higher forces than cylinder 1. Similar to the previous scenarios where cylinder 2 is placed at a distance of $S = 1D$, the incident wave crest is separated by cylinder 1, resulting in a lower wave force on cylinder 2. From $S = 2D$ to $S = 5D$, cylinder 2 is impacted by the overturning wave crest at and around the wave crest level as seen in Fig. (11c) when $S = 4D$, leading to higher wave forces. The maximum peak

force is calculated when $S = 5D$, where the breaker tongue impacts cylinder 2 just below the wave crest level. On increasing S to $6D$, the overturning wave crest rejoins the preceding wave trough during impact with cylinder 2 as seen in Fig. (13c); the wave force on cylinder 2 is reduced.

Discussion

The results show that the wave forces on both cylinders are generally less than the wave force on a single cylinder in the same wave impact scenario (F_0). The exception to this observation are the cases where the breaker tongue impacts the downstream cylinder 2 around the wave crest level. This is particularly the case in scenario D, where the wave breaks behind the upstream cylinder 1 and the overturning wave crest impacts cylinder 2 at or just below wave crest level depending on the separation distance between the cylinders. Another observation is that high runups are calculated on the second cylinder when the cylinders are placed close to each other ($S = 1Dor2D$), but the higher free surface elevations do not correspond to higher wave forces. In fact, for scenarios C3, D4 and D6 the free surface in front of cylinder 2 is lower than that in front of cylinder 1 whereas wave forces are higher on cylinder 2. The close placement of the cylinders leads to a high runup from the water jet developed in the region between the cylinders, but the second cylinder is shielded from breaking wave impact due to the separation of the incident wavefront by the first cylinder.

The trend of the breaking wave forces on cylinder 1 for scenario B varies greatly from the trend seen in the other scenarios for $S = 2D$ and $3D$. This is due to the strong interaction between the incident waves and the waves reflected from the cylinder, as seen in previous studies by Hildebrandt et al. (2008) for cylinders placed close together. In addition, the superposition of the reflected waves on the overturning wave crest is the strongest as seen from Fig. (7a). This leads to a large increase followed by a large decrease in the breaking wave forces for $S = 2D$ and $S = 3D$, respectively, in this scenario. On further increase in S, the breaking wave forces on cylinder 1 are around the values obtained for $S = 1D$, which is the general trend in all the other scenarios.

Some similarities can be drawn between the results for wave forces on tandem cylinders in this study and results for breaking wave forces on a single cylinder in previous studies. With a single cylinder, the maximum wave forces are obtained when the breaker tongue impacts the cylinder just below the wave crest level (Irschik et al., 2002). In the present study, the upstream cylinder 1 also experiences the highest forces in scenario A2 ($F = 13300N$), when the breaking wave impacts the cylinder just below wave crest level. In scenario D4, cylinder 1 experiences one of the lowest forces ($F = 8330N$) when the wave breaks just behind the cylinder. However, the lowest force on cylinder 1 is calculated in scenario B3 ($F = 8174N$) when the overturning wave crest impacts cylinder 1 at the wave crest level. This is due to the interaction between the incident and reflected waves.

For cylinder 2, the highest forces are calculated in scenario D5 ($F = 11564N$), when the cylinder is placed at $S = 5D$ from cylinder 1, and the wave breaks just behind cylinder 1. The overturning wave crest impacts cylinder 2 just below the wave crest level along with the water jet. This is similar to the wave impact scenario leading to the highest breaking wave force on a single cylinder. The lowest force on cylinder 2 ($F = 6300N$) is calculated in scenario A3, where the overturning wave crest rejoins the preceding wave trough before impact with the cylinder. Thus, the results for breaking wave impact on a single slender cylinder by Wienke et al. (2000) and Irschik et al. (2002) are applicable to the case of tandem cylinders as well, though with a few changes due to the interaction between the two cylinders placed in proximity. The results in this study differ from the small-scale experimental results presented by Apelt and Piorewicz (1986), which concluded that the separation between the cylinders did not affect the wave forces on the cylinders when they are arranged in the direction of wave propagation.

CONCLUSIONS

The open-source CFD model REEF3D is used to simulate plunging breaking wave interaction with a pair of cylinders placed in tandem at different separation distances for

different wave impact scenarios. The model was validated by comparing the numerical results for wave forces and free surface elevations with the experimental results for breaking waves on a single cylinder at the Large Wave Flume in Hannover, Germany by Irschik et al. (2002). The free surface features associated with breaking wave interaction with a slender cylinder are presented and correlated to the wave forces on the cylinders, and the following conclusions can be drawn from the results:

- Similar to the results for wave impact on a single slender cylinder, the maximum breaking wave forces in this study is calculated for cases where the breaker tongue impacts the cylinder just below the wave crest level.
- The free surface features behind the first cylinder, such as the separation of the wavefront around the first cylinder, the formation of a water jet, the rejoining of the separated wavefront and the reconnection of the overturning wave crest with the preceding wave trough, have significant influence on the wave forces on the second cylinder. The distance between the cylinders also determines the development of the various free surface features.
- The wave forces on the first cylinder are less than the forces on a single cylinder for the same wave impact scenario for all the cases studied. The highest force on the first cylinder is $0.95F_0$ when the wave impacts the cylinder just below the wave crest level and the second cylinder is at a distance of $2D$.
- The wave forces on the second cylinder are generally lower than the forces on the first cylinder when the wave breaks in front of or on the first cylinder and the separation distance is more than $4D$, with a highest force of $0.71F_0$ when the wave breaks exactly at the first cylinder.
- The wave force on the second cylinder is higher than both the force on the first cylinder and the force on a single cylinder when the breaker tongue impacts the second cylinder around the wave crest level. The highest force on the second cylinder is $1.18F_0$ when the wave breaks just behind the first cylinder and the

second cylinder is at a distance of $5D$.

This study provides insight into the challenging problem of plunging breaking wave interaction with two cylinders in tandem for different wave impact scenarios and distances of separation. Further studies can be carried out and extended to investigate breaking wave interaction with three or more cylinders in tandem, including oblique wave incidence to represent engineering problems including tripod substructures and coastal constructions with multiple cylinders in proximity.

ACKNOWLEDGEMENTS

This study has been carried out under the OWCBW project (No. 217622/E20) and the authors are grateful to the grants provided by the Research Council of Norway. This research was supported in part with computational resources at the Norwegian University of Science and Technology (NTNU) provided by NOTUR, http://www.notur.no (NN2620K).

REFERENCES

Alagan Chella, M., Bihs, H., and Myrhaug, D. (2015a). "Characteristics and profile asymmetry properties of waves breaking over an impermeable submerged reef." *Coastal Engineering*, 100, 26–36.

Alagan Chella, M., Bihs, H., Myrhaug, D., and Muskulus, M. (2015b). "Breaking characteristics and geometric properties of spilling breakers over slopes." *Coastal Engineering*, 95, 4–19.

Alagan Chella, M., Tørum, A., and Myrhaug, D. (2012). "An overview of wave impact forces on offshore wind turbine substructures." *Energy Procedia*, 20, 217–226.

Apelt, C. J. and Piorewicz, J. (1986). "Interference effects on breaking wave forces on rows of vertical cylinders." *Proc. 1st Australasian Port, Harbour and Offshore Engineering Conference, Sydney, Australia.*

Arntsen, Ø. A., Ros, X., and Tørum, A. (2011). "Impact forces on a vertical pile from plunging breaking waves." *Coastal Structures*.

Battjes, J. A. and Sakai, T. (1981). "Velocity field in a steady breaker." *Journal of Fluid Mechanics*, 111, 421–437.

Berthelsen, P. A. and Faltinsen, O. M. (2008). "A local directional ghost cell approach for incompressible viscous flow problems with irregular boundaries." *Journal of Computational Physics*, 227, 4354–4397.

Blenkinsopp, C. E. and Chaplin, J. R. (2008). "The effect of crest submergence on wave breaking over submerged slopes." *Coastal Engineering*, 55, 967–974.

Bonmarin, P. (1989). "Geometric properties of deep-water breaking waves." *Journal of Fluid Mechanics*, 209, 405–433.

Bradford, S. F. (2000). "Numerical simulation of surf zone dynamics." *Journal of Waterway, Port, Coastal and Ocean Enginnering*, 126, 1–13.

Bredmose, H. and Jacobsen, N. G. (2010). "Breaking wave impacts on offshore wind turbine foundations: focused wave groups and CFD." *Proc., 29th International Conference on Ocean, Offshore and Arctic Engineering, Shanghai, China*.

Chan, E. S. and Melville, W. K. (1988). "Deep-water plunging wave pressures on a vertical plane wall." *Proc. of the Royal Society of London. A. Mathematical and Physical Sciences*, Vol. 417, 95–131.

Chaplin, J.and Flintham, T., Greated, C., and Skyner, D. (1992). "Breaking wave forces on a vertical cylinder." *Report no.*, Health and Safety Executive, London, UK.

Chen, G., Kharif, C., Zaleski, S., and Li, J. (1999). "Two-dimensional Navier-Stokes simulation of breaking waves." *Physics of Fluids*, 11, 121–133.

Choi, S.-J., Lee, K.-H., and Gudmestad, O. T. (2015). "The effect of dynamic amplification due to a structure s vibration on breaking wave impact." *Ocean Engineering*, 96, 8–20.

Chorin, A. (1968). "Numerical solution of the Navier-Stokes equations." *Mathematics of Computation*, 22, 745–762.

Christensen, E. D. (1998). "Turbulence in breaking waves – a numerical investigation." *PhD thesis*.

Christensen, E. D. (2006). "Large eddy simulation of spilling and plunging breakers." *Coastal Engineering*, 53(5–6), 463–485.

Christensen, E. D. and Deigaard, R. (2001). "Large eddy simulation of breaking waves." *Coastal Engineering*, 42, 53–86.

Cokelet, E. D. (1977). "Breaking waves." *Nature*, 267, 769–774.

Duncan, J. H. (2001). "Spilling breakers." *Annual Review of Fluid Mechanics*, 33, 519–547.

Durbin, P. A. (2009). "Limiters and wall treatments in applied turbulence modeling." *Fluid Dynamics Research*, 41, 1–18.

Goda, Y., Haranaka, S., and Kitahata, M. (1966). "Study on impulsive breaking wave forces on piles." *Report Port and Harbour Technical Research Institute*, 6(5), 1–30.

Gourlay, M. R. (1994). "Wave transformation on a coral reef." *Coastal Engineering*, 23, 17–42.

Hieu, P. D., Katsutoshi, T., and Ca, V. T. (2004). "Numerical simulation of breaking waves using a two-phase flow model." *Applied Mathematical Modeling*, 28(11), 983–1005.

Higuera, P., Lara, L. J., and Losada, I. J. (2013). "Realistic wave generation and active wave absorption for Navier-Stokes models application to OpenFOAM." *Coastal Engineering*, 71, 102–118.

Hildebrandt, A. and Schlurmann, T. (2012). "Breaking wave kinematics, local pressures, and forces on a tripod structure." *Coastal Engineering*, Vol. 1, 71.

Hildebrandt, A., Sparboom, U., and Oumeraci, H. (2008). "Wave forces on groups of slender cylinders in comparison to an isolated cylinder due to non-breaking waves." *Coastal Engineering*, 3770–3781.

Irschik, K., Sparboom, U., and Oumeraci, H. (2002). "Breaking wave characteristics for the loading of a slender pile." *Proc. 28th International Conference on Coastal Engineering, Cardiff, Wales.*

Jacobsen, N. G., Fuhrman, D. R., and Fredsøe, J. (2012). "A wave generation toolbox for the open-source CFD library: OpenFOAM." *International Journal for Numerical Methods in Fluids*, 70(9), 1073–1088.

Jiang, G. S. and Peng, D. (2000). "Weighted ENO schemes for Hamilton-Jacobi equations." *SIAM Journal on Scientific Computing*, 21, 2126–2143.

Jiang, G. S. and Shu, C. W. (1996). "Efficient implementation of weighted ENO schemes." *Journal of Computational Physics*, 126, 202–228.

Kamath, A., Alagan Chella, M., Bihs, H., and Arntsen, Ø. A. (2015). "Cfd investigations of wave interaction with a pair of large tandem cylinders." *Ocean Engineering*, 108, 738–748.

Kjeldsen, S. and Myrhaug, D. (1978). *Kinematics and dynamics of breaking waves.* River and Harbour Laboratory (NHL) The Norwegian Institute of Technology.

Larsen, J. and Dancy, H. (1983). "Open boundaries in short wave simulations - a new approach." *Coastal Engineering*, 7, 285–297.

Lin, P. and Liu, P. L. F. (1998). "A numerical study of breaking waves in the surf zone." *Journal of Fluid Mechanics*, 359, 239–264.

Miller, R. L. (1987). "Role of vortices in surf zone prediction: sedimentation and wave forces." *The Society of Economic Paleontologists and Mineralogists, Special Publications*, (24), 92–114.

Mo, W., Jensen, A., and Liu, P. L. F. (2013). "Plunging solitary wave and its interaction with a slender cylinder on a sloping beach." *Ocean Engineering*, 74, 48–60.

Morison, J. R., O'Brien, M. P., Johnson, J. W., and Schaaf, S. A. (1950). "Force exerted by surface waves on piles." *Journal of Petroleum Technology*, 2, 149–154.

Nadaoka, K., Hino, M., and Koyano, Y. (1989). "Structure of the turbulent flow field under breaking waves in the surf zone." *Journal of Fluid Mechanics*, 204, 359–387.

Naot, D. and Rodi, W. (1982). "Calculation of secondary currents in channel flow." *Journal of the Hydraulic Division, ASCE*, 108(8), 948–968.

Osher, S. and Sethian, J. A. (1988). "Fronts propagating with curvature- dependent speed: algorithms based on Hamilton-Jacobi formulations." *Journal of Computational Physics*, 79, 12–49.

Peng, D., Merriman, B., Osher, S., Zhao, H., and Kang, M. (1999). "A PDE-based fast local level set method." *Journal of Computational Physics*, 155, 410–438.

Rapp, R. J. and Melville, W. K. (1990). "Laboratory measurements of deep-water breaking waves." *Philosophical Transactions of the Royal Society of London A: Mathematical, Physical and Engineering Sciences*, 331(1622), 735–800.

Sawaragi, T. and Nochino, M. (1984). "Impact forces of nearly breaking waves on a vertical circular cylinder." *Coastal Engineering in Japan*, 27, 249–263.

Schäffer, H. A. and Klopman, G. (2000). "Review of multidirectional active wave absorption methods." *Journal of Waterway, Port, Coastal, and Ocean Engineering*, 126(2), 88–97.

Shu, C. W. and Osher, S. (1988). "Efficient implementation of essentially non-oscillatory shock capturing schemes." *Journal of Computational Physics*, 77, 439–471.

Smith, E. R. and Kraus, N. C. (1990). "Laboratory study on macro-features of wave breaking over bars and artificial reefs." *Report no.*, Coastal Engineering Research Center.

Sparboom, U., Hildebrandt, A., and Oumeraci, H. (2006). "Group interaction effects of slender cylinders under wave attack." *Coastal Engineering*, 4430–4442.

Sparboom, U., Oumeraci, H., Schmidt-Koppenhagen, R., and Grüne, J. (2005). "Large-scale model study on cylinder groups subject to breaking and nonbreaking waves." *Proc. 5th International Symposium WAVES 2005 Ocean Waves Measurement and Analysis, Madrid, Spain.*

Stive, M. J. F. and Wind, H. G. (1982). "A study of radiation stress and set-up in the nearshore region." *Coastal Engineering*, 6, 1–26.

Ting, F. C. K. and Kim, Y. K. (1994). "Vortex generation in water waves propagating over a submerged obstacle." *Coastal Engineering*, 24(1), 23–49.

van der Vorst, H. (1992). "BiCGStab: A fast and smoothly converging variant of Bi-CG for the solution of nonsymmetric linear systems." *SIAM Journal on Scientific and Statistical Computing*, 13, 631–644.

Wang, Z., Zou, Q., and Reeve, D. (2009). "Simulation of spilling breaking waves using a two phase flow CFD model." *Computers and Fluids*, 38(10), 1995–2005.

Watanabe, A. and Horikawa, K. (1974). "Breaking wave forces on a large diameter cell." *Coastal Engineering Proceedings*, 1(14).

Wienke, J. and Oumeraci, H. (2005). "Breaking wave impact force on a vertical and inclined slender pile – theoretical and large-scale model investigations." *Coastal Engineering*, 52, 435–462.

Wienke, J., Sparboom, U., and Oumeraci, H. (2000). "Breaking wave impact on a slender cylinder." *Coastal Engineering Conference*, Vol. 2, 1787–1798.

Wilcox, D. C. (1994). *Turbulence modeling for CFD.* DCW Industries Inc., La Canada, California.

Xie, Z. (2013). "Two-phase flow modelling of spilling and plunging breaking waves." *Applied Mathematical Modelling*, 37, 3698–3713.

Zhao, Q., Armfield, S., and Tanimoto, K. (2004). "Numerical simulation of breaking waves by a multi-scale turbulence model." *Coastal Engineering*, 51(1), 53–80.